



UNIVERSITAT_{DE}
BARCELONA

Development of novel EELS methods to unveil nanoparticle properties

Pau Torruella Besa



Aquesta tesi doctoral està subjecta a la llicència [Reconeixement- Compartigual 4.0. Espanya de Creative Commons](#).

Esta tesis doctoral está sujeta a la licencia [Reconocimiento - Compartigual 4.0. España de Creative Commons](#).

This doctoral thesis is licensed under the [Creative Commons Attribution-ShareAlike 4.0. Spain License](#).

Phd. Thesis

Development of novel EELS methods to unveil nanoparticle properties

Pau Torruella Besa

Directors:

Francesca Peiró Martínez

Sònia Estradé Albiol



UNIVERSITAT_{DE}
BARCELONA

Development of novel EELS methods to unveil nanoparticle properties

Tesi presentada per optar al títol de Doctor per la Universitat
de Barcelona en el marc del programa de Doctorat en
Nanociències

Autor: Pau Torruella Besa
Directores: Francesca Peiró Martínez
Sònia Estradé Albiol
Tutora: Francesca Peiró Martínez

LENS-MIND-IN2UB



UNIVERSITAT DE
BARCELONA

Acknowledgements

Writing this thesis has been a pain in the ass. The years that have led me to this point, however, have been much more interesting. Surprisingly, rather than in the countless hours of lab work and data analysis, when I look back, I find joy in the relationships with all the people that have helped me do this work. I find mandatory to dedicate a few words of gratefulness to all of those that have accompanied me through these years, either with scientific advice, moral support, and, in many cases, both.

I would like to start thanking all the staff from the TEM section of the CCITUB, where I have done most of the TEM work shown in the thesis. Without their care for the equipment and occasional life-saving alignment I could have not done half of what I did. I must also thank Joan Mendoza for his never-ending assortment of nicknames, Quim Portillo for his lengthy and insightful discussion about TEMs and life in general and Félix Mata for his blessing presence.

Although my presence there was much less frequent, I also want to thank the technicians from the ICN2 microscopy facility, Francisco Belarre and Belén Ballesteros, who saved me from the cold with the infamous “batamanta”.

Another place in which I spent many hours in the dark looking at a green phosphorescent screen was the CNME. Many of these hours were shared with Maria Luisa González Ruiz and Almudena Torres Pardo. Their tireless efforts in marathon TEM sessions have certainly had an impact in my PhD, not only with the results that they help to produce, but also by seeing their selfless attitude towards science.

Speaking of results, everything that will be shown in this thesis is a consequence of the collaboration with many excellent scientists. The help of many of them has been invaluable during these years, and it has been a great source of apprenticeship. I must thank Josep Nogués and his team, especially Alejandro Gómez Roca and Marta Estrader, who have provided time and again pretty particles. I have also had a great relation with the team of Albert Figuerola, who can certainly compete in the pretty nanoparticle contest. From his group, I also want to thank Albert, Víctor Fernández Altable and, specially, Mariona Dalmasas, who has done her PhD almost parallel to mine.

I would also like to mention Jordi Sort and his students Enric Menéndez and Alberto Quintana, whom I have met later in my thesis but whose enthusiasm I greatly appreciated.

This section could not be complete without thanking all the collaborators from the CONSOLIDER project and other Spanish projects. Within the participants of the project I found many people to learn from, specially from those with who I worked the closest: Maria Varela, Raúl Arenal, Carlos Díaz Guerra and many more that I cannot list here. They have my sincere gratitude for all the help they have provided me during this time. As for all the other members of the project, although I may have not worked closely to many of them, I sure did enjoy their company in the multiple meetings and dinners.

One of the big leaps forward in the completion of this PhD happened during my stay at the Adam Mickiewicz University NanoBioMedical Center, in Poznan. This was thanks to the excellent working environment and great people that I met. First of all, I must thank Stephan Jurga for giving me the opportunity to work there. I should also thank Grzegorz Nowaczyk for his help in the lab and with the TEM. On another side, I also want to thank all the wonderful people that made my stay during the winter of Poznan much warmer with their friendship. Thank you, Karol Załęski, Ahmet Kertmen, and specially Igor Iatsunskyi, his wife Oleksandra Iliina and their cat for welcoming me as one of their family. Last but definitely not least, there is Emerson Coy, who is the main responsible of the success that this stay was. Whether it was for setting my office, finding where Dragon is, or saving me from the frostbite he was always there with his ever-present cheerfulness, so thank you my friend.

I happened to be lucky enough to also have great colleagues back in Barcelona, specially, at the name-changing electronics department of the UB. I would like to start thanking Albert Cirera, coordinator of the PhD program, not only for the several cases in which he has saved me from being swallowed by bureaucracy but also for the excellent, intellectually-stimulating conversations during many lunch breaks. I also have a great consideration to all the other participants in these, especially for Joan Manel Ramirez and his office-couple, Yonder Berencén, whose fruitful discussions can still be heard in their former office. Speaking of lunch, I also want to mention the great staff from Tinto Pedralbes, where I always left happy, and our beloved Pizza Virona, that made for some epic pizza tower entrances to the faculty.

As for my own office mates, I certainly cannot complain. Many of the great memories that I have during these past years took place in the ten-desk room that has become the so-called “despatx patera”. Many people have come and

gone, but all left their mark, even if it is just old papers in a drawer. In the following lines I want to thank some of the most notable inhabitants of the “despatx”, that have contributed (or the opposite) to my mental health during these years. First to Giovanni Vescio, an Italian as sweet as brownies. Also, to Adrià Huguet, a man with a very bright future, a very tidy table and a very red room. To Oriol Blázquez, who always help me to stay hydrated and with peace of mind. Also, to Martí Busquets, who showed us what good decisions look like. And finally, to Julià López, because I will always be proud to have arrived to work before him (once).

There are also, of course, all the members of the LENS group, who have at one point also stayed at our beloved H23. I must thank Josep Rebled, first for being considerate and letting me finish my thesis first, but most importantly, for his expertise with the air conditioner; then, Gemma Martín, expert in hot sandwiches; Alberto Eljarrat, who taught me a lot about programming, and how to properly schedule our lunch; Lluís Yedra, who taught me so much during my first year and from who I inherited Gumersindo, and who I could only pay back with a warm welcome at Oporto; the other Lluís, with whom I shared room many times and who would help me take good decisions, for the most part; Catalina Coll, my bureaucracy saviour and my suffering partner in one of the hardest studies of this thesis; Javier Blanco, the expert on warfare of the office; and finally the most recent member of the group, Dani to whom I wish the best of luck.

In this last year I left the UB to work at the Microscopy Service of the UAB. The welcome I had as well as the help and understanding of my partners there have made it much easier to finish this PhD. For that, I want to thank Martí de Cabo, Francisca Cardoso, Francesc Bohils, Emma Rossinyol, Judit Pampalona, Ariadna Purroy, Saioa Mendizuri and Núria Barba.

Outside of work I had the great luck to have a group of friends that was always supportive. My friends and former flatmates Jordi García, Núria Fàbrega, Albert Fàbrega, Albert Coberó and Alba Castro have put on with me in my mood swings and struggles, and I am grateful for that. I also want to acknowledge the rest of the “quedem avui” group, Carles Martínez, Isaac Valle, María Sala, Laura Cabezos, Janina Reyes, Marina Ribera, Lidia Puig, Elena Ramírez and Alícia Sánchez for their company during these years.

At this point, I want to dedicate some words to my PhD directors Paqui and Sònia. In the graduate student paradigm, it is frequent to hear so-called “PhD terror stories”, where directors ignore or abuse their students. My reality could not be more opposite to this. Rather than bosses I have ended up having a

university mother and older sister, sort to speak. Undoubtedly, they have made it much easier for me and I hope they continue like with me with the rest of students they will have.

Finally, I want to thank those that are closer to my heart: my mother, Carme, and my father, Lluís, that have always believed in me; my siblings Joan, Miquel and Laura, that have always supported me and asked me to tell them about my PhD, although maybe not understanding half of the time; and also to Sandra, that has been with me all the way through the thesis, both on the good days and the bad days, and that has given me much needed strength in so many moments.

To all of you, thank you.

Index

Acknowledgements	I
Acronym list.....	IX
1. Introduction.....	1
1.1. TEM and AEM	1
1.2. An EELS experiment.....	3
1.2.1. The basics	3
1.2.2. Acquisition modes	5
1.2.3. The EELS spectrum	7
1.3. Advanced instrumentation.....	11
1.3.1. Electron guns	11
1.3.2. Monochromators.....	12
1.3.3. Aberration correctors	15
1.3.4. EELS spectrometers	17
1.3.5. Electron detectors	18
1.4. State of the art of EELS related techniques.....	19
1.4.1. Phonon spectroscopy	19
1.4.2. Ultrafast electron microscopy	20
1.4.3. Electron energy gain spectroscopy.....	21
1.4.4. EELS tomography.....	21
1.5. State of the art of EELS material science applications	23
1.5.1. Single atom detection.....	23
1.5.2. Photonic local density of states.....	24
1.6. Scope of the present thesis	24
2. Mathematical methods for EELS	27
2.1. Multivariate statistical analysis	27
2.1.1. Principal component analysis.....	28
2.1.2. Independent component analysis	33

2.1.3.	Non-negative matrix factorization	34
2.2.	Cluster analysis.....	34
2.2.1.	Introduction to cluster analysis.....	35
2.2.2.	Adapting cluster analysis to EELS.....	36
2.2.3.	Spectrum image simulation test	38
2.2.4.	Experimental spectrum image test	44
2.2.5.	Discussion and conclusions	49
3.	TEM and EELS to understand nanoparticle synthesis	53
3.1.	Introduction	53
3.2.	Iron oxide/silica core-shell nanoparticles from acetate-induced disassembly of iron oxide nanoparticle clusters	54
3.2.1.	Background	54
3.2.2.	Novel synthesis scheme	55
3.2.3.	Characterization	56
3.2.4.	Discussion.....	68
3.3.	Chemistry of noble metal chalcogenide nanocrystals	71
3.3.1.	Introduction	71
3.3.2.	Silver-gold selenide system.....	73
3.3.3.	The silver-gold-sulphur system	81
3.3.4.	Conclusions	92
4.	ELNES analysis applied to nanoparticles.....	95
4.1.	The role of manganese oxidation state in core/shell $\text{MnO}_x/\text{Fe}_3\text{O}_4$ nanoparticles	95
4.1.1.	Synthesis and preliminary characterization.....	97
4.1.2.	EELS assessment of hollow and core/shell nanoparticles	98
4.1.3.	Final testing and additional synthesis.....	102
4.1.4.	Summary	104
4.2.	Atomic resolution cation inversion measurement through EELS in spinel oxides.....	104
4.2.1.	Nanoparticle synthesis.....	106
4.2.2.	Morphological and structural characterization	106

4.2.3.	Cation inversion calculation from ELNES.....	113
4.2.4.	Cation inversion calculation from MVA decomposition.....	120
4.2.5.	Discussion	124
4.3.	Conclusions.....	126
5.	EELS tomography of core/shell nanoparticles.....	129
5.1.	Introduction.....	129
5.2.	EELS tomography of $\text{CoO}_x@FeO_x$ and $\text{CoO}_x@MnFe_yO_x$ core-shell nanoparticles	133
5.2.1.	Integrated EELS signal tomography fundamentals	133
5.2.2.	Synthesis.....	134
5.2.3.	Structural characterization	135
5.2.4.	Integrated edge EELS tomography	142
5.2.5.	Discussion	146
5.3.	EELS tomography of FeO/Fe_3O_4 core/shell nanoparticles.....	148
5.3.1.	MVA-based EELS tomography fundamentals.....	148
5.3.2.	Synthesis of the iron oxide nanocubes.....	149
5.3.3.	Preliminary characterization	149
5.3.4.	EELS tomography acquisition and processing	150
5.3.5.	EELS tomography results	156
5.3.6.	Discussion	160
5.4.	Conclusions.....	160
6.	General conclusions	163
7.	References	171
	Appendix A: Instrumentation list	193
	Appendix B: Collaborations	197
	Appendix C: Resum en català	201
	Appendix D: Scientific Curriculum	209
	Relevant work experience	209
	Education.....	209
	Scientific publications.....	209

Congress contributions211

Acronym list

2D	TWO DIMENSIONAL
3D	THREE DIMENSIONAL
4D	FOUR DIMENSIONAL
ABF	ANNULAR BRIGHT FIELD
AEM	ANALYTICAL ELECTRON MICROSCOPY
AFM	ANTI-FERROMAGNETIC
APTES	3-(AMINOPROPYL)TRIETHOXYSILANE
BF	BRIGHT FIELD
CCD	CHARGE COUPLED DEVICE
CS	COMPRESSED SENSING
CTAB	CETYLTRIMETHYLAMMONIUM BROMIDE
DART	DISCRETE ALGEBRAIC RECONSTRUCTION TECHNIQUE
DDA	DODECYLAMINE
DDD	DIRECT DETECTION DEVICE
DQE	DETECTION QUANTUM EFFICIENCY
EDXS	ENERGY DISPERSIVE X-RAY SPECTROSCOPY
EELS	ELECTRON ENERGY LOSS SPECTROSCOPY
EFTEM	ENERGY FILTERED TRANSMISSION ELECTRON MICROSCOPE/MICROSCOPY
ELNES	ENERGY LOSS NEAR EDGE STRUCTURE
ET	ELECTRON TOMOGRAPHY
FEELS	FEMTOSECOND ELECTRON ENERGY LOSS SPECTROSCOPY
FEG	FIELD EMISSION GUN
FFT	FAST FOURIER TRANSFORM
FiM	FERRIMAGNETIC
FM	FERROMAGNETIC
FT	FOURIER TRANSFORM
FTIR	FOURIER TRANSFORM INFRARED (SPECTROSCOPY)
GPA	GEOMETRIC PHASE ANALYSIS
HAADF	HIGH ANGLE ANNULAR DARK FIELD
HRTEM	HIGH RESOLUTION TRANSMISSION ELECTRON MICROSCOPY
ICA	INDEPENDENT COMPONENT ANALYSIS
IFT	INVERSE FOURIER TRANSFORM
IONP	IRON OXIDE NANOPARTICLE
IONPC	IRON OXIDE NANOPARTICLE CLUSTER
LDOS	LOCAL DENSITY OF STATES

MAPS	MONOLITHIC ACTIVE PIXEL SENSOR
MVA	MULTIVARIATE ANALYSIS
NIR	NEAR INFRARED
NMF	NON-NEGATIVE MATRIX FACTORIZATION
NP	NANOPARTICLE
OA	OLEIC ACID
PCA	PRINCIPAL COMPONENT ANALYSIS
PEELS	PARALLEL ELECTRON ENERGY LOSS SPECTROSCOPY
SI	SPECTRUM IMAGE
SNR	SIGNAL TO NOISE RATIO
SQUID	SUPERCONDUCTING QUANTUM INTERFERENCE DEVICE
STEM	SCANNING TRANSMISSION ELECTRON MICROSCOPE/MICROSCOPY
SV	SPECTRUM VOLUME
TEM	TRANSMISSION ELECTRON MICROSCOPE/MICROSCOPY
TEOS	TETRAETHYLORTHOSILICATE
TOA	TRYOCTYLAMINE
TOAB	TETRAOCTYLAMMONIUM BROMIDE
TOP	TRI-N-OCTYLPHOSPHINE
XAS	X-RAY ABSORPTION SPECTROSCOPY
XPS	X-RAY PHOTOELECTRON SPECTROSCOPY
XRD	X-RAY DIFFRACTION
ZLP	ZERO LOSS PEAK

CHAPTER 1: Introduction

1.1. TEM and AEM

The seminal talk of Richard Feynmann in 1959¹ is generally regarded as the birth of nanotechnology and nanoscience. Remarkably, a long section of the talk was dedicated to electron microscopy and in particular to the relevance of improving the resolution at the time by at least a hundred times, so that you could “Just look at the thing!” to solve many relevant scientific problems. Almost 60 years and many technical advances later, this has been achieved and the impact of transmission electron microscopy (TEM) and TEM-related techniques on nanoscale chemistry, biology and physics has been huge. To highlight this impact let us recall the 4 Nobel prizes in which TEM has played a critical role: to Aaron Klug, 1982 Nobel prize in Chemistry “for his development of crystallographic electron microscopy and his structural elucidation of biologically important nucleic acid-protein complexes”²⁻⁵; to Ernst Ruska, 1986 Nobel prize in Physics “for his fundamental work in electron optics, and for the design of the first electron microscope”⁶, opening the field to which the present thesis is devoted; to Dan Shechtman, 2011 Nobel prize in Chemistry “for the discovery of quasicrystals” first identified in the TEM, through electron diffraction and high resolution TEM (HRTEM)⁷⁻¹⁰; and finally, last year (2017) chemistry Nobel prize to Jacques Dubochet, Joachim Frank and Richard Henderson “for developing cryo-electron microscopy for the high-resolution structure determination of biomolecules in solution”¹¹⁻¹⁵.

These extraordinary works, however, take advantage solely from information related to the elastic scattering of the electrons. However, in parallel to the improvements in TEM spatial resolution and the related material science discoveries, a whole new range of techniques has been developed within the same equipment. These techniques aimed to put some “colour” in the typically black-and-white images of the TEM by obtaining chemical information from the observed sample. This refers to what is typically labelled as analytical electron microscopy (AEM). This collection of methods takes advantage from the variety of inelastic interactions that occur within the TEM to obtain chemical and spectroscopic data at very high resolution.

AEM includes energy dispersive X-ray spectroscopy (EDX), electron energy loss spectroscopy (EELS), cathodoluminescence, and auger spectroscopy among others. However, only the first two have really become mainstream in the TEM. Although the signal, origin and detection mechanism are very different among these techniques, it is possible to classify them in terms of the information they yield. Table 1¹⁶⁻¹⁸ summarizes the most important characteristics of the aforementioned analytical techniques, which use electrons as excitation source in contrast with other local chemical analysis techniques.

An important point to note is that thanks to the development of cold field-emission electron guns¹⁹, scanning TEM aberration correctors^{20,21} and the simultaneous use of multiple EDX detectors²², both EELS and EDX have achieved atomic resolution^{17,18,23-25}. This clearly sets the two techniques apart from all others. Another factor to consider is the last column in table 1. EDX has many advantages, as it is easy to perform and interpret. However, it only yields elemental information, whereas the wealth of information in EELS is much greater.

In addition to elemental quantification, an EELS spectrum can be related to the oxidation state^{26,27} of a given element, its bonding^{28,29}, phonon bands³⁰ in a crystal lattice and the dielectric function of the material³¹ under study among other properties. Having access to the information contained in the different parts of the EEL spectrum, as will be shown in the next section, clearly sets apart the technique from any other existing characterization method.

Technique	Lateral resolution limits	Depth resolution	Detection Limit	Elemental information	Spectroscopic information
EDXS	<1 Å	No	Minor	Yes	No
EELS	<1 Å	No	Minor	Yes	Yes
Auger	10-50 nm	Yes (2-5 nm)	Minor	Yes	Yes
XPS	1-10 μm	Yes (1-5 nm)	Minor	Yes	Yes
XAS	20-200 nm	No	Minor	Yes	Yes

Table 1.1. Comparison of spectroscopy techniques

1.2. An EELS experiment

1.2.1. The basics

Before any further discussion it is necessary to have a broad understanding of how an EELS measurement is carried out in a TEM. A schematic picture of what happens when an electron-transparent sample is observed in the TEM is shown in Figure 1.1.

Let us imagine a crystal upon which an electron beam with kinetic energy E and momentum \mathbf{k} is focused at one point. Incident electrons can suffer scattering from the atomic nuclei that constitute the crystalline lattice. Because of the mass difference between incident electrons and atomic nuclei, little to no energy transfer can happen, and thus these electrons diffract elastically.

In conventional TEM the elastically diffracted beams, after being focused by the objective lens of the microscope, are the ones that generate electron diffraction patterns as well as bright field/dark field and HRTEM images. On the other hand, when the electron beam is focused into a small probe, as in scanning transmission electron microscopy (STEM), electrons elastically scattered can be counted by detectors set at different angles, giving rise to several STEM imaging methods, such as high angle annular dark field (HAADF), annular bright field

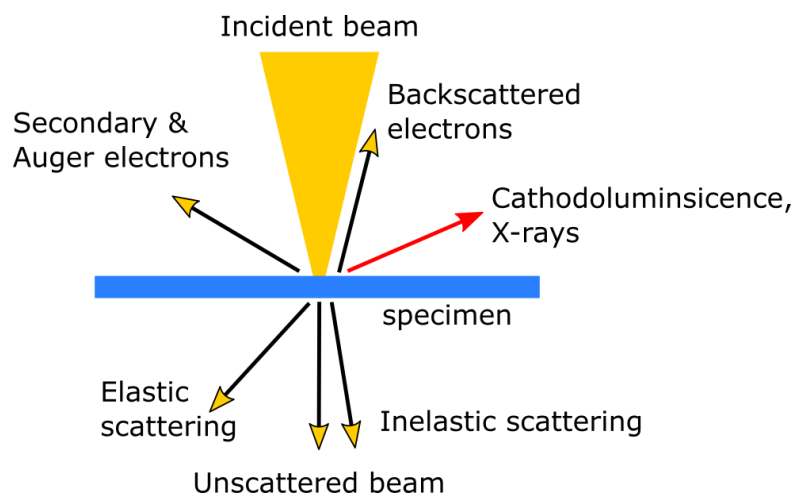


Figure 1.1. Electron-matter interactions in a TEM

(ABF) or STEM bright field (BF). Some of these, such as ABF and HAADF, carry chemical information, mainly related to the mean atomic number of the sample.

However, incident electrons can also scatter with electrons in the sample, an interaction in which a significant amount of energy can be transferred in several processes. The atomic electrons that interact with the incoming beam can be ionized, and in this process generate X-rays, Auger and secondary electrons. On the other hand, for the incident electron, this energy transference will translate into a change in momentum and a reduction of its kinetic energy.

After the interaction with the sample, a fraction of the incident electrons will enter the EELS spectrometer. The simplest design of an EELS spectrometer consists of a circular sector within which a constant magnetic field is directed perpendicular to the electrons trajectory (Figure 1.2). This type of device is a magnetic prism. The Lorentz force that the electrons undergo within the prism magnetic field will bend their trajectories with a radius (R) proportional to their velocity (v), or equivalently, their kinetic energy: $R = \frac{\gamma m_0}{eB} v$.

The electrons will therefore be dispersed along direction (X) depending on the energy that they have lost within the sample. A detector can then be placed in this plane of the spectrometer, thus recording the number of electrons (I) that have lost a certain amount of energy ($\Delta E = E - E'$), and, doing so, recording an EELS spectrum ($I(\Delta E)$).

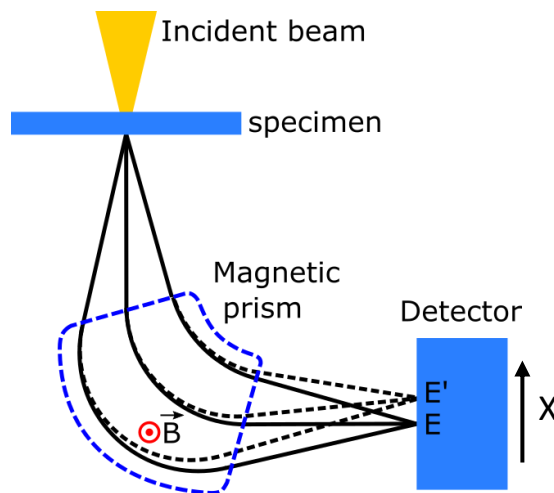


Figure 1.2. Schematics of a magnetic prism spectrometer.

1.2.2. Acquisition modes

Although the physical processes involved in the acquisition of an EELS spectrum have been mentioned, it should be considered that most EELS experiments performed nowadays often do not contend with just a single spectrum. Depending on the considered acquisition mode, EELS measurements may fall into one of four categories: single spectra, spectrum lines, spectrum images (SIs) and more recently, spectrum volumes or EELS tomography.

When considering the electron intensity scattered by a given sample, the relevant variables are the following: the position of the sample at which electrons scatter (x, y, z); the relative orientations of the sample and scattered electrons with respect to the incident beam, and, finally, the energy that the scattered electrons have lost (ΔE). In the previous section, the simplest picture of an EELS measurement was considered, namely an electron beam fixed at one position of the sample. In that case, every other parameter is fixed, and the obtained data is just the scattered intensity for different energy losses, $I=I(\Delta E)$ (Figure 1.3a). Nonetheless, it is possible to acquire successive spectra by scanning the focused electron beam along a certain direction. The measured intensity values will now be a function of probe position and energy loss, $I=I(x, \Delta E)$, a data set referred to as spectrum line (Figure 1.3b). The natural extension of the spectrum line is to scan the beam along two directions, therefore obtaining an intensity that depends on $I=I(x, y, \Delta E)$. This creates an array of spectra much like an image, but with a spectrum associated to each pixel, hence its name: spectrum image (Figure 1.3c). Figure 1.3c highlights the fact that the data acquired in an EELS SI is three-dimensional and is the origin of the term “EELS data cube” that is typically used.

There is another way to visualize the EELS data cube instead of acquiring series of EELS spectra. In energy filtered TEM (EFTEM), images are generated only with electrons that have lost a certain amount of energy. The way to achieve this is to have a slit in the position of the detector in Figure 1.2, so that it blocks all the electrons except those that have lost a certain amount of energy. The slit is followed by the optics that finally project the image onto a camera. As Figure 1.3d shows, this can be understood as observing a slice of the EELS data cube. Its interest relies in the fact that if an appropriate combination of EFTEM images is acquired, at pre-edge, edge and post-edge energy positions, they can be processed to achieve elemental mapping.

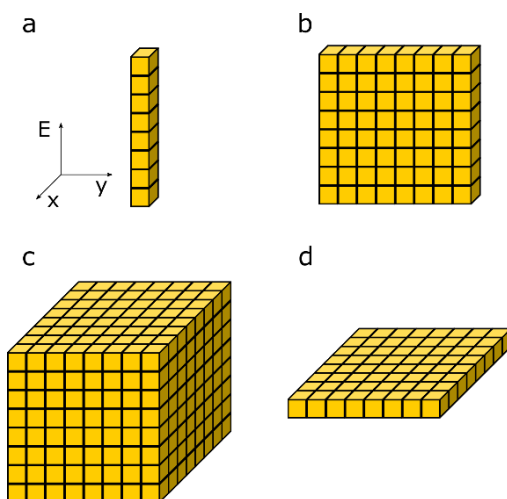


Figure 1.3. Different EELS acquisition schemes: a) single spectrum, b) spectrum line, c) SI and d) EFTEM images.

The last widespread EELS acquisition scheme consists on acquiring a series of SIs at different orientations of the sample (θ) with respect to the electron beam by tilting the specimen along at least one axis. The obtained data now depends on four variables, $I=I(x, y, \theta, \Delta E)$, what can be referred to as an EELS tilt series³². This acquisition scheme pursues to circumvent a shortcoming of SIs, namely that the spectra for each (x, y) actually integrates all the information along the beam direction, and therefore the three-dimensional information of the sample, or in

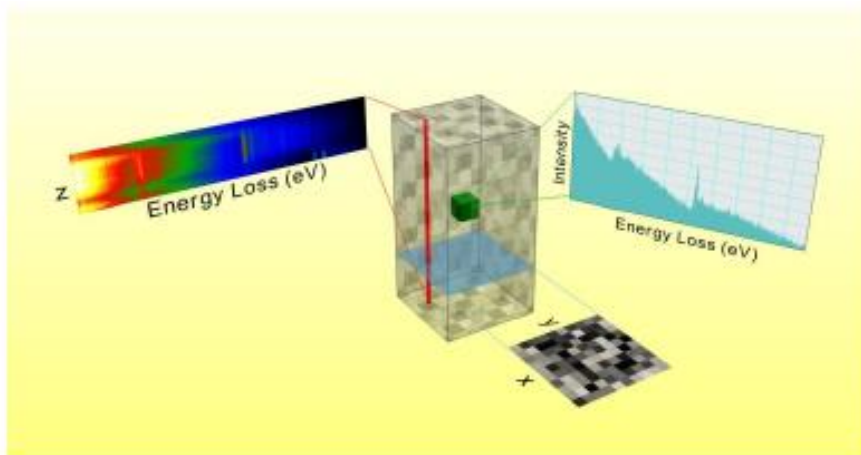


Figure 1.4. Spectrum volume. At each 3D voxel (green cube) an EELS spectrum (right) is contained. Therefore, a line profile along the volume (red arrow) yields a spectrum line (left) and a slice yields a SI (bottom).

other words the z dependence, is lost. By tilting the sample, projections along different angles are acquired and the tilt series can be processed, through electron tomography (ET) methods, into a so-called spectrum volume (SV)^{33,34}. A SV is a data construct that at each three-dimensional (3D) point contains an EELS spectrum ($I=I(x, y, z, \theta)$), as shown in Figure 1.4 (reproduced from the PhD thesis of L.Yedra³⁵).

1.2.3. The EELS spectrum

Now that EELS data acquisition modes have been reviewed, it is time to address which information can be obtained from an EELS spectrum. As previously stated, in its way through the sample, the electron beam can either elastically or inelastically scatter with the electrons and nuclei in the sample, for instance ionizing an atom. The measured energy loss therefore depends on the energy level at which the ionized atomic electron was. However, other processes might be involved in the scattering, such as plasmon or phonon excitation. A basic understanding of atomic and solid-state physics allows us to distinguish between two types of atomic electrons. Atomic electrons in strongly bound states have pretty discrete and highly negative energy levels, whereas, for valence band electrons, the energy levels are continuous and weakly bound, easily ionized, and can be involved in collective oscillations - plasmons. The origin of the distinguishable EELS spectra regions will now be discussed.

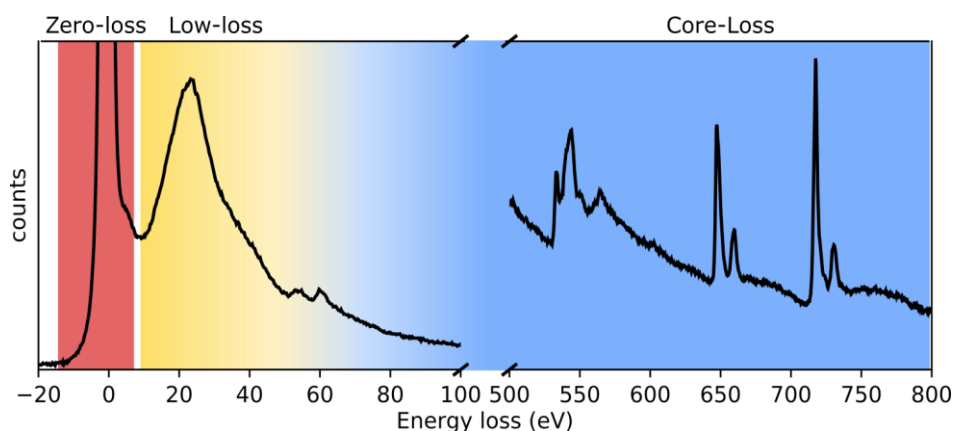


Figure 1.5. Iron/Manganese Oxide spectrum. Zero loss (red), low-loss (yellow) and core-loss (blue) regions are highlighted.

The Zero-Loss Peak

Most electrons that go through the sample will not interact inelastically with it at all. Because of this, when dispersed in the magnetic prism they will have their original kinetic energy, or in other words, an energy loss $\Delta E=0$. This gives rise to the most intense feature of an EELS spectrum, the zero-loss peak (ZLP), labelled in Figure 1.5.

Although the electrons that give intensity to the ZLP have passed through the sample undisturbed, they still can give important information. For instance, the width of the ZLP is generally regarded as the energy resolution of the experiment. The reason for this is that any spectral feature in the spectrum will be convoluted by the original energy spread of the electrons as they are emitted from the electron gun. Additionally, its intensity (I_{ZLP}) can be related to the thickness of the specimen (t). In particular:

$$\frac{t}{\lambda} = \ln\left(\frac{I_{ZLP}}{I_T}\right) \quad (1.1)$$

where λ is the mean free path of electrons in the sample and I_T is the intensity of the whole spectrum.

On the other hand, its position on the spectrometer detector is frequently used to calibrate any offsets.

Low-Loss Region

Energy losses below 100 eV are generally regarded as the low-loss region of the EELS spectra. There are several transitions that give rise to these small energy losses. The phenomena that would contribute to the features with smallest energy losses, at a few meV, would be phonon generation and other vibration excitations on crystalline lattices, although until just recently, a ZLP narrow enough as to not overlap with these features could not be obtained³⁰.

The next interactions in terms of energy loss are surface plasmon resonance excitations, where a surface charge oscillation in the material is induced by the incoming electrons. The surface plasmon distribution of a nanostructure can be

Transition	Energy Loss (eV)
Vibrational excitations	0.05-0.5
Surface Plasmon	1-5
Band Gap	0-10
Bulk Plasmon peak	7-25

Table 1.2. Phenomena that give rise to features in the low-loss region of the energy loss spectrum, listed in increasing energy.

ascribed to size-related and quantum confinement effects, as well as some of its optical properties^{36,37}.

In a similar energy range, band-gap transitions can appear. Since the lowest energy at which an electron can be promoted from valence to conduction band is the band-gap energy itself and no lower energy transitions are allowed, these transitions are reflected as an onset after the ZLP at which the intensity of the spectrum sharply increases again. The position of the onset can be directly related to the band-gap energy³⁸.

At slightly higher energies, a broad and very intense peak or series of peaks generally appear which are related to bulk plasmonic excitations of the specimen. Within the approximations of the Drude model, the position of the plasmon peak can be directly determined from the number of valence band electrons and other composition related parameters, thus making the feature very useful for composition determination³⁹. On the other hand, the width of the plasmon peak can be related to the lifetime of the excitation. In a more general way, the whole plasmon peak is related to the imaginary part of the dielectric function. Therefore, it can be used to directly determine the dielectric function of the studied material. This is performed in the framework of Krammers-Kronig transformations³⁹.

A summary of the interactions reflected in the low loss regime and their energy ranges can be found in Table 1.2.

Finally, some peaks related to strongly bound, discrete electronic states of light elements may be found below 100 eV, but, although their energy falls within the defined low-loss region, because of their origin, they should be considered and treated as core-loss features.

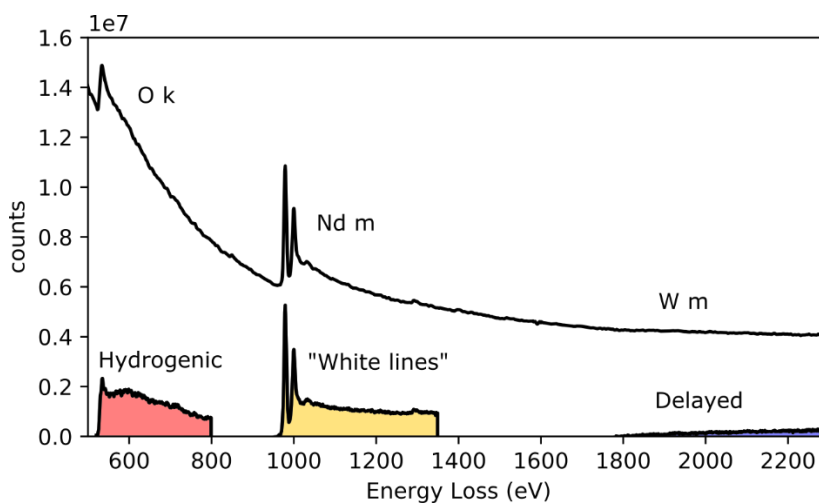


Figure 1.6. EELS spectrum of WNdO, showing a hydrogenic Oxygen K edge, Neodymium M edge white lines and a delayed Tungsten M edge.

Core-Loss Regime

The core-loss regime is typically defined as the energy losses above 100 eV. The origin of these transitions are typically highly bound electron ionizations. The main features that can be observed in this regime are sharp peaks or intensity onsets over a background, referred to as EELS edges. The main contribution to the background is the tail of the plasmon excitations and the previous peaks. It is often modelled as a power law ($I \propto \Delta E^{-\alpha}$). The peaks can be grouped into three broad categories depending on their shape: white lines (yellow in Figure 1.6), hydrogenic edges (red in Figure 1.6) and delayed edges (blue Figure 1.6).

Each edge is related to a single state in an atom, which determines the initial energy level of the ionized atomic electron, and also to the density of free states in the material, which determines the final state of the ionized electron. Therefore, not only can EELS edges yield information on which atoms are present in a specimen and in which amount (elemental quantification), but also on the chemical environment of the atoms. As an example of the latter, the oxidation state of many transition metals can be determined by the relative intensity or the position of their white line peaks^{26,27,40}. This type of information, namely the precise shape of an EELS edge at its onset, is referred to as energy loss near edge structure (ELNES) and is a source of a great wealth of information.

1.3. Advanced instrumentation

Now that the fundamentals of EEL spectroscopy have been reviewed it is important to acknowledge the relevance that equipment development has had and is having in the field. The technique has gone a long way since its beginnings. Its advances, as in many other scientific fields, have been tightly tied to technical developments in the used instrumentation. From large magnetic sectors and photographic plates to electron beam monochromators and acquisitions of thousands of spectra per second, the improvements of the experimental set-up allow not only a higher throughput of data but also the observation and characterization of new phenomena and processes. It is the aim of this section to detail the equipment used in EELS and its latest developments.

1.3.1. Electron guns

One of the most important parts of every microscope is the electron gun. It limits the current and coherence of the electron beam and has direct implications in the resolution and noise of the recorded images and EELS spectra. Most TEMs are nowadays equipped with so-called Field Emission Guns (FEG). To be emitted, the electrons in a solid must overcome a potential barrier. FEGs take advantage of the so called “tip” effect, the fact that for a given voltage the electric field in a tip is inversely proportional to its radius. Therefore, a very narrow tip will experience a very high electric field that lowers the potential barrier, or work function, for the electron emission. In a typical FEG, the process is further aided by heating the tip, which also helps to keep the gun free of contaminants and lowers the vacuum requirements for its operation. This type of gun has good brightness and coherence^{41,42}. However, in recent years a new generation of electron guns with better performance has been introduced.

X-FEG

The extreme-FEG, or X-FEG, is the new generation of electron sources developed by the company formerly known as FEI, now bought by ThermoFisher Scientific⁴³. It is still based on Schottky emission technology, but with an extreme increase in brightness and total beam current as well as better stability. These characteristics are very well suited when the gun is monochromated, since the

starting high brightness leaves a reasonable beam intensity after the energy filtering of the beam.

Cold FEG

As its name implies, a cold FEG is not heated. This has several consequences. The first one is that remnant gases around the tip could adsorb into its surface, therefore changing its work function and hindering the stability of the emission or even preventing it. Both Jeol and Nion companies have overcome these difficulties in two ways. First, keeping the gun in ultra-high vacuum, at the order of 10^{-9} Pa, prevents gun contamination. Secondly, the contamination that may add up during long operations is removed by tip “flashing”, heating the electron source rapidly to eject any surface contamination^{21,44,45}.

The advantages of the cold FEG technology are manifold. A smaller emission region implies a very high brightness, in the order of 10^8 A/m² sr V, increased current density of the emission, and spatial coherence, allowing faster acquisitions of less noisy images and spectra. Additionally, the energy spread of the emission is greatly reduced and can be in the range of the 0.3 eV which, of course, greatly increases the energy resolution of EELS spectra¹⁹.

1.3.2. Monochromators

An EEL spectrum can be understood as the convolution of the electron probe and the unoccupied density of states. Therefore, the width of the energy distribution of the incident electron beam directly limits the resolution of the spectral features. This distribution is given by the ZLP. This brings up another complication, namely that if the zero-loss tail is too intense it masks any spectral feature in the first eV of the spectrum. As explained in the previous section, the energy spread of the ZLP is directly related to the type of gun used and its work function. However, there are tricks to narrow this energy distribution before the beam interacts with the sample. Monochromators have recently been introduced to TEMs to narrow the energy distribution in the ZLP and give access to new information. Apart from filtering the energy spread of the electron beam, thus improving the energy resolution in EELS, they also reduce the chromatic aberration in the imaging system, extending the attainable

information limit in high-resolution imaging⁴⁶. Their features and recent advances in design are discussed in this section.

Single Wien-filter

The simplest TEM gun monochromator design is based on the so-called Wien filter. In it, a magnetic field, an electric field and the optical axis are arranged perpendicularly. Electrons undergo a Lorentz force proportional to the generated field for any velocity different from $v_0 = \frac{E}{B}$, for which electric and magnetic forces balance. This generates a plane where the beam is dispersed in energy. A slit sits in this plane, thus filtering the energy distribution of the beam⁴⁷ (Figure 1.7A).

This is the simplest design of modern monochromators and is the one used by ThermoFischer Scientific⁴⁸. Energy resolutions down to 0.1 eV can be obtained with this set-up. However, the energy dispersion will be present in any image plane of the electron source, which leads to spatial (energy dispersion in the source image) and angular chromaticity (energy dispersion in different trajectories) which are not ideal and are associated to a brightness loss.

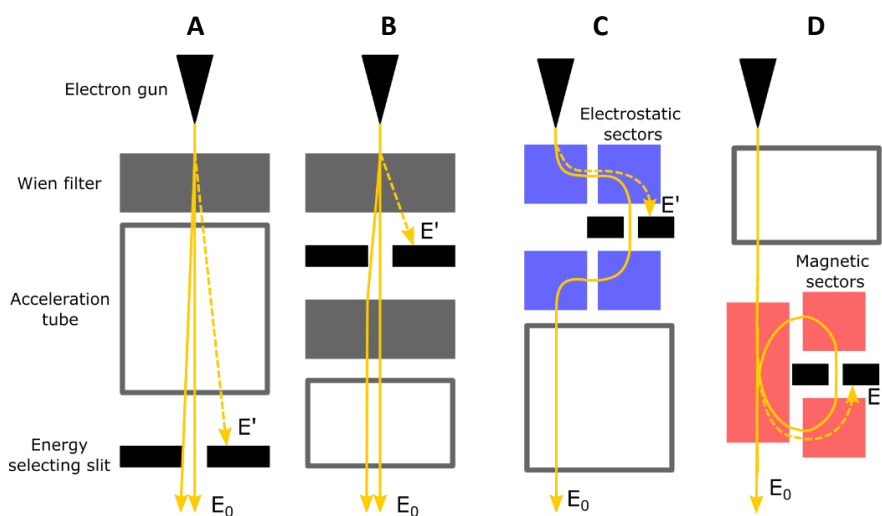


Figure 1.7. Beam diagrams of single (A) and double (B) Wien filters, omega-type (C) and alpha-type (D) monochromators.

Double Wien-filter

In this design, manufactured by Jeol, a second Wien-filter is used after the slit to correct for the energy dispersion in the subsequent source images (Figure 1.7B). This fully corrects for spatial chromaticity and greatly reduces angular chromaticity. A ZLP with an energy resolution down to 0.036 eV at 200 kV can be achieved^{49,50}.

Omega filter

The omega energy filter, developed by CEOS GmbH, is fundamentally different from the previous ones. It consists of four toroidal sector deflectors, arranged forming an Ω -shape, which bend the electron beam only through electrostatic forces⁵¹⁻⁵³ (Figure 1.7C). The monochromator elements are mirrored, with the slit sitting at the mirror symmetry plane. This construction avoids any chromaticity of the source image after the monochromator. ZLPs with a FWHM of 40 meV at 200 kV are reported with this setup, even for relatively long acquisition times (0.5 s).

Alpha filter

The previously described models have in common that the energy filtering occurs before the acceleration tube of the TEM. Therefore, the electrons have an energy of 3-5 keV when they are filtered. The main reason for this is that the fields must be much stronger to produce enough energy dispersion for 200 keV electrons. However, the Nion alpha-type monochromator does just that. Monochromating the beam after it is accelerated allows for correcting instabilities in the microscope high voltage. Additionally, slit charging is much less relevant at these energies.

The device uses a total of three magnetic sectors, one through which electrons travel twice, which bend the beam in an α -shaped trajectory, with a slit in the symmetry plane of the device (Figure 1.7D). Therefore, its optics do not contribute to any chromatic aberration. The magnetic fields disperse the beam in energy and also magnify the dispersion. When implemented, the same current source is used for the monochromator and spectrometer magnetic coils, so that instabilities on that source are automatically compensated⁵⁴.

These technical improvements make it possible for the alpha-monochromator to achieve an energy resolution below 10 meV⁵⁵. This allows for a whole new type of phenomena to be probed with EELS, such as surface phonons and further vibrational spectroscopy³⁰.

1.3.3. Aberration correctors

Spherical Aberration

The spatial resolution attainable in a TEM is diffraction and aberration-limited. By tuning the objective lens and stigmators in a conventional HRTEM, lower order aberrations can be corrected. The optimal resolution (d) attainable in this type of TEM, at the so-called Scherzer condition where defocus balances partially third order spherical aberration⁵⁶, is given by (1.2).

$$d = 0.625 \cdot \lambda^{\frac{3}{4}} \cdot C_3^{\frac{1}{4}} \tag{1.2}$$

Where λ is the electron wavelength and C_3 corresponds to the third order spherical aberration coefficient. From (1.2) it follows that there are only two ways to improve spatial resolution in a TEM, namely, reducing the wavelength of incident electrons (increasing the operation voltage) or reducing third-order spherical aberration. Although the first option has certainly been explored^{57,58}, a true revolution took place in electron microscopy with the development of so-called (spherical) aberration-correctors.

In 1949, the seminal work of Scherzer demonstrated that the spherical aberration was the limiting factor of the achievable TEM resolution and that it could not be corrected by axially symmetric lenses. In 1998, Haider et al.⁵⁹ succeeded in correcting C_3 through two sets of magnetic sextupoles, which was the basic design of the correctors developed by the CEOS company. A year later, O. Krivanek used quadrupoles and octupoles to also correct for this aberration⁶⁰. O. Krivanek later launched the Nion company which manufactures TEMs (actually, dedicated STEMs) with this design of aberration correctors. Further developments of the quadrupole-octupole design allowed the correction of all

aberrations up to fifth order, with an expected resolution given by (1.3), which is limited by $C_{7,8}$, the eight-fold astigmatism of seventh order²⁰.

$$d = 0.6 \cdot \lambda^{\frac{7}{8}} \cdot C_{7,8}^{\frac{1}{8}}$$

(1.3)

In parallel, an effort led by the Japan Science and Technology Agency pursued the correction of the residual fifth order aberration in magnetic sextupole correctors. With three sets of magnetic dodecapoles in a device termed delta-corrector, they succeeded in correcting for six-fold astigmatism, the main residual aberration after C_3 correction⁶¹.

The aberration correctors can be placed either in the condenser system or in the objective lens. The latter is designed to improve HRTEM resolution when the beam is parallel. The former allows obtaining a smaller probe size and the use of higher convergence angles without additional aberrations in STEM mode. This feature greatly improves the resolution in STEM mode and the beam brightness.

These improvements in the electron optics of a TEM have allowed imaging and even EELS mapping with atomic resolution at voltages as low as 30kV, enabling the observation of beam-sensitive materials, such as graphene, which would be damaged at higher voltages^{62,63}. The TEM field is now seeing how fifth-order aberration correctors are coming into scene and its impact is yet to be fully evaluated.

Chromatic aberration correctors

Geometrical aberrations such as spherical aberration are not the only ones to worry about in order to achieve ultra-high resolution. The defocus spread introduced by the energy distribution of the electron beam, instabilities in the high voltage supply and in the objective lens current is characterized by the chromatic aberration coefficient⁶⁴, C_c , and can be the limiting factor of the attainable spatial resolution in latest generation TEMs⁶⁵.

A remarkable tackling of this problem has been carried out in the framework of the TEAM (Transmission Electron Aberration-corrected Microscope) project⁶⁶. The advanced electron optics consisting of magnetic and electrostatic quadrupole-octupoles developed in this project can correct simultaneously for

spherical aberration and chromatic aberration. The principle for correcting chromatic aberration, much like in the case of Wien filters, is to generate crossed electrical and magnetic fields which can filter electron waves of different energies. A precise description of the optics is complex as up to 14 quadrupoles and octupoles are used in the device⁶⁷. A similar design has been pursued by the members of the SALVE (Sub Angstrom Low-Voltage Electron microscope) group⁶⁸. The latter can even account for the energy spread due to the interaction of the beam with the sample, since there are corrector optics after the objective lens. All in all, these efforts have improved the resolution to the absolute information limit, where it is limited by thermal noise in the TEM column⁶⁹.

As for analytical TEM, these designs excel when performing EFTEM, achieving atomic resolution in this mode⁷⁰.

1.3.4. EELS spectrometers

Gatan Inc. is as of today the main manufacturer of EEL spectrometers. The only, and notable, exception is the SESAM microscope, that contains the specially designed MANDOLINE filter, which is capable of performing sub-eV-resolution EFTEM images⁵¹.

The coupling optics to the spectrometer and the magnetic sector that creates the energy dispersed plane necessary for EELS acquisition are also bound to introduce aberrations in the imaging system. These aberrations hinder the energy resolution of acquired spectra. The solution to this problem is to introduce aberration corrector optics to the spectrometer. Gatan introduced a series of eight dodecapoles located after the magnetic sector, which can correct geometric aberrations up to fifth order⁷¹. This system greatly improves the energy resolution, meaning that it is mainly limited by the energy spread of the electron gun emission. Also, fewer axial aberrations allow for the use of higher collection angles in the spectrometer, improving signal to noise ratio and acquisition times.

Electrostatic shutter

With the development of high brightness electron guns, the acquisition times for EEL spectra are bound to be greatly reduced. However, even when having

enough signal there is still the technical limitation of how to acquire spectra at extremely fast rates. The blanking of the electron beam through a strong electrostatic field just after the spectrometer entrance allows for the beam to be stopped extremely quickly and without introducing any hysteresis or complications in the spectrum formation optics, allowing the recording of spectra with acquisition times of a few microseconds^{71,72}.

Dual-EELS

The great variations in intensity in the EEL spectrum, from the low-loss regime to the core-loss regime, have been problematic throughout the history of the technique. Until recently there were no devices with enough dynamic range as to acquire a whole spectrum simultaneously. Nowadays, ultra-fast optics and electronics can record an EELS spectrum in the low loss range and another in the core-loss range with exactly the same conditions, varying only acquisition time in order not to saturate the detector. This has enabled a lot of applications and more precise measurements, since information from the low-loss and core-loss regions can be used simultaneously^{72,73}. Reliable edge onset measurements or high-loss/low-loss deconvolution are just two examples of the newly available possibilities.

1.3.5. Electron detectors

In the early nineties the standard in EELS was the so-called serial detection. Typically, in this scheme, in order to detect the electrons that had interacted with the specimen of interest, a YAG scintillator which generated a light signal when struck by the high energy electrons was coupled to a photodiode²⁷. The system could measure one energy channel at a time and therefore was extremely inefficient in terms of detection quantum efficiency (DQE). At that time, the first implementations of detection systems based on photodiode arrays and charged coupled devices were a great advance. With these devices, all the energy loss channels could be recorded at once, a feature that was named parallel EELS (PEELS)⁷⁴. PEELS massively increased the DQE and shortened acquisition times a hundredfold, as less signal was wasted.

Now a similar breakthrough is taking place. Even if the first PEELS systems were a great improvement with respect to the available technology at the time, they

were still based in the electron-light signal conversion of YAG scintillators. Although necessary to prevent radiation damage on the detector, the usage of scintillators implies certain limitations. A very thin scintillator will produce a small number of photons and will therefore have a low DQE. However, if a thicker scintillator crystal is used, lateral scattering will happen, with an associated loss of spatial resolution. Additionally, some photons are bound to be lost in the optic fibre coupling to the charge coupling device (CCD) camera or photodiode array.

The solution to these issues is the so-called direct detection device (DDD). DDDs are based on Monolithic Active Pixel Sensor (MAPS), a technology that was originally developed for high energy particle physics^{75,76}. DDDs can detect the charge that builds up as highly energetic electrons produce ionizations in a given pixel. The obtainable DQE in commercially available DDDs is as high as 80% and can improve acquisition rates by at least an order of magnitude with respect to the previous technology. These properties have huge advantages to improve the signal to noise ratio of any measurement. In particular, when acquiring data from a beam-sensitive specimen, where a low electron dose is required, DDDs are a must. Moreover, the ability to acquire images and spectra at very high frame rates is bound to disruptively advance EELS and in-situ measurements.

1.4. State of the art of EELS related techniques

Aside from the hardware improvements, the expertise and maturity of the field have translated into an ever-growing number of relevant experiments and new observation modes in EELS. Also, theoretical knowledge and combinations with other techniques have allowed the use of EELS to measure a variety of materials properties that was difficult to image in the past. It is the aim of this section to overview the most interesting developments achieved in recent years.

1.4.1. Phonon spectroscopy

The technical innovations in electron gun monochromators are not simply a great improvement to the energy resolution at which EELS spectra can be acquired. The access to data on the energy range below 1 eV actually opens the path to probing a whole new type of phenomenology, namely phonons and

vibrational information. Previously, only optical spectroscopies such as Raman spectroscopy or Fourier transform infrared (FTIR) spectroscopy could characterize vibration modes in molecules and solids. However, their spatial resolution is at least three orders of magnitude worse than what can be achieved with modern electron microscopes.

The recent detection of an optical vibrational mode of SiO₂³⁰ and C=O, C-H and N-H bond stretching modes in a guanine crystal⁷⁷ constitute practical applications of EELS in this so-called ultra-low energy loss regime⁷⁸. Remarkably, since the delocalization of the electron-matter interaction increases for lower energy losses, the electron beam did not need to be transmitted through the sample in the mentioned works, just close by in the vacuum. This is also a great advantage since radiation damage, a factor limiting the quality of many EELS measurements⁷⁹, can be completely avoided.

1.4.2. Ultrafast electron microscopy

Light-matter and electronic interactions in materials often involve dynamics that occur in both an extremely short timescale and over an extremely small region of space⁸⁰. The motion of electronic wave packets in nanostructures⁸¹ or the dynamics of surface plasmon excitations in metallic nanostructures⁸² are some examples of processes that develop over few femtoseconds and nanometres. A technique capable of observing and characterizing this type of processes must be able to probe electronic properties with the required spatial and temporal resolutions.

In order to achieve this, ultrafast electron microscopy takes advantage of the spatial resolution of TEM and the capability to probe plasmons and other electro-optic phenomena that EELS provides. The method for obtaining the required temporal resolution is to trigger both electron emission from the TEM electron gun and a change in the specimen through a pico-second pulsed laser. The delay between the emission of the pulse and the sample excitation is what determines the temporal resolution of the measurement⁸³.

The combination of this methodology with EELS has been named as femtosecond EELS (FEELS). A recent application of FEELS allowed the observation of chemical bond dynamics in a thin film of graphite and, in particular, the expansion and contraction of the bond length after optical excitation⁸⁴⁻⁸⁶.

1.4.3. Electron energy gain spectroscopy

In a typical EELS experiment, the electrons from the TEM gun can only lose energy due to the scattering with the specimen and, obviously, that is why it is named “energy loss” spectroscopy. However, this needs not always be the case. If a metallic nanostructure is illuminated by an external light source, when the electron beam interacts with it there is a given probability that incident electrons gain a finite amount of energy. If afterwards the electron beam enters an EELS spectrometer, these events will reflect on peaks in the negative region of the EELS spectrum, before the ZLP^{87–89}.

An experimental demonstration of the electron-light coupling in a TEM was achieved by using the same experimental set-up as in the previously described ultra-fast microscopy experiment. A pulsed laser polarized carbon nanotubes which induced energy gain to electrons passing through the evanescent fields at the surface of the nanotubes^{90,91}. This type of measurements not only have pushed forward the theoretical framework of light-matter and plasmonic interactions^{89,92,93}, but also promise a way to explore the optical properties of nanostructured materials in an unprecedented way^{78,87}.

1.4.4. EELS tomography

The fact that electrons are transmitted through the sample in TEM measurements means that the information is projected along the beam direction. This implies the loss of three-dimensional information. Nonetheless, in the early 70s, a way around this issue was developed through the acquisition of images from the specimen along different orientations^{2,3}. These images would then be used to reconstruct the specimen in 3D by taking advantage of the Radon transform⁹⁴ and its link to the Fourier projection-slice theorem.

It took a while until similar principles were used in STEM-HAADF and energy-filtered TEM to obtain Z-contrast and chemically related 3-D reconstructions with subnanometre resolution⁹⁵. The application of these methods to EEL spectroscopy needed further considerations, as an EELS tilt series is actually a four-dimensional (4D) dataset, $I = I(x, y, \theta, \Delta E)$, as opposed to the aforementioned techniques which yield 3D datasets, $I = I(x, y, \theta)$.

There are different methods to process this 4D data set to achieve chemically sensitive tomographic reconstructions. One approach is to integrate the intensity of the spectral signal within an energy window typically containing a characteristic spectral feature (e.g., ionization edge) to form an energy-filtered image. Then, tomography reconstruction algorithms are applied to the corresponding tilt series. The procedure can be repeated for each spectral feature of interest and the results combined for a whole 3D visualization^{32,96,97}. This relatively straightforward method can readily provide volumes with compositional information, although the electronic information in the ELNES would be lost.

Ideally, the tomography reconstruction should contain the full EEL spectrum at each voxel, keeping the energy-loss resolution of the initial spectra. This four-dimensional (4D) construct (i.e., x, y, z spatial coordinates, plus energy loss dimension) has been referred to as a SV^{33,34}. An approach to build such SV is to reconstruct a tomogram for each energy channel in the EEL spectrum⁹⁸. In general, this channel-by-channel approach will require a relatively high signal-to-noise ratio (SNR) in each energy channel to avoid noise-related artefacts dominating in some tomograms. However, obtaining SVs with high SNR may require prohibitively long acquisition times. This leads to a concomitant increased likelihood of cumulative beam damage⁷⁹. In addition, this method has a high computational cost as it may require the reconstruction of many hundreds of tomograms. Alternatively, it is possible to fit reference spectra to the experimental data to obtain the fitting coefficient maps^{32,99} that can be later reconstructed using tomography reconstruction methods^{100,101}.

A more advanced approach would be the use of dimensionality reduction methods, such as Principal Component Analysis (PCA), in order to decompose each EELS core-loss spectra into a linear combination of a few independent components that can often be related to chemical phases in the sample¹⁰².

Notably, the development of PCA enabled EELS tomography was initiated and promoted by the Laboratory of Electron NanoScopies (LENS) group, within which the work for the present thesis has been carried out. Starting from the reconstruction of integrated EELS edge maps³³, the thesis of L. Yedra developed the framework and the requisites that enable the reconstruction of PCA maps obtained from EELS datasets. The fundamental requisite for reconstruction of such maps was their proportionality to the amount of a chemical species present on the sample³⁴. This strategy was successfully applied to characterize complex oxide and magnetic nanocomposites⁹⁶.

1.5. State of the art of EELS material science applications

Throughout the previous sections the fundamentals of EELS and the recent advances in instrumentation have been reviewed. The ability of EELS to solve a wide variety of material science problems has been shown. Some relevant examples from the recent literature are presented in this section.

1.5.1. Single atom detection

The ultimate test to the spatial resolution of any characterization device is single atom detection. It is also a relevant problem since single-atom dopants can strongly affect the electrical, chemical and optical properties of a material. In section 1.3.3 the advances leading to the formation of atomic size electron probes in the TEM have been discussed, but in general EELS acquired at atomic resolution is demonstrated with oriented crystalline specimens rather than with single atoms. The signal that a single atom yields has typically been too small to be discerned.

However, a few years back the identification of single Gd atoms was crudely demonstrated¹⁰³. More recently single atoms of Ca, La, Cs and Eu inside fullerene molecules were observed through EELS spectrum imaging in a DELTA-corrector equipped TEM¹⁰⁴. Although impressive, this work relied heavily on the fact that heavy and rare-earth elements yield very strong EELS signals. Moreover, light atoms are more sensitive to radiation damage which hinders the measurement. It took the capacity to acquire atomic resolution EELS SIs in a TEM operated at 30 kV to detect single atoms of Li, Cl and Na¹⁰⁵.

In recent years a variety of results have reported single atom dopant detection through EELS. Some examples include the detection of nitrogen atoms in N-doped graphene and carbon nanotubes, with emphasis on the C-N bonding and the precise position of the dopants in the carbon lattice^{106,107}. The imaging and bonding characterization of other dopants in graphene such as Si and P has also been possible^{108,109} and for heavier elements, such as Cr, even the assessment of the spin of a single atom¹¹⁰ has also been possible through EELS.

1.5.2. Photonic local density of states

From a theoretical point of view, the optical response of a nanostructure is fully captured in its electric Green tensor and its photonic local density of states (LDOS)¹¹¹. The LDOS is the spatially resolved density of allowed photon wavelengths, and it quantifies the coupling of an atom at a certain position to the modes of a photonic nanostructure and thus describes, for instance, how it affects its optical emission rate¹¹².

Interestingly, the energy loss function of an electron beam passing through or close to a nanostructure can be directly related to the LDOS^{111,113}. This link between EELS and LDOS has opened the door to a wealth of experiments and has allowed researchers to obtain an unprecedented insight into the plasmonic properties of nanostructured materials^{114–116}. Remarkably, in recent years, this concept has been combined with ET^{117–120}. This has allowed mapping the LDOS in three dimensions, thus fully characterizing the interplay of light with the studied nanomaterials in 3D.

1.6. Scope of the present thesis

In the framework of this thesis, advanced EELS analysis methods have been developed and applied to solve state of the art material science problems in combination with other AEM techniques.

In the previous introduction the fundamentals of EELS have been reviewed. The most recent instrumentation developments and the new characterization strategies have also been discussed. Notably, many of the examples presented in this regard do not only rely heavily on the hardware advances, but also on the novel data analysis and computational methods that are being continuously introduced in the field, such as tomography or PCA. Because of their increasing importance, the most widespread and novel mathematical tools will be discussed in chapter 2.

In this context one of the main contributions of this thesis is the adaptation of cluster analysis to EELS datasets. The method is presented in comparison to other state-of-the art EELS analysis tools. The information obtained with clustering and the relevant factors for its use are also discussed in chapter 2.

Finally, an application of this technique to both simulated and real EELS datasets is reviewed in detail to understand the possibilities of this new tool.

The third chapter illustrates the relevance of EELS chemical mapping and other AEM methods such as HAADF imaging to understand critical steps in the synthesis of nanoparticles (NPs). A first example involves a novel synthetic approach to silica @ iron oxide core-shell NPs and the development of a microscopic model of the process. The second work is related to the synthesis of gold/silver chalcogenide NPs through cation exchange reactions. In these NPs, the competition between heterogeneous nucleation of metallic domains and the diffusion of the cation into the crystalline lattice is characterized, again giving an important insight into the microscopic picture of the synthesis.

Further into EELS mapping, the measurement of properties beyond elemental distribution is discussed in two experimental works in chapter 4. In the first part, oxidation state measurements through ELNES analysis and HAADF tomography in transition metal NPs allowed to elucidate the mechanism behind the formation of either core/shell or hollow iron oxide @ manganese oxide NPs. In the second part, ELNES analysis in atomic resolution EELS maps of manganese oxide @ iron oxide core/shell NPs was performed. A method was developed to extract the inversion parameter of these spinel oxide materials. Inversion is a relevant factor in spinel lattices, related to cation distribution in different crystalline sites, with a strong influence on the magnetic properties of these systems.

The last major topic involves the development of EELS Tomography with optimal spatial and energy resolution, as discussed in chapter 5. In the first part of the chapter, EELS tomography based on edge intensity integration is applied to investigate the synthesis of iron oxide @ cobalt oxide and manganese oxide @ cobalt oxide core/shell nanoparticles. In the second half of the chapter, the combination of advanced data treatment and reconstruction methods is used to obtain spectrum volumes with ELNES information. The methods developed are applied to study a FeO/Fe₃O₄ NP in 3D.

Finally, the compilation of the main conclusions is presented in chapter 6.

In summary, with a focus on EELS, the core of the thesis evolves from EELS chemical mapping, to 2D ELNES analysis and ELNES tomography.

CHAPTER 2: Mathematical methods for EELS

The previously discussed advances in hardware have opened a new era to AEM. As acquisition is performed faster and at higher resolutions, new 'big data' challenges are faced in the processing and analysis of multi-dimensional data sets. The ever-increasing amount of measurements acquired in each experiment demands new and sophisticated computational tools to extract relevant information efficiently.

On the other hand, in recent years new concepts, such as machine learning and neural networks, have made their way into microscopy, generating new approaches to TEM/AEM measurements. As an example, automated tomography is an innovative approach to TEM which is a direct consequence of mathematical tools and software being developed for other applications and adapted to microscopy.

Data science has both solved existing problems and enabled completely new applications in the field of electron microscopy. This bidirectional relationship has blossomed into what can be now labelled as computational microscopy.

2.1. Multivariate statistical analysis

Multivariate analysis (MVA)¹²¹ is a family of techniques used to analyse large datasets which contain many variables. MVA has proved useful to gain insight into spectral data in many research fields, such as geological remote sensing¹²², X-ray absorption spectroscopy¹²³, and scanning probe microscopy¹²⁴. In EELS it has been used for more than a decade^{125,126} and so a review of its main applications is mandatory.

The basis of MVA methods involves a linear decomposition of a starting set of measurements ($D_{\vec{x},\Delta E}$), such as an EEL spectrum line or an EELS-SI data-cube, into a series of so-called spectral components ($S_{\Delta E}$) and its corresponding loadings for each spatial position ($L_{\vec{x}}$), effectively splitting the information of the dataset into a spectral basis and its spatial contributions:

$$D_{\vec{x}, \Delta E} = S_{\Delta E} \cdot L_{\vec{x}} \quad (2.1)$$

In the following sections, how to achieve this decomposition and how its use is advantageous for EELS analysis will be discussed.

2.1.1. Principal component analysis

PCA is the most widespread MVA method in AEM. The idea behind PCA is to take a dataset with many correlated variables and to reduce it to a new set of much fewer, uncorrelated variables.

Suppose n measurements of p random variables are performed. Unless p is very small it will often not be very useful to look at the variances of all the p variables and all their correlations and covariances. PCA generates a new set of variables, through linear combinations of the original ones, so that they are uncorrelated, i. e. they are orthogonal and diagonalize the covariance matrix¹²⁷. These new variables represent the spectral components of the MVA linear decomposition, whilst the weights they have for each original measurement are the corresponding loadings.

If those new variables are listed by variance it will often be clear that the first few account for most of the variance in the dataset. This means that to understand how measurements differ from one another, it is enough to consider the first few PCA components and forget about the rest, thus greatly reducing the dimensionality of the problem.

An easier way to understand PCA is to consider an equivalent geometric interpretation. Essentially, our starting dataset contains n points in a p -dimensional space. Now consider the ellipsoid that best fits these points, i. e. an ellipsoid such that the sum of the distances from each point to its surface is minimum. This ellipsoid will have p major axes. PCA finds these major axes, which are the PCA spectral components, and performs a coordinate change so that the original measurements are expressed relative to these major axes. The coordinates in the new basis are no other than the spectral loadings of each measurement.

The dimensionality reduction inherent to PCA can be understood by considering an ellipsoid that is very flat in one direction. By knowing all the coordinates of a

point except that in which the ellipsoid is flat, we already know with great accuracy where the point is, and so, for most purposes information in that direction is not necessary.

Although it is one of the most widespread methods used in EELS analysis, it may be sometimes hard to develop an intuition on how PCA works. To address this let us look at a practical application of PCA in an easily understandable example. In the framework of a 1977 project led by Dr. Jerry Snyder, anthropometric measurements of children were performed at a large scale¹²⁸. Over 50 body measurements, such as height, arm length or waist circumference were acquired from more than 4000 children. In this case, the variables are the height, weight etc. measurements. Therefore, in this case $p=50$ and $n=4000$.

At this point one may be interested in how these measurements are distributed. However, the variables are clearly correlated as can be appreciated in Figure 2.1, where three of these measurements are plotted for all children.

After the diagonalization of the covariance matrix, three eigenvectors with their corresponding eigenvalues are obtained. These are a linear combination of the original measurements as detailed in Table 2.1.

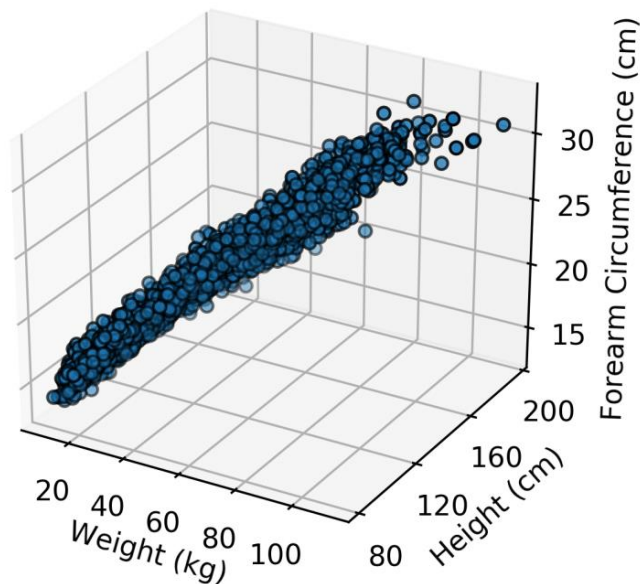


Figure 2.1. Weight, height and forearm circumference from children of the Snyder data archive.

PCA factors	Weight (kg)	Height (cm)	Forearm Circumference (cm)
0	46.5	151.3	22.1
1	32.0	131.8	19.5
2	41.5	119.8	22.3

Table 2.1. Relation between PCA factors and original variables.

The eigenvectors are the PCA spectral components in this context. As explained, they can define new axes to represent the data. In Figure 2.2 the directions defined by the PCA components are shown with the original data. Clearly, how spread the points are in each of the new directions varies greatly. This can be quantified by looking at the fraction of the total variance that is contained in each of the directions (Figure 2.3). This type of plot, known as scree plot, helps to assess how many of the PCA factors are relevant. Incidentally, the fraction of the variance is related to the eigenvalue associated to each PCA factor.

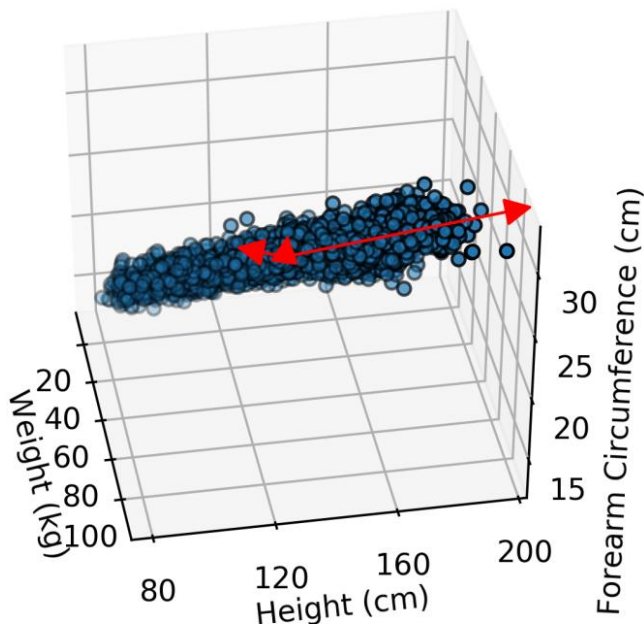


Figure 2.2. New basis defined by the PCA components (in red) along the original measurements.

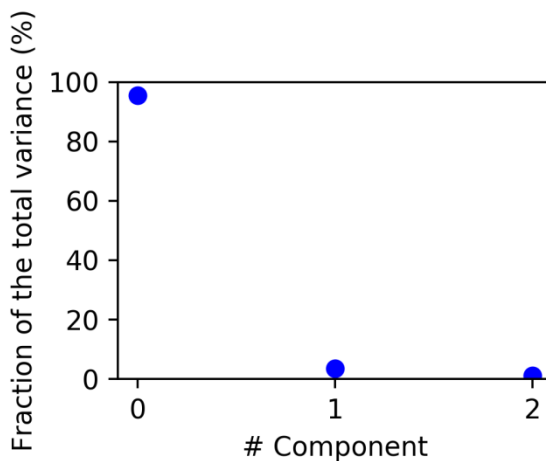


Figure 2.3. Fraction of the total variance for each of the new PCA factors.

Figure 2.3 shows that over 90% of the variation in the data can be explained with one variable, rather than the original 3: weight, height and forearm circumference. This variable would be the first PCA component. To further set the geometrical interpretation of PCA we can plot the PCA ellipsoid (Figure 2.4).

Therefore, we can summarize the information of the dataset into just one variable, the first PCA component, greatly simplifying the original dataset. Now if we understand the information contained in that component, by relating it to

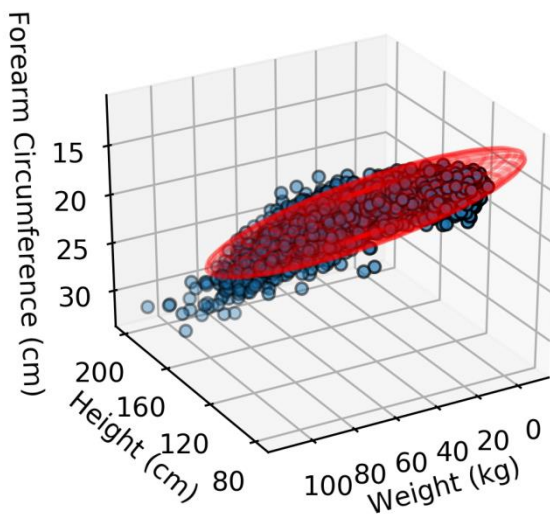


Figure 2.4. Ellipsoid defined by the PCA components (red) alongside the measurements.

an underlying relevant property, we can gain great insight into the dataset. In this case, if we plot the loadings of the first component against the age of each child, we obtain Figure 2.5, and so we can conclude that the main variation of the dataset reflects the usual growth of children.

The use of PCA is now very widespread within the EELS community. Since it was first implemented in Hyperspy¹²⁹, a python-enabled multidimensional signal analysis library, it has been used in EELS analysis in multiple occasions^{33,34,102,130-132}, with many papers dedicated exclusively to algorithm modifications and how they affect EELS data analysis¹³³⁻¹³⁵.

In the framework that has been established in this section, we can consider a spectrum line or SI as a dataset where the variables are the values of each energy channel and a single EEL spectrum is a measurement of those variables. Clearly the values of different energy channels are correlated. For example, energy channels in the background region of core-loss spectra will generally be proportional to each other. In fact, any deviation from this proportionality should be related to noise in the acquisition. Moreover, if noise is the main source of these deviations, they will account for a small portion of the variance in the data. Therefore, after PCA, it can be inferred that most of the components that contain little variance will be related to noise. It follows that with the dimensionality reduction the advantage of noise cleaning of the dataset is gained.

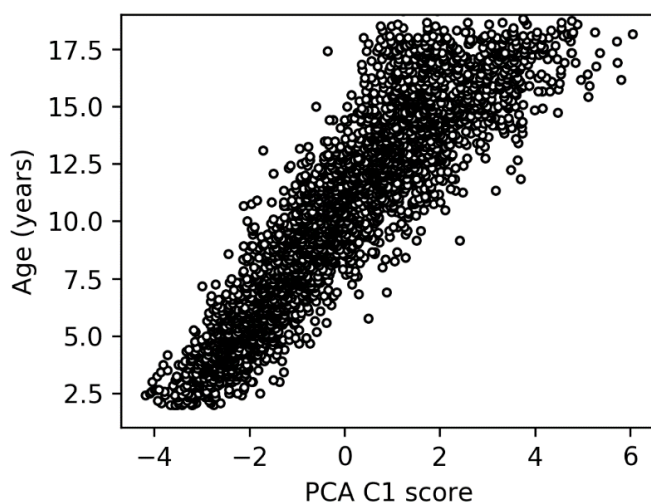


Figure 2.5. First PCA factor scores of each child vs. age of the child.

Three reasons to perform PCA on EELS datasets can be considered. First, the dimensionality reduction: the analysis of fewer variables can be much easier than the starting dataset. Secondly, component interpretation: in favourable cases PCA components can be interpreted in terms of sample composition^{33,132}, much in the same fashion as in the presented example, where the first PCA factor has been interpreted in terms of children age, and so, PCA can give insight into the relevant physical parameters of the measurements. Last, noise reduction: rebuilding the original dataset in terms of just the first few components is an efficient way to denoise EELS measurements.

2.1.2. Independent component analysis

As previously stated, PCA decomposes the spectra onto orthogonal components. This orthogonality requirement in the PCA spectral basis often hinders the recovery of real spectra, i. e., spectra that a given element or compound may yield^{102,136}. Independent Component Analysis (ICA) on the other hand, focuses on finding statistically independent components, i.e., obtaining a spectral basis such that the shared information between its elements is minimized. Deciding what a good measure of mutual independence of the basis vectors (in this case spectra) is can be a complex matter. A given ICA algorithm must choose a function that is maximized when the greatest degree of information independence between components is achieved. Different choices of such functions give rise to a wide range of ICA algorithms^{130,137}.

However, because of the ICA sensitivity to noise and the fact that ICA is very demanding computationally, a very widespread practice is to first apply PCA to the dataset and only then ICA to a model of the first few PCA components¹⁰².

Following this approach several remarkable results have been obtained from EELS data. In particular ICA has enabled the recovery of EELS SVs through ET, i. e. obtaining a 3D model of a sample in which a full EELS spectrum is contained in each voxel^{33,34,96,132}. Moreover it has been used in a wide variety of EELS measurements from samples ranging from perovskite-based solar cells¹³⁸ to III-V semiconductor nanostructures¹³⁹ or to relate ICA components to surface plasmon resonance modes in nanocubes¹⁴⁰.

2.1.3. Non-negative matrix factorization

There are infinite many ways to perform a linear decomposition such as the one described by eq.(2.1). Therefore, additional constraints are always added. In the case of PCA, the constraint is orthogonality between spectral components. In the case of non-negative matrix factorization (NMF), as its name implies, the constraint is that values of both the spectral components matrix ($S_{\Delta E}$) and the loading matrix ($L_{\vec{x}}$) contain only non-negative values¹⁴¹.

The non-negativity constraint is very natural for EELS data since any spectral component should fulfil it to be directly interpretable. Thanks to this, its application to EELS has been successful in many cases, such as the mapping of the plasmonic response in metallic nanocubes, where the obtained NMF spectral components could be directly related to the different excitations modes of a single cube¹⁴². In a similar analysis of surface resonances, NMF allowed the separation of proximal and distal localized surface plasmon resonance modes in Au/Pd octopods as well as the contribution of interband transitions to the EEL spectrum¹⁴³. Also in the low-loss region of the EELS spectrum, NMF allowed the extraction of the signal from silicon nanocrystals from the signal of the silicon oxide matrix in which they were embedded³¹.

2.2. Cluster analysis

All the approaches discussed in the previous section, although starting from different assumptions, aim to find a new basis of spectra with which to represent the information of an EELS dataset. This is certainly useful when one of the elements of the basis can be directly related to a property. However, they are not always easy to interpret in a physically meaningful way.

During the development of the present thesis an effort was made to contribute to make MVA analysis of EELS data more readily interpretable. The result of this effort is the adaptation of cluster analysis for EELS, which will be described in this section.

2.2.1. Introduction to cluster analysis

When wielding the power of modern mathematical tools to tackle EELS analysis, it must be kept in mind that the goal of EEL spectrum imaging is mapping the spatial distribution of properties reflected in the shape of individual EEL spectra. In many cases, this implies finding a way to segment a given SI into different regions, where each corresponds to a different material or has a different property. This can be thought of as classifying spectra into groups with similar characteristics, such as spectra with a peak at the same energy position or spectra showing two edges with a similar intensity ratio. Interestingly, the task of grouping sets of objects by similarity is a well-known problem in data science, named cluster analysis or, simply, clustering^{144–146}.

In general terms, clustering aims to classify a number of objects, n , that have a number of attributes, p , in groups such that objects in the same group have similar attributes amongst them and as different as possible from those in other groups¹⁴⁷. An EELS SI with X -by- Y pixels and E channels can be understood as a series of $n=X \cdot Y$ spectra (our objects), that have $p=E$ attributes (the intensity value in each channel). It is straightforward to transform any SI into an $n \cdot p$ matrix, where each individual spectrum is a row. This matrix is a suitable input for most data clustering algorithms. This can also be understood as representing each spectrum as a point in a p -dimensional space. In this context, the concept of similarity between two spectra is simply the distance between the two corresponding p -dimensional points in any desired metric.

In this frame, a clustering algorithm would label each of these points, or spectra, as pertaining to one cluster or another according to the distances between them. These labels can be assigned a colour and represented into the shape of the original SI, resulting in an image where pixels of the same colour contain spectra from the same cluster. If applied successfully, the spectra clusters should segment the SI into regions with different chemical signatures, revealing the morphology and composition of the studied sample.

There are a variety of clustering algorithms available. K-means, density based methods and agglomerative clustering algorithms are widely used^{145,147} and should be suitable for EELS. In this thesis the scope was limited to explore hierarchical agglomerative clustering because of its speed and simplicity. Its workflow is now described.

Assume initially there are n points in a p -dimensional space to study. Let us denote the coordinates for a given point in that space by x_k ($k = 1 \dots p$). In the first iteration of the algorithm, each of these points would be considered as a different cluster that contains one point. In successive iterations, if the usual Euclidean metric is used the distances between each point are calculated as

$$d_{ij} = \sqrt{\sum_i^p (x_k^i - x_k^j)^2} \quad (2.2)$$

Then the algorithm looks for the two points that belong to different clusters that are the closest. Let us name the distance between these points at iteration h by $\min(d_{ij})^h$. Once these points are found, the two clusters to which they belong are “linked” and in following iterations considered to be the same cluster. If n iterations are performed, all the points will be linked in one single cluster. The term “agglomerative clustering” describes this sequential linking of clusters, agglomerating points that are closer together, until there is only one cluster encompassing all the data¹⁴⁷. But obtaining this final cluster does not provide any information or insight into the data. The way to identify significant clusters is to choose the iteration at which to stop the clustering process. A way to do this is to choose a distance threshold, so that the process is stopped at iteration h for which the condition $\min(d_{ij})^h > d_{\text{threshold}}$ is fulfilled. Therefore, if the last $l=n-h$ links would occur across distances higher than the threshold, $l+1$ clusters would be obtained. The way to choose an adequate value for $d_{\text{threshold}}$ is to consider how $\min(d_{ij})$ evolves with each iteration. Usually it will be small until a certain iteration from which it grows steeply. Defining the $\min(d_{ij})$ value before that significant increase will yield an adequate threshold.

2.2.2. Adapting cluster analysis to EELS

Let us consider a SI simply as a collection of spectra. Let us now consider each of these spectra as a point in a p -dimensional space whose coordinates are the intensity of the spectrum for each value of energy loss. Now, by understanding the spectra in a SI as a collection of p -dimensional ($p=E$) points the algorithm can be directly applied to EELS data.

However, clustering performed this way is merely a segmentation method and some spectral variance might still be present in a given cluster. Nonetheless, there is no hindrance to perform PCA on each cluster, obtaining scores and factors that represent the data on that region. This would assure that all the information in a SI is being used.

Another important factor to consider is noise in the spectra. If it is too severe, different clusters may overlap, hampering the clustering process. Additionally, the computational time of the clustering algorithm would be proportional, among other factors, to the number of energy channels of the spectra. These issues can be simultaneously addressed by following a different strategy to adapt cluster analysis to EELS. If PCA is initially carried out, a series of components and their corresponding score maps will be obtained. Let us assume that the first c components explain all the relevant variance of the SI and the rest are noise. Now, the SI can be represented with only c values for each pixel, each one corresponding to the weight of a component in that pixel. This can also be understood in the clustering nomenclature as having $n=X \cdot Y$ objects each with c attributes (the scores of each PCA component). This great reduction in the number of attributes means that the clustering algorithm will now deal with a much smaller, mostly noise-free dataset, improving the computational time and accuracy in the cluster formation.

Within the scope of this thesis, the three proposed strategies to apply clustering to EEL SI were explored:

- Performing data clustering on the raw data.
- Performing PCA within data clusters.
- Performing clustering on the score maps of an initial PCA decomposition.

The different methods have been tested both with simulated and experimental EELS data, to study how they perform in different scenarios and what pre-processing is necessary in each approach.

2.2.3. Spectrum image simulation test

An artificial EELS SI was generated with 128x128 pixels containing a 1024 channel spectrum each. The spectra reflect the composition of the model shown in Figure 2.6A. It was chosen to be a particle with four main regions: a FeO core of constant composition (depicted in blue in Figure 2.6A), a FeCoO region (as if it was a precipitate, depicted in red in Figure 2.6A), an internal void (depicted in black in Figure 2.6A) and, finally, a shell with varying Fe/O ratio (depicted in green in Figure 2.6A). The intensity of the iron edge in this shell increases linearly from the edge of the particle to the core region, while the oxygen edge intensity decreases in the same proportion. For each of these regions, the spectrum in each pixel was built as a linear model comprised of several factors. First, a power-law background was used. The corresponding hydrogenic cross-sections for each element were added, with an intensity proportional to the chosen concentration of the element. Two gaussian curves were used to model the $L_{3,2}$ white lines for Fe (at 710 eV and 724eV) and Co (at 781 eV and 796 eV). Finally, gaussian and poissonian noise with a signal-to-noise ratio (SNR) of 10:1 were added, resulting in the spectra in Figure 2.6C for the positions highlighted in Figure 2.6B.

In Figure 2.6D the intensity of the channel corresponding to an energy loss of 781 eV (corresponding to Co L_3) is plotted against the intensity of channel 710 eV (corresponding to Fe L_3), where each simulated spectrum is represented by a single point. The latter panel serves to discuss the spectral variance distribution within an SI. It is clear that the data form groups related to the different compositions present in the sample, even with the presence of noise, demonstrating that the EELS data does not follow a normal, PCA-suitable distribution. With this visualization, the adequacy of data clustering in EELS can be appreciated.

Raw data clustering

The simulated SI was transformed into a matrix of 128x128=16384 rows and 1024 columns according to the previously discussed data interpretation. The

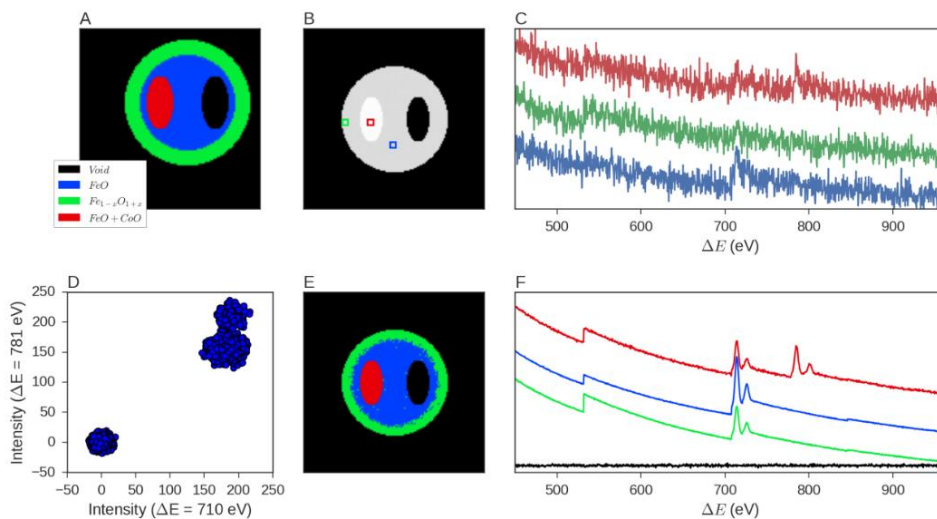


Figure 2.6. A) Model used for the simulated SI. B) The grey level in this panel is related to the sum of all the channels of the spectrum in each pixel. C) Spectra from the markers positions in B): in red a sample spectrum of the iron-cobalt oxide, in green an iron oxide spectrum from the outer iron oxide shell and in blue a spectrum from the central iron oxide. D) Intensity of the 781 eV channel against the intensity of the 710 eV channel, where each point corresponds to a spectrum. E) Results of data clustering: each pixel has been given a colour based on the cluster at which its spectrum belongs. F) Averaged, normalized spectra from each cluster.

simulated data was then fed to the hierarchical agglomerative clustering algorithm.

An interesting way to visualize the clustering process is to plot the so-called linkage tree of the clustering process. The clusters are laid along the x-axis of the plot, sorted by an arbitrary identification number. The y-axis represents distance as defined by (2.2). A vertical line arises from each cluster. These vertical lines are linked by horizontal lines at a height which corresponds to the $\min(d_{ij})$ at which they were merged together in the clustering process. The result is a tree-like plot, denominated “dendrogram plot”, which can be seen in Figure 2.7, that gives an idea of the clustering evolution.

In Figure 2.7, it is evident that the last three links occur across distances at least an order of magnitude greater than the previous ones, indicating that this would be an adequate $d_{\text{threshold}}$. Consequently, previous clusters are discarded, yielding four clusters. The output of the algorithm is a vector of length 16384 which contains the labels of the cluster to which each spectrum pertains. This vector can be reshaped into the original image as shown in Figure 2.6E, where pixels

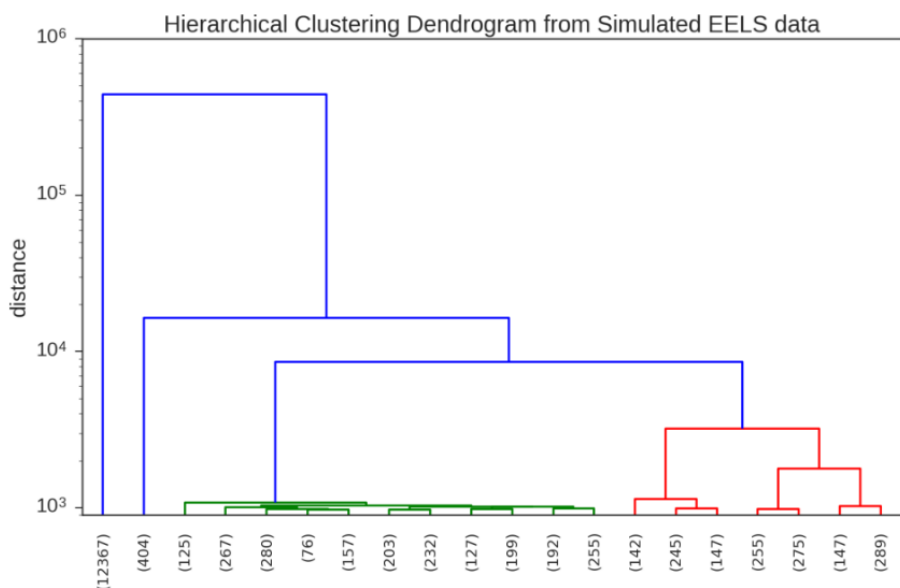


Figure 2.7. Dendrogram plot for the last 20 hierarchical clustering links of the simulated data. Horizontal axis represents individual clusters, identified by an id number. A link is represented by a horizontal line that goes from one cluster id to another. The height at which the links form is the distance between the two linked clusters. Green and red link trees occur below the chosen distance threshold.

that contain spectra from a given cluster are displayed with the same colour. Here they are chosen to match those used in the model, green for the shell cluster, blue for the core cluster, red for the FeCoO region and black for the pixel cluster that represents the background. Clearly, the obtained clusters give an excellent representation of the data, recovering the initial composition of the simulated SI. Moreover, it is now possible to obtain the average spectrum of each cluster (Figure 2.6F), showing the chemical composition from each of the image segmented regions.

Nevertheless, according to Figure 2.6E, the procedure seems to have failed in identifying the existence of the composition gradient in the shell. This exemplifies a case where there are relevant differences within a spectra cluster.

Figure 2.8 shows the segmentation results with three different threshold values, revealing several clusters within the shell related to the linear variation of Fe and O. This illustrates the relevance of an appropriated choice of the free parameter $d_{\text{threshold}}$ to unveil all the significant information contained in the spectra. Still, discrete segmentation of a property that varies continuously is a suboptimal representation and an inherent limitation of this “only clustering” approach. Nonetheless, this limitation can be overcome by performing PCA for each cluster.

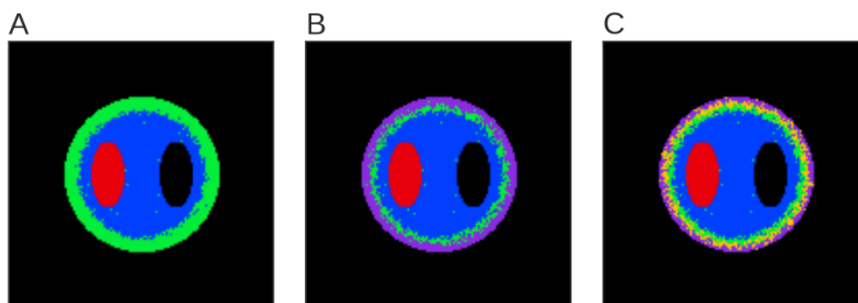


Figure 2.8. Clustering results of the simulated SI with different distance thresholds. A) corresponds to a distance threshold of 5000 counts. B) corresponds to a distance threshold of 2500 counts. C) corresponds to a distance threshold of 1500 counts. These values correspond to the y-axis of Figure 2.7.

Principal component analysis within a cluster

Instead of searching for an adequate threshold value that reveals the spectral variation in the outer shell of the particle, it is possible to apply PCA to the spectra that comprise this cluster. This is equivalent to performing PCA while masking the spectra for all pixels not pertaining to the cluster.

The results of PCA applied to the $\text{Fe}_{1-x}\text{O}_{1+x}$ shell of the simulated data (green cluster in Figure 2.8A) are shown in Figure 2.9. The algorithm resolves that two main components explain the data, a mean iron oxide spectrum (Figure 2.9A) and a spectrum of positive oxygen signal and negative iron signal that varies in intensity along the shell (Figure 2.9B). The second factor demonstrates a varying Fe/O ratio in the shell, which is the origin of the problems in the segmentation of the shell seen in Figure 2.8. With this secondary analysis, the use of all the information in the SI is assured, and no compositional changes are missed. This second factor also shows a common effect of PCA, that is, to yield factors with negative values. Although in this case it can be directly interpreted in terms of compositional gradient, it is typically hard to assign physical meaning to spectra with negative features.

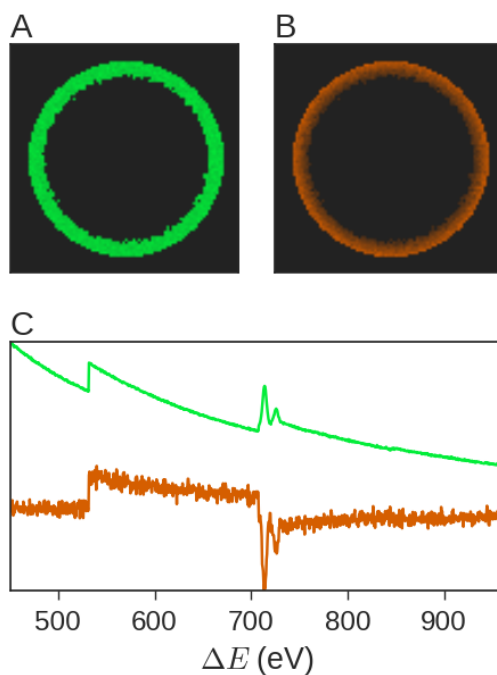


Figure 2.9. A) Score map from the first PCA component of the shell in the simulated SI of Figure 2.6. B) Score map from the second PCA component of the shell in the simulated SI. C) Factors of the corresponding score maps in panel s A) and B).

Clustering PCA scores

If the SNR of the simulated spectra decreased, the point groups in Figure 2.6D would be more spread, and different clusters could overlap. This would obviously hinder the clustering process and is one of the reasons to perform clustering on PCA score maps rather than on the raw data.

PCA of the simulated SI demonstrates that the data can be explained with only three components (Figure 2.10A). This means that now the SI information can be represented by only three values per pixel, and that the clustering input matrix will have 16384 rows and three columns.

The clustering result on these PCA scores is essentially the same as on the raw data, as seen in Figure 2.11. However, now, less pixels in the core of the particle are mislabelled as shell, and the segmentation into two shells occurs at a slightly higher distance, meaning that the different clusters are more clearly segmented

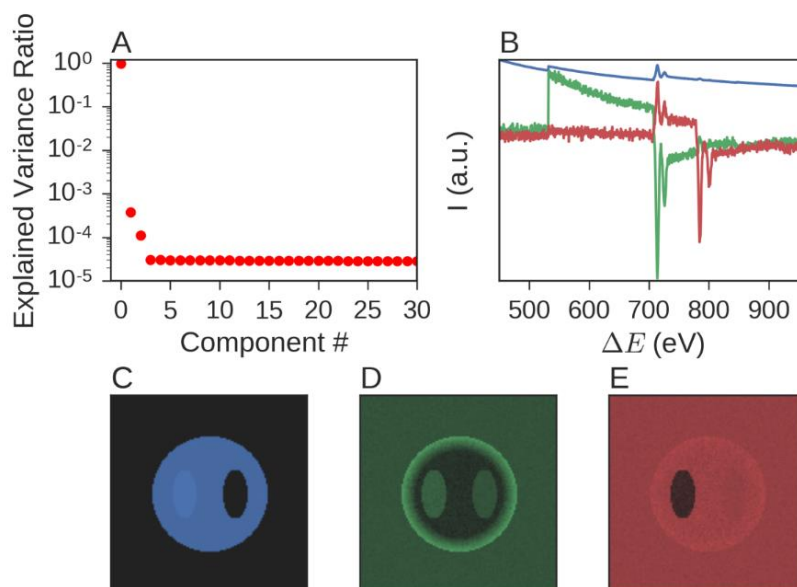


Figure 2.10. PCA decomposition results of the simulated SI. A) Normalized variance ratio of each PCA component from the SI of Figure 2.6A. B) The three first factors of the PCA decomposition. C-E) Score maps for each factor. Colour coded.

(dendrogram tree in Figure 2.12). Note that a segmentation of the shell into several clusters is a better representation of the composition variation. Otherwise, the (wrong) idea that the shell is uniform might be apparent. Additionally, links of the dendrogram tree at higher distances, more spaced, mean that the algorithm is able to distinguish the differences between clusters more easily. These results demonstrate a significant improvement with respect to the raw spectra clustering, and the benefits may be even more noticeable in SI with lower SNR.

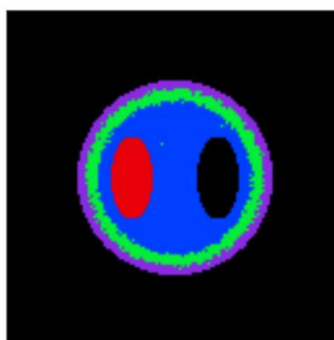


Figure 2.11. A) Clustering result on the first three PCA scores from Figure 2.10. Each colour corresponds to a spectra cluster.

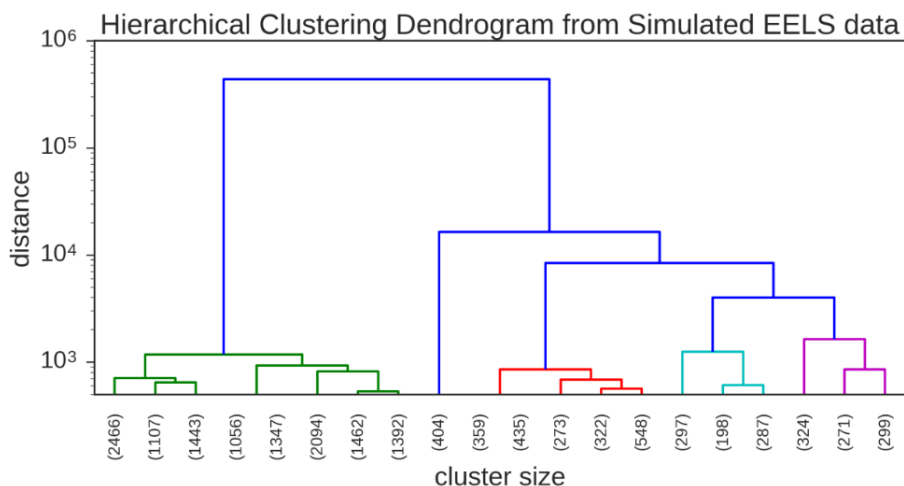


Figure 2.12. Dendrogram plot for the last 20 hierarchical clustering links of the PCA scores from the simulated data decomposition.

These are promising results, allowing identification of regions with different chemical composition and demand further testing with experimental data.

2.2.4. Experimental spectrum image test

The three described strategies have also been tested in an experimental SI. The sample studied consisted in $\text{Fe}_3\text{O}_4/\text{Mn}_3\text{O}_4$ core/shell NPs. The NPs were obtained using the seeded-growth method^{148,149} where the Mn oxide layer was grown on 11 nm Fe_3O_4 seeds by hot injection¹⁵⁰. An EEL SI of the NPs was acquired in an aberration-corrected Nion UltraSTEM200 operated at 200 kV and equipped with a Gatan Enfina spectrometer (Gatan). The simultaneously acquired scanning TEM dark field image of the SI is shown in Figure 2.13A. Previous analysis of the NPs was performed through ELNES parameter fitting¹⁵¹. This was done with the Oxide Wizard software. This software, developed within the LENS group, serves to quantify all the ELNES parameters of a “white lines” EELS spectrum with minimal user input, so as to obtain values as reliable as possible. It basically interprets a white lines spectrum as the sum of two gaussians and a cross-section curve. By fitting this model to the experimental spectra, all the relevant ELNES parameters can be obtained: L_3 onset, L_3 - L_2 distance, L_3/L_2 ratio etc. The obtained ELNES parameter maps revealed that the core of the NP was Fe_3O_4 . Mn L_3/L_2 ratio maps showed the surrounding manganese oxide to be Mn_3O_4 nanocrystals with an external shell of MnO.

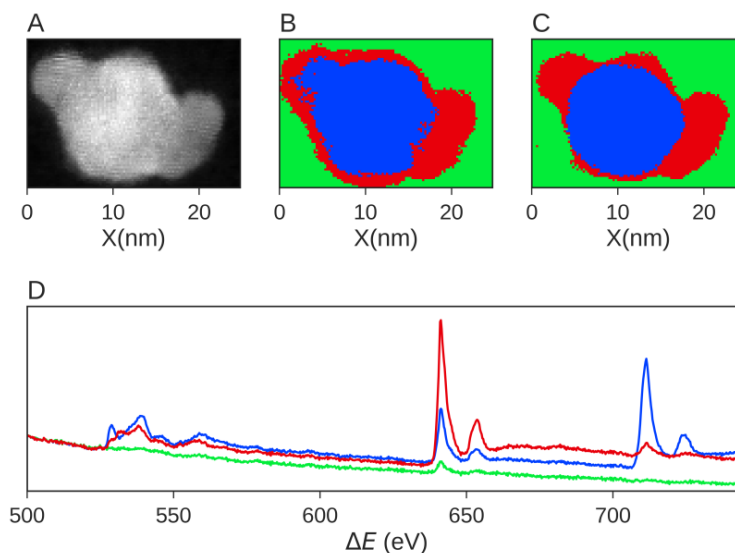


Figure 2.13. A) HAADF image simultaneously acquired with the SI for the $\text{Fe}_3\text{O}_4/\text{Mn}_3\text{O}_4$ core/shell NP. B) Clustering results of the SI without normalization. Each colour corresponds to a cluster. C) Clustering results of the SI with intensity normalization. D) Averaged spectra from each cluster.

Raw data clustering

Even though the simulated example demonstrates how clustering can correctly identify regions of an SI with different compositions, some considerations must be made before moving on to experimental data. Most TEM samples have changes in thickness that would hinder clustering in terms of chemical composition. Regions with the same composition but different thicknesses would be at large distances because, even if the “shape” of the spectra is the same, the total intensity is very different. This effect is shown in Figure 2.13. The clustering analysis of the raw data (Figure 2.13B) yielded three different clusters, which fail to adequately represent the chemical composition of the NP^{150,151}, since the blue cluster spans regions of both the central and the left crystal which have different composition.

To circumvent this problem, the normalization of each spectrum by the integrated intensity of all energy channels is proposed. After normalization, the three data clusters that are found (Figure 2.13C) and their corresponding mean spectra (Figure 2.13D) clearly segment the SI into manganese oxide (red), iron

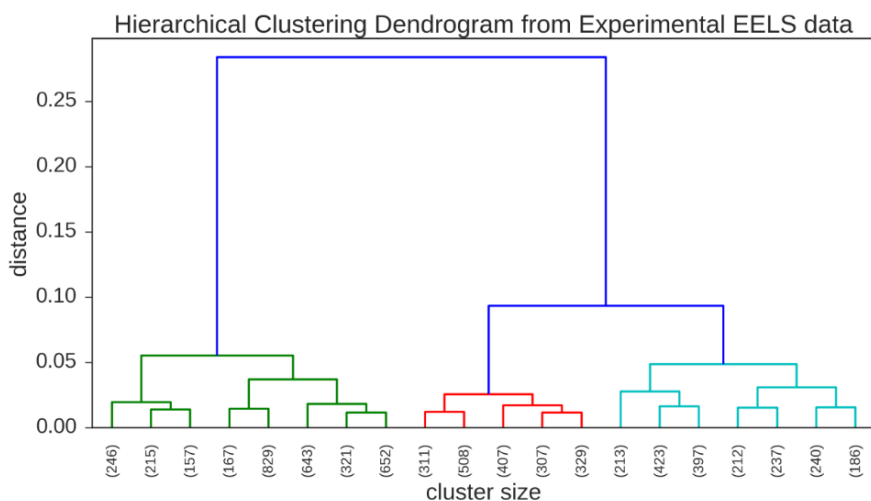


Figure 2.14. Dendrogram plot for the last 20 hierarchical clustering links of the experimental SI.

oxide (blue) and supporting grid (green). This shows that automatic segmentation of real data into chemically distinct phases is possible through spectra clustering.

In this positive result two things should be noted. Firstly, the average spectrum of the NP core has some manganese signal. Its origin is the three-dimensional nature of the NP and, thus, the presence of some manganese oxide above the iron core. The type of image segmentation that clustering provides cannot unmix these signals. Additionally, this first method fails to “see” different Mn oxidation states. The chosen clustering threshold is shown in Figure 2.14, where it is clear that links occur at very similar distances after the first two (which after being discarded yielded the three clusters on Figure 2.13C).

Principal component analysis within a cluster

If PCA is performed on the manganese oxide related data cluster, labelled in red in Figure 2.13C, the components shown in Figure 2.15 are obtained. Clearly, the PCA factors (Figure 2.15C) have Mn L edges with very different L_3/L_2 intensity ratios. The value found for the blue component is $L_3/L_2 \approx 2.2$ and for the red component $L_3/L_2 \approx 4.3$. Actually, the components with this ELNES features^{27,40,152} directly map the Mn^{3+} (Figure 2.15A) and Mn^{2+} (Figure 2.15B) concentrations. It must be pointed out that such clear results are very hard to obtain straight away

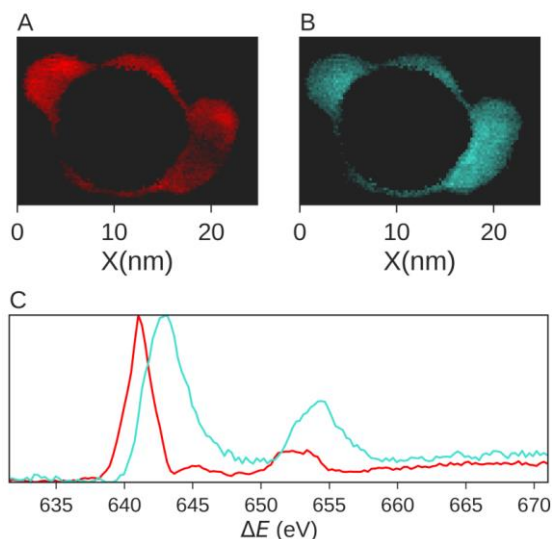


Figure 2.15. A) Score map from the first PCA component of the manganese oxide shell of Figure 2.13C. B) Score map from the second PCA component of the manganese oxide shell of Figure 2.13C. C) Factors of the corresponding score maps in panels A) and B).

from PCA. In fact, PCA of the whole raw data set was performed (Figure 2.16) and no physically meaningful components with straightforward interpretation were obtained, demonstrating the virtues of the clustering plus PCA scheme.

Clustering PCA scores

Last but not least, the clustering on PCA scores strategy was tried out. From Figure 2.16 it follows that the first 6 components are enough to explain the data of the SI. Again, normalization must be undertaken in order to get results related to chemical composition rather than just related to thickness variation. In this case, each score map was divided by its maximum value. After hierarchical clustering (final clustering tree in Figure 2.17), four spectra clusters were found. As can be seen in Figure 2.18, they correspond to the support membrane, iron oxide, and two different manganese oxides. The average spectra for each of these regions show manganese oxide spectra with different Mn L_3/L_2 intensity ratios, demonstrating the already known $Mn_3O_4 - MnO$ structure of the crystals. Therefore, the fact that the PCA representation cuts a lot of the noise was critical to allow the segmentation of both oxidation states.

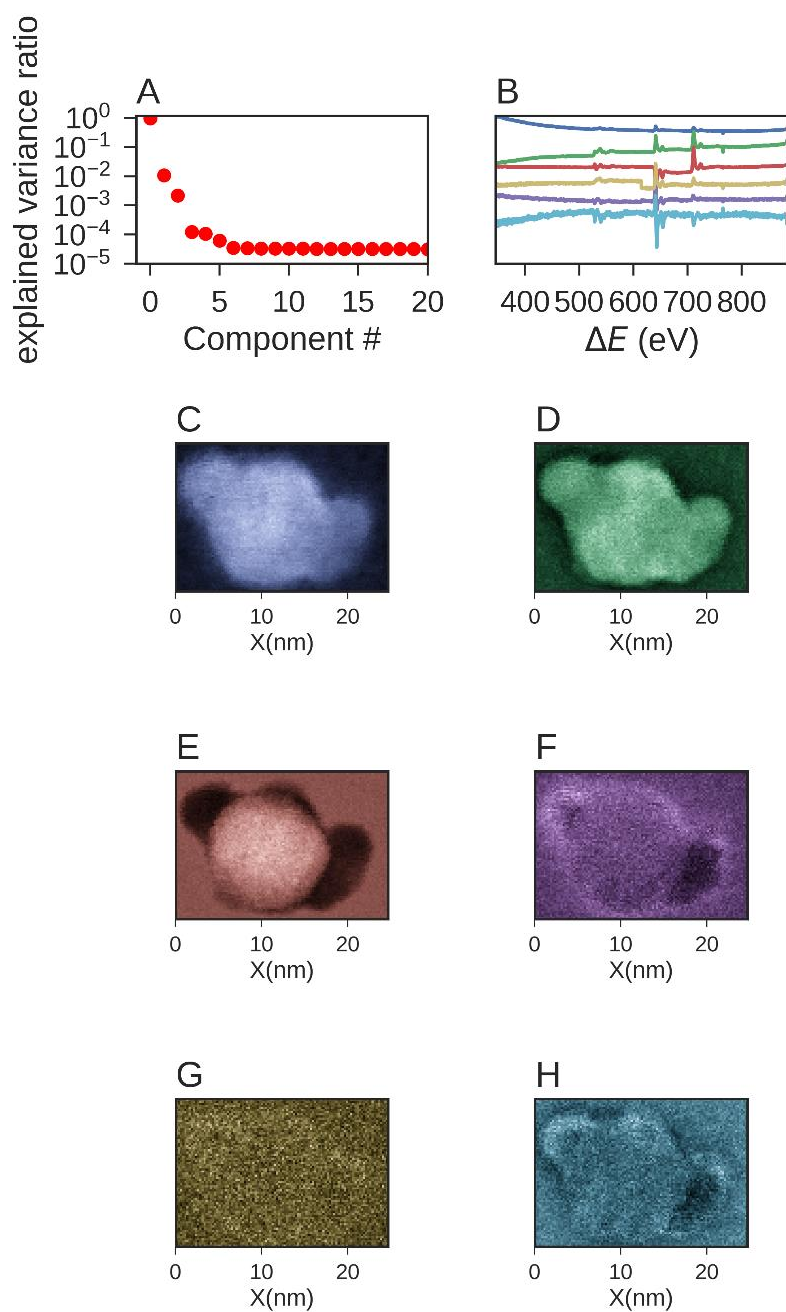


Figure 2.16. PCA decomposition results of the experimental SI. A) Normalized variance ratio of each PCA component from the SI of Figure 2.13. B) The six first factors of the PCA decomposition. C-H) Score maps for each factor. Colour coded.

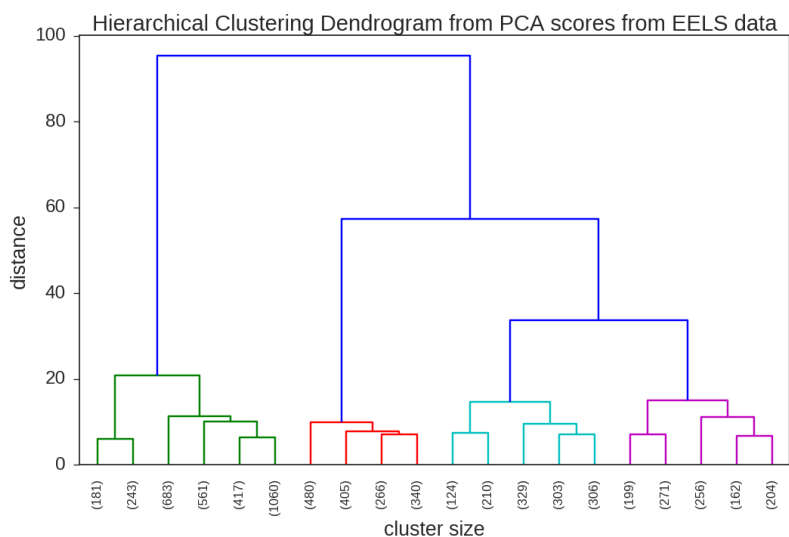


Figure 2.17. Dendrogram plot for the last 20 hierarchical clustering links of the six first PCA scores from the experimental SI.

2.2.5. Discussion and conclusions

The presented results show that data clustering is a suitable analysis tool for EELS data sets. It is able to identify regions of different composition without any prior assumption concerning the data. This is certainly an advantage over the mentioned spectra modelling, which is limited to well-understood spectral features such as white lines. This advantage is shared with PCA and ICA. ICA, in particular, is expected to yield physically meaningful components, but that

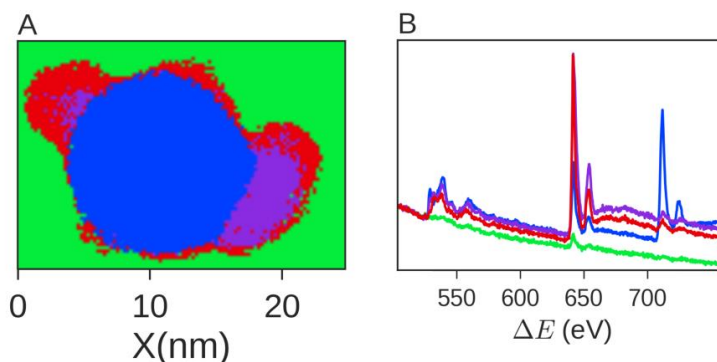


Figure 2.18. A) Clustering results on the first six PCA scores from Figure 2.16. Each colour corresponds to a cluster. C) Clustering results of the spectrum image with intensity normalization. D) Averaged spectra from each cluster.

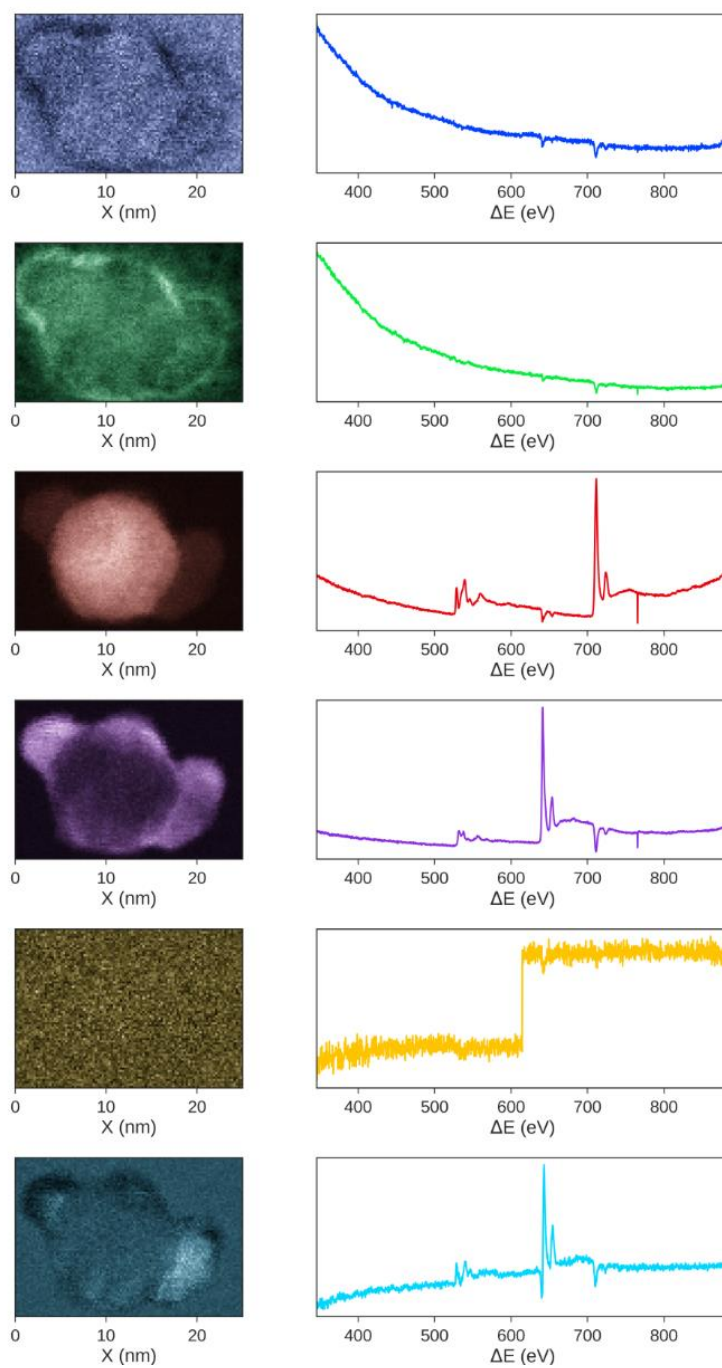


Figure 2.19. ICA results using 6 components with the default settings of the Hyperspy toolbox¹⁵³.

is not always the case. In the present case ICA was applied to the data for completion, yielding the results in Figure 2.19. Although some components can be related to the different oxidation states of manganese and to the iron oxide core, a direct interpretation is not possible since all of them have non-physical features (negative edges, negative background, detector intensity steps...). On the contrary, clustering is bound to yield easily interpretable results since the averaged spectra from a cluster will always be physically meaningful.

Moreover, data clustering can be seen as a complementary tool. Spectra modelling could certainly benefit from having an SI segmented and allowing different models to be used in different clusters. Performing spectral decomposition techniques on segmented images has already been demonstrated to give good results³¹, but this segmentation is usually performed manually. Clustering can be used as an automatic segmentation to be implemented in more challenging data sets or when consistency and automation is required. Lastly, the benefits of working with PCA plus clustering have already been demonstrated in Figure 2.9, 2.11, 2.15 and Figure 2.18, namely, the obtaining of physically meaningful components, noise reduction and lack of missing information.

The obtained results clearly show the usefulness and robustness of data clustering methods to deal with large EELS datasets. SI segmentation according to chemical composition can be obtained for EEL spectra, even recovering ELNES information. The three different strategies presented here will likely enable the use of data clustering in a wide range of problems, allowing easy and fast EELS data exploration.

CHAPTER 3: TEM and EELS to understand nanoparticle synthesis

Now that EELS instrumentation and different analysis methods have been discussed in detail it is the moment to apply them in order to solve different material science problems. There are many synthetic routes to obtain different types of nanoparticles. Often the structure of the resulting nanocomposite will be related to complex phenomena occurring at the nanoscale. In this chapter TEM and EELS is used to investigate such phenomena.

3.1. Introduction

NPs / nanocrystals can be defined as crystals that do not exceed 100nm in any direction. They constitute arguably the most fundamental example of a system exhibiting enhanced properties respect to its bulk counterpart, the characteristics on which nanotechnology is based. Certainly, the first application that can be considered nanotechnology is based on NPs. The Lycurgus Cup is an artefact that dates back to the IV century AD. The crystal of the cup has the particular property of showing dichroism, having a different colour when light is shined upon it from its inside or from the outside. This effect could be traced to the colloidal dispersion of 50-100 nm silver-gold NPs in the glass¹⁵⁴. More recently, the technical skill developed in NP synthesis has enabled controlled fabrication of very complex nanosystems, such as core/shell or dimer NPs with a wide variety of morphologies. Moreover, NPs can find applications that range from novel cancer therapies¹⁵⁵⁻¹⁵⁷ to catalysis¹⁵⁸⁻¹⁶⁰ among many other fields, and are already finding its way to the consumer market¹⁶¹⁻¹⁶³.

The final properties of a given NP system often depend on very intimate parameters. In a core/shell NP it can be the size or morphology of its constituents, as shown in many reported shape-dependent and size-dependent effects¹⁶⁴⁻¹⁶⁶. The precise chemistry of the crystals is also very relevant and therefore the localization and distribution of a specific element in a NP can alter its properties. These factors are not easily controlled and many times the tailoring of a given nanosystem requires a process of design, simulation, synthesis and testing, where characterization with great spatial resolution is

required at each step, given the exceedingly small size that these systems can have.

In this regard, few techniques can accomplish as much as the TEM measurements, EELS being particularly useful as it allows the mapping of different elements and ions in the NPs at atomic resolution. The information that these techniques can yield is often crucial both to understand and tailor the properties of a NP system. In the following sections, two cases in which TEM and EELS provided the necessary information to unveil key aspects of the synthesis processes for different NP types are presented. First, the investigation of a synthesis of iron oxide/silica core/shell nanoparticles will be shown, where an unexpected ligand exchange mechanism is unveiled, and it was possible to develop a detailed microscopic model of the synthesis process from the obtained results. In the second section, the object of study is the synthesis of gold/silver sulphide and selenide NPs. The NPs, obtained through cation exchange reactions, were produced under a wide variety of conditions, leading to many different morphologies and compositions.

3.2. Iron oxide/silica core-shell nanoparticles from acetate-induced disassembly of iron oxide nanoparticle clusters

3.2.1. Background

Magnetic NPs have shown numerous practical applications. An example would be their use as magnetic resonance imaging contrast agents, to enable magnetic manipulation of cells and other biocomponents, or as key components in hyperthermia cancer therapies^{167–173}. All of the mentioned medical/biological related applications impose important requirements to the NPs. A sufficiently small size and high magnetization is crucial for most of the applications. Additionally, their synthesis must yield very monodisperse NPs, both in terms of shape and composition, in order to perform medical and toxicity tests reliably. They also should not aggregate and be hydrophilic, so as to be soluble in a biological system, and not undergo degradation in the complex chemical environment of an organic medium. Because of these reasons, pure magnetic NPs are generally not used for these types of applications.

Magnetite is a magnetic material which can be synthesized in the form of NPs in a relatively reliable, monodisperse and efficient way^{174–177}. However, it can easily be oxidized/reduced in a biological environment. Nonetheless, a surfactant coating can be used on iron oxide NPs (IONPs) to provide them with long-term stability. Oleic acid (OA), for example, has proven to be a great stabilizing surfactant in this aspect.

However, surfactant stabilized IONPs are generally hydrophobic, a major drawback. To deal with this, IONPs can subsequently be coated by a biologically stable hydrophilic and resilient material. As a coating, silica has been used in several cases. A reason for SiO₂ to be so convenient is that the coating of the IONPs can be obtained through water-in-oil microemulsion reactions, which are relatively inexpensive, do not involve toxic chemicals and have good throughputs¹⁷⁸.

However, complex phenomena can happen in the coating process, as soluble and insoluble precursors and particles interact with each other. Micro emulsions of IONP clusters (IONPCs) can form in this context. Notably, the behaviour and functional properties of IONPCs in chemical reactions have been largely neglected and are still not well understood. In this section the results obtained by TEM, STEM and EELS from several synthesis processes are presented. From these experiments, a detailed insight into the mechanisms of IONPs@Silica core/shell NPs synthesis and the role of IONPCs in this process can be obtained, ultimately describing unexpected phenomena.

The results, which eventually lead to a recent publication¹⁷⁹, demonstrate a novel route for the obtention of IONPs@SiO₂. Not only was it facile, efficient and yielded extremely monodisperse NPs both in morphology and size, but also showed an unusual chemical ligand exchange mechanism.

3.2.2. Novel synthesis scheme

The synthesis can be divided in the following steps:

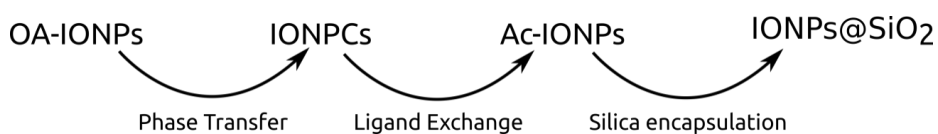


Diagram 3.1. Workflow of the synthesis microscopic model.

As a starting point, oleic acid capped IONPs (OA-IONPs) were synthesized by thermal decomposition of an iron oleate complex, according to a previously described method¹⁸⁰. Initially, a metal-oleate complex was prepared by reacting iron chloride and sodium oleate at 70 °C for four hours in organic solvents. When the reaction was completed, an organic layer containing the iron-oleate complex was obtained. After washing, solvents were evaporated, resulting in an iron-oleate complex in a waxy solid form. Then the iron-oleate complex and oleic acid were dissolved in 1-octadecene. The reaction mixture was heated to 320 °C for 30 min. When the reaction temperature reached 320 °C, a severe reaction occurred, and the initial transparent solution became turbid and brownish black. The resulting solution contained the OA stabilized IONPs.

OA-IONPs were dispersed in chloroform (oil phase) into an aqueous cetyltrimethylammonium bromide (CTAB) solution. This resulted in IONPCs that formed when OA-IONPs were partially encapsulated by CTA⁺ molecules at the liquid-liquid interface. This was performed under high CTAB surfactant-to-IONP concentration ([CTAB]/[IONP]) ratio conditions, according to a slightly modified version of the method reported by Qiu et al.¹⁸¹

The alkaline dispersion of the IONPCs was then heated to 60 °C in an oil bath. Then ethyl acetate, tetraethylorthosilicate (TEOS), and 3-(aminopropyl)triethoxysilane (APTES) (the latter two, being silica precursors) were consecutively added, and the mixture was refluxed at 72–76 °C for 3.15 h. When the ethyl acetate is introduced to the alkaline dispersion of IONPCs, and acetate ions gained access to the IONP surfaces, an acetate/oleate ligand exchange took place. At this point silica precursor transferred to the IONPCs and the silica shell growth kicked off on the IONPs. Eventually the reaction stopped with the release of individual IONP@silica core/shell NPs.

To investigate the processes detailed in Diagram 3.1, OA-IONPs, IONPCs, Ac-IONPs and IONPs@SiO₂ have to be characterized.

3.2.3. Characterization

OA-IONPs Phase transfer

In Figure 3.1A-B, TEM images of the OA-IONPs are shown. The size distribution from the TEM images is shown as an inset in Figure 3.1B, obtaining a NP diameter value of 12.4 ± 0.9 nm. Figure 3.2A displays an HRTEM image of the

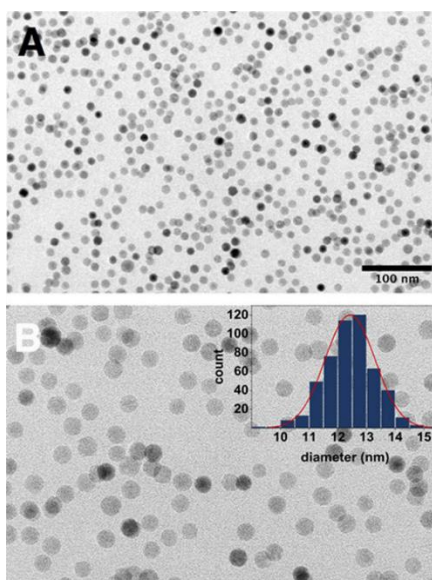


Figure 3.1. A) Low magnification TEM image of the OA-IONPs, B) A high-magnification TEM image of the OA-IONPs. The size distribution is shown as an inset.

same sample and its corresponding Fast Fourier Transform (FFT) (Figure 3.2B). The analysis of the observed plane spacings and symmetry in this [123] zone axis demonstrates a magnetite phase crystal.

EELS spectrum imaging was carried out at high resolution for OA-IONPs. From the SIs, the carbon K edge signal was mapped, yielding the results in Figure 3.3. It can be noted that the carbon K edge maps show an organic layer surrounding the IONPs. However, this layer is patchy and scarce for the OA-IONPs. The thickness of this layer was evaluated to be 2.3 nm.

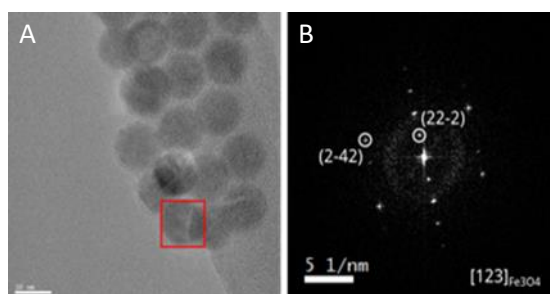


Figure 3.2. A) HRTEM and B) corresponding FFT of the OA-IONPs showing that the iron oxide structure is magnetite.

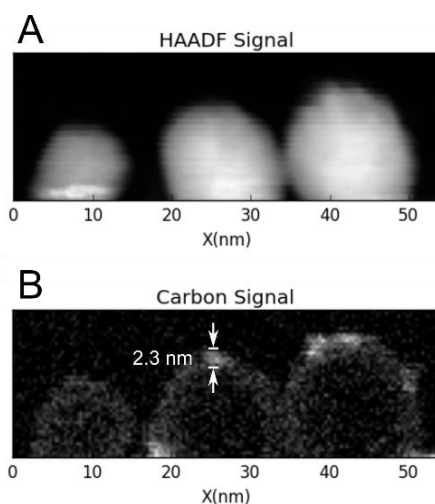


Figure 3.3. A) HAADF image and B) EELS C K edge map of dried OA-IONPs.

After the mixing of the IONPS with the aqueous CTAB solution cryo-TEM measurements were performed to observe the formed clusters in native state. In Figure 3.4A-B, TEM images of IONPCs are shown. The size distribution of these IONPCs was found to be pretty wide, with cluster diameter ranging between 100 and 200nm.

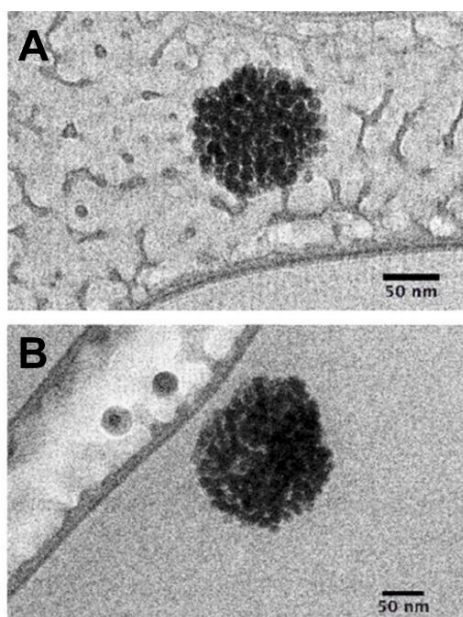


Figure 3.4. A,B) cryo-TEM images of the IONP clusters.

Ligand Exchange

Previously to the incorporation of silica precursors a sample was prepared by adding just ethyl acetate. This sample will be referred to as Acetate IONPs (Ac-IONPs). To evaluate the potential modification of the magnetite core and to assess the nature of the IONPs capping at different stages of the reaction, a detailed characterization by HRTEM and EELS and Raman spectroscopy was carried out on OA-IONPs and on Ac-IONPs.

In Figure 3.5A, the 200-700 cm^{-1} Raman fingerprint region for Ac-IONP and dried OA-IONP (dOA-IONP) revealed at least five Raman active modes ($3T_2g + E_g + A_{1g}$) that belong to cubic inverse-spinel structure of magnetite (Fe_3O_4). The spectrum of OA-IONP in comparison to Ac-IONP shows identical band patterns in this region. On the other hand, the bands representing the 355, 505 and 695 cm^{-1} could be regarded as the indication of T1, E and A1 modes of maghemite ($\gamma\text{-Fe}_2\text{O}_3$). The strong peak observed at 719 cm^{-1} was attributed to the oxidation of Fe (II) to Fe(III) at the octahedral sites.

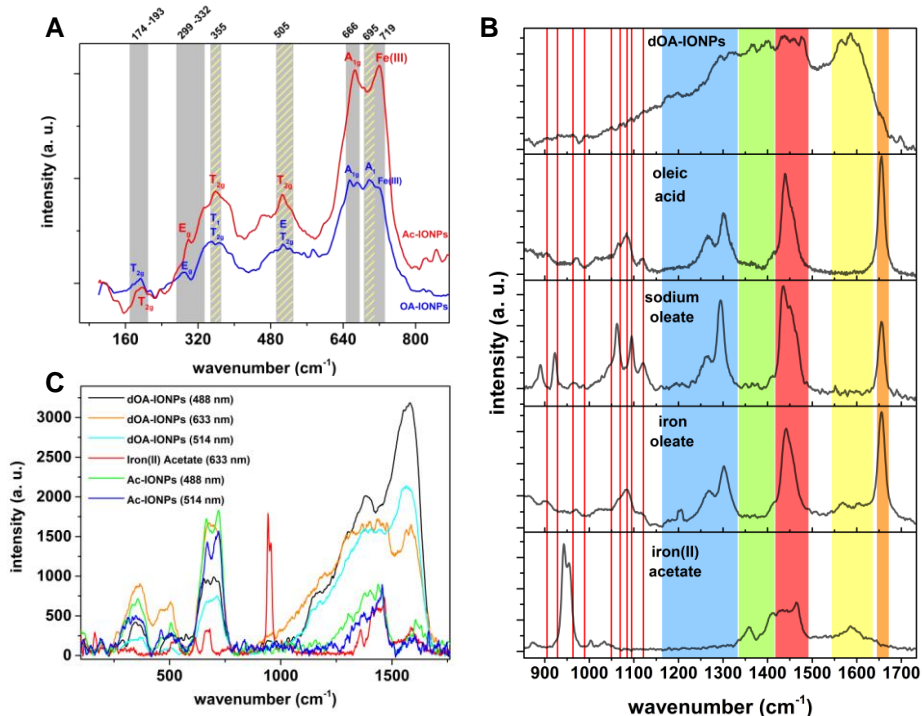


Figure 3.5. A) Raman spectroscopy analyses of dOA-IONPs (dried OA-IONPs) and Ac-IONPs at the iron oxide fingerprint region; B) Raman spectroscopy analyses of OA-IONPs in comparison to oleic acid, sodium oleate, iron oleate and iron(II) acetate; C) Comparison of the OA-IONPs and Ac-IONPs under different laser excitations.

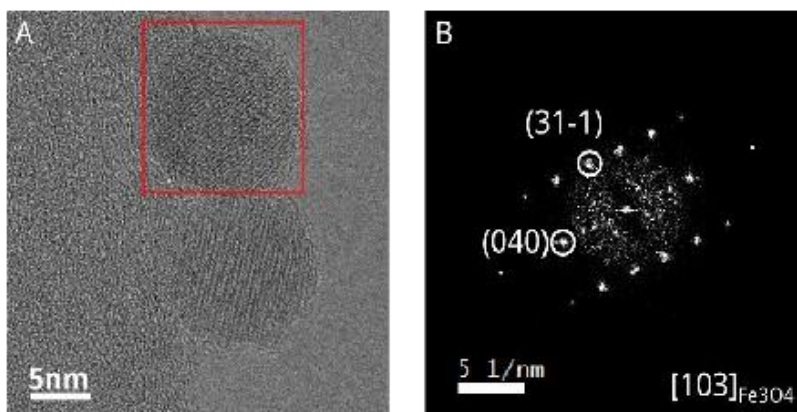


Figure 3.6. A,B) HR-TEM and corresponding FFT of the Ac-IONPs showing that the iron oxide structure is magnetite.

Analyses of the OA-IONPs and Ac-IONPs in the organic fingerprint region, $850\text{--}1750\text{ cm}^{-1}$, are shown in Figure 3.5B-C. In Figure 3.5B, 633 nm excited OA-IONPs were compared to oleic acid, sodium oleate, iron oleate (IONP precursor) and the iron(II) acetate to distinguish the differences between the complexation of oleate and acetate species with iron.

The orange band in Figure 3.5B indicates the C=C bond of the oleic acid¹⁸² which is observed as a shoulder in OA-IONPs. Interestingly, this feature is lacking for the Ac-IONPs spectra, shown in Figure 3.5C in green and blue.

TEM images were acquired for the Ac-IONPs. Figure 3.6 displays an HRTEM image of the Ac-IONP sample (Figure 3.6A) and its corresponding FFT (Figure 3.6B). The analysis of the observed plane spacings and symmetry demonstrates a magnetite phase crystal with no maghemite observed.

EELS spectra were also acquired on OA-IONPs and Ac-IONPs samples. In Figure 3.7, spectra from OA-IONPs and Ac-IONPs are displayed (after normalization). The spectra are remarkably similar. Moreover, spectral features such as the oxygen pre-peak at 528 eV, the third peak on the O K edge at 545 eV, as well as the Fe L_3 peak position are in good agreement with the mixed valence state characteristic of magnetite^{27,40,183}. Overall, the results show that the composition of the structures are identical and ligand exchange did not result in any significant modification of the magnetite structure.

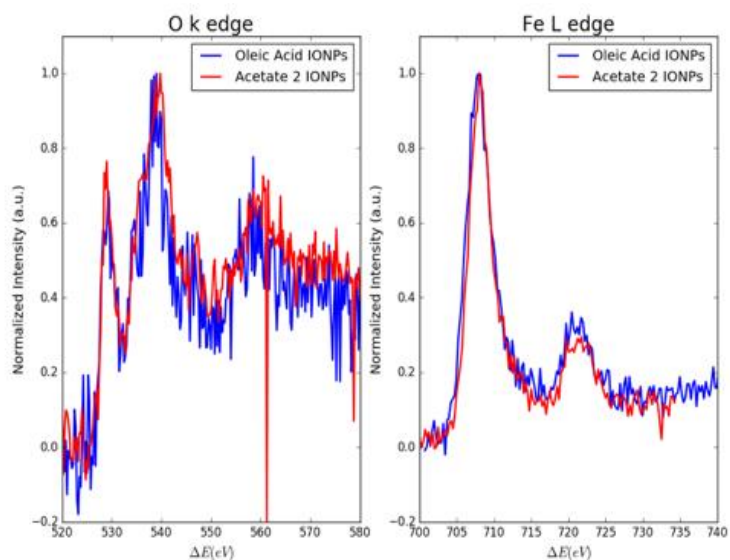


Figure 3.7. Oxygen and Iron EELS analysis of Ac- and OA-IONPs.

The EELS carbon signal was also mapped (Figure 3.8). The carbon layer is homogenous for Ac-NPs, as opposed to that of OA-IONPs (Figure 3.3). The thicknesses of the carbon shells around the NPs are similar although the hydrocarbon content of oleic acid is much larger than for acetate. This indicates that acetate is deposited in large amounts.

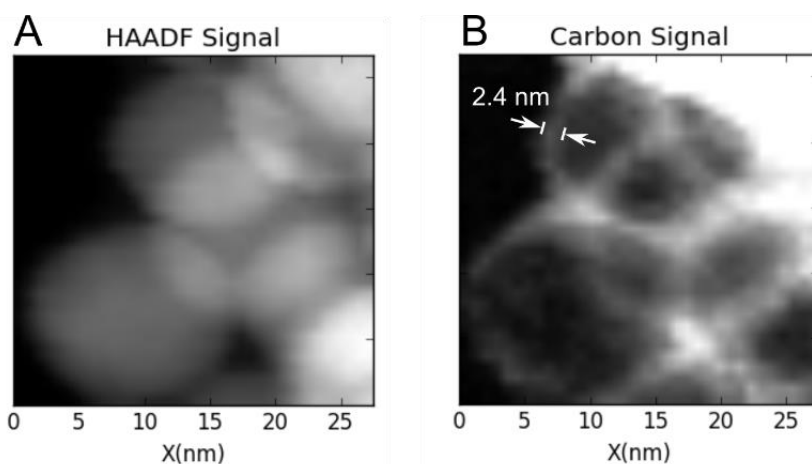


Figure 3.8. A) HAADF image and B) EELS C K edge map of acetate coated IONPs.

Silica encapsulation

To continue studying the synthesis, a new batch was prepared following through with the silica shell growth. During the process, after the addition of silica precursors, samples were extracted and inhibited at 15 minute intervals, obtaining the images in Figure 3.9. Essentially, Figure 3.9A-G demonstrate that silica growth onto the IONPs started from the inside of the IONPCs. Figure 3.9H-L demonstrate the dismantling of the IONPCs into individual IONPs@SiO₂ core/shell NPs.

The sample resulting of stopping the reaction at 180 min (Figure 3.9A-C) was examined by STEM-HAADF at higher magnification. The corresponding images are shown in Figure 3.10. Apart from the IONPs@SiO₂ core/shell NPs, other much smaller – 1 nm in diameter – particles can be observed. The contrast of the smaller particles is brighter than the silica shell, indicating that they could correspond to pure iron oxide.

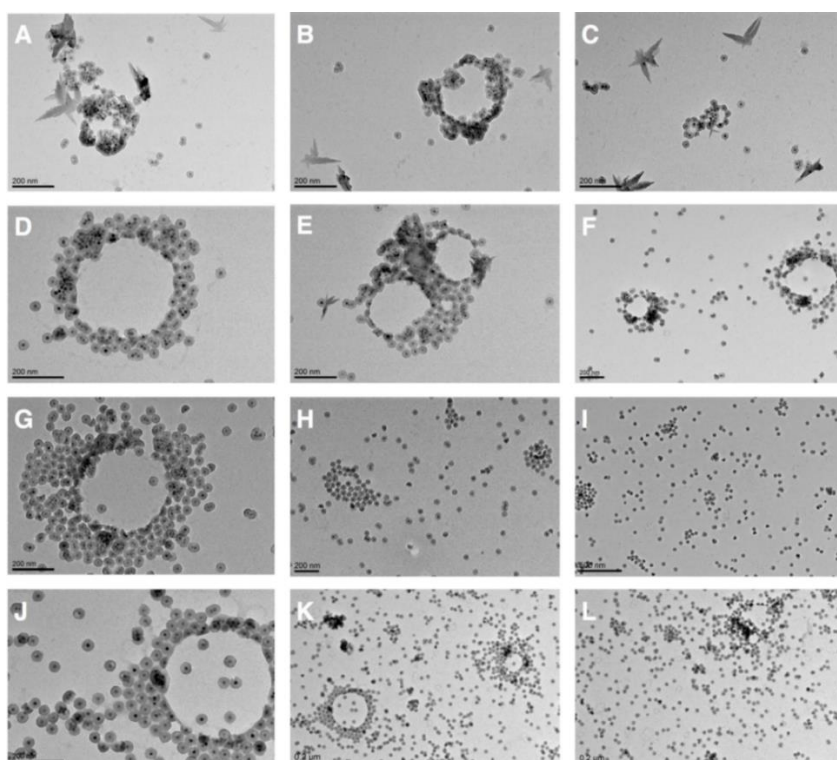


Figure 3.9. Time resolved TEM observation of the silica coating reaction progress: A-C) 180 min after the silica precursor addition; D-F) 195 min after the silica precursor addition; G-I) 210 min after the silica precursor addition; J-L) 225 min after the silica precursor addition.

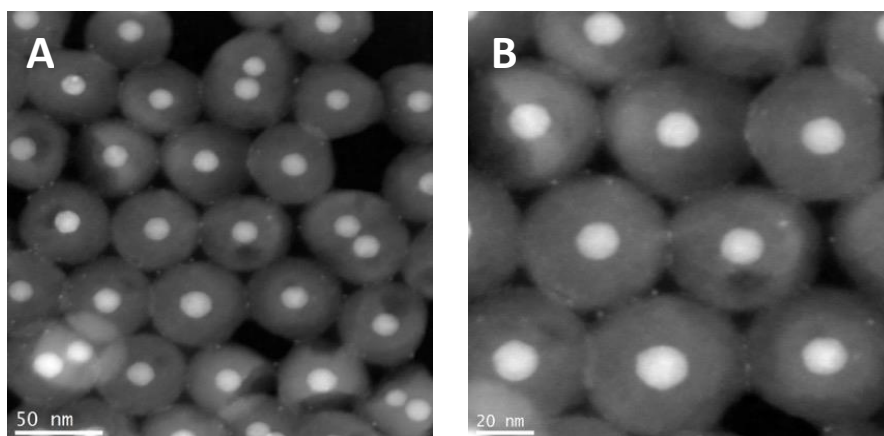


Figure 3.10.A-B) STEM-HAADF images of NPs after 180 minutes of reaction.

The core/shell NPs at 180 min already had a nice silica shell but had not been washed and were still in a base medium when obtained. All of this points towards the fact that the observed small particles were produced by breakage/cleavage of the IONPs.

After the silica growth process was completed, HRTEM images were acquired from the obtained core-shell NPs. As can be seen in Figure 3.11A, D, these images convey amorphous silica shells with a thickness of 10-20 nm. These silica shells have all at least one apple-bite like notch. In the case of Figure 3.11A, the apple-bite is at the right side of the core/shell NP, whereas in Figure 3.11D it is facing front and left. HRTEM images of the central IONPs are shown in Figure 3.11B, E. The images show a cubic crystal lattice that perfectly matches that of magnetite Figure 3.11C, F).

Extensive EELS of the IONP@Silica NPs was carried out in the 200 eV - 800 eV energy loss region of the spectra, which contains the oxygen K edge (532 eV), the iron L_{32} edge (708 eV) and the carbon K edge (284 eV).

Large SIs were denoised using PCA. In particular, for the SI shown in Figure 3.12, only two PCA components were enough to describe the spectral variation of the image. The component in the top panels of Figure 3.12 shows no signs of iron signal, only an O K edge with ELNES features compatible with pure silica¹⁸⁴. In the corresponding PCA map, three NP shells can be seen. All of them have the typical apple-bite, the leftmost having it pointing towards the central particle, the central particle having it facing up, and the rightmost particle having a bite in either side. The second component, shown in the bottom panels of Figure 3.12, demonstrates a strong Fe L_{32} edge as well as a small peak at 528eV. The

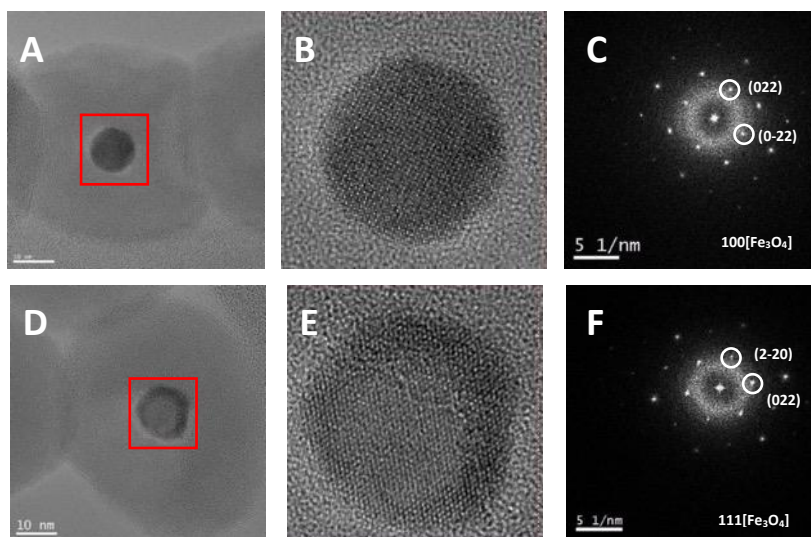


Figure 3.11 (A, D), HRTEM images of IONPs@SiO₂ structures, (B, E) magnified views of the regions highlighted by red squares and corresponding FFT images (C, F). Images unambiguously show that the cores of the NPs are perfectly crystalline and consistent with magnetite (Fe₃O₄) and the silica shells are found to be amorphous.

small peak corresponds to the oxygen prepeak characteristic of samples with Fe³⁺ ions, such as magnetite. The map corresponding to this PCA component shows signal only in the three small IONPs cores. These results confirm the uniformity in the composition of the silica shell and magnetite cores.

At this point it is important to know whether the IONPs have undergone any chemical change, oxidation or reduction, during the synthesis. In Figure 3.13 the Iron L_{3,2} edge spectrum from the initial OA-IONPs before the phase transfer reaction is compared to the spectrum from the IONPs on the core of the NPs after the silica encapsulation. The spectra show no relevant changes, having almost the same onset and L_{3,2} ratio. Only a small increase of signal in the continuum region after the ELNES energy range can be observed, which is related to the thickness increase due to the silica shell growth.

Carbon distribution was studied with EELS. From the highlighted NP in Figure 3.14A an EELS SI was acquired. Oxygen (Figure 3.14B) and carbon (Figure 3.14D) signal maps and carbon relative composition (Figure 3.14C) were obtained from it. While the oxygen maps show the already demonstrated uniform composition of the silica shell, there is a high concentration of organic species in its outermost surface.

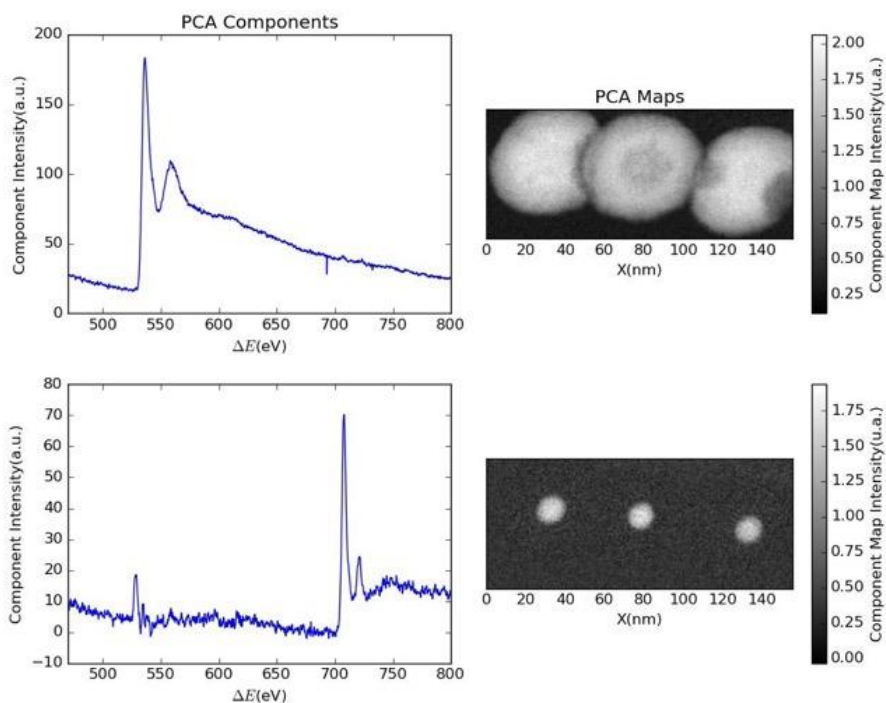


Figure 3.12. PCA decomposition maps. Only two components were enough to reproduce the experimental spectra. This demonstrates uniform composition of SiO_2 (upper panels) shells and Fe_3O_4 cores (lower panels).

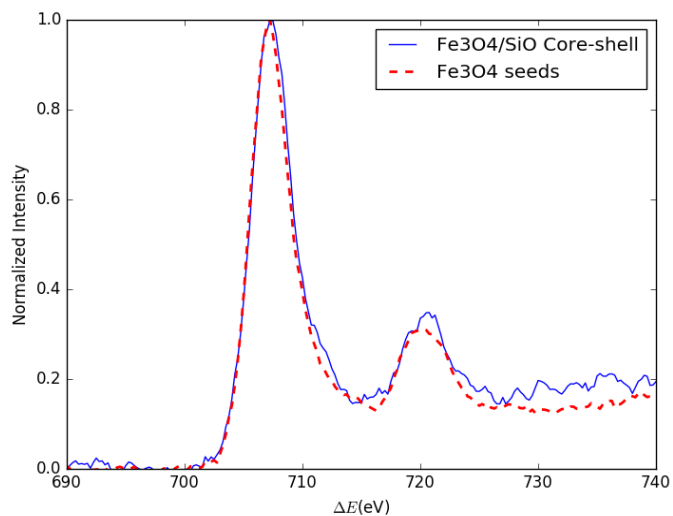


Figure 3.13. IONP@ SiO_2 and IONP Iron Fe L_{32} edge comparison.

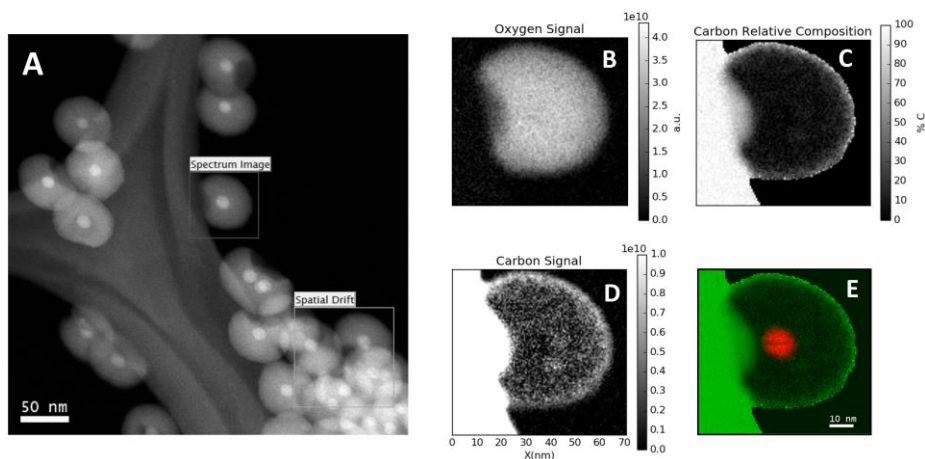


Figure 3.14. A) HAADF image with a highlighted region where an EELS SI was taken. B) Oxygen signal coming from silica. C) Carbon relative composition from the EELS SI. D) Carbon signal. E) Coloured map of carbon relative composition (green) with iron signal (red).

One of the critical points to understand in this process is the interaction of different ligands in the surface of the IONPs. Because of this, a detailed characterization of the IONP/silica interface is mandatory. For this reason, EELS maps at high resolution were obtained from the IONP cores and its immediate environment. The spectra were calibrated with the oxygen K edge and normalized. Then, oxygen pre-peak signal, iron L_3 onset and carbon signal were mapped. These maps can be seen in Figure 3.15.

Figure 3.15B, D display oxygen pre peak and carbon signal maps around a core of the IONP@SiO₂ NP, highlighted in Figure 3.15A, the HAADF image. The presence of a pre-peak in the oxygen edge in FeOx is consistent with the iron core being Fe₃O₄. These parameters maps indicate that oxidation state of the iron oxide cores is homogenous. This was further confirmed by mapping the iron L_3 peak position (Figure 3.15C). Shifts in the Fe L_3 position of 1-2eV are known to be related to changes in the oxidation state of iron. However, the peak onset was constant throughout the particle, indicating no changes in the iron oxidation state.

However, a slightly stronger carbon signal can be seen around the iron oxide core of the NP. This could prove that an organic capping of the IONPs is still present in the final core-shell NP. However, the carbon signal in the exterior of the NP partially masks this signal. Note that the bright region at the top of

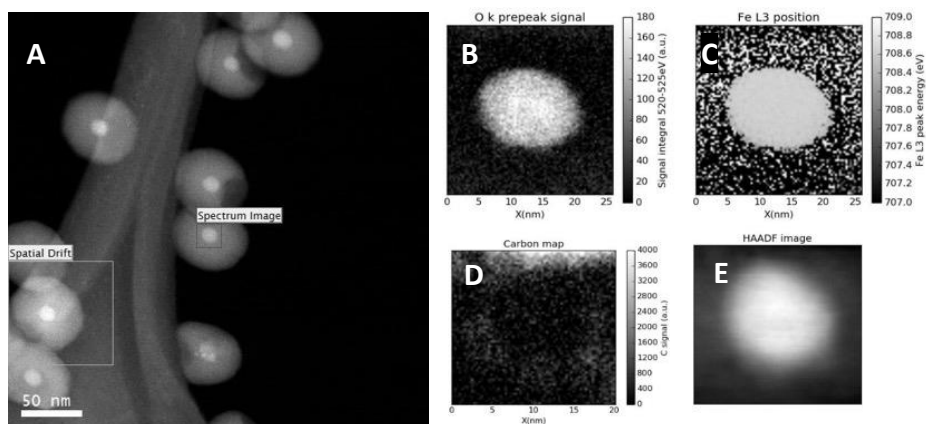


Figure 3.15. A) HAADF image of IONPs@SiO₂; B) Oxygen pre-peak signal and C) Fe L₃ onset EELS fine structure parameter maps. D) Carbon EELS signal map after PCA denoising. E) Co-acquired HAADF image showing the region where EELS SI was taken from. F) Fe L₂₃ edge from the core shell particles and from the seeds.

Figure 3.15D corresponds to the surface of the hole in the silica populated with a high concentration of carbon.

To deal with this and to confirm that there are organic molecules at the core-shell interface of the particles, a dialysis treatment was applied to the IONPs@SiO₂ NPs to remove the organic components on the external surface of the silica shell. EELS mapping results from this sample are shown in Figure 3.16. Figure 3.16A-C show maps of the O K edge, Iron L edge and Carbon K edge signals respectively. From them, it is clear that the IONP@SiO₂ morphology was not altered by the dialysis process. Moreover, some of the outer organic shell was removed, as can be appreciated by its patchiness in Figure 3.16C. Now, the signal from the organic shell around the IONP core can be clearly appreciated. The colour mix of Figure 3.16A-C (Figure 3.16D) clearly shows the presence of an organic capping around the core of the NP.

At this point, the TEM characterization has provided evidence of the ligand exchange that takes place in the IONPC, prior to the silica encapsulation, as well as the role of the CTAB as a templating agent for the silica growth. The exact mechanism by which oleic acid is substituted by acetate molecules on the surface of the IONPs is suspected to proceed via breakage of tiny iron particles from the surface of the IONPs.

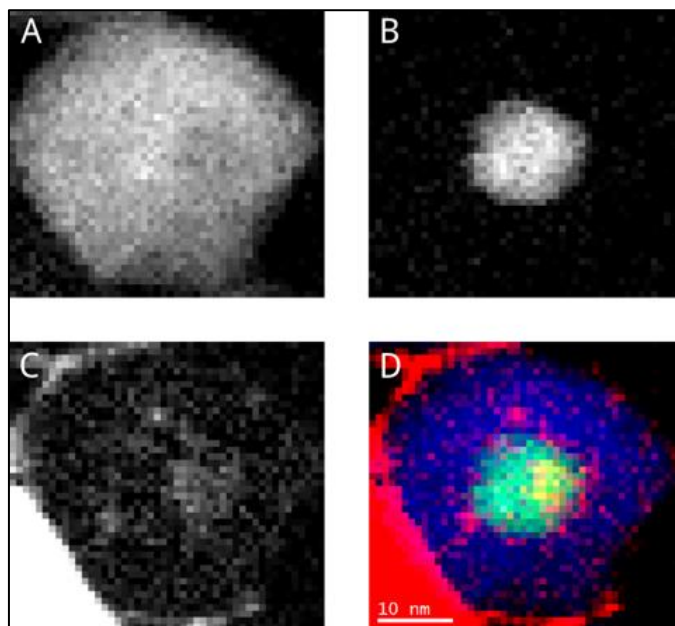


Figure 3.16. EELS analysis showing: A) oxygen signal, B) iron signal, C) carbon signal, D) coloured map of oxygen (blue), iron (green) and carbon (red).

3.2.4. Discussion

The characterization of the different samples detailed in the previous section can be summarized into the following points:

- (1) The IONPs are composed of iron oxide in the magnetite phase.
- (2) The composition of IONPs remains constant during the whole synthesis.
- (3) Changes in the organic capping of the IONPs occur after the formation of IONPCs.
- (4) A thick layer of organic components remains on the outer silica surface after its growth
- (5) Organic capping of the IONPs remains at the silica core/shell interface.
- (6) Very small particles (1nm) appear during the reaction.
- (7) Silica growth process has been observed to occur within IONPCs.

With this knowledge it is possible to understand with greater detail the process roughly depicted in Diagram 3.1. This led to the development of the microscopic reaction model depicted in Figure 3.17.

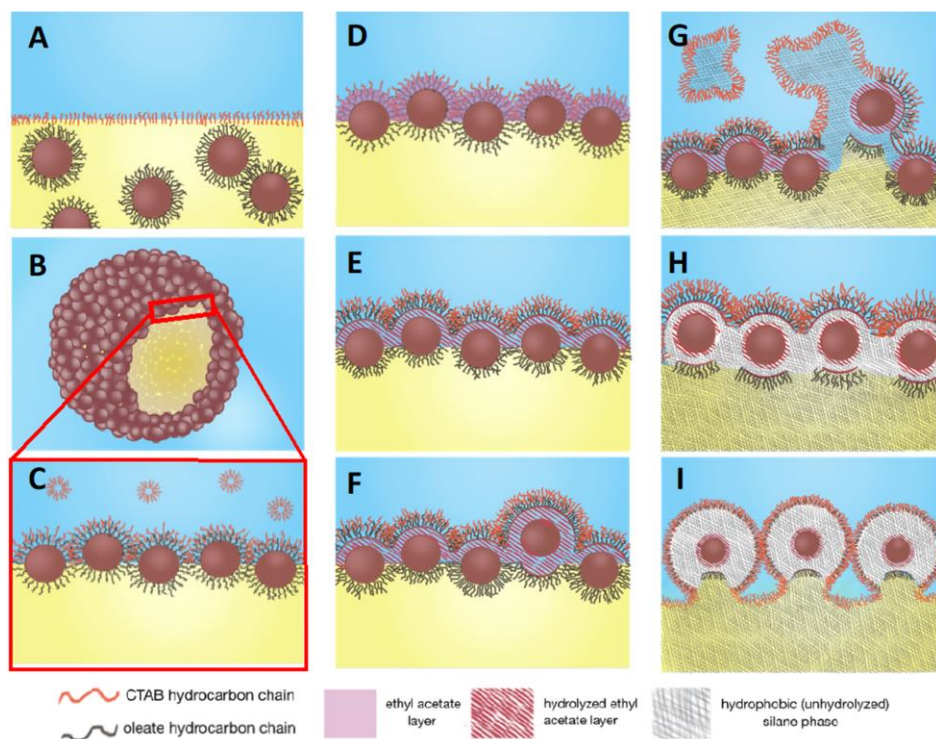


Figure 3.17. Micellar Fusion mechanism leading to formation of IONPs@acetate@SiO₂ structures: A) Initial mixtures of aqueous CTAB solution (blue) and OA-IONPs dispersion in oil phase (yellow). B) OA-IONPs are stabilized at the liquid-liquid interfaces resulting in IONPCs. C) IONPs at the liquid-liquid interface and some micellar structures of CTA⁺ in aqueous phase. D) Ethyl acetate disperses within the CTA⁺-oleate bilayer on the surface of IONPCs. E) Acetate ions interact with iron oxide surface and break iron oxide structure. F) Acetate removes the oleate-only coated surface of the IONPs. G) Silica precursors form nanoemulsions with excess CTAB molecules/micelles in solution. H) Encapsulated silica precursors start to accumulate at the space between the dynamic CTA⁺-oleate bilayer and acetate coated IONPs. Silica eventually starts to form. I) Silica shell continues to grow, forming monodispersed IONPs@acetate@SiO₂.

First, as oil-dispersed OA-IONPs are dispersed in the aqueous CTAB solution (Figure 3.17A), IONPCs are formed (Figure 3.17B), probably leaving some excess CTA⁺ molecules in solution (Figure 3.17C). The formation of IONPCs has been proven through their direct observation (Figure 3.4).

Then when ethyl acetate is added, the Raman measurements of Figure 3.5, and the change in carbon capping morphology seen between Figure 3.3 and Figure 3.8 show that an OA/Acetate ligand exchange takes places. At this moment, points (1) and (2) are an important observation, as they discard many chemical processes that could have been involved in the ligand exchange mechanism.

Also, they confirm that the observed maghemite signal in the Raman measurements is most likely due to heating of the sample from the laser excitation¹⁸⁵.

With the obtained observations a possible ligand exchange mechanism may be the following. The unhydrolyzed excess of the ethyl acetate phase directly interacted with the CTA+–oleate bilayer on the IONP surfaces (Figure 3.17C,D). A large fraction of ethyl acetate was immediately hydrolysed in the aqueous phase because of the saponification reaction. Ethyl acetate exchanged continuously between the CTA+–oleate bilayer and the water phase, which resulted in the diffusion of acetate ions within the bilayer.

As soon as the acetate ions gain access to the IONP surfaces, the acetate/oleate exchange proceeds via breakage of the iron oxide particles (Figure 3.17E, F). This would explain the presence of small iron particles in Figure 3.10. Then, part of the CTA+–oleate bilayer is probably carried away along with the tiny iron oxide NPs.

The CTA+–oleate bilayer holding the detached iron oxide particles must have undergone dynamic rearrangements. Consequently, the displaced IONP building blocks of the IONPCs serve as tiny gates between the nanoemulsions of silica precursors (depicted in the top-left of Figure 3.17G) and the hydrophobic phase in the core of the IONPCs.

The precursor nanoemulsion-IONPC fusion process starts (Figure 3.17G) when the hydrophobic phase of silica precursors transfers into the hydrophobic core of the IONPCs. Hydrolysis of the silica precursors must have started as soon as the IONPCs and nanoemulsion fusion is complete. Silica shells in spherical morphologies are induced by the additional CTA+ molecules supplied by the nanoemulsions to the CTA+–oleate bilayers. This scenario leads to the formation of a thick carbon template around the silica shells, that was observed in Figure 3.14. The continuous accumulation of silica precursors from the hydrophobic core of the IONPCs to the space between the oleate–CTA+ bilayer and acetate-capped IONP cores grows the silica shells (Figure 3.17H). This remaining acetate layer surrounding the IONP cores was directly observed, determining the final product as IONP@acetate@SiO₂ NPs (Figure 3.16D).

Condensation of the precursor into silica around the IONP continues till the CTA+–oleate bilayers lose their mobility, when the silica shells reach their maximum size (~60 nm). Release of individual IONPs@acetate@SiO₂ core–shell structures from the nanoemulsion–IONPC hybrids finally starts when the unity

of CTA+--oleate bilayers is lost (Figure 3.17I). The direct observation of the silica shell growth and dismantling of the IONPCs (Figure 3.9) perfectly fits this model and highlights the critical role of the cluster formations and water-oil interfaces in the synthesis.

This information could only be obtained thanks to the spatial resolution and chemical sensitivity that analytical TEM characterization provides. These results were essential in the process of tuning and understanding the demonstrated new synthesis process.

3.3. Chemistry of noble metal chalcogenide nanocrystals

3.3.1. Introduction

Noble metal chalcogenides have attracted a lot of interest from various fields in the recent years. Silver chalcogenides, in particular, are low band gap semiconductor materials that have shown tuneable emission in the near-infrared (NIR) spectral range with potential interest for biosensing and in vivo imaging, as well as potential applications as photodetectors¹⁸⁶⁻¹⁸⁹. Additionally, their efficient charge transport, superionic character, and high magnetoresistance have motivated the study as solid electrolytes for electrochemical applications as well as magnetic sensors^{190,191}. Binary silver chalcogenides have also been tested as thermoelectric materials, which show thermoelectric figure of merit (ZT) values close to unity in some cases¹⁹²⁻¹⁹⁶.

Because of the detailed potential applications of these materials, the tailoring of nanocomposites of building blocks from these materials is highly promising. In this regard, modern colloidal synthesis appears to be suitable for several reasons. Besides controlling size and shape of NPs, it allows sequential deposition of several materials in the form of a single hybrid NP, it fully exploits unconventional reactivity of nanomaterials such as cation or anion exchange, and it stabilizes metastable phases¹⁹⁷⁻²⁰⁰. In particular, it enables the fabrication of metal-semiconductor and alloyed ternary phases with many potential applications. As an example, in the context of thermoelectricity, Xiao et al. have reported higher ZT values for ternary Ag₄SeS alloyed NPs compared to those of the binary Ag₂Se NPs²⁰¹. Other materials in the research spotlight are CuAgSe, AgSbSe₂, and AgBiSe₂ systems, which are currently emerging as promising

thermoelectric materials with enhanced ionic and electronic mobilities and ultralow thermal conductivities^{202–205}.

There are several synthetic pathways to this type of ternary chalcogenides. Some of them include dry synthesis by fusing, annealing and cooling^{206,207} or solvo-thermal routes²⁰⁸. Other methods which have the benefit of being less energy consuming and allow the control of morphology at the nanoscale are exchange reactions.

The typical cation exchange reaction involves a binary ionic crystal, with anions A^- and cations C^+ , surrounded by a liquid medium rich in a different type of ions C'^+ . In this circumstance, at the surface of the crystal the substitution of C cations by C' cations will occur as a diffusion mediated process. The speed and extent of the substitution is determined by the thermodynamic potential difference between the CA and the $C'A$ compounds and the cation mobility in the crystal²⁰⁹.

In a bulk system, this type of reaction is extremely slow, heavily hindered by the high activation energies for the diffusion of atoms and ions in solids and in most cases can only happen at very high temperatures or pressures^{210,211}. However, in nanocrystals the picture is completely different as it has been shown that a total cation exchange can occur in less than a few hours or even in seconds at room temperature^{209,212}.

Cation exchange allows chemical modification of nanostructured materials under soft conditions in solution while fully preserving their size and shape. Therefore, it circumvents the need to develop direct and elaborate synthetic protocols of materials for which this might represent a struggling task²¹³. In particular, the direct synthesis of ternary or quaternary materials entails the search of multiple precursor and reactive species that are prompt to react and decompose at the same temperature and with similar kinetics in order to assure the homogeneous formation of the final NPs²¹⁴. Alternatively, performing partial cation exchange in a controlled manner in simple parental binary materials can lead to the formation of multielement materials with a high degree of homogeneity even at low temperatures when appropriate precursors are used^{215–217}.

Chalcogenide-based semiconductor nanostructures have strongly benefited from cation displacement processes: Alivisatos and co-workers pioneered this field already in 2004 by reporting for the first time the possibility to exploit cation exchange reactions as a chemical transformation tool at the nanoscale for a few chalcogenide materials²⁰⁹. Later, in 2007, the same group envisaged

further limits of this post-synthetic approach and confirmed the possibility to perform non-homogeneous cation exchange reactions on CdS nanorods, leading to segmented and elongated superlattices formed by alternating CdS and Ag₂S domains²¹⁸. From that moment many groups have devoted their efforts to expand these strategies to other materials and also to investigate the critical factors underlying the mechanisms of such reactions^{219–222}.

The importance of structural and morphological parameters, the influence of the oxidation state and coordination environment of the outgoing and incoming ions, and the presence of appropriate precipitating and/or complexing agents that might significantly alter the thermodynamics, making the exchange favourable or unfavourable, are among the subjects explored in the most recent years^{223–227}. Considering and controlling all these factors becomes especially critical when cation exchange competes with other potential reactions. In particular when intending to exchange cation species by others with high electron affinity, like Au, in which full reduction to metallic Au can easily occur, hindering the cation substitution process, if reaction conditions are not accurately controlled²²⁸.

3.3.2. Silver-gold selenide system

The objective of this section is to explore cation exchange of silver by gold starting from Ag₂S NPs. The different synthesis paths within the ternary Ag-Au-Se system that were investigated are summarized in Figure 3.18.

As a starting point, Ag₂Se NPs were prepared following a simple hot-injection method²²⁹. Essentially, tri-n-octylphosphine (TOP) solutions of Se and Ag precursors were prepared, and room-temperature TOP-Ag is added to hot TOP-Se in the presence of oleylamine. Then, solutions of gold (III) ions on toluene were prepared using different phase-transfer agents, either dodecylamine (DDA) or tetraoctylammonium bromide (TOAB), in different concentrations following the protocols detailed in a previous work²¹². Briefly, after an aqueous solution of gold salts was prepared, it was mixed successively with ethanol solutions of DDA/TOAB under stirring. After addition of toluene and vigorous stirring, the gold (III) solution was extracted as the supernatant phase. Afterwards, the gold ion solution and the NPs were stirred together at room

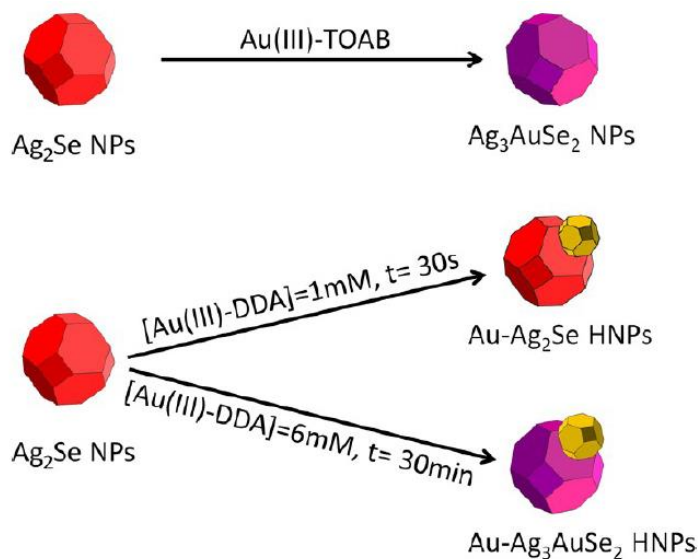


Figure 3.18 Strategy for the synthesis of alloyed and hybrid NPs based on the Ag–Au–Se ternary system.

temperature during varying times, inducing the incorporation of gold to the Ag_2Se NPs.

The phase-transfer agent, its concentration and the reaction time were varied to achieve different nanocomposites. Different combinations of these parameters yielded three distinct nanocomposites as shown in Figure 3.18.

These products were confirmed through X-ray diffraction (XRD) measurements. The X-ray diffraction (XRD) spectrum in Figure 3.19A, corresponding to the Ag_2Se seed NPs indicates that the orthorhombic silver selenide phase ($\beta\text{-Ag}_2\text{Se}$, naumannite) is predominant, although $t\text{-Ag}_2\text{Se}$ can also be identified as a minor product. The spectrum of Figure 3.19B, corresponding to the cation exchange reaction in presence of TOAB can easily be assigned to the fischerite phase through its most intense diffraction peak at 33° assigned to the (321) planes, and by a peak at 12.5° originating from the (110) family of planes with large interplanar distance, both characteristic of the cubic Ag_3AuSe_2 crystal structure. For the XRD measurement of the DDA synthesis after a short reaction time, the spectrum can still be explained only with the peaks of $\beta\text{-Ag}_2\text{Se}$ and $t\text{-Ag}_2\text{Se}$. Longer reaction times allowed the complete transformation of orthorhombic Ag_2Se into $\text{Au-Ag}_3\text{AuSe}_2$ NPs, as shown in Figure 3.19D.

Following, the characterization using HRTEM, STEM imaging, EDX and EELS mapping of the described NP products will be presented.

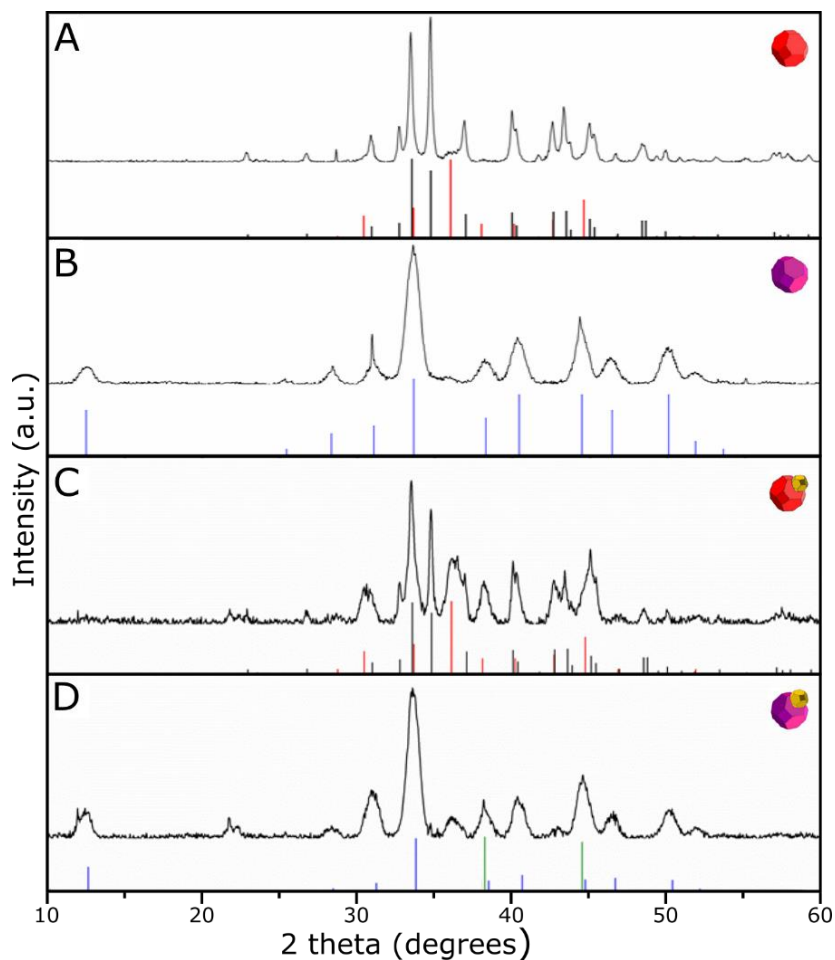


Figure 3.19. A) XRD spectra of Ag_2Se NPs, $\beta\text{-Ag}_2\text{Se}$ (JCPDS 00-024-1041, black) reference pattern and $t\text{-Ag}_2\text{Se}$ calculated (red) pattern. B) XRD spectra of Ag_3AuSe_2 NPs and Ag_3AuSe_2 (JCPDS 01-072-0392, blue) reference pattern. C) XRD spectrum of Au- Ag_2Se HNPs, $\beta\text{-Ag}_2\text{Se}$ (JCPDS 00-024-1041, black) reference pattern and $t\text{-Ag}_2\text{Se}$ calculated (red) pattern. D) XRD spectra of Au- Ag_3AuSe_2 NPs, Ag_3AuSe_2 (JCPDS 01-072-0392, blue) and Au (00-002-1095, green) reference patterns.

Pure fischesserite (Ag_3AuSe_2) nanoparticles

An HRTEM image from the NPs obtained in the TOAB-based reaction is shown in Figure 3.20. Image simulations using the TEMSIM open source image simulation software²³⁰ were carried out to analyse the obtained results. The

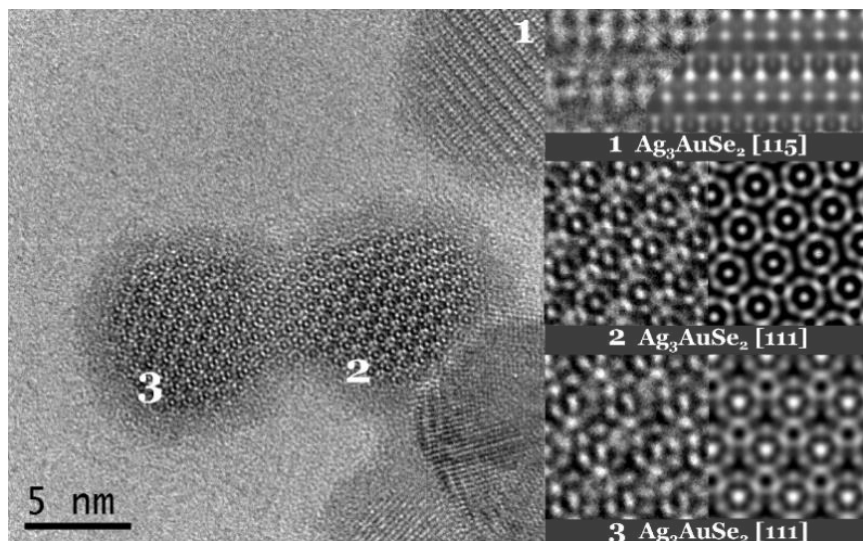


Figure 3.20. HRTEM characterization of Ag_3AuSe_2 NPs. In the right panel HRTEM image simulation of the fischerite structure in different orientations are shown compared to the marked regions of the acquired image.

zone axes of the NPs are $[115]$ for particle 1 and $[111]$ for particles 2 and 3. Close-ups of the images match perfectly with the simulations of the fischerite crystal.

The size of the resulting NPs was found to be almost the same as that of the parent Ag_2Se nanocrystals²³¹. The images reveal that the single-crystal character of the seed particles has been generally preserved after the reaction and that the crystal lattice corresponds to the cubic Ag_3AuSe_2 structure. As a result of the reaction, an amorphous shell of about 1 nm thickness is observed in all NPs.

Hybrid Au- Ag_2Se nanoparticles

When the phase transfer agent is chosen to be DDA, a slightly reducing amine, and the reaction is inhibited after just 30 seconds, the outcome of the synthesis are hybrid Au- Ag_2Se NPs. Figure 3.21 shows STEM-EDX characterization of the resulting NPs.

The sample was found to be exclusively composed of nanodimers as the one shown in Figure 3.21A, with a highly contrasted small spot in each nanocrystal, presumably corresponding to the metallic Au domain. In Figure 3.21B, a Fourier-filtered image of the crystal shows a good match with a simulated HAADF image of $\beta\text{-Ag}_2\text{Se}$ in the $[531]$ zone axis. This confirms that the crystalline structure of

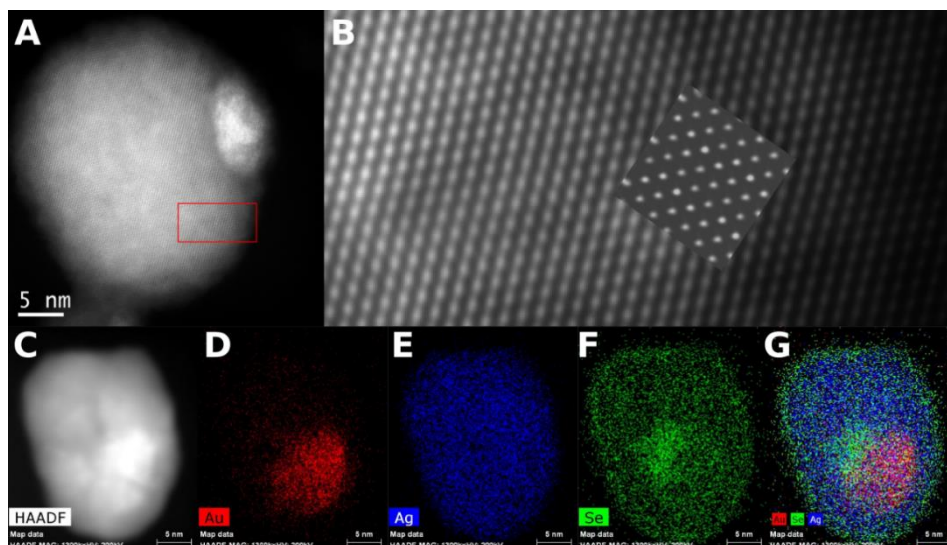


Figure 3.21. A) HAADF-STEM image of one of the dimer particles from the Au-Ag₂Se sample. B) Fourier filtered image from the highlighted region in A. The inset is a STEM-HAADF image simulation of Ag₂Se along the [531] zone axis. C) HAADF-STEM image of another particle from the same sample. D-F) EDX elemental maps corresponding to Au, Ag, Se respectively. G) D-F maps superimposed.

the large domain corresponds to that of the orthorhombic Ag₂Se. Detailed interface analysis of the NPs showed that the two domains are not related by any specific epitaxy and that the two crystalline lattices are randomly oriented in the nanostructures.

EDX elemental mapping performed on the dimer NP displayed in Figure 3.21C shows the spatial distribution of Au, Ag, and Se elements in the structure (Figure 3.21D–G). The EDX maps evidence that the large domain is made of binary Ag₂Se and from its quantitative analysis the expected 2Ag:Se stoichiometry is observed. On the other hand, the analysis suggests that Au is located almost exclusively in the form of small crystals in the surface of the Ag₂Se. Although some degree of diffusion of Au(I) into the β-Ag₂Se structure cannot be totally excluded, this value remains very low, if non-zero.

Even if the presence of Au could not be inferred from XRD, this is most probably due to the small size of the domains^{232,233}. HRTEM images of dimers depicted in Figure 3.22, showed the *d*-spacing values observed in the small contrasted areas clearly correspond to *fcc* Au.

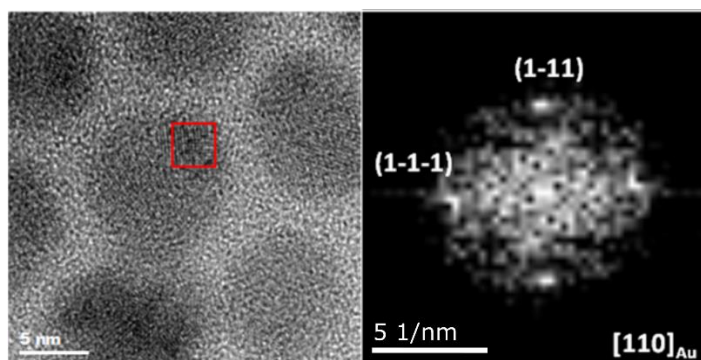


Figure 3.22. HRTEM image and FFT analysis of Au-Ag₃AuSe₂ NPs

Hybrid Au-Ag₃AuSe₂ nanoparticles

If the DDA-Au(III) solution is allowed to react for longer times, up to 30 minutes, with the Ag₂Se seeds, hybrid Au-Ag₃AuSe₂ NPs are obtained as, after the rapid formation of gold domains on the surface of the Ag₂Se NPs, the remaining gold ions in solutions diffuse into the silver selenide seeds.

Figure 3.23A shows a HAADF-STEM image of a typical dimer NP. As in the previous case, the higher intensity at the small domain suggests that this corresponds to metallic Au. Interplanar distances corresponding to both cubic Ag₃AuSe₂ and metallic Au were identified in the dimers and the analysis of the images suggests that the two domains do not follow any specific epitaxy. Figure 3.23B shows a STEM-HAADF image simulation of fischesserite in the [111] zone axis. A zoom of a region that belongs to the upper domain of the experimental image in Figure 3.23A is shown in Figure 3.23C. The latter has been rotated and its contrast adjusted for comparison with the simulation in Figure 3.23B. As observed, both simulated and experimental images match excellently. A fischesserite crystalline structure model seen along the [111] zone axis has been superimposed to the STEM-HAADF image of the Ag₃AuSe₂ domain oriented along the same zone axis, which coincides to a large extent (Figure 3.23D). The images confirm that the initial β-Ag₂Se crystalline structure has been fully transformed into cubic Ag₃AuSe₂. EELS spectra were recorded on the dimer NP displayed in Figure 3.23A to confirm the new expected chemical distribution. The corresponding chemical mappings for Au and Se are shown in Figure 3.23F-H. It is clear from the images that Au is largely distributed all through the particle, with a higher density in the region that belongs to the metallic domain. The Se/Au atomic ratio is close to 2, as obtained from quantification of the

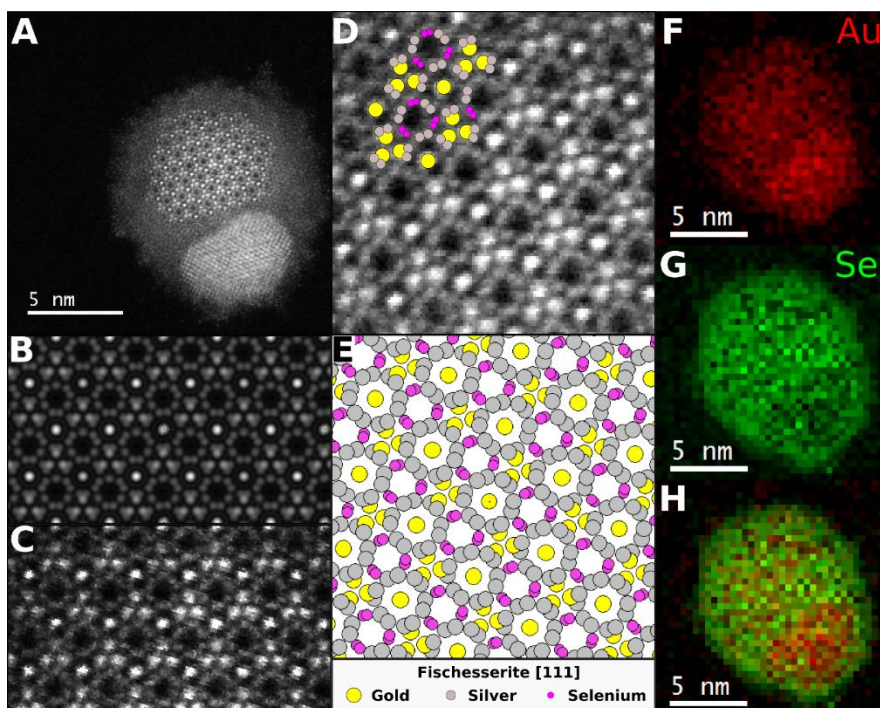


Figure 3.23. A) STEM-HAADF image of a single dimer particle from the sample. B) STEM-HAADF image simulation. C) Zoom of a region from A. Image has been rotated and contrast adjusted for comparison with the simulation. D) Zoom from A with fischesserite model in [111] zone axis. F) EELS gold signal from the particle in A. G) EELS Selenium signal from the particle in A. H) F and G superimposed.

spectra recorded along the semiconductor section, in agreement with the value expected from the Ag_3AuSe_2 stoichiometry.

Additional EELS measurements were performed for a different hybrid NP of the same sample to figure out the relative abundance of Ag and Se in the dimeric structures (Figure 3.24).

Figure 3.24 indicates the homogeneous distribution of the Ag and Se species in the centre of the particle and the formation of an amorphous outer shell of about 1 nm thickness containing mainly Se. This shell is analogous to that observed after the formation of single crystal Ag_3AuSe_2 NPs. The measured Ag/Se ratio in the centre of the particle is close to unity and consequently slightly lower than the theoretical one for Ag_3AuSe_2 , most likely due to the thin Se-rich coverage.

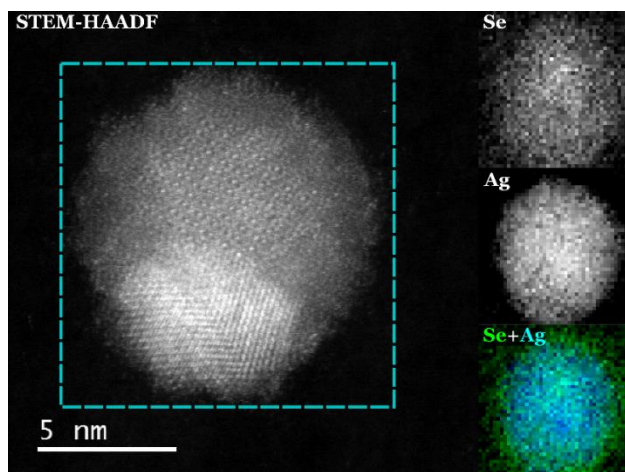


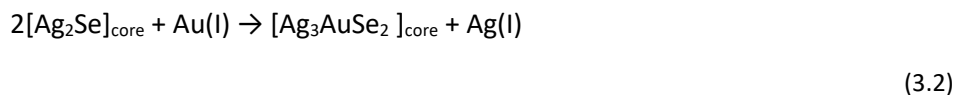
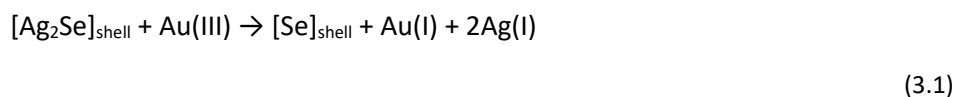
Figure 3.24. EELS quantification of an Au-Ag₃AgSe₂ NP. The selenium and silver signals were measured on a SI acquired over the highlighted region in the STEM-HAADF image.

Discussion

The observation of small gold domains in the “fast” DDA reactions allows to conclude that the amine-induced reduction of Au(III) ions to Au⁰ and the heterogeneous nucleation and growth of the metallic domain are the fastest processes. In comparison, the partial reduction of Au(III) to Au(I) ions and the diffusion of the latter into the β -Ag₂Se crystal lattice with the concomitant phase transformation require longer times. Nonetheless, both processes take place at room temperature and with very short or moderate reaction times.

However, the full reduction of Au(III) ions to metallic Au and the consequent formation of hybrid NPs occur exclusively in the presence of an aliphatic amine in the reaction medium, that is, DDA. This is in total agreement with the previously observed reducing character of long chain amines and with their well-known ability to form noble metal NPs both homogeneously and heterogeneously in solution using metal salts as precursors^{200,234}. On the other hand, it is shown that the presence of an amine in the reaction medium is not necessary for the formation of Ag₃AuSe₂ NPs or nanodomains since these are formed also when using only TOAB as surfactant. TOAB, being a surfactant formed by a quaternary ammonium cation without nonbonding electron pairs, is unable to act as a reducing agent, contrary to a primary amine-like DDA. Thus, there must be another chemical species acting as reducing agent, which must

be not only strong enough so as to reduce Au(III) to Au(I) ions allowing the formation of fischerite domains, but also weak enough so as to prevent the full reduction of Au ions to form metallic Au crystals. As shown, the formation of the ternary Ag_3AuSe_2 domains, either as single crystal or hybrid NPs, is accompanied by the formation of a Se-rich amorphous shell of about 1 nm thickness (see Figure 3.21, Figure 3.23, Figure 3.24). The latter is not observed in the Ag_2Se -precursor NPs that show excellent crystallinity²³¹ and hence it can be concluded that it forms only as a result of the reaction with an Au(III) precursor, either Au(III)-TOAB or Au(III)-DDA. Based on the presented results, the following mechanism was suggested as the most plausible explanation for the formation of the ternary fischerite phase: first, Au(III) ions are reduced to Au(I) by oxidizing the most external layers of Ag_2Se NPs, which act as a sacrificial shell forming elemental amorphous Se (3.1). Next, the newly formed Au(I) ions suffer a solid-state diffusion through the underlying β - Ag_2Se lattice (core) simultaneously exchanging one-fourth of its Ag(I) ions, leading to the formation of the ternary phase (3.2).



The same reactions are expected to take place when using either Au(III)-TOAB or Au(III)-DDA stock solutions as precursors, although the partial Au(III) to Au(I) reduction competes with the faster Au(III) to metallic Au reduction in the second case. Both the oxidation of Ag_2Se to Se and the cation exchange reaction are accompanied by the release of Ag(I) ions to the solution that precipitate in the form of AgBr. In fact, microcrystalline AgBr impurities are observed in the XRD spectrum when the sample is not appropriately cleaned²³¹.

3.3.3. The silver-gold-sulphur system

The silver-gold-sulphur system was also investigated, again, in terms of the cation exchange of gold cations into silver sulphide (Ag_2S) seeds.

The most notable products from this synthesis approach are summarized in Figure 3.25. The main difference with respect to the Ag-Au-Se system is that the

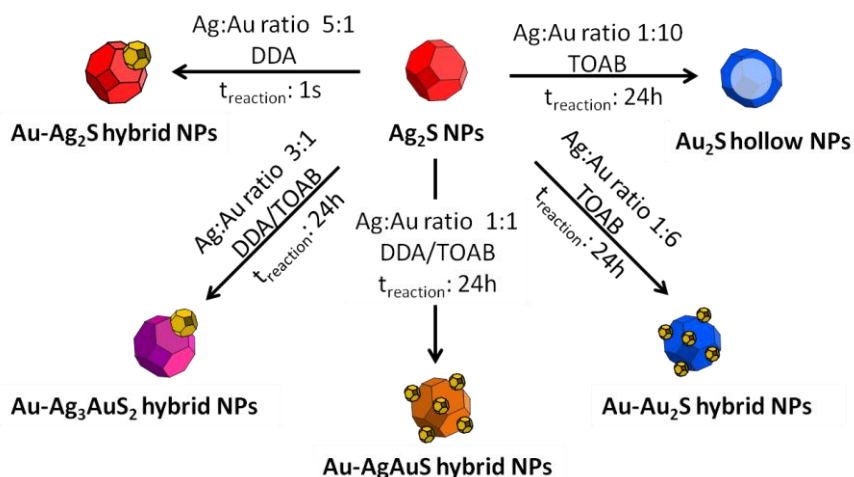


Figure 3.25. Obtained Ag-Au-S nanocomposites, indicating the parameters used in their synthesis.

phase diagram in the sulphur case contains two possible stoichiometric compounds, namely Ag_3AuS_2 (*uytenbogaardtite*) and AgAuS (*petrovskaitite*).

The products from the schemes of Figure 3.25 were analysed by XRD (Figure 3.26). Ag_2S phases were identified in seeds and 5:1 Ag:Au ratio conditions (Figure 3.26A, B). As Ag:Au ratio was increased, Ag_3AuS_2 (Figure 3.26C), AgAuS (Figure 3.26D) and Au_2S (Figure 3.26E, F) phases were observed.

Following, the characterization using HRTEM, STEM imaging, EDX and EELS mapping performed in the context of the present thesis of the different obtained nanocrystals of the Au-Ag-S system will be shown.

Ag₂S NP seeds

For the synthesized Ag_2S NPs to be used as seeds, HAADF imaging (Figure 3.27A) demonstrates the size and shape uniformity of the NPs, with a size distribution of $9 \pm 2 \text{ nm}$ (Figure 3.27B). It also reveals two domains of different contrast in some particles.

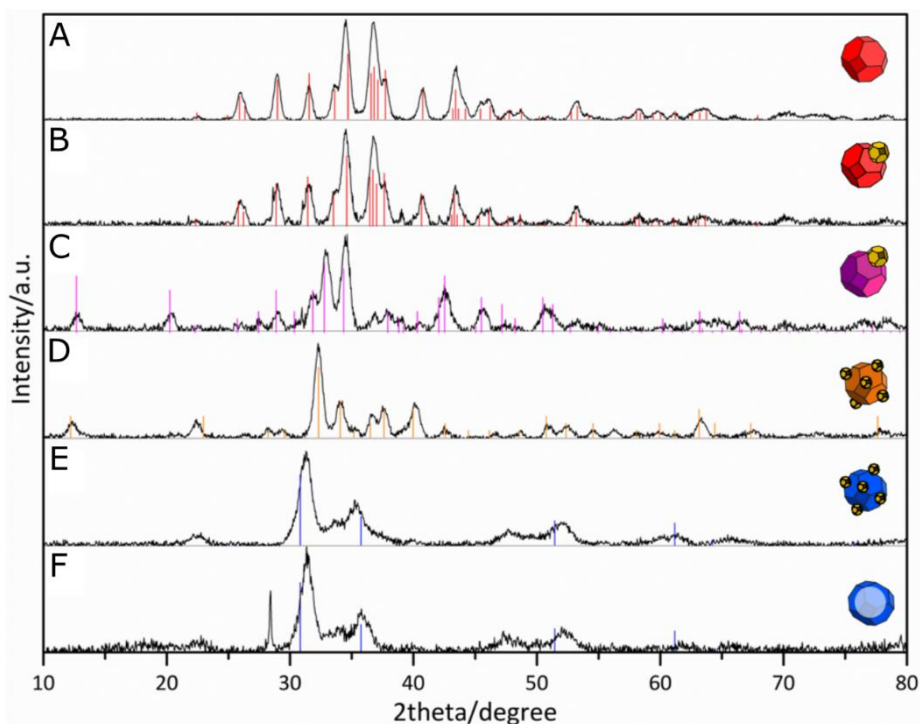


Figure 3.26. XRD patterns of (A) Ag_2S NPs, (B) Au- Ag_2S hybrid NPs, (C) Au- Ag_3Au_2 hybrid NPs, (D) Au-AgAuS hybrid NPs, (E) Au- Au_2S hybrid NPs and, (F) Au_2S hollow NPs. XRD reference patterns: monoclinic Ag_2S (JCPDS 024-0715, red), tetragonal Ag_3Au_2 (JCPDS 020-0461, pink), monoclinic AgAuS (JCPDS 038-0396, orange) and, cubic Au_2S (JCPDS 085-1997, blue).

Ag_2S can show three crystallographic phases depending on temperature: α - Ag_2S , acanthite, with a monoclinic crystal structure stable at low temperatures below 177°C ; β - Ag_2S , argentite, a super-ionic conductor with cubic symmetry usually observed in the range between 177 and 586°C , and γ - Ag_2S , a high-temperature cubic phase, stable at temperatures above 586°C .^{235–237} HRTEM analysis (Figure 3.27C,D) confirmed acanthite as the main phase in the sample but it also revealed the presence of a few NPs in lower frequency whose interplanar distances matched the high temperature cubic phase of Ag_2S , argentite (Figure 3.27H,I). Additionally, HRTEM allowed to identify as Ag the small metallic domains on the surface of a few NPs (Figure 3.27E-G).

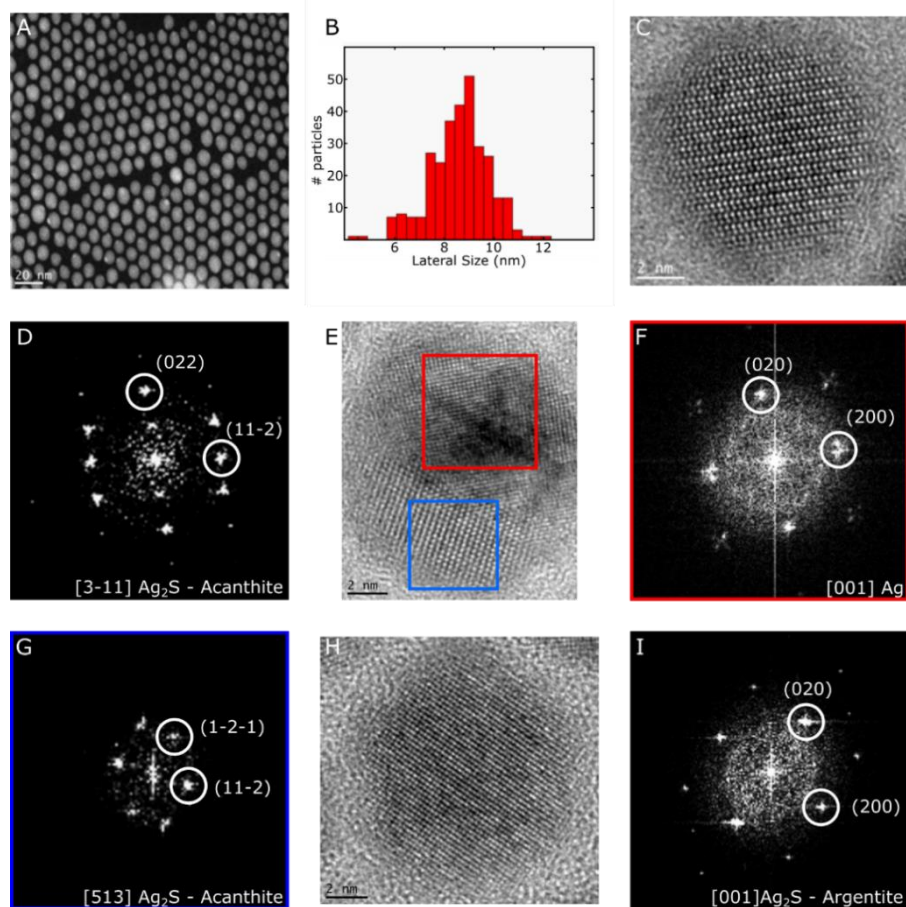


Figure 3.27. Ag_2S seeds characterization. A) HAADF image. B) Particle size distribution from HAADF images. C) HRTEM image of a representative acanthite NP. D) FFT from panel C). E) HRTEM image of a rare hybrid Ag- Ag_2S NP. F) FFT from the red region of panel E). G) FFT from the blue region of panel E). H) HRTEM image from a rare argentite NP. I) FFT from panel H).

Hybrid Au- Ag_3AuS_2 nanoparticles

A similar characterization was carried out after the Ag_2S seeds were made to react with an Au(III) solution at a 3:1 silver to gold ratio. The resulting NPs were very similar when the gold solution was in DDA or TOAB, meaning that in this case the chosen phase transfer agent was not relevant. The HAADF images (Figure 3.28A-B) demonstrated dimer-like NPs with two distinct domains and an overall size of $15 \pm 5 \text{ nm}$ (size distribution in Figure 3.28C). From the HRTEM analysis (Figure 3.28D-I) the two phases could be identified as gold and

uytenbogaardtite (Ag_3AuS_2). It is worth noting that the NPs have notably increased in size (from 9 to 15 nm), in agreement with the microscopic model of gold incorporation into the lattice.

Apart from that, a barrier of darker contrast in the HAADF images (lighter in the HRTEM ones) was observed between the two domains of the dimers. This and the clear lack of epitaxy seen in the HRTEM images, evidence an amorphous interface between the domains.

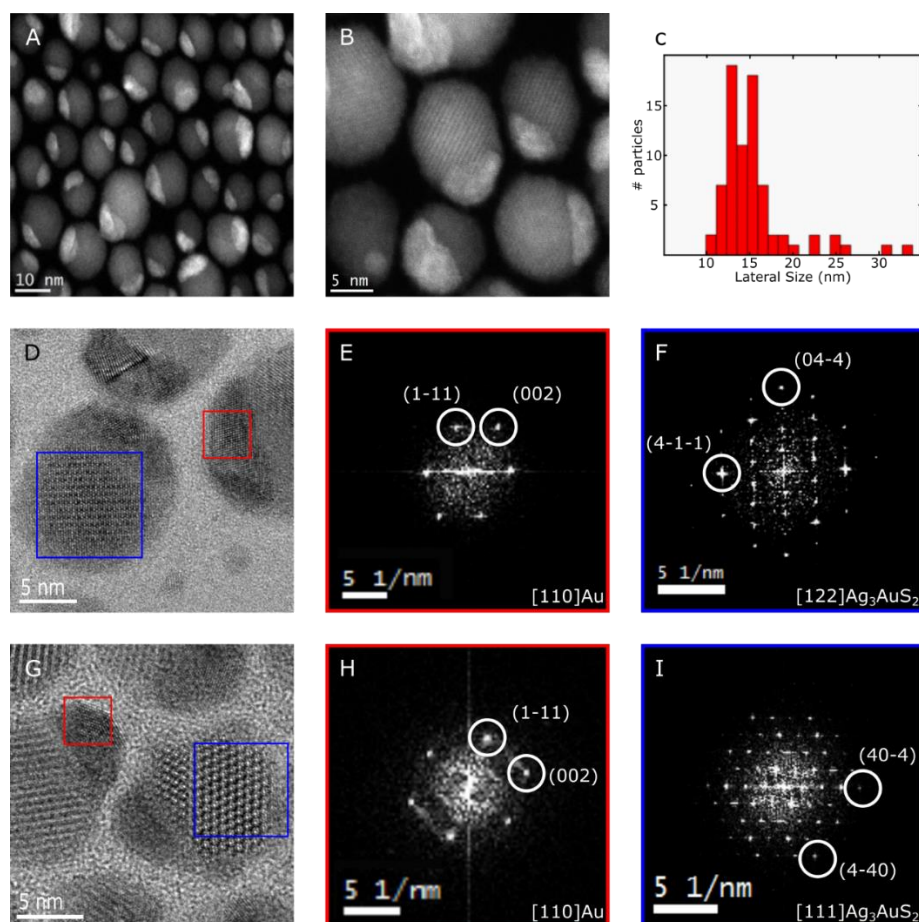


Figure 3.28. Au- Ag_3AuS_2 hybrid NPs characterization. A-B) HAADF images. C) Particle size distribution from HAADF images. D,G) HRTEM images of the Au- Ag_3AuS_2 hybrid NPs. E,H) FFT from the red region of the corresponding HRTEM image, indexed as gold. F,I) FFT from the blue region of the corresponding HRTEM image, indexed as uytenbogaardtite.

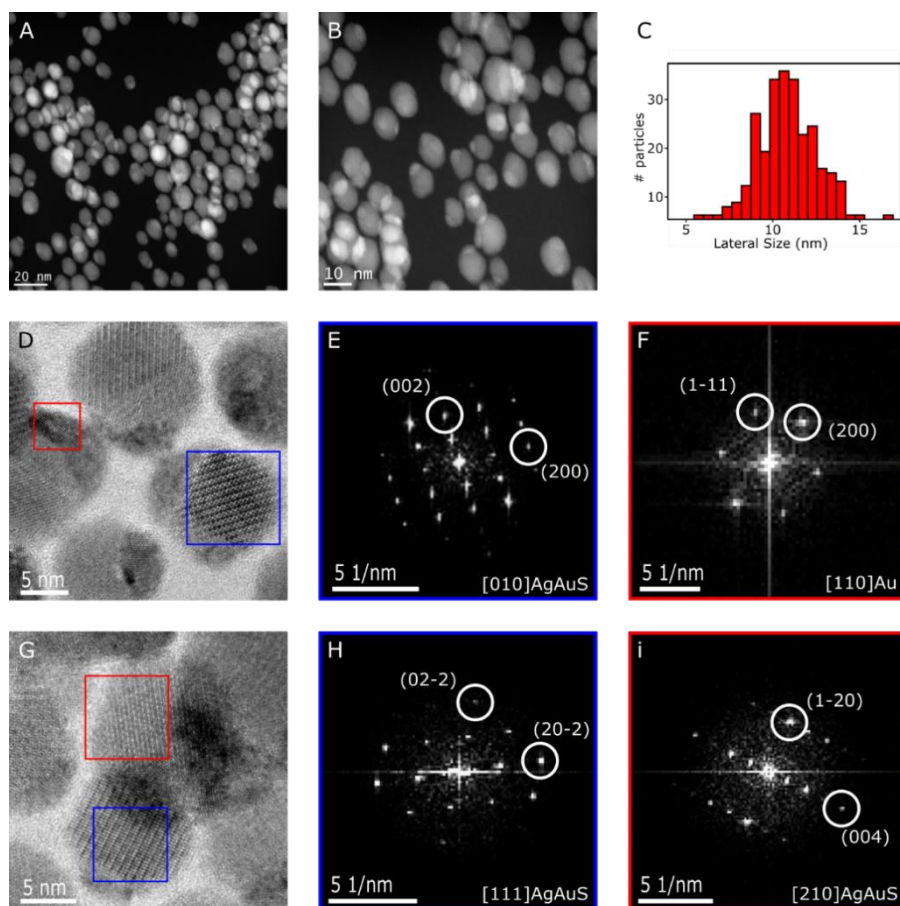


Figure 3.29. Au-AgAuS hybrid NPs characterization. A-B) HAADF images. C) Particle size distribution from HAADF images. D,G) HRTEM images of the Au-AgAuS hybrid NPs. E,F,H,I) indexed FFT from the highlighted regions in the corresponding HRTEM image.

Hybrid Au-AgAuS nanoparticles

When the silver sulphide seeds were stirred with an Au(III) solution at a 1:1 silver to gold ratio, the resulting NPs were those shown in Figure 3.29. As in the previous case, no notable differences were appreciated when using DDA or TOAB. However, with a lower gold content in the solution, the petrovskite (AgAuS) phase was preferably stabilized in the final product. The HAADF images (Figure 3.29A,B) show that these NPs also have two different domains, resulting in particles with a size distribution of 11 ± 4 nm (size distribution in Figure 3.29C). The observed lattices for the two domains in the HRTEM images and

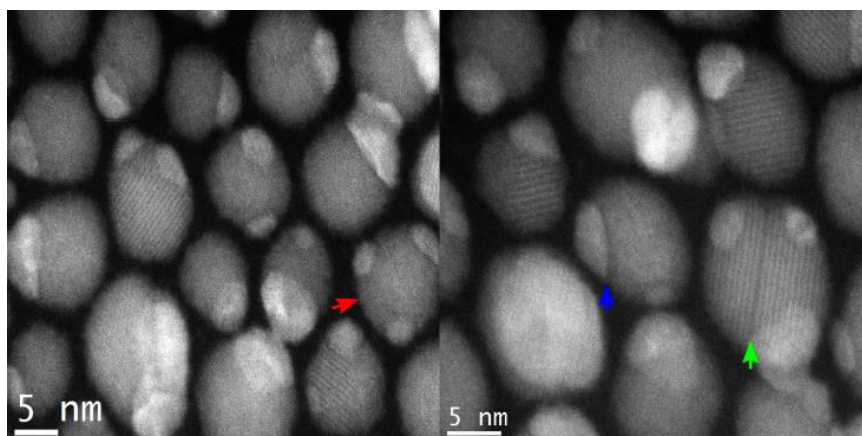


Figure 3.30. HAADF images of Au-AgAuS hybrid NPs. The red arrow highlights a NP with multiple gold domains; the blue one, the amorphous interface appearing as a dark fringe surrounding the gold domains; the green one, a defect on an AgAuS crystal.

corresponding FFTs match those of petrovskite and gold respectively (Figure 3.29D-I).

Nevertheless, it was found with further HRTEM analyses that there still was a presence of Ag_3AuS_2 , which gave an idea of the mechanism of the reaction as will be discussed later. HAADF images of the sample are shown in Figure 3.30. As it was mentioned before, these images are useful to identify nanostructures with multiple domains. The red arrow in the left-hand side image shows a NP with more than one domain of gold. Moreover, the boundary between the gold and the semiconductor domains can also be seen (the blue arrow in the right-hand side image), as well as some defects in the semi-conductor crystals (green arrow in the left image shows a planar defect). Although these defects are also seen in the previous sample, they were more frequent in the current one.

EDX analyses of these two samples were carried out. Different punctual spectra and averaged scans from wider areas were acquired for each sample. The spectra were quantified, and the average results showed the mean composition of Ag-Au-S crystals of each sample. Whereas sample derived from an Ag: Au ratio of 3:1 had $75\pm 2\%$ of silver and $25\pm 2\%$ of gold, sample derived from an Ag: Au ratio of 1:1 had $54\pm 2\%$ of silver and $46\pm 2\%$ of gold. These results perfectly agree with the stoichiometry of the two ternary materials. Figure 3.31 shows the averaged spectra for both samples.

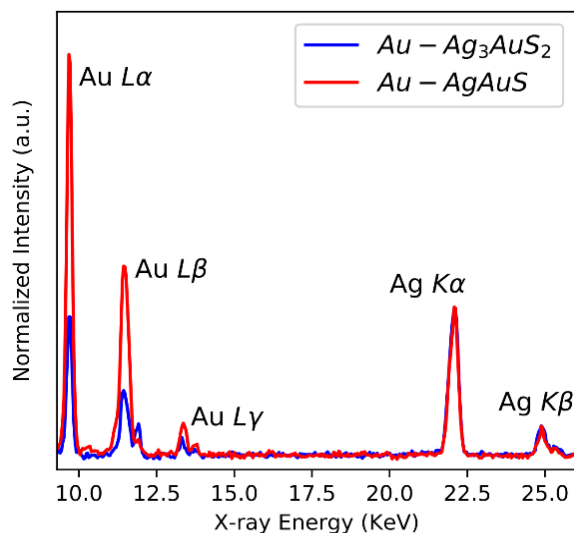


Figure 3.31. EDX spectra from the Au- Ag_3AuS_2 and Au-AuAuS samples. Background has been subtracted and spectra have been normalized by the intensity of the Ag $K\alpha$ peak.

Hollow Au_2S nanoparticles

When an Ag:Au ratio of 1:10 was used in the experiment, the shape of the NPs was radically altered. As can be seen in the HAADF images of Figure 3.32A-B, the NPs appear to be cubic shaped and to have holes. From HRTEM and FFT indexing (Figure 3.32C-I) the cubic Au_2S phase was identified.

Cation exchange with rod-like nanoparticles

The same conditions for exchange reaction were also tested with Ag_2S rod-like NPs to investigate the effects of the seed morphology. For the synthesis of Ag_2S nanorod seeds the procedure described by Jang and co-workers was used²³⁸. The obtained nanorod seeds were very monodisperse, as can be appreciated in the HAADF images (Figure 3.33A), and presented the acanthite phase as demonstrated in the HRTEM analysis (Figure 3.33B-C). They measured an average of 50 nm in length and 10 nm in width. Performing exchange reactions with a 1:1 Ag:Au ratio, petrovskite (AgAuS) nanorods were obtained with small gold domains (Figure 3.33D-F) as in the spherical seed analogous case. When a 1:10 Ag:Au ratio was tested, a mixture of hollow rods and solid rods with gold domains was obtained. In this case the shape of the seed was not altered (Figure 3.33G-I).

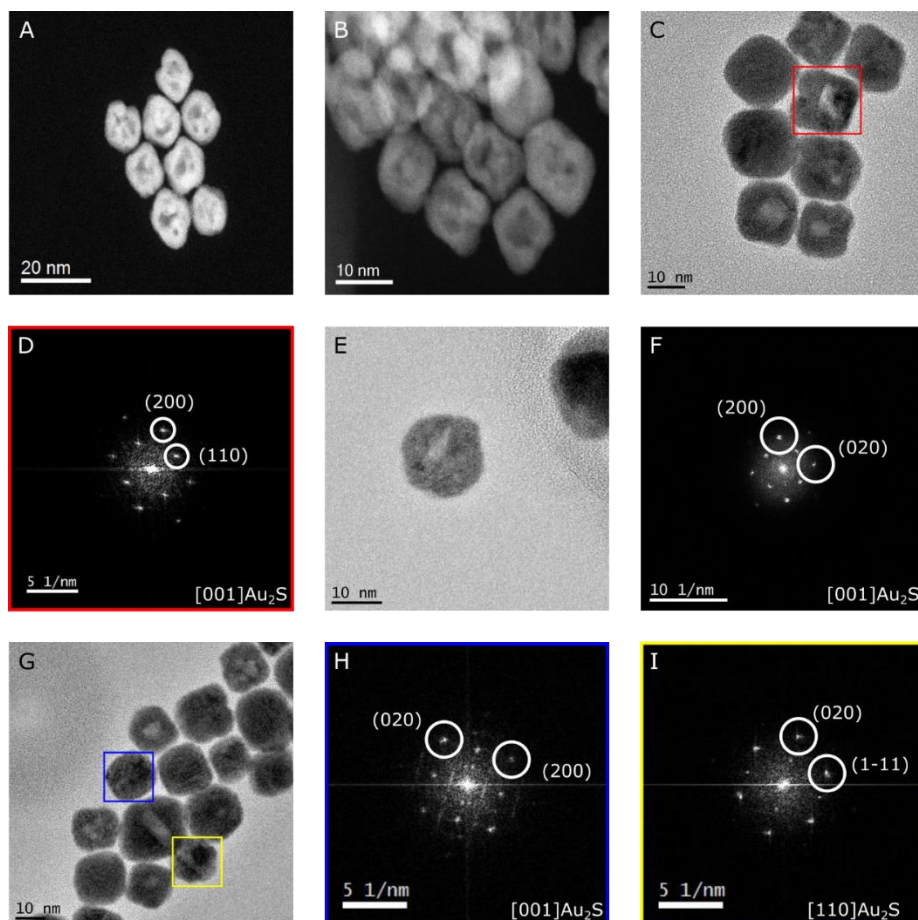


Figure 3.32. Au₂S NPs characterization. A-B) HAADF images C) HRTEM image of the NPs. D) indexed FFT from the highlighted region in C. E) HRTEM image. F) Indexed FFT from panel E. G) HRTEM image of the NPs. H, I) Indexed FFTs from the highlighted regions in G.

Discussion

Again, the competition between two different chemical pathways can be observed. On one hand, there is the full reduction of Au(III) cations to metallic Au and further heterogeneous nucleation of the noble metal at the surface of the semiconductor NP. On the other hand, there is a partial reduction of Au(III) to Au(I) ions followed by solid state diffusion and cation exchange reaction within the semiconductor. The competition can be unbalanced to one side or

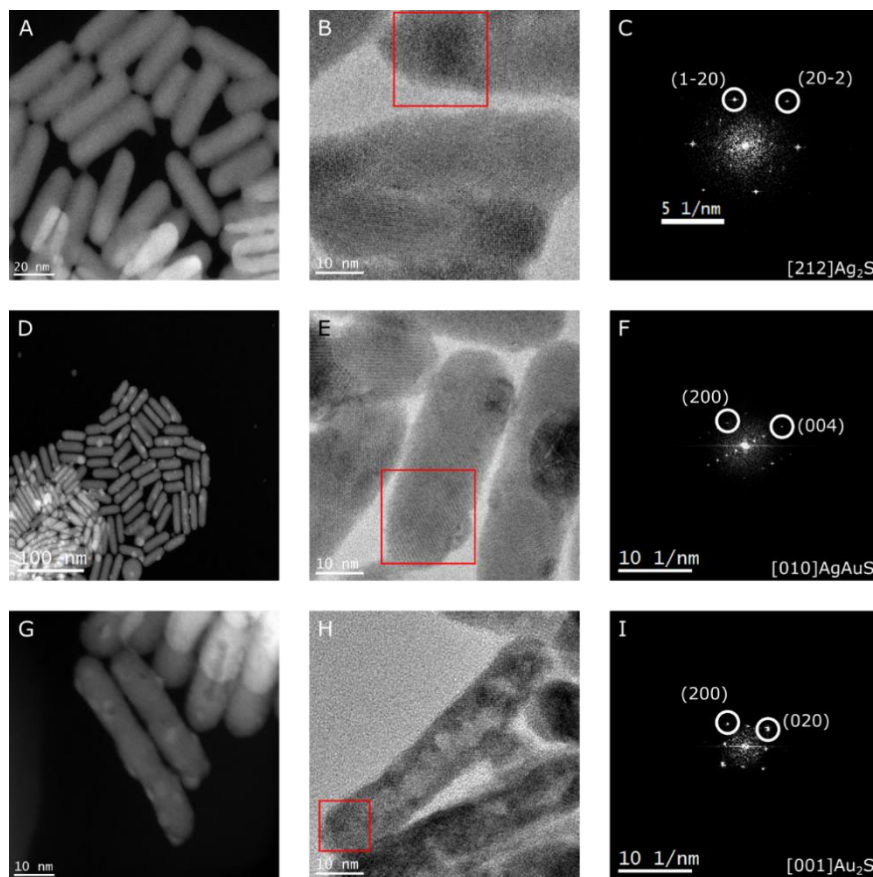


Figure 3.33. Characterization of rod-seeded processes. A) HAADF image, B) HRTEM image and C) corresponding indexed FFT of Ag_2S rods. D) HAADF image, E) HRTEM image and F) corresponding indexed FFT of hybrid Au-AgAuS rods. G) HAADF image, H) HRTEM image and I) corresponding indexed FFT of Au_2S rods.

another by the presence of specific chemical species. As with the analogous Ag_2Se system, the presence of alkylamines like DDA perceptibly enhances the first pathway favouring the formation of dimeric hybrid NPs where the formation of ternary materials can be entirely suppressed under certain conditions. On the contrary, and due to the lack of non-bonding electron pairs, the use of a quaternary alkylamine bromide like TOAB seems to partially hamper this process in benefit of the cation exchange reaction.

The heterogeneous nucleation of Au seems completely inevitable in the S-based system even when using TOAB as surfactant, contrary to the Se-based system case where ternary Ag_3AuSe_2 NPs without metallic Au domains could be easily isolated under similar reaction conditions. This fact suggests the presence of a stronger reducing environment in the current system.

The extent of cation exchange achievable constitutes another important dissimilarity between the two analogous systems: the Ag/Au/S ternary phase diagram indicates a much higher miscibility of the three elements giving rise to a wider variety of structures and stoichiometries including not only the tetragonal Ag_3AuS_2 compound, but also the monoclinic AgAuS alloy. Surprisingly, the formation of Ag/Au/S alloyed nanostructures is lacking in most of the reports working with this ternary system^{239,240}, even when metallic Au diffusion is tracked through a Ag_2S domain from a core to a surface position²⁴¹. As the only two exceptions, Liu et al. and Li et al.^{242,243} recently reported on ternary NPs obtained from the progressive sulphurization of AgAu alloy colloids, although an in-depth characterization was not performed in these cases. Furthermore, cation exchange reactions can be performed to completion in this system, obtaining Au_2S nanostructures whose formation is most likely stabilized thanks to the covalency of the Au-S bond that shows a binding energy 2 eV higher than that of the Ag-S in the parental Ag_2S ²⁴⁴. The formation of hollow nanostructures in the fully exchanged Au_2S NPs evidences an imbalance between the outwards diffusion of Ag(I) cations towards the reaction medium and the slower Au(I) inwards diffusion can be deduced. Probably the hollow morphology could not be achieved in the case of the Se-based system since at most one out of four Ag(I) ions could be exchanged ($2 \text{Ag}_2\text{Se} \rightarrow \text{Ag}_3\text{AuSe}_2$) and therefore very few vacancies are generated so as to create a hole in the Ag_3AuSe_2 NPs. Consequently, the possibility to obtain fully exchanged hollow Au_2S NPs and the observation of some $\text{Au-Ag}_3\text{AuS}_2$ in the Au-AgAuS suggest that the NPs undergo a gradual structural and chemical transition until the final compound is obtained. The gradual cation exchange is also accompanied by an increasing number of structural defects, as it can be concluded from both XRD and HRTEM analysis: XRD shows an increasing width of the peaks with the growing amount of Au(I) in the structure, while in HRTEM micrographs several defects can be observed as the cation exchange proceeds.

The question still remains on which is the main Au(III) reducing agent in these systems: the reaction mixtures contain oleylamine-capped Ag_2S NPs, and Au(III)-TOAB or Au(III)-DDA reactive species dissolved in toluene. At first glance, DDA is expected to be the most reducing species, although experiments point out that Au(III) is reduced to Au(I) and even to Au(0) also in TOAB and complete absence of DDA. We therefore suggest two possible Au(III) reducing agents, based on the reactive species present in the medium and our previous observations: on the one hand, oleylamine molecules working as stabilizing agents already coordinated at the surface of pre-synthesized Ag_2S NPs; on the other hand, the

S(-II) anion of the inorganic crystal lattice as in the Se case. In fact, HRTEM micrographs also point to the formation of a thin amorphous shell after the cation exchange reaction (Figures 29D,G and 30D,G). Although, in principle, S(-II) should be less reducing than Se(-II), experimentally the nucleation of Au(0) is observed in all samples prepared with S and could not be avoided, contrary to what happens with Se.

The role of two different surfactants in the reaction medium can also be described as follows: while dodecylamine favours the heterogeneous nucleation of metallic Au on the surface of the semiconductor domains in detriment of the cation exchange reaction, the use of TOAB turns out to be crucial for the enhancement of the exchange in order to reach even full cation substitution.

Finally, the morphology of the seeds has been shown to have little effect on the cation exchange/Au(0) nucleation processes. However, the larger overall size of the rod seeds prevented the distortion of the shape into more thermodynamically favourable shapes as in the case of the cubic Au₂S NPs from spherical seeds. The fact that size improves the shape resilience of seed NPs in cation exchange reaction had already been reported²⁴⁵.

3.3.4. Conclusions

The results shown represent the characterization of a large number of ternary semiconductor NPs. Through them, a deep understanding of the cation exchange between gold and silver chalcogenides has been achieved. The reducing effect of amine chains in the Ag-Au-Se/S systems has been observed. An additional reducing agent has been found in the sacrificial amorphous Se/S layer that appears in the NPs. Also, the fact that the transition between Ag₂X and Au₂X through exchange reactions occurs gradually through intermediate phases has been proven. The characterization of the products with both analytical and imaging techniques in the TEM has been critical to unveil these mechanisms.

CHAPTER 4: ELNES analysis applied to nanoparticles

As described in the introduction of this thesis, EELS actually probes the joint density of states of a material and it thus provides information that goes far beyond compositional mapping. The local measurement of properties, such as oxidation state and bonding, can be used to understand nanoscale phenomena. This chapter presents material science problems in which this advanced EELS analysis has provided valuable information. In the first half of the chapter, a synthesis pathway is explored, much in the same fashion as in the previous chapter. Either hollow or core/shell NPs were obtained with the small change of adding water traces to the NP solution. The key to understand these phenomena was elucidated through measurements of the oxidation state of the relevant elements by EELS. In the second half of the chapter, a method to measure the inversion parameter, a figure related to the cation distribution in a given crystalline lattice, from ELNES analysis is discussed. Its application to core/shell NPs gave interesting insight into their nature. The results presented here represent a step forward from the previous chapter taking full advantage of the information available in EELS data.

4.1. The role of manganese oxidation state in core/shell $\text{MnO}_x/\text{Fe}_3\text{O}_4$ nanoparticles

As seen in the previous chapter, the design and synthesis of NPs by colloidal chemistry with appealing physicochemical properties has a great potential. The control of the different chemical processes at the nanoscale can result in a wide range of novel nanostructures with unique morphologies.²⁴⁶ Among these novel structures, hollow NPs of metal oxides are attracting considerable attention because of their potential for applications in energy storage,²⁴⁷ catalysis,²⁴⁸ or drug delivery.²⁴⁹

Hollow NPs can be obtained through a variety of chemical processes.^{250–252} In the particular case of hollow metal oxide nanostructures, acid etching²⁵³ and Kirkendall processes²⁵⁴ are the most frequently used ones. Moreover, recently, the synthesis of hollow iron oxide NPs by galvanic replacement using divalent iron ions and manganese oxide NPs as seeds has been achieved.²⁵⁵ This process

allows the combination of seeded-growth methods, extensively developed for the growth of core/shell particles, to obtain complex hollow heterostructures.

In this section, the elucidation through AEM of the synthesis mechanism responsible for the obtention of either full-dense core/shell or hollow Mn-Fe oxide NPs is presented, through the characterization of samples exposed to different amounts of oxidizing agents.

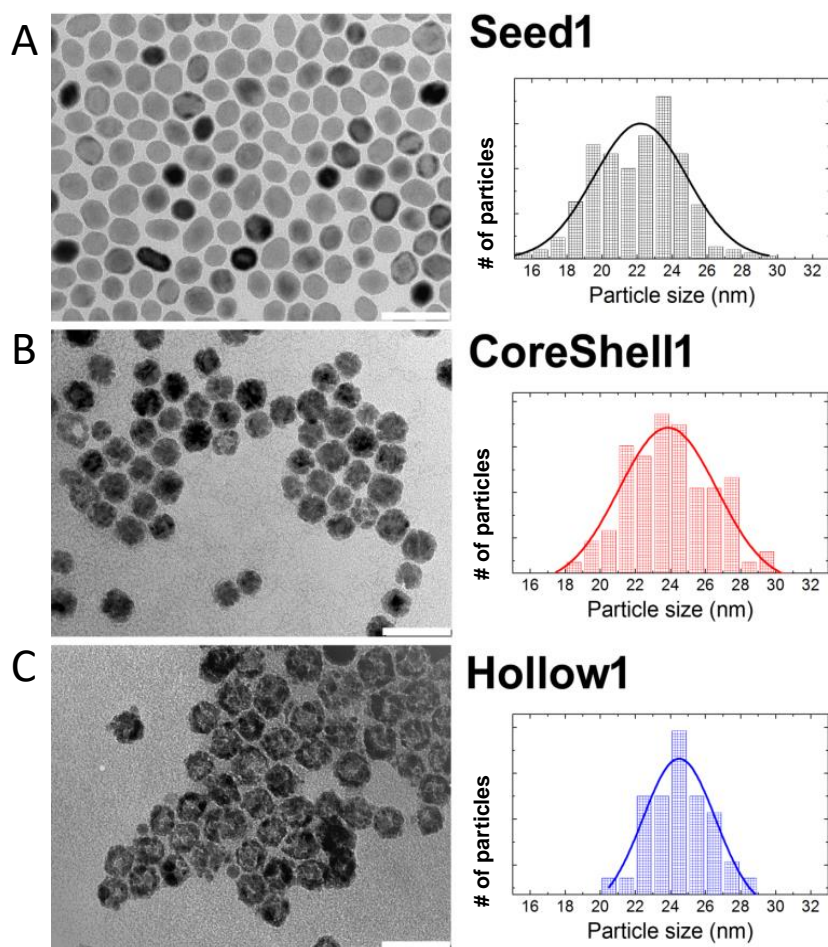


Figure 4.1. TEM images and their corresponding particle size histograms for A) Seed1, B) CoreShell1 and C) Hollow1 NPs. Scale bars correspond to 50 nm.

4.1.1. Synthesis and preliminary characterization

Manganese oxide/iron oxide core-shell NPs were synthesized by seeded-growth following previous reports.^{149,150} Briefly, in a first step, manganese oxide NPs were prepared by thermal decomposition of manganese oleate in 1-octadecene (sample Seed1). Subsequently, these particles (Seed1) were used as seeds to grow an iron oxide shell by the addition of an iron (III) precursor solution (sample CoreShell1 – CS1) and heated to 220 °C for an hour. In a second approach, 0.5 mL of milliQ H₂O (> 1% in weight) were added to the solution containing the seeds before following the same iron precursor hot injection procedure (sample Hollow1 – HW1).

The three samples have similar particle size and narrow size distribution (22±2, 24±3 and 25±2 nm for Seed1, CoreShell1 and Hollow1, respectively) being both heterostructures slightly larger than the initial Seed1 NPs. TEM images clearly evidence that the presence of H₂O in the reaction has a tremendous effect on the morphology of the heterostructures (Figure 4.1), even if both syntheses use precisely the same procedure and identical manganese oxide seeds.

Heterostructures synthesized without the presence of H₂O show the expected fully dense core/shell morphology, whereas heterostructures grown adding H₂O exhibit a hollow morphology with a void in the centre of the particle

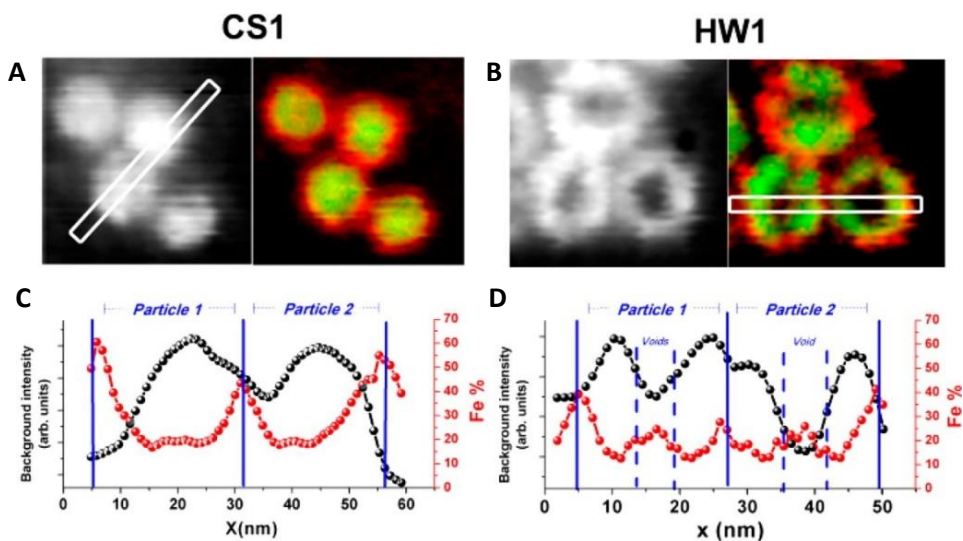


Figure 4.2. A,B) HAADF images and EELS mapping (red and green refer to the Fe and Mn L_{2,3}-edge signals). C,D) Background and Fe elemental percentage profiles along two NPs for CS1 and HW1, respectively.

4.1.2. EELS assessment of hollow and core/shell nanoparticles

The EELS mappings for sample CoreShell1 sample confirm the core/shell architecture with iron and manganese in the shell and core, respectively. Integrated EELS background (proportional to thickness) and iron/manganese percentage signals are presented in Figure 4.2A-B. The maps from the CoreShell1 (Figure 4.2A) sample demonstrate central core of manganese oxide (in green) particles surrounded by iron oxide (in red). This corroborates the formation of the fully dense structure. From a profile extracted along the highlighted region in Figure 4.2A, an iron-rich 6 ± 2 nm shell thickness was measured (Figure 4.2C). However, for sample Hollow1 the maps are more complex. From the outside to the inside, shells of iron oxide (in red), manganese oxide (in green) and a void are observed (Figure 4.2B). Traces of iron can also be detected in the inner surface of the manganese oxide. The background profile extracted along the highlighted region confirms the hollow morphology, with voids of 6 to 7 nm in diameter. Iron signal is present all over the particle indicating that the iron is located in a shell covering the entirety of the manganese oxide (Figure 4.2D).

From a deeper analysis of the CoreShell1 EELS maps in Figure 4.2A it was clear that there was some Fe-Mn intermixing in the particle. Fe/Mn ratio for two types of NP were simulated. The simulations considered the signal for each element proportional to its projected thickness and the acquisition process was modelled by a gaussian point spread function. The first simulated model consisted on a spherical particle of manganese oxide surrounded by a spherical shell of iron oxide, i.e. a prototypical core-shell NP, named "single shell" in the first column of Figure 4.3. The second simulation has an external iron oxide shell, a manganese oxide core, and an additional region between the two where the composition linearly varies from iron oxide to 50% iron 50% manganese oxide to pure manganese oxide, thus representing a core-shell NP with diffusion from the shell cations into the core. The results corresponding to these models are shown in the central column of Figure 4.3. By comparing the simulations to the experimental data (right column), it is clear that the diffusion picture is more accurate.

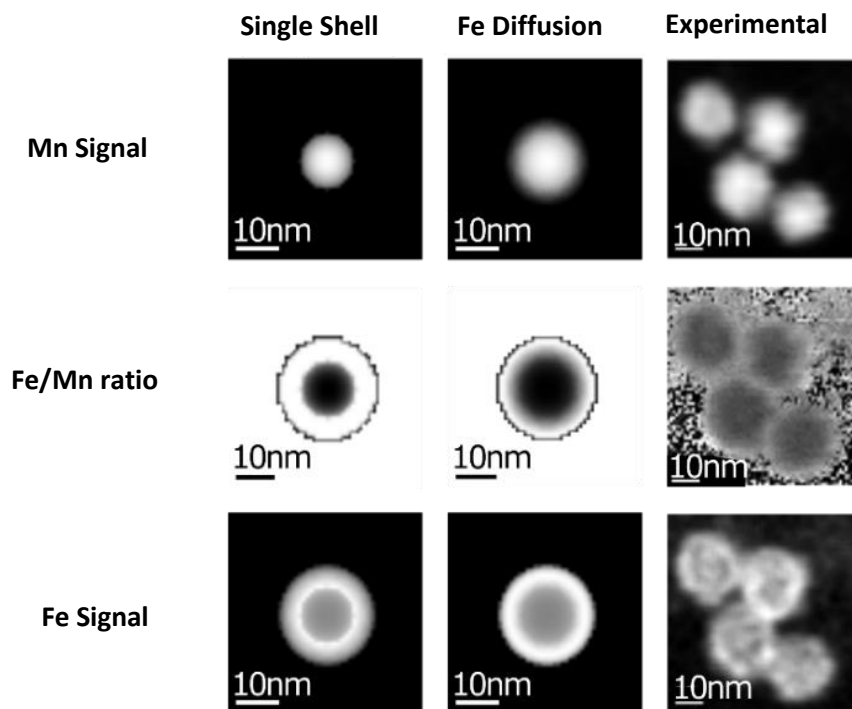


Figure 4.3. EELS simulations from geometric models. The signal maps and Fe/Mn ratio simulations of a purely core-shell $\text{MnO}_x\text{-FeO}_x$ NP (single shell), a core-shell with diffusion of Fe into the core (Fe diffusion) and the experimental data.

Moreover, the Mn L_3 edge of the Hollow1 and CoreShell1 samples show significant differences (Figure 4.4A). An EELS quantitative analysis was performed using the Oxide Wizard software¹⁵¹. Reference samples of manganese oxides (MnO_2 , Mn_3O_4 , Mn_2O_3 , MnO) were previously analysed with Oxide Wizard and, so, the parameters for different oxidation states of manganese were calibrated (coloured circles in Figure 4.4). When the obtained values for the CoreShell1 sample are compared to them, it is revealed that the core region is mainly composed by Mn^{2+} ions (MnO) (Figure 4.4B). However, for the Hollow1 sample, the analysis matches Mn_3O_4 , denoting a more oxidized manganese.

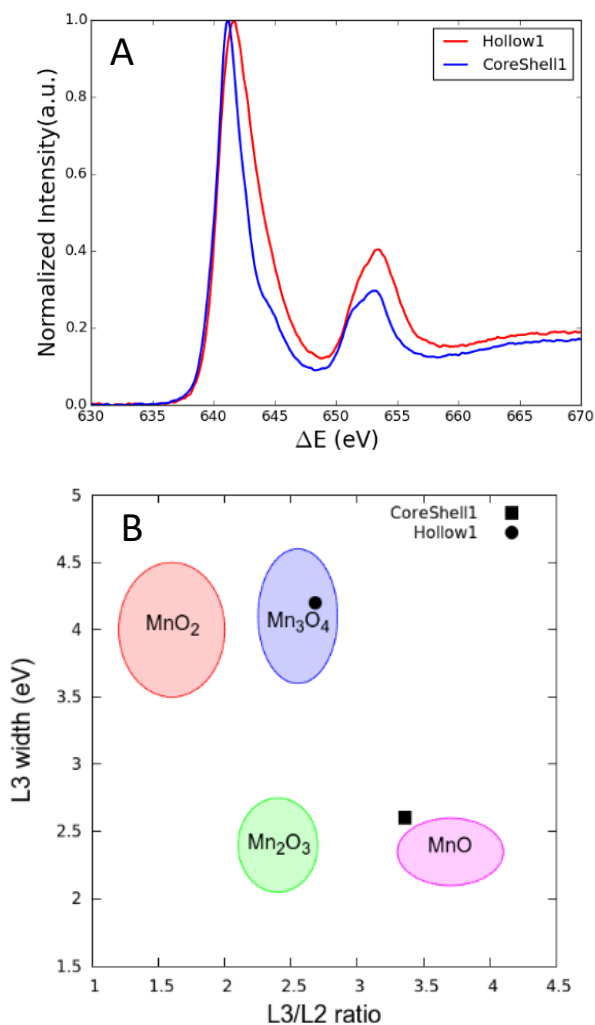


Figure 4.4. A) Spectra from MnO_x regions in samples Hollow1 and CoreShell1. B) Plot of the fine structure parameters from spectra in (A) compared to the literature values¹⁵¹.

A 3D Reconstruction from HAADF-STEM tomography was performed to get a better understanding of the morphology of sample Hollow1. It can be observed that NPs present a complex web of holes that connect the hollow inside of the particle with the outside (see Figure 4.5).

At this point, it is clear that the addition of water in the synthesis, apart from resulting in completely different morphologies for the final NPs, also leads to the presence of Mn₃O₄ in the hollow NPs as opposite to MnO in the dense core-

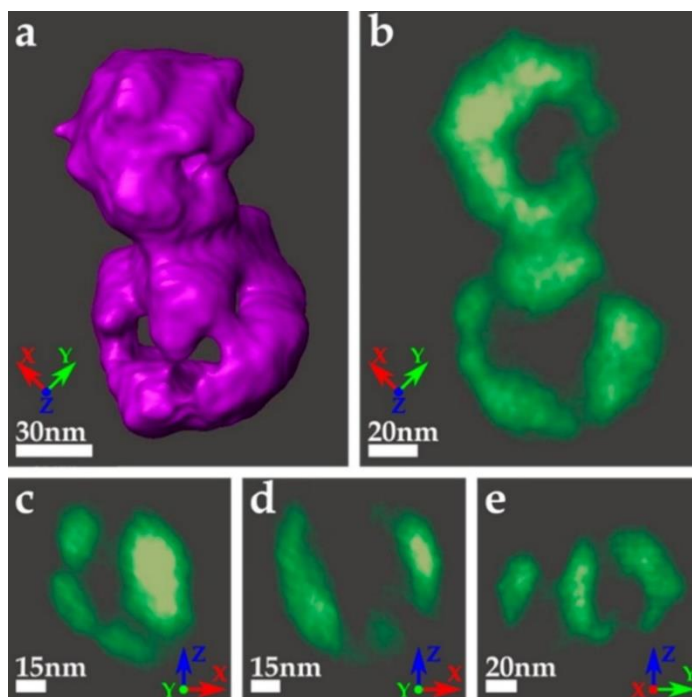


Figure 4.5. (A) 3D tomographic reconstruction of two NPs of the HW1 sample. Slices of the 3D tomographic reconstruction in the (B) XY, (C-D) XZ (for each particle), and (E) YZ planes.

shell NPs. Also, the presence of pinholes in the Hollow1 particle and the presence of iron oxide in the inner wall is demonstrated. Finally, the shell in the CoreShell1 sample shows intermixing of iron and manganese oxides. From these results it is possible to start creating a picture of the processes occurring in the synthesis.

In previous works²⁵⁵, it had been proposed that the Fe^{2+} deposition onto the surface of Mn_3O_4 NPs in aqueous media allows the formation of hollow structures due to their relative reduction potential values (i.e., $E_{\text{Fe}^{3+}/\text{Fe}^{2+}} = 0.77 \text{ V}$ and $E_{\text{Mn}_3\text{O}_4/\text{Mn}^{2+}} = 1.82 \text{ V}$). The initial Fe^{2+} ions start a redox process decreasing the amount of Mn^{3+} in the seed (being reduced to Mn^{2+}) while Fe^{3+} is deposited in the outer and inner surface of the hollow structure. In our case the iron precursor is in a trivalent oxidation state which can be reduced to Fe^{2+} in the environment during the decomposition of the organic chain of the metal precursor^{256–258}, leading to the kick-off of the galvanic replacement. Mn_3O_4 is a tetragonal spinel with a normal configuration where all trivalent cations are located in octahedral positions. Hence, the iron oxide growth based on the galvanic process could be interpreted by part of the process where the partial

$\text{Mn}^{3+} \rightarrow \text{Mn}^{2+}$ reduction permits the diffusion of Fe^{3+} ions into the tetrahedral voids, diffusing into the Mn_3O_4 seeds and keeping the spinel stoichiometry. As the chemical reaction progresses, small pure Fe_3O_4 grains are formed on the surface of the NPs and the inner Mn^{3+} ions in the Mn_3O_4 are reduced forcing their dissolution through pinholes created in the NP, which allows the hollowing process.

Conversely, it is possible that in the CoreShell1 sample there was no hollowing effect since the process is thermodynamically not favoured due to the presence of an inner Mn^{2+} -rich structure. That is, while the initial iron deposition and diffusion occurs possibly in an external, more oxidized layer of MnO_x , the $\text{Mn}^{3+} \rightarrow \text{Mn}^{2+}$ reduction cannot take place in the inner MnO of the seed, so the hollowing process does not occur.

In this picture, the effect of water in the synthesis would be to catalyse the oxidation of the MnO seeds into Mn_3O_4 . This would completely explain the results shown.

4.1.3. Final testing and additional synthesis

To test this, the seeds were treated under different oxidizing conditions and temperatures prior to the addition of iron precursors. These conditions were adding water that had been fully degassed, water bubbled with compressed air and finally oxygenated water (H_2O_2) and heating the samples at 110 °C and 220 °C. The seeds were then characterized by XRD, obtaining the results depicted in Figure 4.6, where the black curves correspond to the unheated seeds, the red one to 110 °C and the blue one to 220 °C for each treatment. The XRD spectra show that for the degassed H_2O the seeds remain unchanged by the degassed water. Their crystal phase is mainly MnO, although a shoulder at 36 ° indicates the presence of some Mn_3O_4 . This result is in agreement with having initially MnO seeds with an external, more oxidized, Mn_3O_4 shell. However, for the other two samples, treated under more oxidizing conditions and at 220 °C, the seeds completely change their phase, turning completely into Mn_3O_4 as can be seen in the spectra from Figure 4.6B-C. Finally, it was tested that, when completing the reaction with oxidized seeds, hollow NPs were also obtained (Figure 4.7). Therefore, the role of water in the previously studied synthesis was to carry oxidizing agents that turn MnO seeds into Mn_3O_4 seeds at the synthesis temperature.

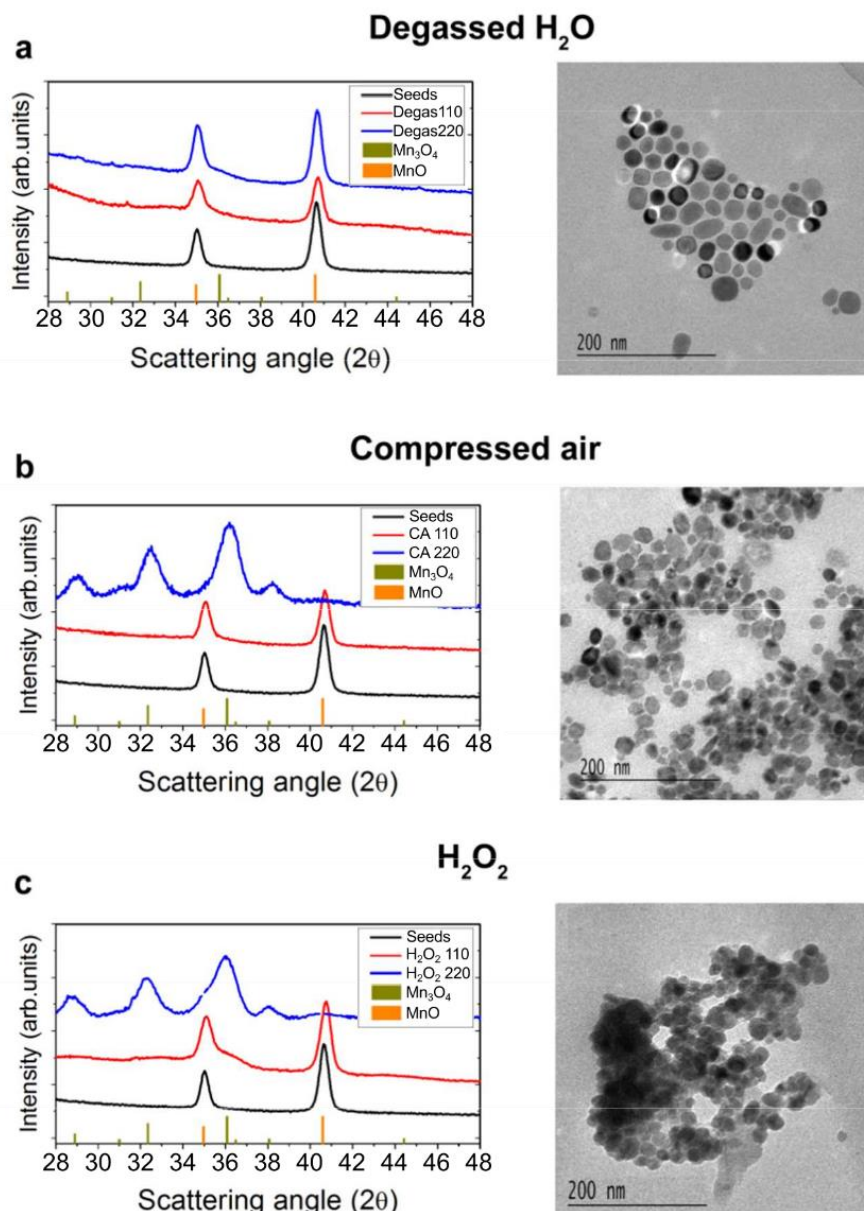


Figure 4.6. XRD patterns and TEM images for samples treated with (A) degassed H₂O, (B) compressed air–bubbled H₂O and (C) H₂O₂.

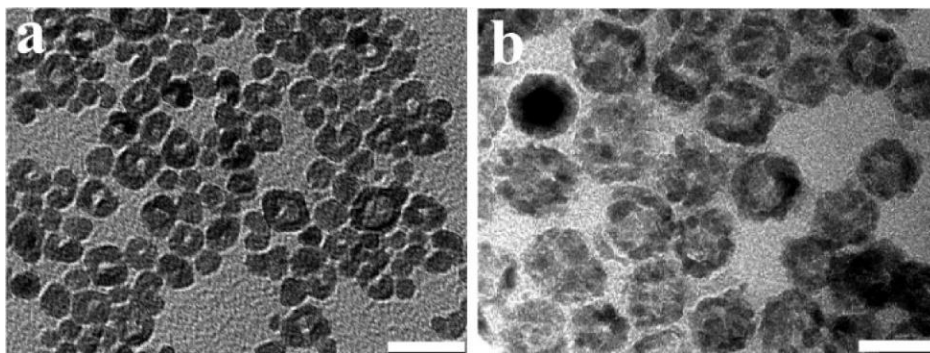


Figure 4.7. TEM images for heterostructures obtained from oxidized seeds. Scale bars correspond to 20 nm

4.1.4. Summary

It has been shown that, in the synthesis of $\text{Mn}_3\text{O}_4/\text{Fe}_3\text{O}_4$ heterostructures, the role of the H_2O is to oxidize the seed NPs from $\text{MnO}/\text{Mn}_3\text{O}_4$ to fully oxidized Mn_3O_4 . The presence of Mn^{3+} ions in the core of the seeds allows the formation of hollow structures by galvanic replacement. On the other hand, Mn^{2+} ions in the core hinder the redox process that originates the hollowing, leading to core/shell structures, as revealed by the ELNES analysis. After the realization of the additional synthesis (Figure 4.6, Figure 4.7) the initial manganese oxide phase of the seeds was proven to be the critical factor in the outcome of the synthesis.

4.2. Atomic resolution cation inversion measurement through EELS in spinel oxides

Spinel oxides have been frequently used in NP synthesis, such as the ones in the previous section, due to the appealing fundamental properties linked to their unique structure, with uses ranging from everyday materials, like ceramics, to advanced applications in biotechnology^{259–263}. In fact, given the structural similarities, spinel materials are particularly suited to grow core/shell structures with enhanced multifunctional properties^{150,168,264–269}.

Spinel materials are characterized by an AB_2Z_4 structure, where A and B are divalent and trivalent cations, respectively, and Z is a divalent anion, typically

oxygen. The A cations occupy the tetrahedral positions (T_h) in the structure, whereas the B cations occupy the octahedral (O_h) ones. However, depending on the nature of the A and B cations (e.g., ionic radius) and the external conditions (e.g., temperature or pressure) the distribution of the cations in the structure can be altered. This distribution is characterized by the degree of inversion, x , where the structure is represented as $(A_{1-x}B_x)[A_xB_{2-x}]Z_4$, where “()” denote T_h positions in the structure and “[]” O_h positions, respectively. Thus, normal spinels, $(A)[B_2]Z_4$, have $x = 0$, a material with a completely inverted structure, i.e., $(B)[AB]_2Z_4$, would have $x = 1$ and is called an inverse spinel, while x is equal to $\frac{2}{3}$ for a completely random cation distribution²⁷⁰. Although the different spinel materials are normally classified in specific spinel categories (e.g., $FeAl_2O_4$ is a normal spinel), depending on different factors such as the synthesis approach (e.g., thermal decomposition, sol-gel), processing methods (e.g., quenching, ball-milling), morphology (e.g., thin films, NPs) or size, a cation inversion different from the nominal one can take place, leading to a change in the inversion parameter with respect to bulk materials. Interestingly, the degree of inversion has been shown to play an important role in the functional properties (e.g., electronic, transport, optical, magnetic, mechanical or structural) of spinel materials^{271–279}. However, despite its relevance, the inversion parameter is seldom studied in detail, particularly in nanostructured materials.

Several techniques exist that can assess the coordination of chemical species in a crystal, such as x-ray and neutron diffraction refinement, Mössbauer spectroscopy, x-ray absorption or nuclear magnetic resonance^{280–283}. In general, these techniques yield averaged information, typically from rather large volumes. Nonetheless, when dealing with complex systems such as core/shell NPs, a few unit cells can determine the resulting overall properties of the system, often making classical bulk approaches unsuitable. In fact, the atomic scale determination of the inversion parameter has never been reported. Therefore, it is clear that novel approaches are required to selectively characterize the different ions in NPs with high spatial resolution.

As explained in the introduction of this thesis, aberration- corrected TEM is an extremely useful technique to probe materials at the atomic scale. Moreover, when coupled to EELS, the oxidation state of chemical species^{23–27} and their distribution in a crystalline lattice can be mapped^{284,285}. These characteristics are very well-suited to the measurement of cation inversion. In this section, a study of the oxidation state and the cation inversion parameter in Fe_3O_4/Mn_3O_4 core/shell NPs is presented, through EELS atomic resolution mapping.

4.2.1. Nanoparticle synthesis

The Fe₃O₄/Mn₃O₄ core/shell nanoparticles were synthesized using a seed-growth approach^{150,284}. Fe₃O₄ nanoparticles were previously synthesized and used as seeds for the subsequent growth of the Mn₃O₄ shells. The Fe₃O₄ seeds were synthesized by thermal decomposition of iron(III) oleate in 1-octadecene in the presence of oleic acid. The reaction mixture was heated to 320 °C with a heating rate of 3 °C/min under argon flow and kept at this temperature for 30 min. The reaction mixture was then cooled to room temperature. The purification process subsequently involves several centrifugation cycles with a mixture of hexane and ethanol. Finally, the particles were dispersed in hexane. The subsequent growth of a Mn₃O₄ layer onto the Fe₃O₄ seeds was performed by dispersing the Fe₃O₄ nanoparticles and oleic acid in dibenzyl ether and degassed under several cycles of vacuum and argon to remove any hexane traces. Then, the suspension was heated to 220 °C under an argon flow. At this moment, a solution of manganese(II) acetylacetonate, 1,2-hexadecanediol, and oleylamine, previously heated to 100 °C, was injected at a fast rate. The reaction mixture was kept at 220 °C for 60 min and then cooled to room temperature. The core/shell nanoparticles were purified several times by magnetic separation after mixing with hexane and acetone.

4.2.2. Morphological and structural characterization

The STEM-HAADF images (Figure 4.8A-B) show rounded, monodisperse particles. From their size distribution (Figure 4.8C) a 14.7 nm average size and a standard deviation of 1.2 nm were estimated. EEL Spectrum Imaging at high resolution for the region in Figure 4.8D was performed. The EELS signal maps for the oxygen K edge (Figure 4.8E), manganese (Figure 4.8F) and iron (Figure 4.8G) reveal the core/shell nature of the NPs. The maps demonstrate that the NPs are composed of iron oxide cores surrounded by irregular manganese oxide shells with a 1-2 nm thickness (Figure 4.8H).

From this kind of maps, iron and manganese signal profiles were extracted along the core-shell interface of the NPs (Figure 4.9). On these profiles, it was considered that the core-shell interface extends between the region in which the iron signal drops from 75% to 25% compared to that in the middle of the particle. By measuring the interface width of several NPs, the core/shell

interface was estimated to extend 0.31 ± 0.05 nm, which can be considered as atomically sharp. The observed oxygen relative composition, as measured by the so-called Egerton method³⁹, is around 58% (Figure 4.10). This value points to magnetite (Fe_3O_4) in the core and hausmannite (Mn_3O_4) in the shell as the most likely phases in the nanostructure. This was further studied by analysing the fine structure of the Mn $L_{2,3}$ -edge. EELS spectra acquired over the shell of several NPs were analysed using OxideWizard¹⁵¹ to compare their ELNES parameters to the reference values. As can be seen in Figure 4.11, the obtained L_3/L_2 ratio and L_3 onset with respect to the O K edge have a best match with Mn_3O_4 . The spectra were also compared to reference spectra from other reports^{151,183} demonstrating that the shell is indeed hausmannite (Figure 4.12).

The detailed structural analysis from atomic resolution STEM-HAADF images is in agreement with the manganese oxide shell being the tetragonal spinel phase²⁸⁶ and the iron oxide core its cubic spinel phase²⁸⁷. The FFT from the centre of a core/shell NP, highlighted in blue in Figure 4.13B, where the manganese signal is very low, matches excellently the Fe_3O_4 spinel crystal lattice²⁸⁷, in agreement with the EELS characterization (Figure 4.13A). In particular, Figure 4.13E corresponds to a $[110]_{\text{Fe}_3\text{O}_4}$ zone axis, where spots related to the $(2-20)_{\text{Fe}_3\text{O}_4}$ (2.9 \AA plane distance) and the $(004)_{\text{Fe}_3\text{O}_4}$ (2.0 \AA) planes can be observed (nominal spacings for these planes are $d(2-20)_{\text{Fe}_3\text{O}_4}=2.968 \text{ \AA}$ and $d(004)_{\text{Fe}_3\text{O}_4}=2.099 \text{ \AA}$).

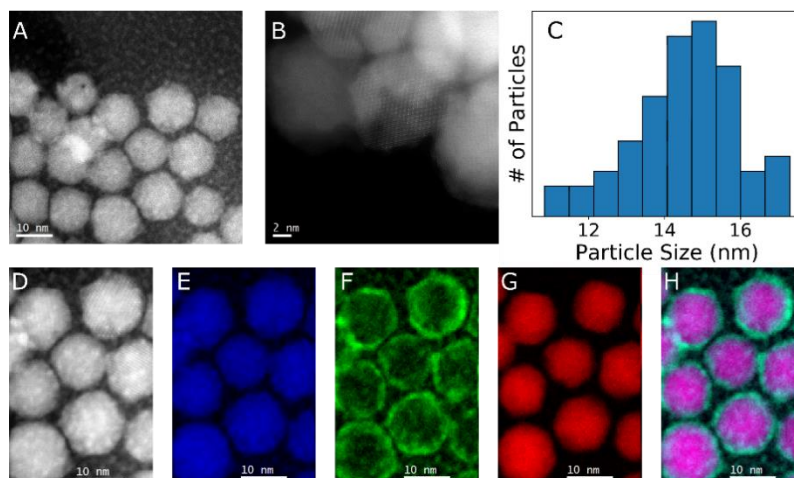


Figure 4.8. STEM-HAADF and EELS characterization of the NPs A) at medium resolution and B) at higher resolution. C) Size distribution of the NPs obtained from STEM-HAADF images. D) STEM-HAADF image from the region where EELS spectrum imaging was performed to map the E) oxygen signal, F) manganese signal and G) iron signal. H) Colour mix of panels E-G.

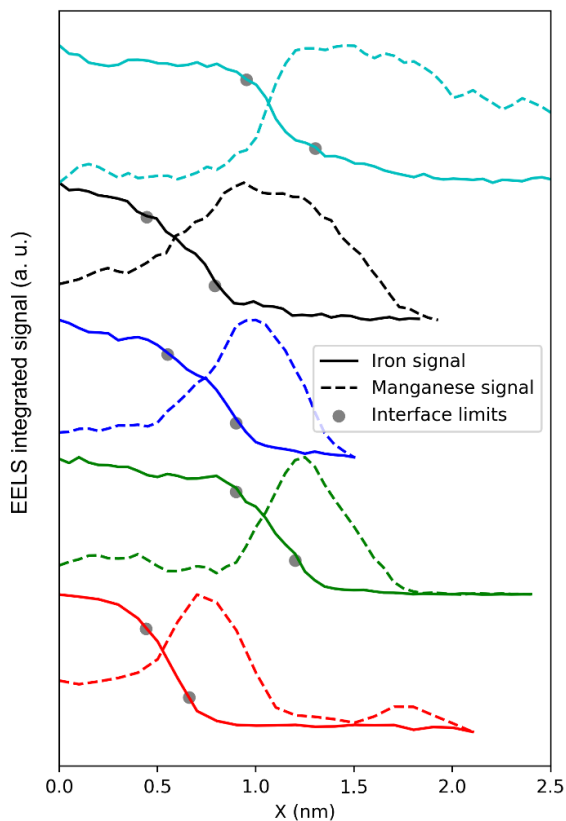


Figure 4.9. Fe $L_{2,3}$ and Mn $L_{2,3}$ edge integrated signals along core/shell interfaces of different NPs. The interface limits were taken where Fe signal drops between 75% and 25% of the mean core signal.

The FFT calculated from the shell region in red in Figure 4.13B corresponds to the $[100]$ zone axis of the Mn_3O_4 Hausmanite phase²⁸⁶ (Figure 4.13D). The 2.9 Å planes in Figure 4.13D correspond to the $(020)Mn_3O_4$ and the 2.3 Å to the $(004)Mn_3O_4$ planes (nominal spacing for these planes are $d(004)_{Mn_3O_4} = 2.348$ Å and $d(020)_{Mn_3O_4} = 2.870$ Å, respectively).

In zone axis orientation, $[001]Fe_3O_4//[001]Mn_3O_4$ are perpendicular to the plane of the interface between the core and the shell, a direction referred to as out-of-plane direction (Figure 4.13C). Accordingly, $[1-10]Fe_3O_4//[010]Mn_3O_4$ are found along the in-plane direction.

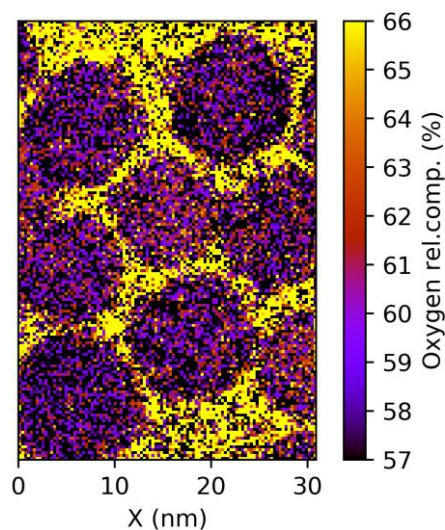


Figure 4.10. Oxygen relative composition from the SI in Figure 4.8D-H, calculated through the Egerton quantification method³⁹.

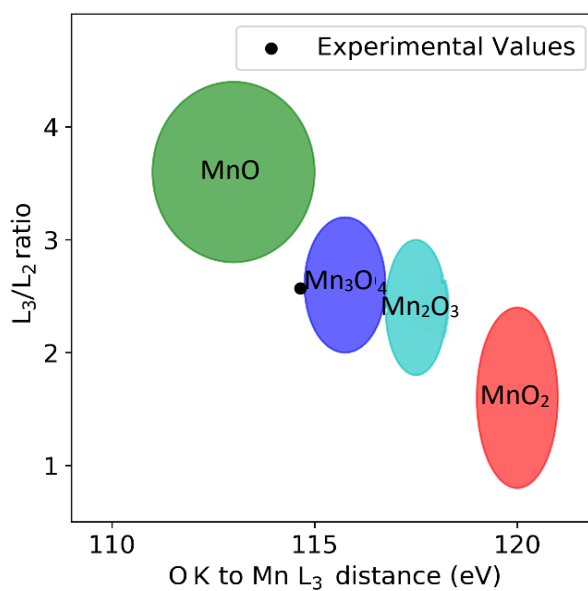


Figure 4.11. Comparison between the Mn $L_{2,3}$ -edge ELNES parameters obtained from the NPs (black dot) and the ranges of reported values for different Mn-oxides, calculated through the Oxide Wizard application¹⁵¹.

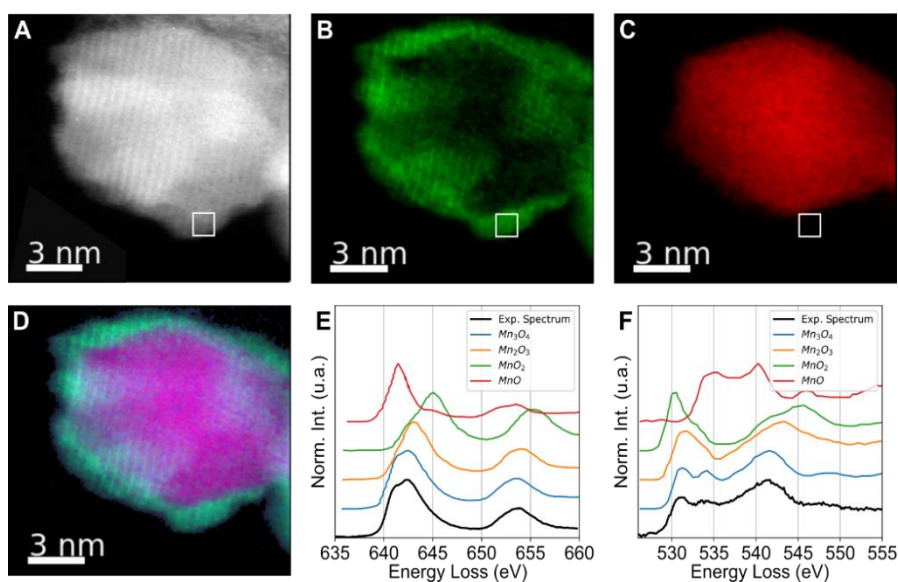


Figure 4.12. A) HAADF image. B) Mn signal. C) Fe signal. D) Colour mix of the elemental signals. E) EELS spectrum in the region of the Mn L edge compared to data from the literature¹⁸³. F) O K edge compared to data from the literature¹⁸³.

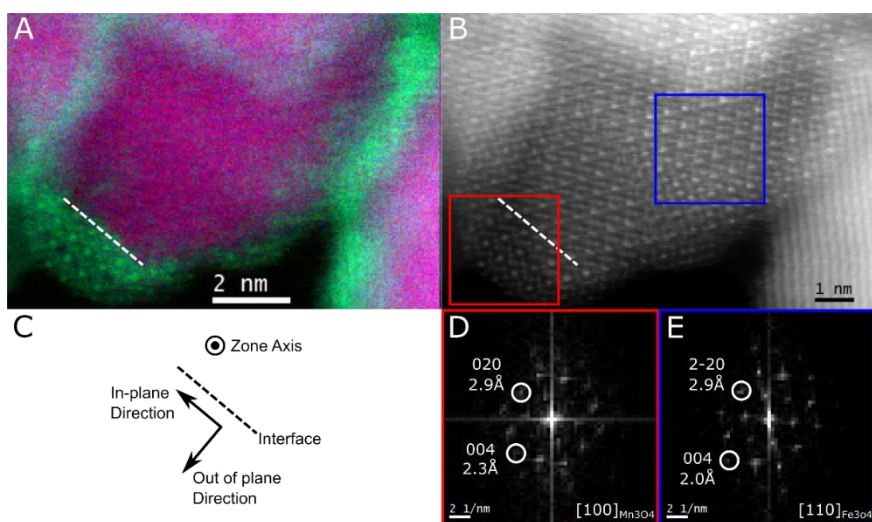


Figure 4.13. A) Manganese (green), iron (red) and oxygen (blue) signals. B) Atomic resolution STEM-HAADF image. The dotted line indicates the position of the interface. C) Scheme of the nomenclature used to describe the core/shell epitaxial relationships. D) FFT from the region highlighted with a red square in panel B. The highlighted spots correspond to (020)_{hausmanite}, 2.9 Å, and (004)_{hausmanite}, 2.3 Å, seen along the [100]_{hausmanite} zone axis. E) FFT from the region highlighted with a blue square in panel A. The highlighted spots correspond to (2-20)_{magnetite}, 2.9 Å, and (004)_{magnetite}, 2.0 Å, seen along the [110]_{magnetite} zone axis.

For the in-plane direction the lattice spacing in the shell region remains roughly the same as in the core, indicating an in-plane matching. For the out-of-plane direction, the lattice spacing is of 2.0 Å in the Fe₃O₄ core and 2.3 Å in the shell, indicating an expansion of up to 10% in the shell with respect to the core region.

The variations in lattice spacings of the crystal can be clearly visualized with Geometric Phase Analysis (GPA) (Figure 4.14). GPA is able to obtain maps of distortions in a crystal lattice with respect to a reference region. In this case, the reference region was chosen in the Fe₃O₄ core. Figure 4.14 shows GPA strain maps of the NP seen in the HAADF image of Figure 4.13B. The Exx image shows the strain along the in-plane direction (named X). The Eyy image reveals the strain along the out-of-plane direction (named Y). The strain map in the X direction is essentially flat with only a planar defect showing up in the form a bright line in the map. This demonstrates that the manganese oxide lattice grows adapted to the magnetite core. To probe that the lattice expansion along Y happens solely in the manganese shell region, a superposition of the strain map and HAADF image is provided in Figure 4.15.

The adaptation of the two lattices at the interface has an associated mismatch of $\frac{d(1-10)_{Fe_3O_4} - d(010)_{Mn_3O_4}}{d(1-10)_{Fe_3O_4}} = \frac{5.936\text{Å} - 5.740\text{Å}}{5.936\text{Å}} = 3.3\%$. This, together with the fact that hausmanite has a tetragonal space group, should induce strong stresses and frustration in the shell when growing onto a (cubic space group) magnetite core. Consequently, it is not a surprise to see planar defects in the NPs (Figure 4.16). The STEM-BF image in A shows clear twinning planes at the surface in the three highlighted positions. A GPA strain map of the crystal (Figure 4.16B) evidences the three domains in which the crystal is divided. A second type of defect can be seen in Figure 4.16C where a stacking fault is present near

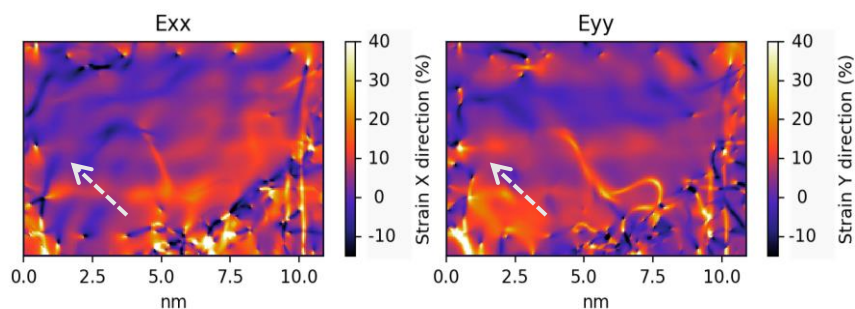


Figure 4.14. GPA strain maps from Figure 4.13B. The Exx image maps the strain in the in-plane direction $[1-10]_{Fe_3O_4} // [010]_{Mn_3O_4}$ (X in the axis). The image Eyy maps the strain along the out-of-plane direction $[001]_{Fe_3O_4} // [001]_{Mn_3O_4}$ (Y in the axis). The dotted arrows indicate the position of the core/shell interface.

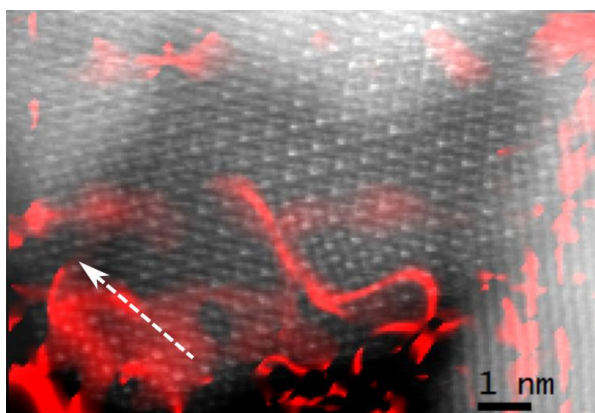


Figure 4.15 HAADF image (greyscale) superimposed to the Eyring GPA strain map (red) (strain perpendicular to the interface). The arrow indicates the core/shell interface.

the edge of the particle. The stacking fault becomes more visible in the corresponding GPA strain map (Figure 4.16D). These two types of defects, both of which originate at the surface of the NPs, are the most common among all the acquired images.

EELS $L_{2,3}$ -edge intensity maps (Figure 4.17) of the NP oriented along a high symmetry zone axis further confirm the spinel structure of both the magnetite core and the hausmannite shell. Figure 4.17A corresponds to the HAADF image of the NP in $[100]Mn_3O_4//[110]Fe_3O_4$ zone axis orientation and Figure 4.17B-D present the EELS elemental maps at atomic resolution in the shell (Figure 4.17C) and the core (Figure 4.17D), respectively. From these images it was possible to understand the core/shell interface at the atomic level, schematically shown in Figure 4.17E, F. However, to gain further insight into the intimate configuration of these NPs, the location of 2+ and 3+ species of each element in the different oxygen coordination sites must be unveiled.

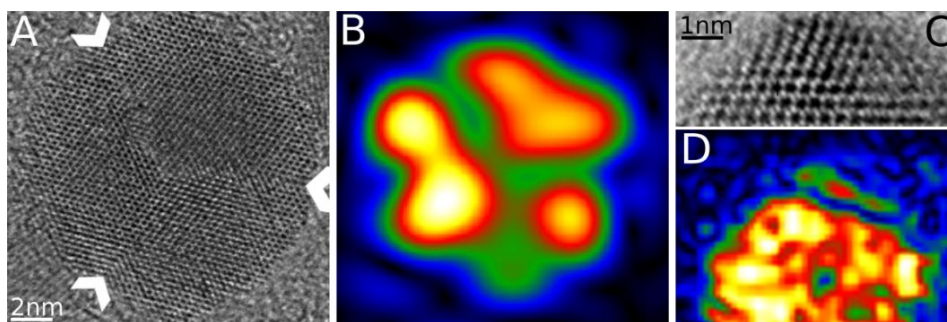


Figure 4.16. A) STEM-BF image of a NP. B) GPA phase map from panel A. C) STEM-BF image of the edge of a NP. D) GPA phase map from panel C.

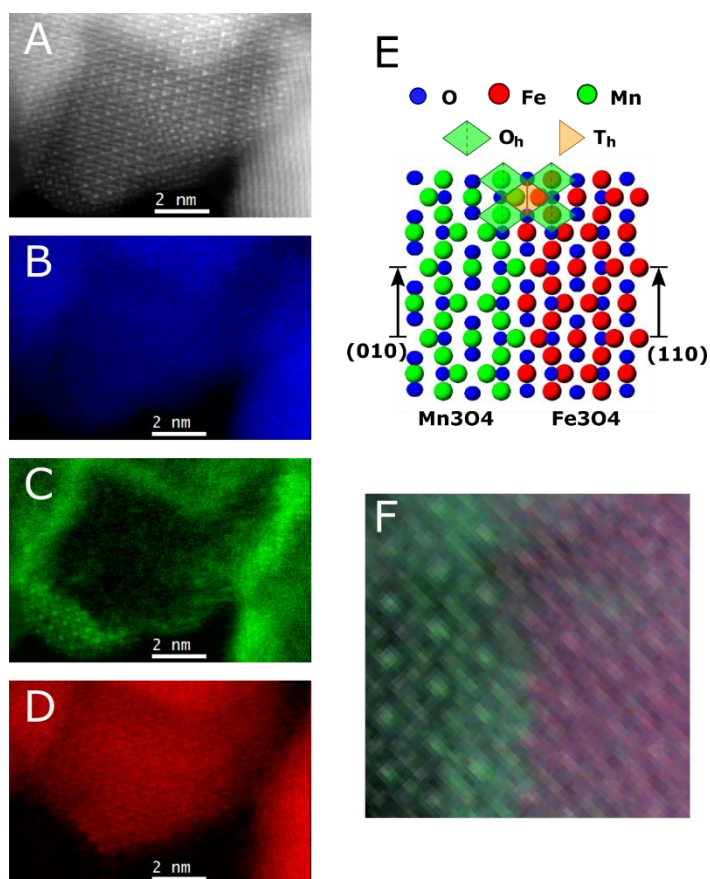


Figure 4.17. EELS spectrum imaging of the NPs at atomic resolution. A) HAADF survey image. Integrated EELS signal from the B) O K-edge, C) Fe $L_{2,3}$ -edge and D) Mn $L_{2,3}$ -edge. E) Atomistic model of the core/shell interface. F) Superposition of the O, Fe, Mn and HAADF signals at the interface.

4.2.3. Cation inversion calculation from ELNES

As described on previous chapters, ELNES analysis may allow oxidation state mapping of a given element^{132,152,183,288}. In transition metal white lines, the associated ELNES parameters are the onset of the peaks, their relative position or their relative intensity. In the particular case of manganese, the determination of the oxidation state can be achieved by using the Mn L_3 /Mn L_2 intensity ratio and the onset of the Mn L_3 peak^{151,152,289}. On the other hand, for iron, the onset of the Fe L_3 -edge has been reported to shift linearly to higher energies as its oxidation state increases from Fe $^{2+}$ to Fe $^{3+}$ ^{27,40,132,290}.

Interestingly, these ELNES features allow the calculation of the cation inversion, provided that spectra from individual atomic columns can be obtained and that careful considerations are made. When performing ELNES measurements in nanostructured materials, certain experimental issues can arise. For example, NPs are usually in arbitrary zone axes, and signals from different ions and unit cells can be superimposed. Moreover, it is not always easy to obtain “absolute” data for some ELNES parameters. In particular, the position of an EELS edge may be offset by a detector-dependent value or by electron beam instabilities.

A way to handle these problems is by considering the shift in the EELS peak position instead of its absolute position cancelling any spectrometer misalignment. Also, if a linear relationship between the oxidation state and the L_3 peak position is assumed (reasonable for many transition metals¹⁸³), the following expression for the spinel coordination inversion parameter can be derived:

$$x = \frac{2}{3} \left(1 - C \frac{S}{S_{ref}} \right) \quad (4.1)$$

Assuming (i) that an EELS spectrum is being acquired from a given atomic column, labelled by P, of a spinel oxide and (ii) that the energy value of a certain EELS edge (E_p) is given by the average between the value for 2+ ions (E^{2+}) and 3+ ions (E^{3+}) weighted by the number of atoms of each type in P. If in P there are A sites of tetrahedral oxygen coordination and B sites of octahedral oxygen coordination, and the coordination inversion parameter for that crystal is x, the expression for E_p is the following:

$$E_p = \frac{A(E^{2+}(1-x) + E^{3+}x) + B \left(E^{2+} \frac{x}{2} + E^{3+} \left(1 - \frac{x}{2} \right) \right)}{A + B}$$

Considering the position of the EELS edge for two columns (P=1 and P=2), the EELS edge position shifts between column 1 and 2 by the following amount:

$$S \equiv E_1 - E_2 = \frac{A_1(E^{2+}(1-x) + E^{3+}x) + B_1 \left(E^{2+} \frac{x}{2} + E^{3+} \left(1 - \frac{x}{2} \right) \right)}{A_1 + B_1} - \frac{A_2(E^{2+}(1-x) + E^{3+}x) + B_2 \left(E^{2+} \frac{x}{2} + E^{3+} \left(1 - \frac{x}{2} \right) \right)}{A_2 + B_2}$$

From the previous expression, it is just a matter of rearranging terms to recover (4.1), where $S_{ref} = E^{3+} - E^{2+}$ and $C = \frac{(A_1+B_1)(A_2+B_2)}{B_1A_2-A_1B_2}$.

This approach was pursued with an SI from a particle oriented along a low symmetry zone axis: [541] (the plane indexation of the image can be found in Figure 4.18). Figure 4.19A shows the atomic resolution STEM-HAADF image of the particle. An atomic resolution EELS SI was acquired from the highlighted region of panel A, which shows the expected (111) planes in this zone axis (Figure 4.19B). Notably, the (111) planes of magnetite (labelled with numbers in the image) contain iron atoms only in octahedral coordination (12 per unit cell). On the other hand, between these planes, in the regions with darker contrast in Figure 4.19B, iron atoms are distributed in both octahedral and tetrahedral coordination (8 T_h and 4 O_h positions per unit cell; Figure 4.19C). The bright planes have been labelled with a number (i), in Figure 4.19B-C while the darker planes will be referred as i' .

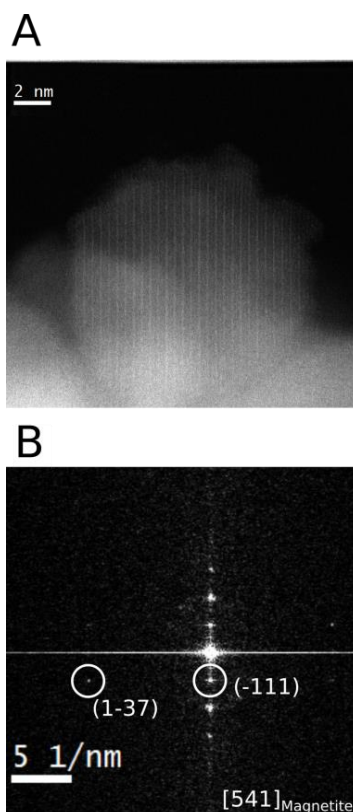


Figure 4.18. A) HAADF image and B) FFT with plane indexation of the NP in Figure 4.19.

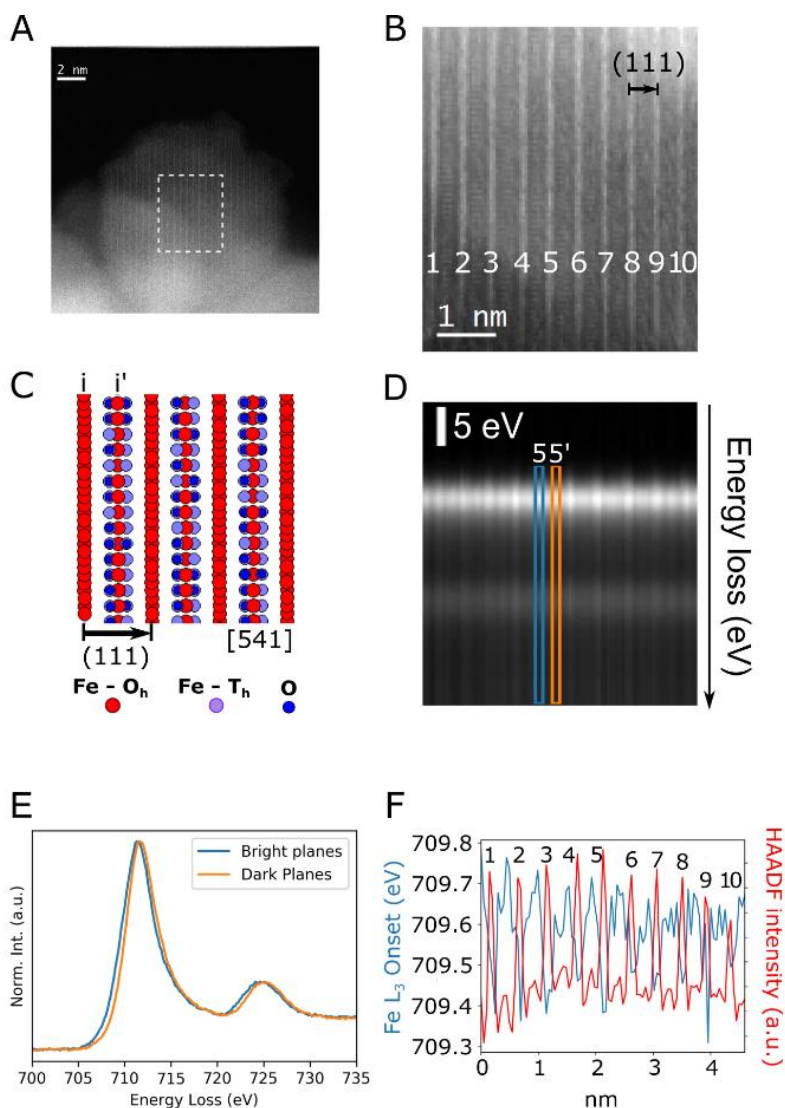


Figure 4.19. Fe_3O_4 core ELNES mapping. A) STEM-HAADF image. B) STEM-HAADF signal co-acquired with an EELS SI from the highlighted region in panel A. C) corresponding atomistic model of magnetite along the observed zone axis. D) Plot of the spectrum line obtained by vertical addition of the spectra. E) EELS spectra extracted from the positions 5 and 5'. A shift of L_3 is observed. F) Profiles of the iron L_3 onset along the $[111]$ direction and the corresponding HAADF signal.

A SI was acquired from the region displayed in Figure 4.19B. To improve the signal to noise ratio, and given the symmetry in the image, spectra were added along the vertical direction to obtain a spectrum line (displayed in Figure 4.19D), where the horizontal axis is the same as in Figure 4.19B and the vertical one

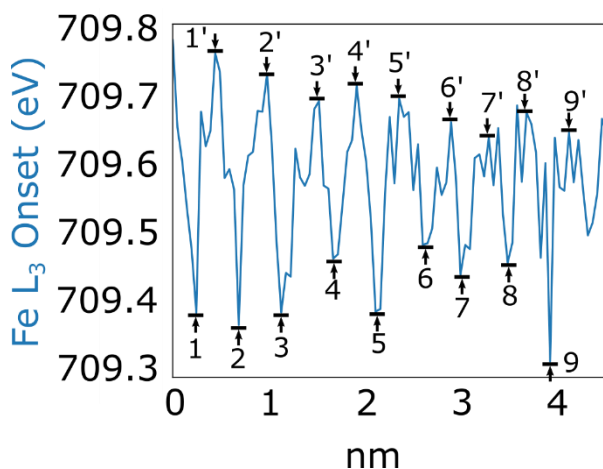


Figure 4.20. Measurements of Fe L_3 shift from Figure 4.19F. The values obtained are 0.38 eV, 0.37 eV, 0.31 eV, 0.25 eV, 0.32 eV, 0.18 eV, 0.22 eV, 0.24 eV, 0.35 eV resulting in an average value of 0.29 eV with a standard deviation of 0.07 eV.

corresponds to the energy loss. As an example, the spectra corresponding to positions 5(5') (highlighted in blue (orange) in Figure 4.19D) are plotted in Figure 4.19E. The onset of the Fe L_3 edge was calculated as the energy at which half the intensity of the peak was attained. The variation of the Fe L_3 onset along the [111] direction is plotted in Figure 4.19F (blue line). Note that the L_3 onset is lower when the HAADF signal is higher, indicating a variation between bright and darker planes (which are labelled by i/i' respectively in Figure 4.20). The shift between adjacent $i-i'$ of planes can be observed in the example of Figure 4.19E, which demonstrates an uneven distribution of iron ions with different oxidation states. This Fe L_3 shift between the two types of planes was calculated to be of 0.3 eV on average (see Figure 4.20).

From this measurement, expression (4.1) can be applied to calculate the cation inversion parameter of the magnetite core in the NP. After taking $S_{\text{ref}} = 1.7$ eV from the literature²⁹⁰ and $C = -3/2$ from the analysed planes, the inversion parameter of the iron oxide core was found to be $x = 0.84 \pm 0.02$, where the error was estimated from the standard deviation of the Fe L_3 shifts.

A similar approach was used to calculate the inversion parameter of the hausmannite shell. Figure 4.21A shows an enlarged view of the Mn_3O_4 shell of the same NP as in Figure 4.17. The comparison with the atomistic model (Figure 4.21B) demonstrates that, in this orientation, the observed atomic columns

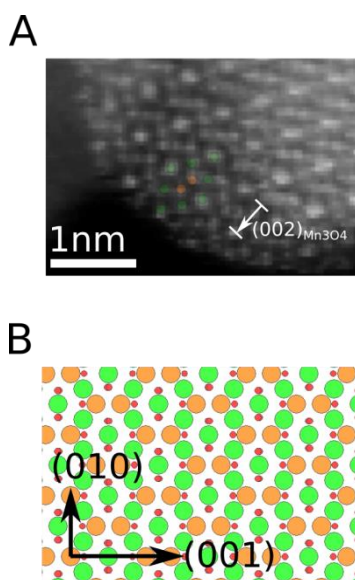


Figure 4.21. Mn_3O_4 shell lattice. A) Close up of Figure 4.2A on the manganese oxide shell, where the atomic columns containing Mn atoms in exclusively tetrahedral or exclusively octahedral coordination are marked in orange and green, respectively. The direction and extent of the $(002)\text{Mn}_3\text{O}_4$ planes have been highlighted. B) Model of the hausmannite crystal lattice seen in the $[100]\text{Mn}_3\text{O}_4$ zone axis. Mn ions in tetrahedral coordination are shown in orange and those in octahedral coordination in green.

contain exclusively either ions in tetrahedral coordination (orange) or in octahedral coordination (green). The Mn L_3 onset was mapped, as shown in Figure 4.22A, where regions with low Mn signal (the Fe_3O_4 core and vacuum) have been masked. A histogram of the Mn L_3 energy onset in pixels corresponding to columns of tetrahedral and octahedral coordination is shown in Figure 4.22B. The tetrahedral/octahedral column positions were manually chosen from the correlated HAADF image.

The centres of the distribution of the Mn L_3 energy onsets are shifted 0.65 eV between octahedral and tetrahedral Mn coordination. From this measurement, the cation inversion parameter was calculated to be $x = 0.39 \pm 0.10$, using $C = 1$ for the corresponding zone axis and atomic columns and $S_{\text{ref}} = 1.6$.²⁸⁹ The cation inversion uncertainty has been estimated from the width of the EELS energy onsets distributions of Figure 4.22B. It should be noted that the uncertainty in this measurement is much larger than for the one corresponding to magnetite.

Remarkably, X-ray absorption experiments (a well-established method to assess cation coordination inversion^{291–293}) on the NP powder samples confirm the presence of cation inversion in Mn_3O_4 , with a stoichiometry of about $(\text{Mn}^{2+})_{0.56}$

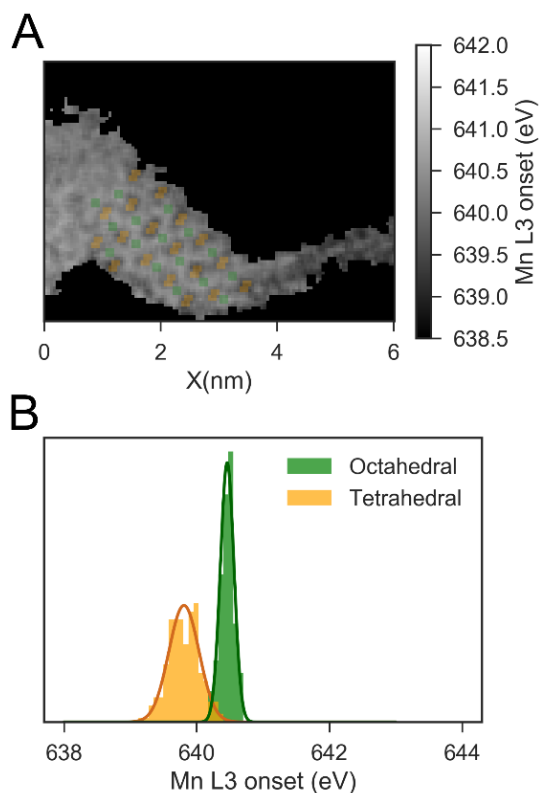


Figure 4.22. Mn L₃ onset distribution. A) Mn L₃ energy onset. Note that, in A), regions of low Mn signal have been masked. Overlaid in green and orange are the pixel selections for cation atomic columns with either tetrahedral or octahedral oxygen coordination. B) Histogram of the Mn L₃ energy onset for the selected pixels in panel A.

$\text{Mn}^{3+}_{0.44}\text{Th}[\text{Mn}^{2+}_{0.44}\text{Mn}^{3+}_{1.56}]\text{OhO}_4$, i.e., $x \sim 0.44$ (see Figure 4.23A and Table 4.1), in reasonable agreement with the atomic scale cation inversion measurement. Similarly, for Fe_3O_4 , some degree of cation inversion is also observed, with $(\text{Fe}^{2+}_{0.14}\text{Fe}^{3+}_{0.86})\text{Th}[\text{Fe}^{2+}_{0.86}\text{Fe}^{3+}_{1.14}]\text{OhO}_4$, i.e., $x \sim 0.86$ (see Figure 4.23B and Table 4.2). The small differences in cation inversion between the two techniques probably stem from the statistical average character of the x-ray absorption and to a certain extent from the somewhat non-univocal nature of the X-ray absorption fits.

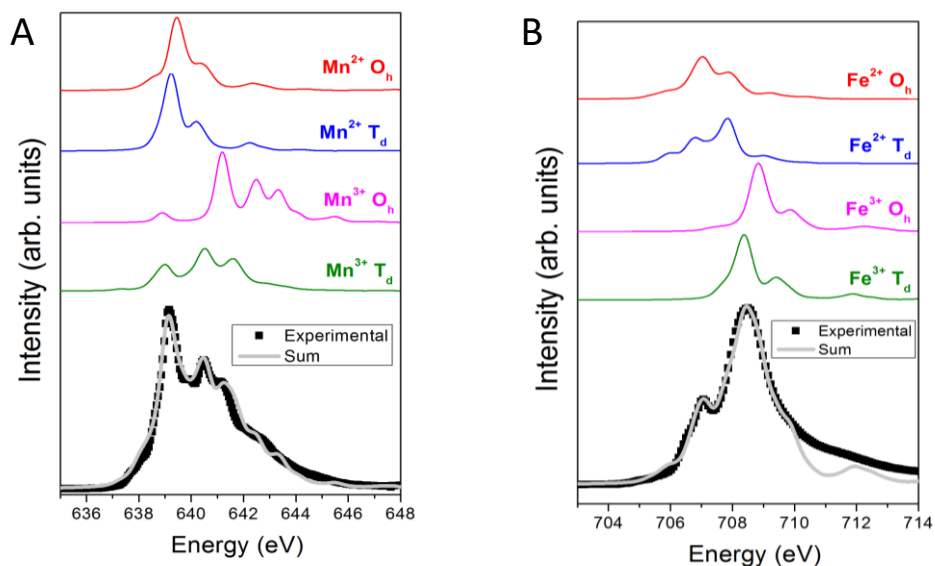


Figure 4.23. Experimental x-ray absorption spectra at the Mn (A) and the Fe (B) $L_{3,2}$ -edge (symbols) and the corresponding simulation (grey line) obtained as a combination of the theoretical spectra of the 2+ and 3+ ions in either T_h or O_h environments (red, blue, magenta and green thin lines).

4.2.4. Cation inversion calculation from MVA decomposition

An alternative way to unravel the contribution of the different cations in each crystallographic site can be considered. MVA and spectral decomposition techniques have been used in the past to obtain maps related to the density of a specific ion^{33,102,132}. If such maps are obtained at atomic resolution, for a spinel crystal the cation inversion can be estimated simply as the fraction of signal from the 3+ ion at the tetrahedral coordination positions:

$$x = \left(\frac{I_{3+}}{I_{3+} + I_{2+}} \right)_{T_h} \quad (4.2)$$

PCA was applied to the SI shown in Figure 4.17 for the energy range corresponding to the Mn $L_{3,2}$ -edge. The results revealed that 3 components were enough to describe the whole dataset as Figure 4.24, demonstrates. Then, a 3-component spectral decomposition was performed through NMF²⁹⁴,

yielding the components depicted in Figure 4.25A. The component C0 has no relevant spectral features, and is considered a background, basically related to the thickness at each point of the image. On the other hand, components C1 and C2 show Mn L-edges with very distinct features. In particular, the L_3/L_2 intensity ratio is much higher for C1 than for C2 and the L_3 peak is at lower energies for C1 than for C2. By further comparison with reference spectra^{40,152,289} it is possible to assign C1 to be proportional to the Mn^{2+} ion density and C2 to the Mn^{3+} ion density. In Figure 4.25B, the score maps of C1 (orange colour scale) and C2 (green colour scale) are combined, highlighting the Mn^{2+} and Mn^{3+} sublattices. The maps have an excellent correspondence with the different oxygen coordination sites, similarly to previously atomic resolution EELS maps obtained through multilinear least square fitting in hausmanite²⁸⁵, with the map of C1 and C2 having higher intensity in the T_h and the O_h sites, respectively (Figure 4.25B).

Mn L_3 -edge	Number of ions for $x = 0$	% of ions for $x = 0$	Simulated number of ions	Simulated % of ions
$Mn^{2+} O_h$	0	0	0.44	15
$Mn^{2+} T_h$	1	33	0.56	19
$Mn^{3+} O_h$	2	66	1.56	51
$Mn^{3+} T_h$	0	0	0.44	15

Table 4.1. Results of the simulated X-ray absorption Mn-edge spectrum compared to the ones for nominal Mn_3O_4 (i.e., $x = 0$).

Fe L_3 -edge	Number of ions for $x = 0$	% of ions for $x = 0$	Simulated number of ions	Simulated % of ions
$Fe^{2+} O_h$	1	33	0.86	28
$Fe^{2+} T_h$	0	0	0.14	6
$Fe^{3+} O_h$	1	33	1.14	38
$Fe^{3+} T_h$	1	33	0.86	28

Table 4.2. Results of the simulated X-ray absorption Fe-edge spectrum compared to the ones for nominal Fe_3O_4 . (i.e., $x = 1$)

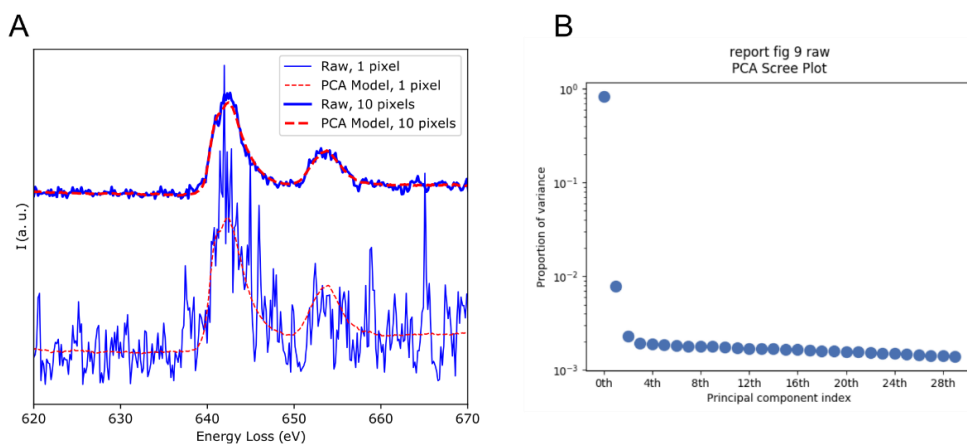


Figure 4.24. A) Comparison of raw data and PCA model for the spectra of 1 pixel and for the summed spectra of 10x10 pixels. B) Scree plot of the Mn edge PCA, where only 3 components stand out.

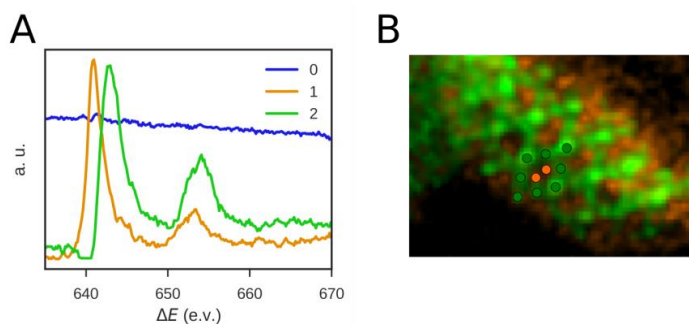


Figure 4.25. Mn L-edge spectral decomposition. A) NMF components of the Mn L-edge in SI of Figure 4.21. B) Colour composition of component 1 (orange) and component 2 (green) score maps.

Once the maps proportional to the Mn^{2+} (C1) and Mn^{3+} (C2) are obtained, they must be normalized so that (4.2) can be reliably used. In this case, each map was divided by the integrated signal of their corresponding spectrum. The resulting information is plotted in Figure 4.26. Figure 4.26A shows an image of the manganese oxidation state, calculated by the weighted average of 2+ and 3+ ions $\frac{2I_{\text{Mn}^{2+}} + 3I_{\text{Mn}^{3+}}}{I_{\text{Mn}^{2+}} + I_{\text{Mn}^{3+}}}$. The inversion parameter is displayed as a color-coded spot over each atomic column of tetrahedral coordination. The x values range between 0.20 and 0.45, with an atomic column frequency distribution (Figure 4.26B) centred at about $x = 0.35$, in quite good agreement with the results obtained from the previous approach.

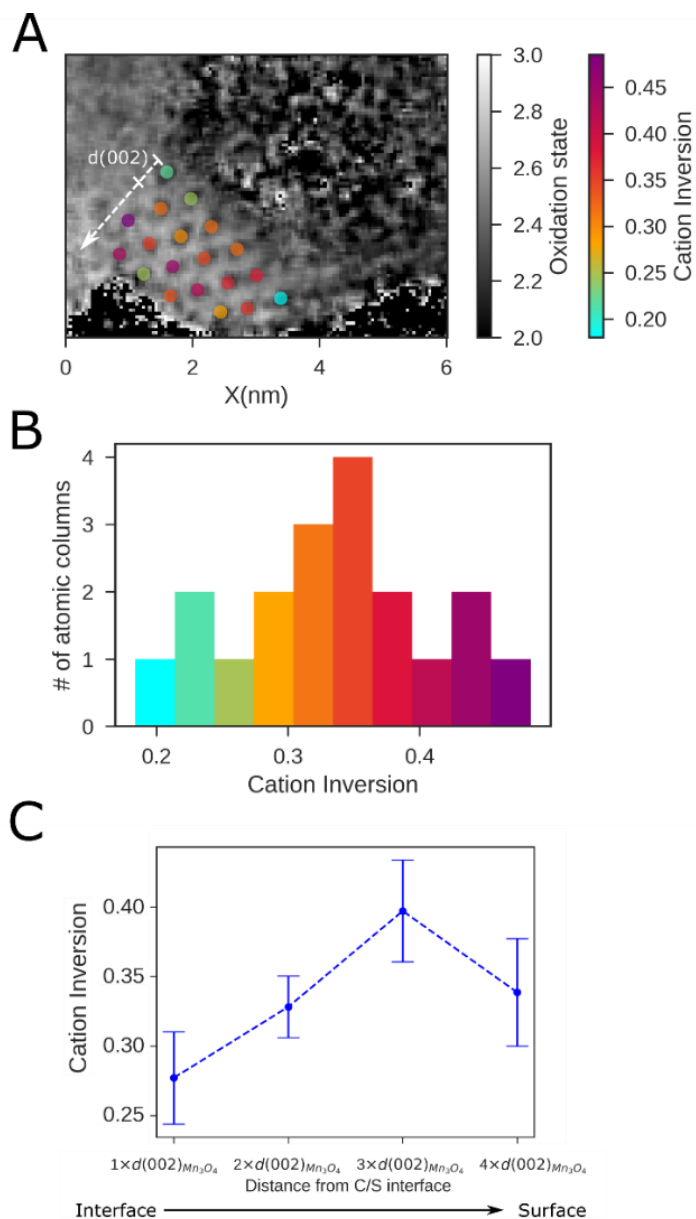


Figure 4.26. Cation inversion for tetrahedral atomic columns. A) Mn oxidation state map in grayscale. The calculated inversion parameters are displayed, colour coded, over their corresponding atomic column. B) Frequency histogram of the calculated inversion parameters from panel A. C) Inversion parameter of hausmannite vs. distance from the core/shell (C/S) interface measured in number of (002) planes [$d(002)=4.7\text{\AA}$]. The error bars were determined as the standard deviation of the values for each plane.

Interestingly, the measurements shown in Figure 4.26 allow the observation of an “inversion gradient” from the core/shell interface to the surface of the particle. The spatial variation can be better observed if the inversion parameter for the tetrahedral atomic columns is averaged for each (002)Mn₃O₄ plane (Figure 4.26C). It can be clearly observed that x is smaller closer to the interface than at the surface of the NP.

4.2.5. Discussion

In this section of the chapter two main objectives have been attained: (i) the thorough characterization of Fe₃O₄/Mn₃O₄ core/shell NPs at the atomic scale has been achieved, and (ii) two different methods to calculate the cation inversion parameter of spinel crystals with unprecedented spatial resolution have been demonstrated. These methods will be referred to as the “ELNES approach”, associated with (4.1) and demonstrated in Figure 4.19, Figure 4.20 and Figure 4.22, and the “MVA approach”, associated with (4.2) with the corresponding results shown in Figure 4.25 and Figure 4.26.

The iron oxide cores have been found to be Fe₃O₄, i.e., nominally, an inverse spinel with $x = 1$. However, the cation inversion parameter of the iron oxide core was measured to be $x = 0.84 \pm 0.02$ through the ELNES analysis approach. Although this value is smaller than that expected for Fe₃O₄, this is not overly surprising, since magnetite NPs prepared by different methods with inversion parameters lower than 1 have already been reported^{295,296}. This cation inversion can stem from different factors such as structural defects, surface effects or iron vacancies in the lattice.

The cation inversion for the hausmannite shell has been evaluated to be $x = 0.39 \pm 0.10$ following the ELNES analysis approach. However, the rather broad distribution of the Mn L₃ energy onset leads to a high uncertainty in the value of the cation inversion parameter ($\Delta x = 0.10$). Actually, the MVA approach, depicted in Figure 4.26, evidenced that this uncertainty is related to a spatial variation of the cation inversion rather than an intrinsic lack of precision of the method. This illustrates a possible drawback of the ELNES approach. Namely, the inversion is measured relative to, at least, two different atomic columns and, therefore, it is not possible to determine the x values with a higher resolution than the distance between the two columns. Moreover, the two different atomic columns used to calculate S are unavoidably chosen arbitrarily in this

approach. Additionally, the evaluation of the inversion through (4.1) requires a reference value (S_{ref}) for the energy shift of an edge related to the oxidation state of a given element. Nonetheless, reference spectra are available for most elements that can be found in a spinel lattice. Finally, the assumption of a linear dependence between onset shift and oxidation state may not always hold, although (4.1) may be adapted to higher order dependences.

Remarkably, all of these issues are avoided with the spectral decomposition (MVA) approach. As shown in Figure 4.26, cation inversion measurements with true atomic resolution can be achieved through (4.2) with the only limitation being the ability to obtain a sufficiently good spectral decomposition. The average x value obtained by this approach is consistent with the one from the ELNES approach. However, it is worth emphasizing that the MVA approach has allowed the unprecedented observation of an atomic resolution spatial variation in the cation inversion in the hausmannite shell (Figure 4.26C).

Although the origin of this spatial variation is not clear at present, it may lie in the fact that the hausmannite is actually stressed, as it grows epitaxially onto the magnetite as shown in Figure 4.13-4.15. In fact, cation inversion can act as an accommodation mechanism. As for the inversion drop at the surface of the NP, surface reordering of the free bonds does surely affect the electronic environment of the lattice and may also play a role in how the Mn^{2+}/Mn^{3+} populations are distributed. Similarly, the vacancy distribution (which could affect x) in the Mn_3O_4 may be different at the interface than at the surface.

In conclusion, precise determination of the oxidation state of iron and manganese in an Fe_3O_4/Mn_3O_4 core/shell NP has been performed. The analysis of the oxidation states, using either ELNES or MVA approaches, has been proven to enable determination of the cation inversion at atomic column resolution from spinel oxides. The obtained mean cation inversion value for the magnetite core is $x = 0.84$, whilst for hausmannite it is $x = 0.39$ (confirmed by x-ray absorption measurements in the whole sample). The analysis also reveals that while the cation inversion in the Fe_3O_4 core is spatially uniform, in the Mn_3O_4 shell it exhibits a decrease in inversion close to the core/shell interface. These novel approaches set the stage for further exploration of oxide nanosystems through EELS at a very high resolution, which should lead to an improved control of the physicochemical properties of these materials.

4.3. Conclusions

The works presented in this chapter are a practical demonstration of the value of ELNES information. In the first section of the chapter, the oxidation state determination of manganese was used to unveil the microscopic mechanism behind a complex NP synthesis. MnO was present in the core-shell MnO-Fe₃O₄ NPs. The Mn₃O₄ present in the hollow NPs pointed towards the presence of Mn²⁺ as the responsible of a frustrated galvanic exchange reaction, which was then proven by preparing seeds in different oxidation conditions.

In the second section, it is shown how ELNES data can be used, not only for oxidation state determination, but also to calculate other interesting properties of materials; in the presented case, cation inversion. The results reported in section 4.2 are the first ones to show the measurement of this property through EELS at atomic spatial resolution. Interestingly, EELS findings are in good agreement with XAS measurements (that have much lower spatial resolution). Thus, cation inversion can be added to the long list of properties that are accessible through EELS such as excitation life times, dielectric constant, or magnetic spin amongst others^{39,297}.

CHAPTER 5: EELS tomography of core/shell nanoparticles

In section 1.4.4 of the introduction, the state of the art of EELS tomography has been presented. It is a technique that is gaining a lot of interest in the recent years in the field of EELS since it enables the study of materials with complex morphologies. In this section the virtues of EELS tomography will be put to test in two nanoparticle systems: cobaltite/ferrite nanoparticles and FeO/Fe₃O₄ core/shell nanoparticles.

5.1. Introduction

In general tomography consists in acquiring information with a high number of spatial dimensions from a set of several measurements of lower dimensionality. A prominent example is X-Ray tomography used in medical diagnosis, where series of 1D projections are used to reconstruct a “slice” of the patient, and several slices put together to have a full 3D reconstruction of a part of the patient body.

The tomography processing is based on the Radon transform. The transformation reconstructs an object from several of its projections⁹⁴. The first approach to solve this problem was based on the fact that the Fourier transform (FT) of a projection is a slice of the FT of the whole object. Therefore, by acquiring several projections, interpolating them and performing an inverse FT (IFT) it is possible to achieve a tomographic reconstruction. In 1968, these fundamentals were used to obtain a 3D model of a macromolecule from TEM BF images^{3,298}, starting the field of so-called electron tomography (ET).

The acquisition of a set of TEM images at different angles suitable for tomography, a tilt-series, as described in the first chapter, presents several challenges. The most important one is the fact that space inside the TEM column is limited and often acquiring images at more than 70° is not possible since the sample holder would impact with the objective lens polar piece. Therefore, information between 70° and 90° might not be accessible. This leads to a lack of points in Fourier space, the missing wedge, which asymmetrically limits the resolution of the reconstructions in many algorithms.

The second factor limiting ET resolution is the number of images acquired in the tilt-series. Often, to reduce the electron dose during the acquisition to prevent radiation damage, the images must be acquired every 4° , or even larger intervals, far more spaced than the ideal. In Fourier-based algorithms and more widespread iterative reconstruction algorithms²⁹⁹, this leads to artefacts and lower quality reconstructions.

There exists a final requisite to apply most common reconstruction algorithms, and that is that the images must fulfil the projection requirement. The projection requirement states that the intensity at each pixel for each image in the tilt series must be proportional to the projected thickness (or any other extensive property of the sample, such as the amount of a given chemical species) at that point. This can be a problem in many instances, for example if beam damage occurs during the acquisition or if the sample is too thick, where dynamical scattering and electron absorption break down this proportionality relation.

These challenges are being tackled in the state of the art of the field through innovative algorithms, such as discrete algebraic reconstruction technique (DART)³⁰⁰ or compressed sensing (CS) tomography³⁰¹. The main way these algorithms attempt to minimize artefacts is by incorporating some kind of “previous knowledge” of the sample. In the case of DART, it is assumed that the sample can be described with a small, discrete number of grey levels. For CS it is assumed that the sample can be sparsely described in a given representation. This is quite an abstract requirement, but in practice the total-variation (gradient) representation of the sample is taken^{302,303} and so, the assumption translates to having a sample with sharp “edges” as opposed to a tomogram with slowly varying grey levels .

However, all the discussed algorithms are devoted to the reconstruction of 3D volumes from 2D TEM/STEM images, being STEM-HAADF contrast the most used signal to obtain the projection. That is because its contrast is directly proportional to the density/thickness projection of the sample, automatically fulfilling the projection requirement.

On the other hand, an EELS tilt series yields 3D projections $(x, y, \Delta E)$ of a 4D object, the SV $(x, y, z, \Delta E)$. Therefore, some additional processing must be done if the same algorithms from ET are to be used. The most common processing strategies to obtain a chemically sensitive tomography from an EELS tilt series are listed below.

- Integrated edge signal reconstruction:

One approach is to integrate the intensity of the spectral signal within an energy window typically containing a characteristic spectral feature (e.g. ionization edge) to form an energy-filtered image. Then, tomography reconstruction algorithms are applied to the corresponding tilt series. The procedure can be repeated for each spectral feature of interest³², and the results combined for a whole 3D visualization. This relatively straightforward method can readily provide volumes with compositional information, although the electronic information lying within the ELNES is lost.

This was the first method ever used to obtain 3D information from EELS data. In 2009, Jarausch et al. developed this idea to study a silicon-tungsten contact, by preparing a nanopillar from the semiconductor device with FIB and acquiring a EELS-SI tomographical series³². They were able to map the distribution of titanium, nitrogen and cobalt in the device, using the fairly conventional SIRT algorithm. The results allowed the direct observation of a fabrication failure of the device.

Other notable examples of this method are the 3D reconstruction of an ytterbium doped silicon-aluminium alloy, that allowed locating the distribution of precipitates in the material³⁰⁴, or the 3D mapping of iron and cobalt in $\text{Fe}_x\text{Co}_{(3-x)}\text{O}_4$ impregnated Co_3O_4 mesoporous NPs⁹⁶. As these examples show, this type of EELS tomography can readily provide useful results.

- Channel by channel reconstruction.

A single channel of an EELS-SI is equivalent to an EFTEM image, and so it fulfils the projection requirement. To build the SV, a tomogram can be reconstructed for each energy channel in the EEL spectrum. Then if all the reconstructions are considered together, each voxel will contain an intensity value for each energy loss and thus, the SV will be recovered.

This method was used for the first 3D reconstruction that revealed information on the oxidation state of a chemical element in a NP, as it showed the preferential oxidation of ceria in certain facets of a cerium oxide NP⁹⁸.

- Decomposition map reconstruction^{33,34,132,142}.

A different strategy can be used to process the spectral data of the tilt series before the tomographic reconstruction, based on the use of machine learning algorithms. PCA³⁰⁵ combined with ICA³⁰⁶ can be applied to decompose the EELS spectra into a linear combination of few independent components that can often be related to chemical phases in the sample^{102,137}. When applying these methods to the tilt series, the obtained maps of coefficients for each component and angle can be further reconstructed in 3D, effectively retrieving the SV, retaining the original energy resolution of the spectra.

With this strategy several notable results have been reported. The pioneering results of L. Yedra, that implemented this method for the first time, resulted in the mapping of all the components in cobalt/iron oxide mesoporous NPs³⁴. A little later the method was used to investigate ferromagnetic/ferroelectric cobalt ferrite/bismuth ferrite composite³³, and also in the low-loss region, using NMF, to map the surface plasmons of a silver nanocube¹⁴².

Other methods that integrate the full EELS SI into the algorithms exist, such as the use of reference spectra within iterative reconstructions algorithms rather than prior model-based fitting¹⁰⁰, or using the EELS projections as an input to solve the dielectric response of the studied nanostructure to obtain the LDOS^{118,119}, but these are not very widespread at present.

EELS tomography, in all its variants, has many advantages compared to other analytical tomography techniques, such as EDX or EFTEM tomography. These stem from the differences between EDX and EFTEM detailed in the first chapter, namely, the fact that EELS has a much higher collection yield compared to EDX, and that it has access to the ELNES information that EDX lacks and EFTEM cannot resolve in detail.

In this chapter, characterization of functional nanoparticles through EELS tomography will be presented, making an emphasis in both the methods used and the information gathered from the technique. In the first part the integrated edge intensity method will be used, demonstrating how the EELS chemical information can enhance the knowledge that standard HAADF electron-tomography provides. On the second part, the MVA reconstruction approach is used, obtaining ELNES, oxidation state related information in 3D, an

improvement respect to the exclusively element-sensitive method of the previous section. These works present and advance in a very new field, as evidenced by from the small number of references available.

5.2. EELS tomography of $\text{CoO}_x@FeO_x$ and $\text{CoO}_x@MnFe_yO_x$ core-shell nanoparticles

5.2.1. Integrated EELS signal tomography fundamentals

The most straightforward way to gather projections suitable for tomographic reconstruction from an EELS tilt series is to subtract the background before an edge and integrate its intensity. Provided that multiple scattering and other absorption effects are weak, the map obtained will be proportional to the projected density of that element in the sample, via the scattering cross section. Mathematically, the projection P of a function f along a given direction \vec{n} is given by equation (5.1).

$$P_{\vec{n}}(f, x', y') = \int_{L_{\vec{n}}(x', y')} f(x, y, z) dl \quad (5.1)$$

If we consider the density distribution of a certain chemical element in a particle, $N(x, y, z)$, and neglect plural scattering, its projection is proportional to the edge intensity of the edge related to that element:

$$P_{\vec{n}}(N, x', y') = \int_{E_{N_i}}^{E_{N_i} + \Delta} \frac{I_{N_i}^{\vec{n}}(x', y', E)}{\sigma(E)} dE \quad (5.2)$$

$I_{N_i}^{\vec{n}}(x', y', E)$ is the EELS signal of the edge, acquired along the projection direction, and σ is the scattering cross-section of the edge. E_{N_i} and Δ refer to the edge onset and the chosen energy integration window for the edge.

Therefore, while (5.2) holds, an EELS-SI tilt series can yield a projection tilt series for every edge on the acquired spectra. Tomographic reconstruction can then

be undertaken for every edge to unveil the 3D distribution of every element in the sample.

The described methodology was applied to investigate iron/manganese/cobalt oxide NPs, with potential applications as magnetic imaging contrast agents due to their promising magnetic properties.

5.2.2. Synthesis

In an initial step, cobalt oxide NPs were synthesized by the following method: Cobalt(II) acetate tetrahydrate (1 mmol), TOP (0.2 mmol), oleic acid (8 mmol), oleylamine (14.3 mmol) were added into a three-necked round-bottomed flask containing 25 ml of trioctylamine (TOA). The temperature was increased up to 140 °C (6 °C/min ramp rate) and then kept at this temperature while magnetically stirring for 45 min. After that, the solution was again heated to reflux, up to 300 °C (3 °C/min ramp rate). Upon reaching the reflux, the solution was kept this way 5h and subsequently centrifuged and washed.

Following, CoO@MnFe₂O₄ (CoO@MFO) and CoO@CoFe₂O₄ (CoO@CFO) NPs were obtained by means of a hot-injection thermodecomposition of iron and manganese, or iron and cobalt acetate precursors, with the previously synthesized cobalt oxide NPs used as seeds. Thus, 0.267 mmol of the pre-synthesized CoO NPs, 1.6 mmol of oleic acid and 25 ml of TOA were placed in a three-necked round-bottomed flask and heated up to 210 °C while stirring. Once this temperature was reached, a 500 µl solution including 19.16 µmol of iron acetate and 9.58 µmol of manganese or cobalt acetate, was injected drop-by-drop, trying to avoid an important decrease in temperature. After that, the solution was heated up to reflux (~300 °C (3 °C/min ramp rate) and kept at this temperature for 3 hours. Upon heating, the solution changed colour, from brown to black. Once cooled to room temperature, ethanol (~25 ml) was added into both solutions to precipitate NPs, helped by centrifugation. The NPs were thus separated from the supernatant containing the solvent, ligands, by-products, etc. This procedure was repeated at least three times.

5.2.3. Structural characterization

CoO@CFO nanoparticles

The first sample consists in NPs of lateral sizes between 30-60 nm (Figure 5.1). The NPs seem to have many holes and irregularities. Although the particles are crystalline and in some cases the planes observed are compatible with the Fe/Co spinel structure (Figure 5.2), there are evidences of Moiré patterns in some particles, indicating polycrystallinity (Figure 5.3).

The HAADF images (Figure 5.4) reveal defects, regions of lower density or even holes in the particles. However, some of the particles also appear faceted, such as the highlighted one in Figure 5.4A. EELS SI were acquired from the highlighted regions in Figure 5.4. Maps of the Co L₃₂ (780 eV), Fe L₃₂ (710 eV), and O K (530 eV) edge signal were obtained. These results are shown in Figure 5.5 and Figure 5.6.

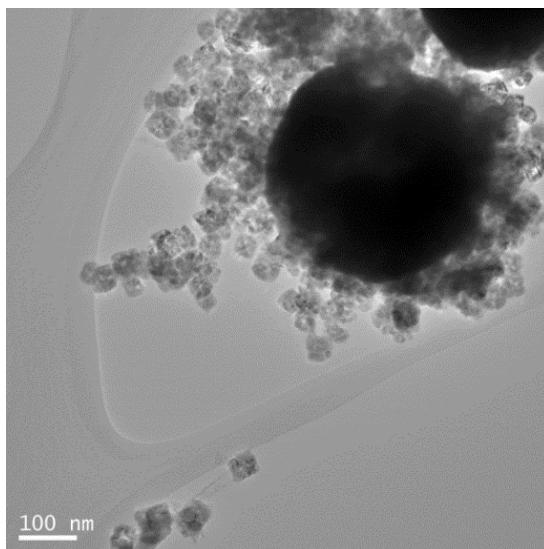


Figure 5.1. TEM image of the sample.

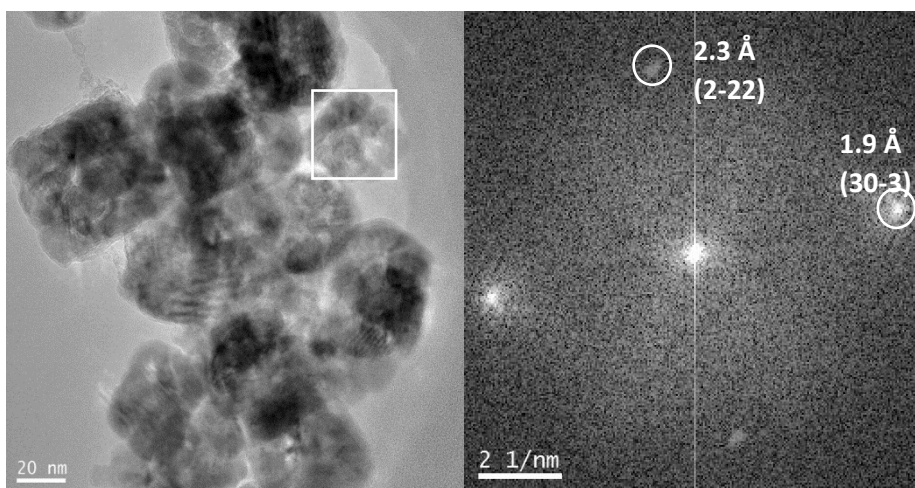


Figure 5.2. TEM image and FFT of the highlighted region.

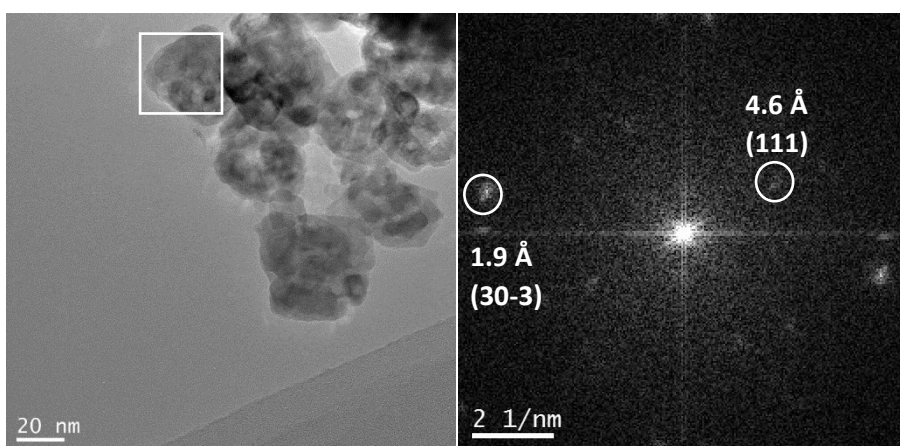


Figure 5.3. HRTEM image and FFT of the highlighted region.

EELS analysis reveals that the grains in the particles are mainly Co_3O_4 surrounded by a 3-4 nm thick iron rich layer. The composition of this layer according to EELS is on average 25%Co, 15%Fe, 60%O. In the holes and other defect regions of the particles, the iron content also increases, as can be seen in the central panels of each image corresponding to iron.

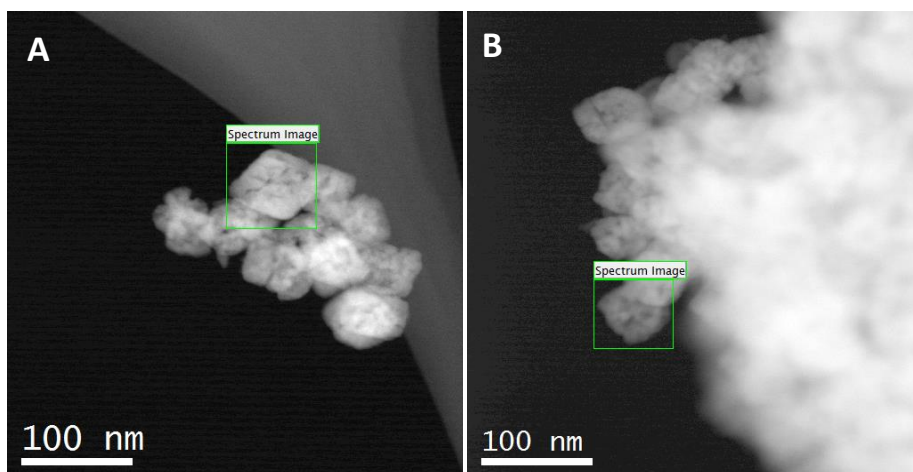


Figure 5.4. HAADF image from regions where EELS SIs were acquired.

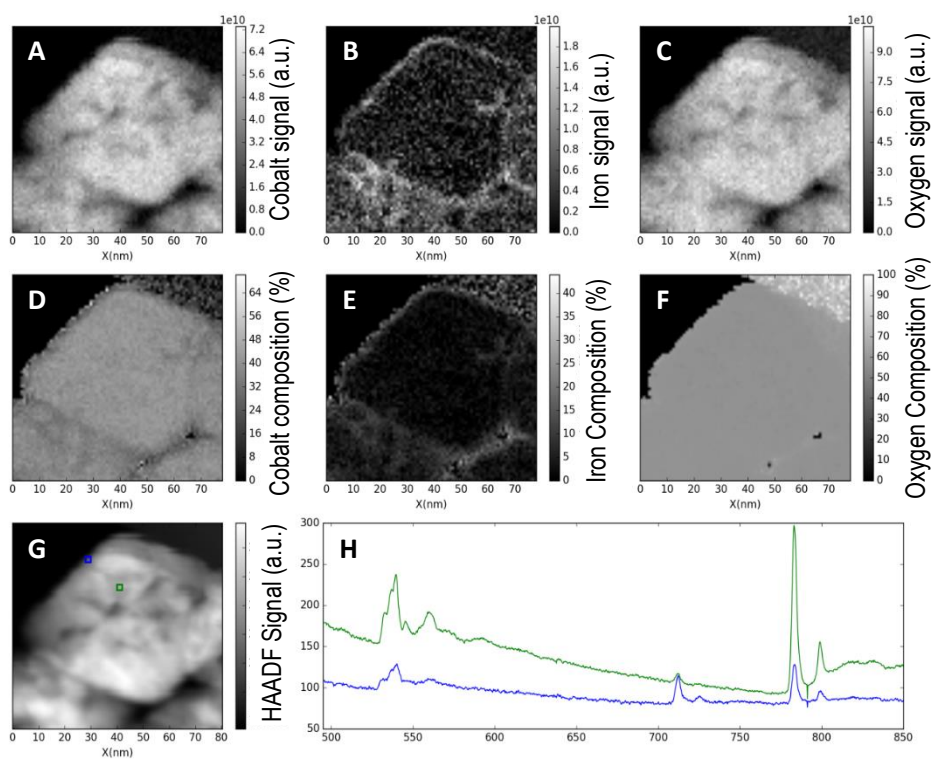


Figure 5.5. EELS analysis from the acquired SI of Figure 5.4 left panel. A) Cobalt signal, B) iron signal, C) oxygen signal, D) cobalt relative composition, E) iron relative composition, F) oxygen relative composition, G) HAADF coacquired image and H) spectra from the highlighted points in the HAADF image.

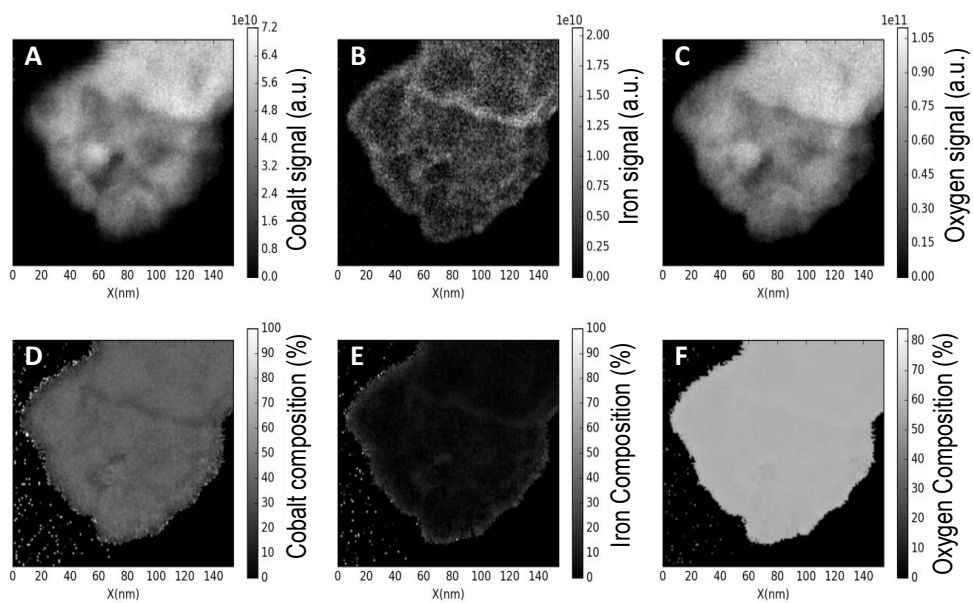


Figure 5.6. EELS analysis from the acquired SI of Figure 5.4 right panel. A) Cobalt signal, B) iron signal, C) oxygen signal, D) cobalt relative composition, E) iron relative composition, F) oxygen relative composition.

CoO@MFO nanoparticles

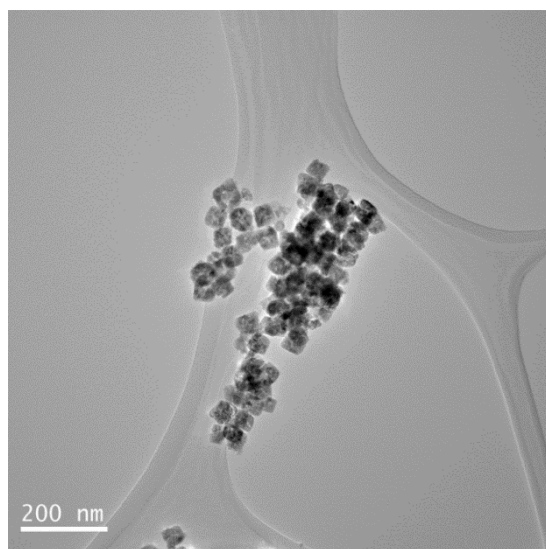


Figure 5.7. TEM image of the sample.

The second sample consisted in slightly bigger NPs, with lateral sizes between 40-80 nm (Figure 5.7). The NPs seem to have the same type of holes and defects as in the previous sample and also appear to be faceted, as can be appreciated in the HAADF images (Figure 5.8, Figure 5.9). Atomic resolution HAADF images allowed the identification of the crystalline structure as Co_3O_4 (Figure 5.8).

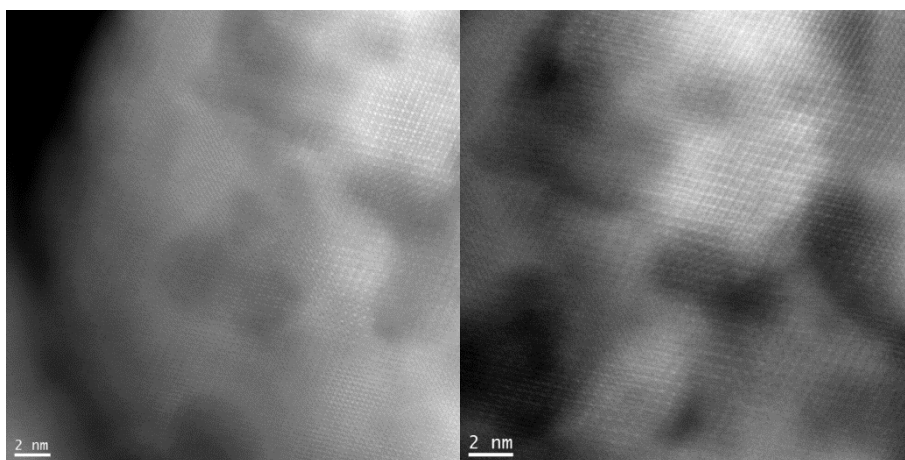


Figure 5.8. Atomic resolution HAADF images of the sample. The images could be identified as Co_3O_4 seen along the [110] Zone axis.

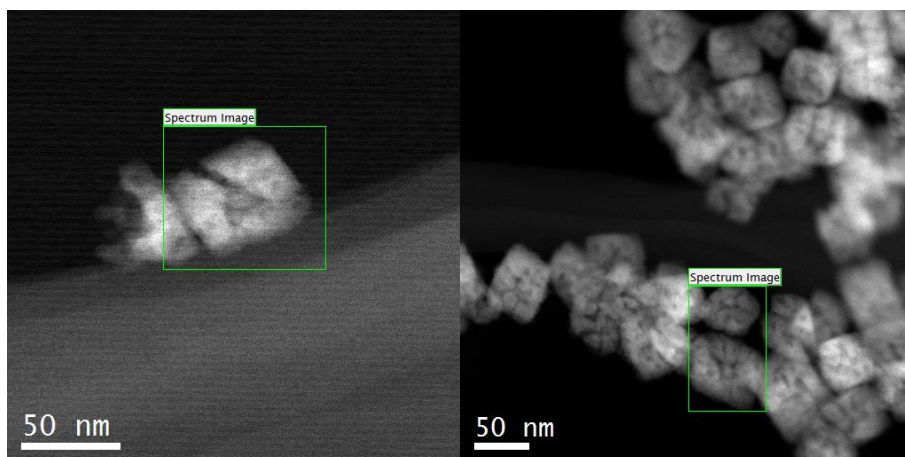


Figure 5.9. HAADF image from regions where EELS SIs were acquired.

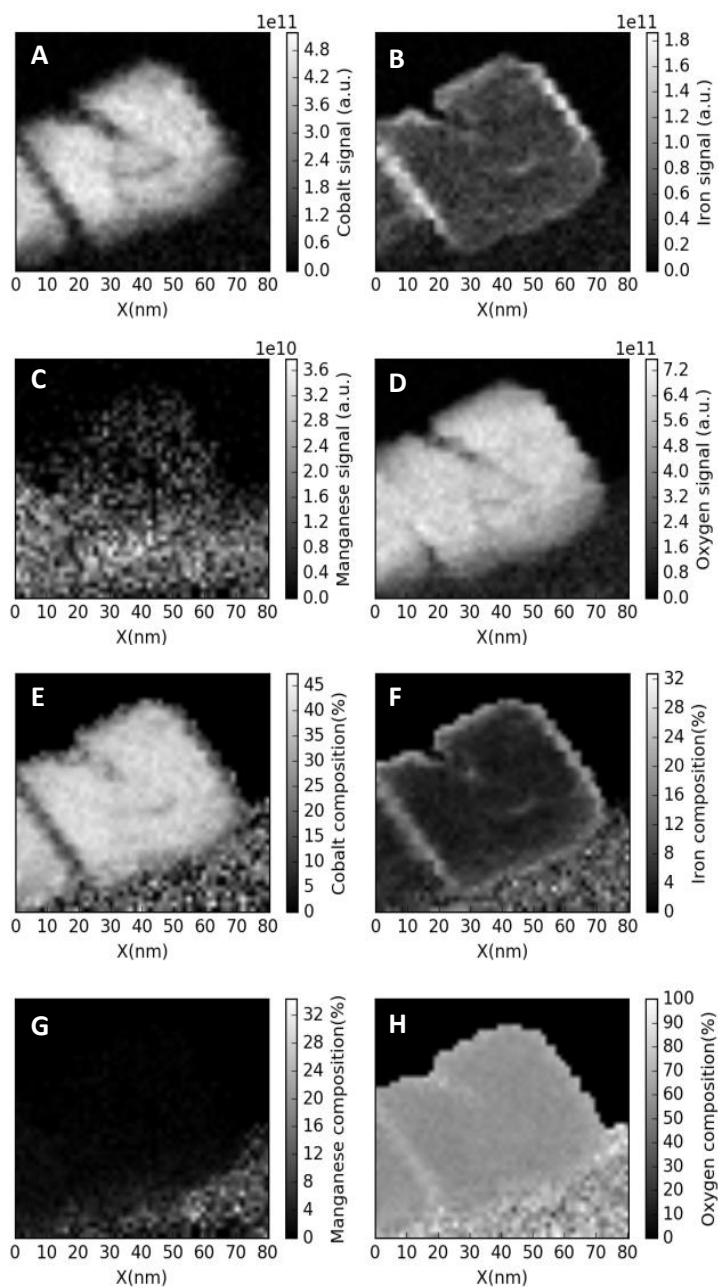


Figure 5.10. EELS analysis from Figure 5.9 left panel. A) Cobalt signal, B) iron signal, C) manganese signal, D) oxygen signal, E) cobalt relative composition, F) iron relative composition, G) manganese relative composition and H) oxygen relative composition. The slight rippling in the outer surface is an artefact from the spatial drift correction used during the acquisition.

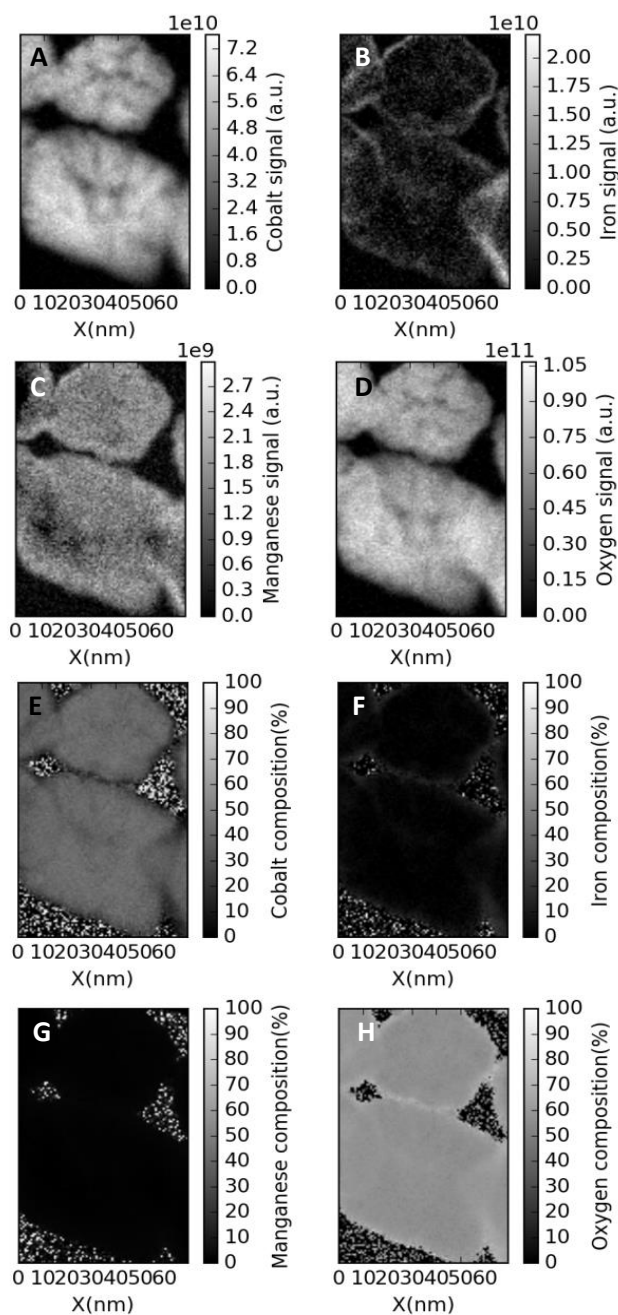


Figure 5.11. EELS analysis from Figure 5.9 right panel. A) Cobalt signal, B) iron signal, C) manganese signal, D) oxygen signal, E) cobalt relative composition, F) iron relative composition, G) manganese relative composition and H) oxygen relative composition.

EELS maps were obtained from the highlighted regions in Figure 5.9. The edge signal maps in Figure 5.10 and Figure 5.11 demonstrate that the composition is similar to that of the previous sample: a Co_3O_4 core with a 10%Fe/35%Co shell. As for the manganese, it could only be detected after the use of statistical analysis (PCA) to clean noise off the spectra. Afterwards, EELS signal maps for Co, O, Mn and Fe were obtained, and are shown in Figure 5.11. The results reveal that the Mn relative composition is below 5% and barely detectable. Note that, although the manganese signal image in Figure 5.11C looks clear, the intensity is an order of magnitude lower than for iron or cobalt.

5.2.4. Integrated edge EELS tomography

For each of the two samples a series of 128 by 128 pixels core-loss EELS SIs was acquired in a Jeol ARM 200 at 200 kV. The tilt series spanned from -60° to $+60^\circ$ in 4° intervals. The data was then processed with HyperSpy¹⁵³ to align the spectra by taking the oxygen K edge as a reference, and to remove the background and integrate the signal of the O K, Mn L_{32} (if present), Fe L_{32} and Co L_{32} edges for each image. The maps obtained for the CoO@CFO sample at -30° , 0° and $+30^\circ$ for oxygen, iron and cobalt are shown Figure 5.12, while equivalent maps for the CoO@MFO NPs are shown in Figure 5.13. In the case of CoO@MFO it was not possible to acquire suitable Fe or Mn maps because of the low signal. The noise that ultimately made the Fe reconstruction impossible can clearly be appreciated in the top row of Figure 5.13.

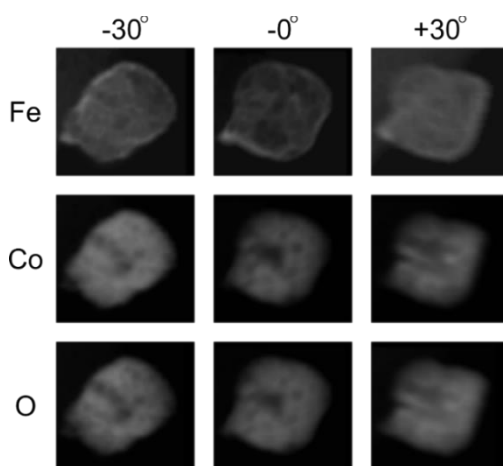


Figure 5.12. EELS maps from the tilt series at -30° , 0° and $+30^\circ$ for iron, cobalt and oxygen for CoO@CFO.

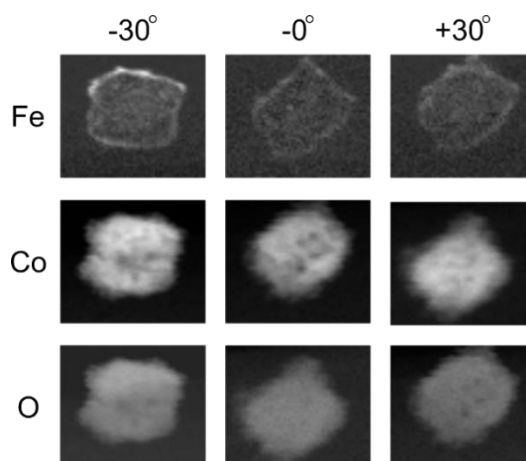


Figure 5.13. EELS maps from the tilt series at -30° , 0° and $+30^\circ$ for iron, cobalt and oxygen for CoO@MFO.

Afterwards, the cobalt and iron maps, as well as the coacquired HAADF images, were aligned for every angle and SIRT reconstruction was performed using the FEI Inspect 3D software.

The reconstructions for a CoO@CFO NP are shown in Figure 5.14. The HAADF reconstruction (Figure 5.14A-C) shows that the particle is an octahedron, with eight triangular faces. To highlight this, blue lines have been superimposed along the edges of the particle in Figure 5.14B-C. This reconstruction also shows the presence of a hole in one of its faces.

The reconstruction of the cobalt signal shows essentially the same features as the 3D HAADF model, albeit the model is a few nm narrower. This may be appreciated when comparing panels C and F of Figure 5.14, which show the particle along the same direction and with the same magnification. The particle on panel F appears slightly smaller. This is because the iron layer is missing in the 3D Co model. Figure 5.14G-I show the reconstruction of the iron signal. From them, the thickness of the shell can be clearly appreciated. This thickness is found to vary from 2 to 4 nm amongst the faces. Moreover, this highlights the fact that iron is not only on the surface of the particle but also in the inside, filling a complex web of channels that propagate from the hole on one of the faces of the particle. This can be observed in Figure 5.14I-K where the reconstructions of iron (Figure 5.14I) and iron and cobalt are shown simultaneously, cut in half. Last, a much higher density of iron was observed on a protuberance in one of the corners of the octahedron. This can be clearly

appreciated in a slice of the Fe reconstruction shown in Figure 5.14L. This may indicate the presence of a metallic Fe precipitate at that point.

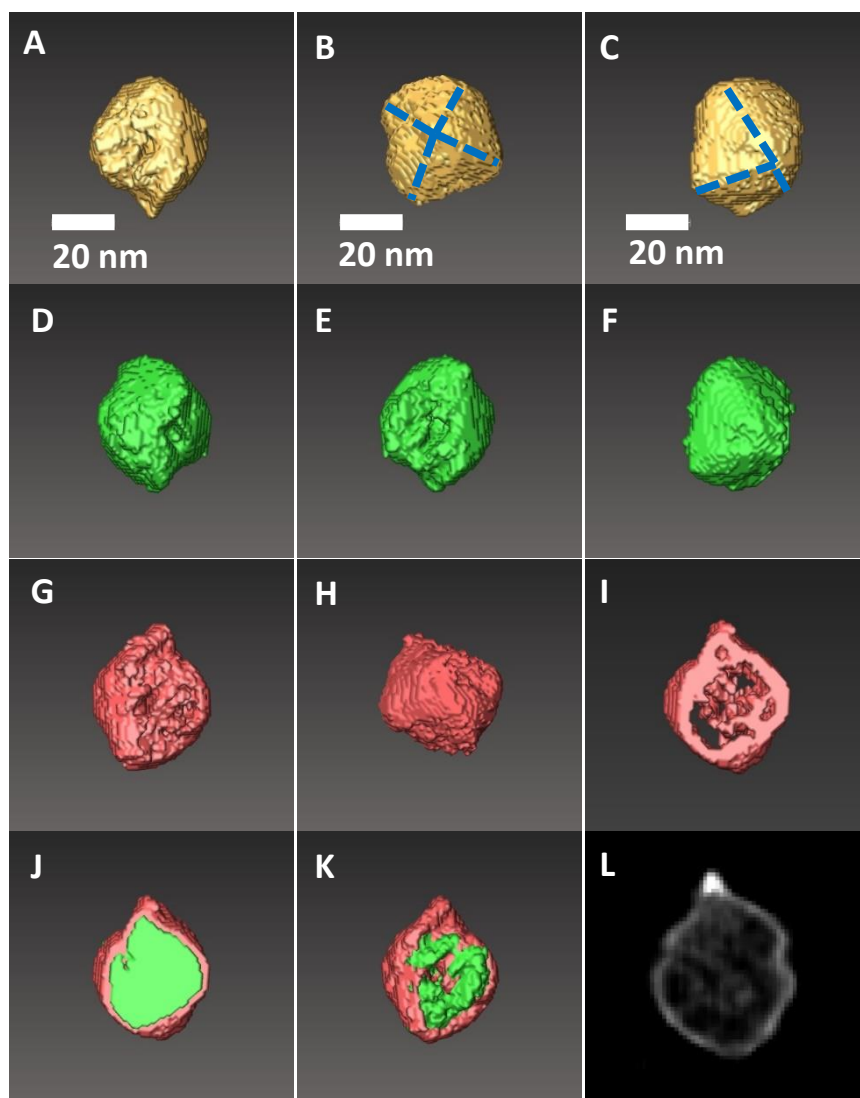


Figure 5.14. Tomography results. A-C) the HAADF image reconstruction. D-F) EELS cobalt signal reconstruction. G-I) EELS iron signal reconstruction. J-K) Iron and cobalt reconstruction. L) Iron intensity on the central slice of the reconstruction. In panels I and J the reconstruction has been cut in half to appreciate the inner details of the reconstruction.

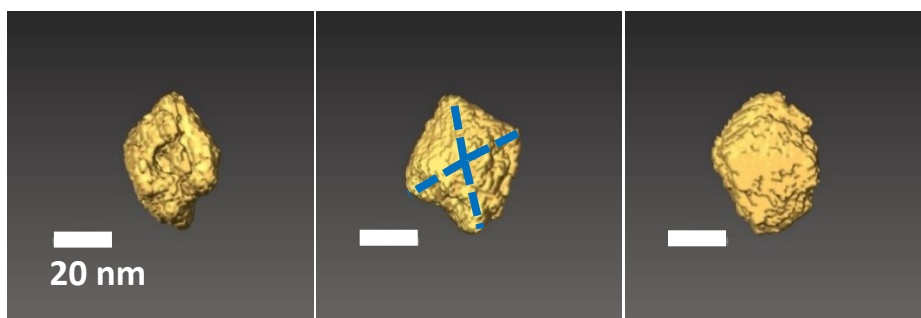


Figure 5.15. HAADF tomography of a CoO@MFO particle.

The results concerning this sample show that the NPs are not a typical core/shell. Although it has been observed that the particles have a cobalt oxide core, this is not solid and consists of several grains. The iron oxide growth also takes place in the small gaps between the cobalt oxide grains, leading to the formation of iron channels observed inside the particle. As for the reduced iron precipitate observed in Figure 5.14L its origin is not clear, and it might not be ruled out that it is an artefact due to the high electron dose during the tilt series acquisition.

For CoO@MFO only reconstructions for the HAADF, cobalt and oxygen signals could be obtained. Figure 5.15 shows the HAADF model of a particle from this sample. It also presents an octahedral shape. Edges have been highlighted in the middle panel of Figure 5.15. The reconstruction also shows a hole in one of the particle sides, even more prominent than in the CoO@CFO particle reconstruction of Figure 5.14. In Figure 5.16 the results of EELS signals 3D reconstructions can be seen. Figure 5.16A-B depict the reconstruction of the cobalt signal, Figure 5.16C-D the oxygen signal and Figure 5.16E-F show both simultaneously. Panel A has the edges of NP highlighted demonstrating its octahedral shape. It should be noted that the oxygen signal extends beyond the cobalt signal (see panels E-F), indicating a uniform layer of iron oxide in the surface, as can be deduced from the preliminary characterization. This allows an indirect measurement of the shell width from the difference between the surface of the oxygen reconstruction and the surface of the cobalt reconstruction. It is thus inferred that the thickness varies between 1 nm and 4 nm at different points.

5.2.5. Discussion

The obtained characterization reveals several relevant points. The CoO@MFO synthesis yields cobalt oxide/iron oxide core/shell octahedral NPs. From the EELS maps of Figure 5.5 and Figure 5.6 it was observed that the shell was actually a cobalt-iron oxide, while from the tomography reconstructions, the thickness of this shell and the presence of voids and iron channels inside the NP was observed.

For the CoO@MFO, the octahedral core/shell morphology was also observed. In this case, the shell is also shown to be a cobalt/iron oxide with a small amount of Mn which was hard to map due to its low signal. The tomographic reconstructions of this sample show very similar holes and diffusion of iron into the inside of the NPs through a complex web of channels.

The feature of voids and cracks in the samples could be explained by a Kirkendall effect based on a solid-solid diffusion process³⁰⁷, in a very similar fashion to the case presented in section 4.1. Yin et al.³⁰⁸ reported the formation of cobalt sulphide, selenide and oxide hollow NPs using the Kirkendall effect.

In our case, the probable presence of an intermediate organometallic compound confined inside the particle and with a different diffusion coefficient than CoO produces a net outward diffusion from the core to the surface and with subsequent porosity generation through this chemical gradient. Another point to take into account is that the octahedral CoO nanocrystals are probably oxidized to Co₃O₄ at least on the surface, as evidenced by Figure 5.8, which is probably promoted by the manipulation of the sample in open-air conditions and the presence of polar (111) facets^{309,310}. This leads, consequently, to a diffusion process, in which the presence of Co³⁺ facilitates redox reactions at the interface³¹¹. Analogously, once the spinel shell is formed, there are at the core/shell interface several transition metals in different oxidation states. Consequently, galvanic reactions can be promoted, given the standard reduction potentials of Fe³⁺/Fe²⁺ (0.77 V), Mn³⁺/Mn²⁺ (1.51V) and Co³⁺/Co²⁺ (1.82 V) pairs (values for aqueous solutions), that can lead to hollow structures, and so, to the observed morphology of the NPs.

EELS edge signal integration tomography has been proven to be useful to understand this process.

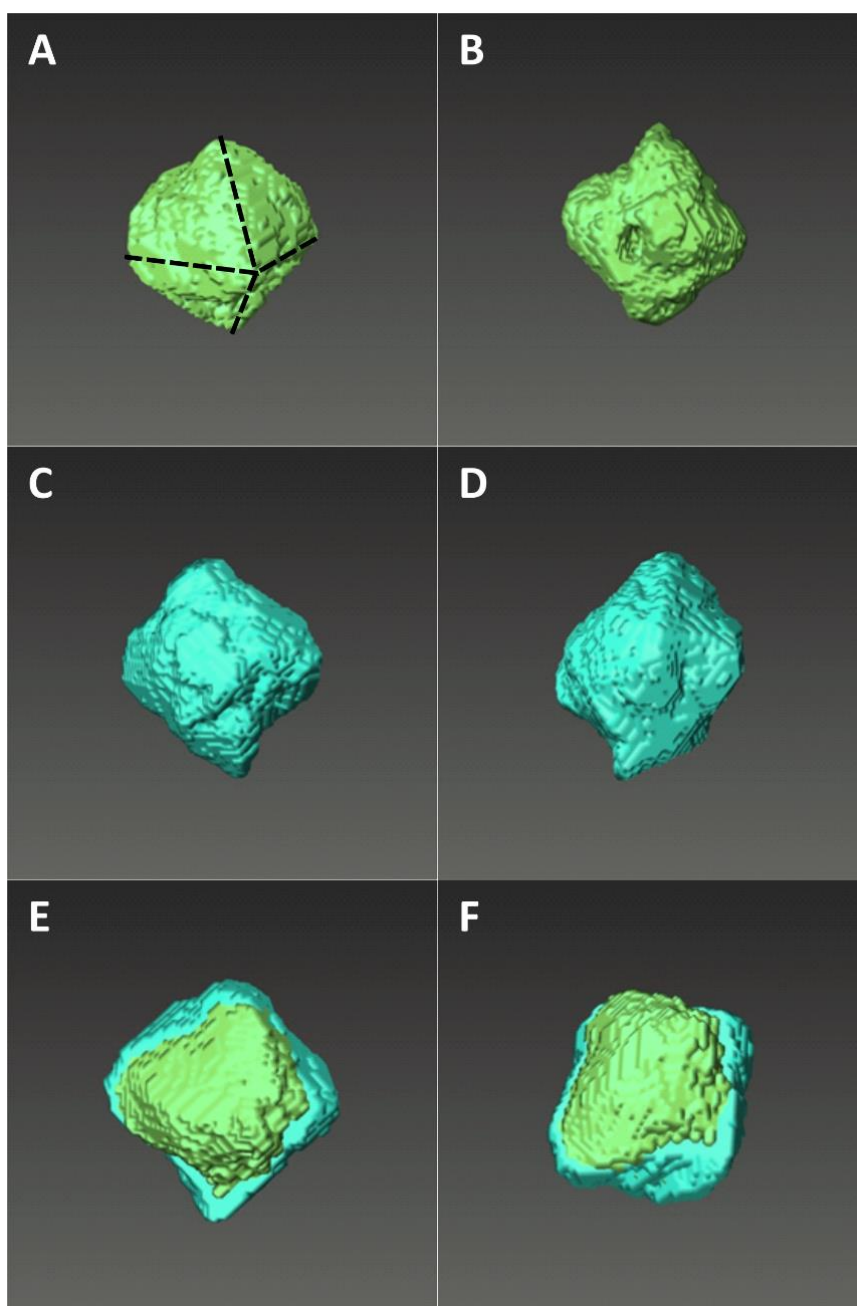


Figure 5.16. CoO@MFO EELS Tomography results. A-B) EELS cobalt signal reconstruction. C,D) Oxygen signal reconstruction. E-F) Oxygen+Cobalt reconstructions.

5.3. EELS tomography of FeO/Fe₃O₄ core/shell nanoparticles

5.3.1. MVA-based EELS tomography fundamentals

MVA-based EELS tomography can be understood by including the concept of projection to a MVA decomposition. Let us start by considering a MVA decomposition in which all the components can be related to the signal of a given chemical species (N_i) in the sample. The signal in the EELS-SI can then be expressed as:

$$I^{\vec{n}}(x, y, E) = \sum_i L_i^{\vec{n}}(x, y) S_i(E) = \sum_i \sigma P_{\vec{n}}(N_i, x, y) S_i(E) \quad (5.3)$$

Where S_i , L_i are the spectral components and the corresponding loadings of the decomposition as described in equation (2.1). As long as L_i is proportional to the projected thickness of the i -th chemical species in the sample (i.e. the projection requirement is fulfilled) its tomographic reconstruction can be performed. Now, once each loading is rebuilt in 3D the SV can be recovered undoing the linear decomposition:

$$SV(x, y, z, E) = \sum_i L_i(x, y, z) S_i(E) \quad (5.4)$$

In this section, the efficiency of this method to retrieve a SV with relevant ELNES information is demonstrated by the 3D-reconstruction of the oxidation states of Fe in a ~40 nm FeO_x/FeO_y core/shell cube-shaped NP.

FeO_x/FeO_y nanocubes have shown potential applications in hyperthermia treatments and as magnetic contrast agents among others^{168,312}, and because of this, a precise knowledge of its morphology, local oxidation state, core and shell thickness and interface nature are of uttermost relevance, as they greatly affect their magnetic properties.

5.3.2. Synthesis of the iron oxide nanocubes

The nanocubes were synthesized according to a previously reported procedure²⁵⁶. The process started by dissolving 2 g (1.95 mmol) of iron(III) oleate and 0.09 g (0.32 mmol) of oleic acid in 20 ml of 1-octadecene. The reaction system was degassed at 100 °C under magnetic stirring by carrying out cycles of vacuum/argon. Subsequently, the mixture was heated up to 320 °C (at 7–8 °C min⁻¹) in argon and kept for 30 min. The NPs were washed by several cycles of coagulation with ethanol, centrifugation at 2000g, disposal of supernatant solution and re-dispersion in hexane.

5.3.3. Preliminary characterization

HRTEM images of the nanocubes were first acquired. Its analysis reveals excellent crystallinity, as seen in Figure 5.17A and the FFT analysis of the selected region (Figure 5.17B). However, the HRTEM imaging mode is unable to reveal the core/shell structure, as the shell has grown epitaxially on the core. On the other hand, the contrast in HAADF-STEM imaging is sensitive to the variation in atomic number³¹³. Consequently, the HAADF image in Figure 5.17C exhibits a small reduction in intensity in the shell region, indicating that the Fe:O ratio is lower than in the core.

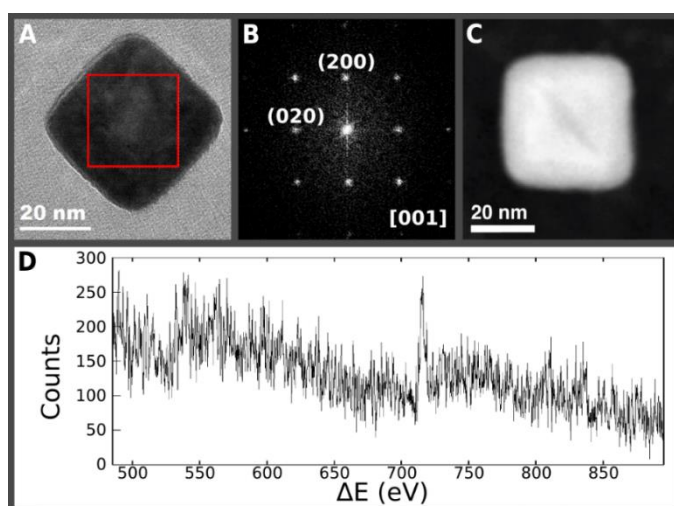


Figure 5.17. A) HRTEM image and B) its corresponding FFT of a nanocube. C) STEM-HAADF image. D) Raw EEL spectrum of the center of the cube.

This variation in contrast, however, is extremely small. Because of this, a proper assessment of the nanoparticle structure can only be carried out by EELS. Moreover, 3D information is necessary in this case, as any defect or variation in a given direction could induce magnetic anisotropies.

5.3.4. EELS tomography acquisition and processing

In order to obtain a quantitative 3D oxidation map of the particle, a STEM-EELS SI tilt-series was acquired using a probe-corrected FEI Titan Low Base, equipped with a XFEG source and a Gatan Tridiem 865 ESR spectrometer, operated at 80 kV. 36 SIs (and their corresponding HAADF-STEM images) were acquired from -69° to $+67^\circ$ every 4° , each containing 64×64 pixels with spectra in the energy range 478-888 eV, at 0.2 eV/pixel dispersion, as the one shown in Figure 5.17D. Several HAADF images acquired simultaneously to the EELS SIs at different angles of the tilt series are shown in Figure 5.18.

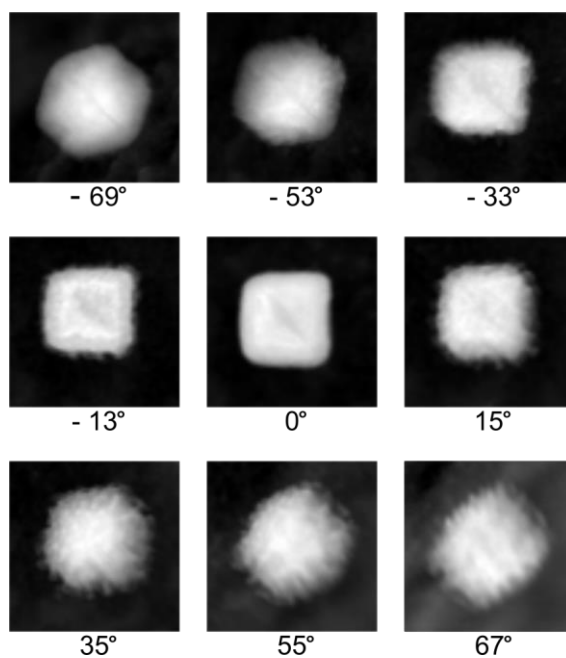


Figure 5.18. HAADF images at different angles acquired in the tomographical series.

The relatively high electron dose used for this EELS tomography acquisition resulted in accumulated beam damage apparent in the second half of the dataset as can be seen in Figure 5.18. Thanks to the cubic shape of the particle, it was possible to select the -69° to 0° subset of the SI tilt series and impose mirror symmetry along one diagonal of the cube.

The EELS data analysis was performed using HyperSpy¹²⁹. After removing the X-ray spikes, weighted PCA³¹⁴ was performed on the EELS tilt series, restricted to the spectral area of interest, 686-888 eV, containing in total $64 \times 64 \times 18$ spectra with 1011 energy-loss channels. PCA decomposed the dataset in 1011 spectral components and distribution maps. Close inspection of the scree plot (see Figure 5.19) showed that the first six components were sufficient to explain the whole dataset (the other 1005 components mostly related to noise). Components 0, 3 and 5 show no remarkable features in the Fe $L_{2,3}$ ionization energy and seem rather related to the background of the spectra due to their power-law behaviour, while component 1 is almost constant and therefore could be related to the dark noise in the detector.

With this knowledge, ICA was performed on the first derivative of the first six spectral components using the FastICA³¹⁵ algorithm in the scikit-learn³¹⁶

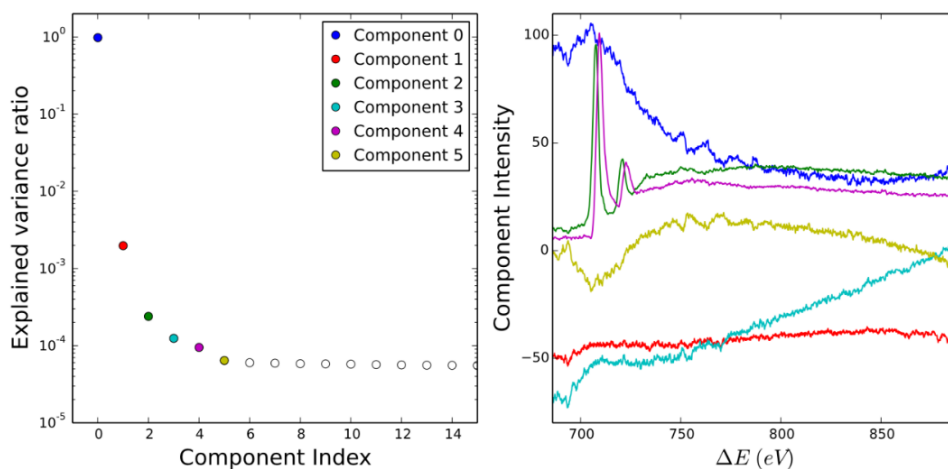


Figure 5.19. Left panel shows the explained variance ratio of the PCA decomposition. The six first components, which are enough to explain the whole data set, are plotted in the right panel.

software package. Two of the independent components, labelled C1 and C2 in Figure 5.20 (left panel), were related to the Fe ionisation edge. Their corresponding loadings derived from the SI acquired at 0° are shown in the right panel of Figure 5.20 and for all the acquired angles in Figure 5.21 and Figure 5.22, respectively. The remaining four components were related again to background and the detector dark current.

Both C1 and C2 show very clear ELNES features that can be identified as the Fe L_3 and Fe L_2 white lines. The position of the maximum of the Fe L_3 of C2 is shifted +1.9 eV with respect to Fe L_3 maximum in C1. For comparison, Figure 5.20 also shows reference EEL spectra corresponding to the Fe- $L_{3,2}$ edges for wüstite (Fe_{1-x}O), with predominantly Fe^{2+} ions and hematite (Fe_2O_3), with predominantly Fe^{3+} ions³¹⁷. From the good agreement between the reference spectra and the ICA components, we can conclude that the C1 component corresponds primarily to the contribution of Fe^{3+} ions to the spectra, while C2 corresponds to Fe^{2+} .

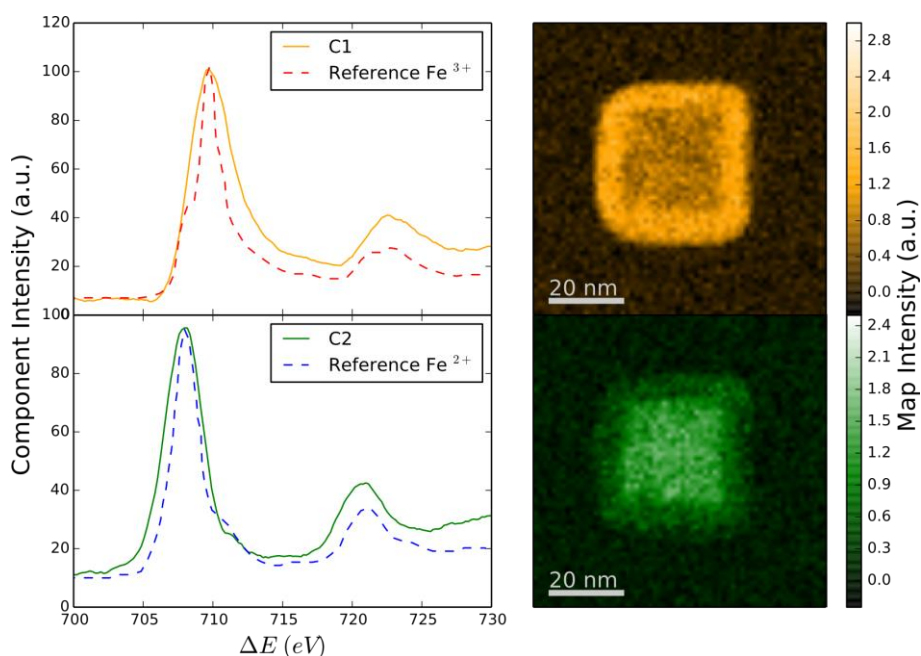


Figure 5.20. Spectral decomposition of the EELS-SI dataset. The left panel shows the main spectral components C1 and C2 obtained through ICA, plotted together with reference spectra for Fe^{3+} and Fe^{2+} from the literature³¹⁷. The corresponding distribution maps at 0° tilt are displayed in the right panels.

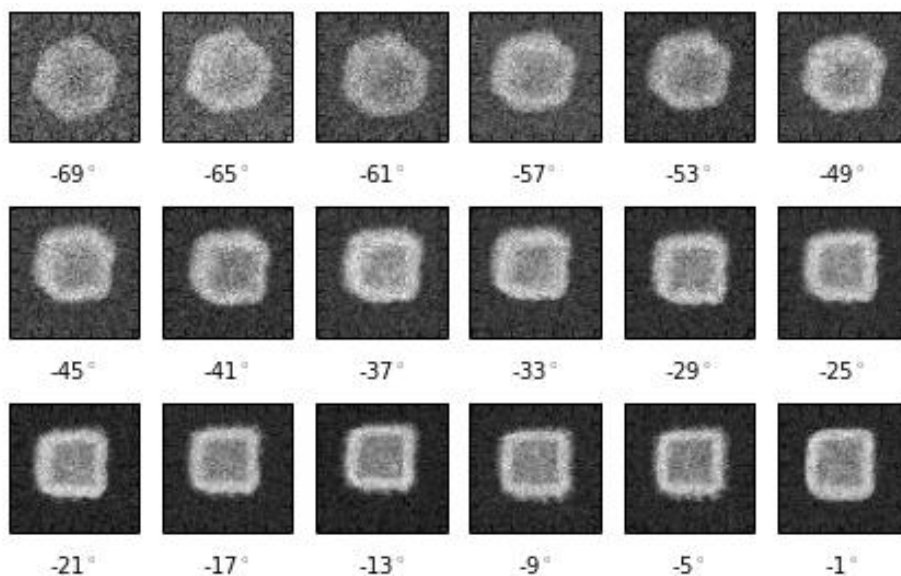


Figure 5.21. Loading map tilt series of component C1.

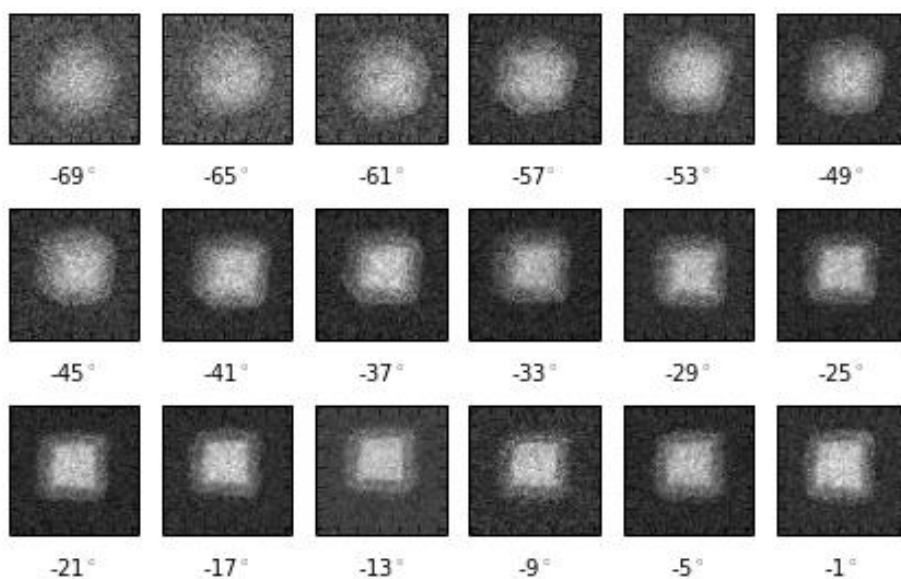


Figure 5.22. Loading map tilt series of component C2.

As already mentioned, to reconstruct in 3D the distribution maps from the tomographic tilt series, the images must satisfy the projection requirement. Namely, the image signal should vary monotonically with the underlying physical property of the object to be reconstructed⁹⁵. In the present case, we assume that the spectral signals correspond, to a good approximation, to single

scattering events. Thus, spectral intensity should be proportional to the total amount of Fe^{2+} or Fe^{3+} ions along the electron path, multiplied by an absorption factor. This factor depends on the materials composing the sample, their thickness and the TEM settings³⁹. Usually the absorption factor is estimated using EELS low-loss spectra of the same area. Alternatively, here we estimate it using the co-acquired HAADF-STEM images, assuming that (i) the support is perfectly flat, (ii) the sample does not change throughout the tilt-series and (iii) the plural scattering is negligible.

The intensity that ionisation from the Fe $L_{3,2}$ subshells by the electron beam contributes to the EELS spectrum acquired at coordinates x, y and tilt-angle θ at energy E is given by:

$$I_{FeL_{3,2}}(x, y, \theta, E) = N_{Fe}(x, y, \theta) e^{-\left(\frac{t_{particle}(x, y, \theta)}{\lambda_{particle}} + \frac{t_{substrate}(\theta)}{\lambda_{substrate}}\right)} \sigma_{FeL_{3,2}}(E) \quad (5.5)$$

where $N_{Fe}(x, y, \theta)$ is the projected iron amount, $\sigma_{FeL_{3,2}}(E)$ is the cross section for ionisation from the Fe $L_{3,2}$ subshells, $t_{particle}$ and $t_{substrate}$ are the thickness of the particle and the substrate (in this case the film of the TEM grid in which the particles are supported), respectively, and $\lambda_{particle}$ and $\lambda_{substrate}$ their mean free paths. Here we are neglecting plural scattering and the small mean free path difference between Fe_3O_4 and FeO .

We estimate $t_{particle}(x, y, \theta)$ and $t_{substrate}(\theta)$ from the high-angle angular dark field images by segmenting the images through thresholding. From (5.6), the intensity of the Fe^{3+} and Fe^{2+} EELS maps that we have obtained by ICA are given by:

$$I_{Fe^{2+,3+}}(x, y, \theta) = k_1 N_{Fe^{2+,3+}}(x, y, \theta) e^{-\left(k_2 t_{particle}(x, y, \theta) + k_3 t_{substrate}(\theta)\right)} \quad (5.6)$$

where k_1 , k_2 and k_3 are constants. Summing over x and y and rearranging:

$$\sum_{(x,y)} N_{Fe^{2+,3+}}(x, y) = k^{-1} \sum_{(x,y)} I_{Fe^{2+,3+}}(x, y, \theta) e^{k_2 t_{particle}(x, y, \theta) + k_3 t_{substrate}(\theta)} \quad (5.7)$$

Notice that we have used $\sum_{(x,y)} N_{Fe^{2+,3+}}(x, y) = \sum_{(x,y)} I_{Fe^{2+,3+}}(x, y, \theta)$ which follows from the fact that the whole particle is contained in the analysed

volume. The only unknowns in this equation are k_1 , k_2 and k_3 . k_1 is irrelevant for our purposes. (5.7) is used to estimate k_2 and k_3 numerically.

Once the absorption factors were obtained, the distribution maps were then divided by the appropriate absorption factor in order to obtain a signal that varies monotonically with the quantity of Fe^{3+} and Fe^{2+} species.

Subsequently, the distribution maps were aligned by their centre of mass, and tomographic reconstructions were performed using CS-ET^{142,302,318–320}. Unlike the conventional back-projection-based algorithms²⁹⁹, CS-ET relies on the idea that the object to be reconstructed can be sparsely represented in a certain domain, i.e., a small proportion of the voxels contain most of the information about the object. This property implies that the volume to be reconstructed is “compressible”, analogous to the familiar compression of images into joint photographic experts group (jpg, jpeg) formats^{318,321}. In the present case of a core/shell structure, sparsity in the image domain and in the gradient domain was imposed^{302,318}. The algorithm to obtain the tomogram is based on the minimization of the following equation:

$$\arg \min_x \|FX - y\|_2 + \lambda_1 \|X\|_1 + \|\Psi X\|_1 \quad (5.8)$$

where X is the reconstructed tomogram, F is the under sampled Fourier transform operator, y is the Fourier transform matrix of the measured projections, Ψ is the total variation operator and λ_i are free parameters. The algorithm first reconstructs the tomogram X taking advantage of the central slice theorem, and then starts the process of non-linear optimization to minimize (5.8). The input signals (y in (5.8)), are the loading maps of the components C1 and C2 for each tilt angle.

The promotion of fidelity to the original projections (first term), image domain sparsity (second term) and total-variation domain sparsity (last term in (5.8)) leads to a reconstruction quality enhancement. In this process, CS-ET improves the signal-to-background ratio and minimizes artefacts related to the relatively large tilt increment (4°) and missing wedge³⁰².

Once the distribution maps of C1 and C2 are reconstructed in 3D, by linearly combining them with their corresponding spectral components, we obtain a SV. From this SV, single spectra, spectrum lines or SIs can be extracted at any specific coordinates.

5.3.5. EELS tomography results

As can be seen in the 3D surface reconstruction of the core and the shell given in Figure 5.23, the technique unambiguously highlights the 3D core/shell configuration of the cubic NP. Figure 5.24 shows the central slice through the reconstructed C1 (orange) and C2 (green) volumes. Measurements of the core and shell along mutually perpendicular directions yield an average shell thickness of 9 nm and average core edge length of 28 nm. It is interesting to notice that there is some Fe^{2+} signal (C2 component) present in the shell region, where the Fe^{3+} (C1 component) is predominant. Interestingly, this indicates the oxide phase forming the shell presents both types of ions, Fe^{3+} and Fe^{2+} . A histogram of the C2 intensity values for voxels in the Fe_3O_4 shell and voxels in the FeO core is plotted in Figure 5.25. Shell distribution is centred at a signal of 500 a. u. while for the core voxels is centred at 1000 a. u., thus giving a ratio of 2. This is consistent with the shell being Fe_3O_4 ($\text{Fe}_{3+}/\text{Fe}_{2+} \approx 2$), whereas the core, with mainly Fe_{2+} ions, consists primarily of FeO.

It is important to emphasize that the SV allows measurements at inner regions of the nanocube, impossible to be independently accessed during the experiments. As an example, the central orthoslice of the reconstruction presented in Figure 5.26B shows the map of the intensity of the C1 and C2 components without contribution of the top and bottom facets of the cube. Figure 5.26A shows two spectra extracted from the core and shell regions (squared markers in Figure 5.26B). A chemical shift of 1.4 eV is highlighted, which is compatible with previously reported values (1.1 ± 0.4 eV)⁴⁰. Figure 5.26C shows the intensity plot of the whole spectrum line acquired along the y direction as indicated in Figure 5.26B.

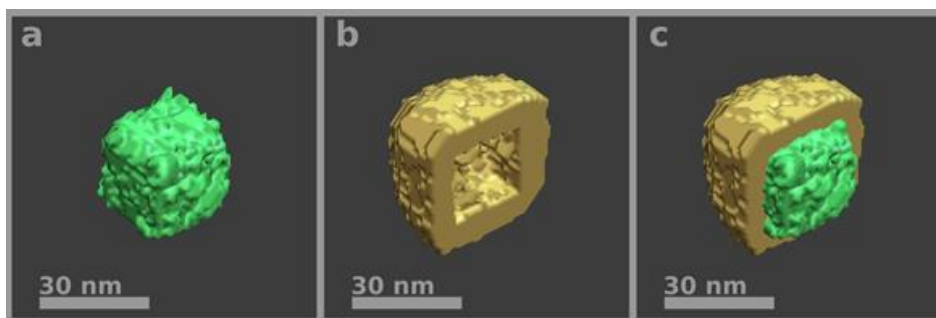


Figure 5.23. 3D surface visualization of the core and the shell. Panels correspond to (A) core only (green), (B) shell only (yellow) and (C) core and shell.

This plot now conveys the chemical shift in the onset of the iron L_3 peak edge moving from the shell to the core (at 16nm) and back to the shell again (at 44 nm), i.e., at the $\text{FeO}/\text{Fe}_3\text{O}_4$ core/shell interfaces. Importantly, this spectrum line has no contribution from the top and bottom shell facets of the nanocube, since it is extracted from a chosen sub-volume, which is impossible to achieve directly from the experiment.

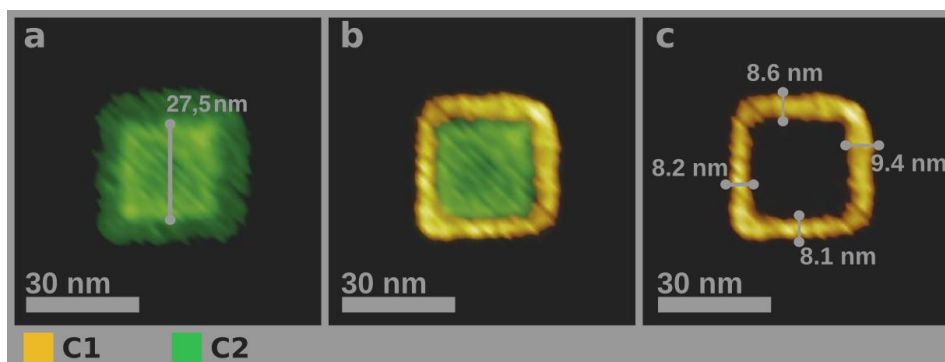


Figure 5.24. A-C) X-Y orthoslices showing the size determination for (A) the core and (C) the shell. (B) Both slices superimposed. The volumes have been oversampled by a factor 10 for the visualization.

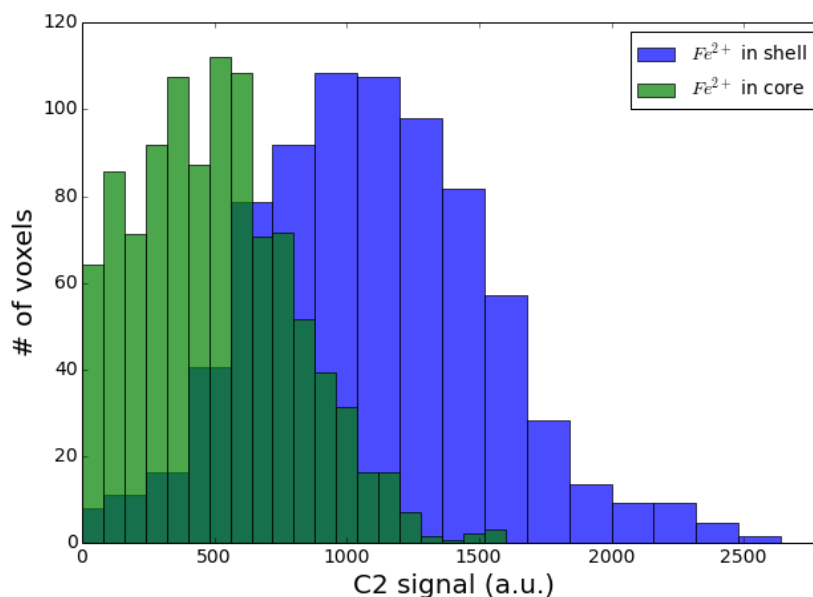


Figure 5.25. Histogram of C2 signal in voxels corresponding to different regions.

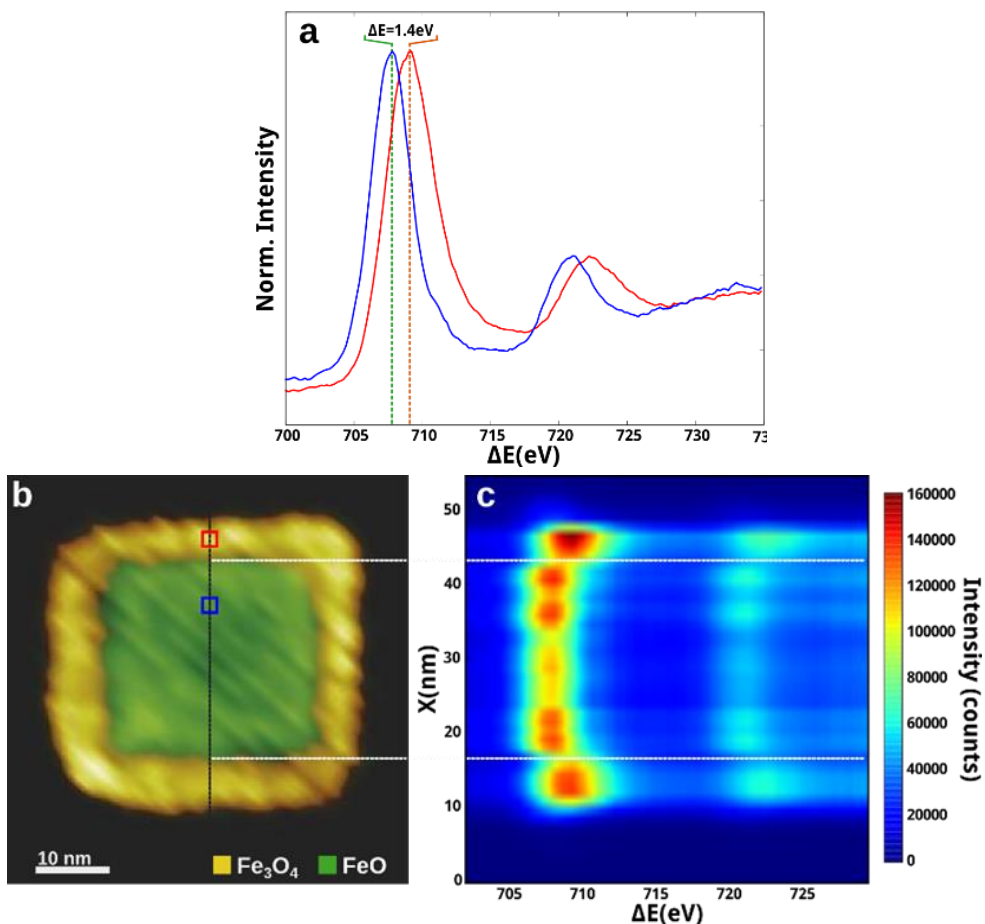


Figure 5.26. (A) Spectra extracted from the SV from the markers in (B). (B) Central slice from the SV in the X-Y plane. (C) Spectrum line from the region marked in (B).

Magnetic measurements were also carried out on the NPs²⁵⁶ in a superconducting quantum interference device (SQUID) magnetometer with a maximum field of 70 kOe. The zero field cool magnetization measurements were carried out at 10 Oe with increasing temperatures from 10 K after cooling the sample in zero field from the 300 K remnant state. The field cooled hysteresis loop was measured (up to 70 kOe) at 10 K after cooling the sample in $H_{FC} = 70 \text{ kOe}$ from room temperature.

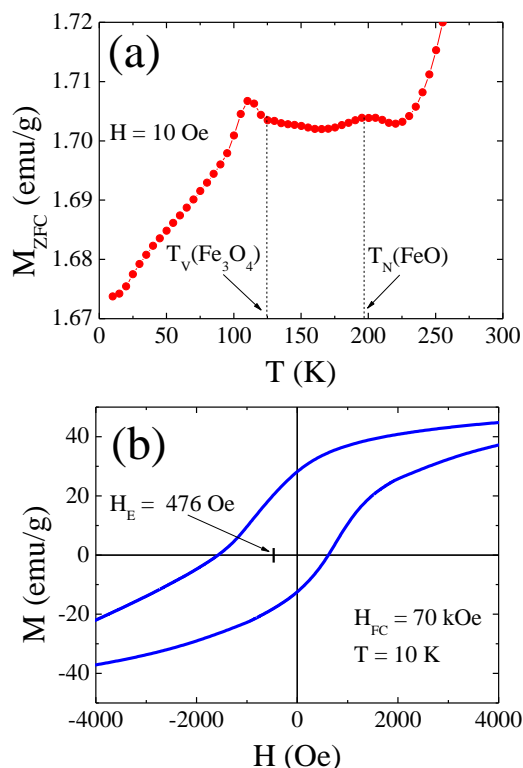


Figure 5.27. A) Temperature dependence of the zero field cooled magnetization, M_{ZFC} , of the FeO/Fe₃O₄ NPs measured at $H = 10$ Oe. The bulk transition temperatures of the Fe₃O₄ Verwey transition, T_V , and the FeO Néel transition, T_N , are shown. B) Enlarged hysteresis loop at 10 K after field cooling in $H_{FC} = 70$ kOe. The loop shift, H_E , is highlighted in the figure.

As can be seen in Figure 5.27A, the zero-field cooled magnetization, M_{ZFC} , exhibits two clear features at $T \sim 110$ K and at $T \sim 200$ K. The low temperature transition can be identified with the Verwey transition, T_V , typical of Fe₃O₄. Since Fe₃O₄ is the only iron oxide featuring this transition, it confirms the presence of Fe₃O₄ in the NPs as revealed by EELS tomography. Moreover, the rather sharp T_V indicates that the Fe₃O₄ must be rather well structured. On the other hand, the high temperature transition can be assigned to the antiferromagnetic (AFM) Néel transition, T_N , of FeO. Since no other iron oxide exhibits any transition in this temperature range, we can safely identify the second counterpart as FeO, in concordance with the EELS-tomography results. Finally, the low temperature hysteresis loop measured after field cooling from room temperature (Figure 5.27B) shows a clear loop shift in the field axis, which is typical for ferrimagnetic (FiM) (Fe₃O₄) – AFM (FeO) exchange coupling, i.e., exchange bias³²². In fact, the

rather large exchange bias shift likely indicates the presence of a sharp interface between the FiM and AFM phases, as observed in Figure 5.24. All these results are perfectly compatible with the structure unveiled through EELS tomography.

5.3.6. Discussion

The process to obtain quantitative 3D maps of the iron oxidation states of FeO/Fe₃O₄ core/shell nanocubes from a combination of EELS, ET and machine learning methods has been demonstrated. The analysis has been successful even from a reduced and noisy starting dataset. Importantly, the construction of a SV also enables extracting novel and important information about nanoscale objects that would have been otherwise unavailable. In particular, this approach allows accessing the spectral information from the FeO core without superposition of the shell signal. Thus, the proposed method is a viable alternative to investigate nanomaterials, especially for nanostructures with complex morphologies and non-homogeneous elemental and electronic distribution. The method is particularly suited to data acquired in challenging low-dose low-voltage experimental conditions.

5.4. Conclusions

EELS tomography is a powerful tool to investigate nanocrystals and nanocomposites with complex chemical structures. The different methods used to obtain these reconstructions have been discussed. A practical case has been shown both for the integrated signal reconstruction and for the MVA-enabled reconstruction method. In the first case, the diffusion of iron into the cobalt oxide polycrystalline NPs and the octahedral shape of the core/shell NPs has been shown. Then, the possibility to obtain oxidation state-sensitive 3D reconstructions has been demonstrated. To achieve this, different methods had to be developed such as an absorption correction method from HAADF images and the integration of state-of-the-art CS tomography algorithms with PCA/ICA generated maps. The results yielded relevant information on the intimate structure of the FeO_x/FeO_y core/shell NP that would otherwise not have been accessible.

CHAPTER 6: General conclusions

The aim of this thesis has been two-fold. First, to develop new processing and analysis tools and strategies for extracting information from EELS data, and second, to apply the methods to different nanoparticle systems to shed light to relevant phenomena related to their synthesis and properties. In this regard, chapter 1 presented an overview of the EELS fundamentals and of the state of the art of the technique. Chapter 2 was focused on the advanced computational methods related to EELS data analysis. Moreover, the application of cluster analysis to EELS was introduced, showing its possibilities as an image segmenting and phase identification tool. The following chapters were devoted to the investigation of different material science problems related to NPs that take advantage of the capabilities of quantitative EELS.

The results were grouped by increasing complexity of the performed analysis, with chapter 3 devoted to characterizations that were mainly carried out using EELS elemental mapping, chapter 4 being related to ELNES analysis and chapter 5 to EELS tomography. In the following section, the main findings in these chapters will be summarized.

In chapter 2, the adaptation of data clustering algorithms to the analysis of EELS data, developed within the scope of the present thesis, has been undertaken:

- The literature identifies the clustering problem as grouping objects with a certain number of attributes so that objects in the same group have similar attributes and objects on other groups have very different attributes. A first approach to adapt this to EELS is to think of an object as an EELS spectrum and its attributes as the values for each energy channel that it contains.
- The previous interpretation requires the spectra to be normalized by their total intensity in order to obtain clusters related to different chemical composition and not to different thicknesses.
- The parameter that defines how many clusters are obtained is the threshold that limits the furthest distance of an object (a spectrum) with respect to the centre of its cluster.
- This approach is able to segment a spectrum image in different regions, according to their chemical composition.

- The segmentation achieved can be used as a masking method for subsequent analysis algorithms, such as PCA. This enables the detection of fine gradients in composition, or small variation in the ELNES of the spectra.
- Another way to adapt clustering analysis to EELS is to first perform PCA and then consider an object as a pixel, and its attributes as the values of the loadings in that pixel for the different PCA components. This allows for a clearer, less noisy segmentation. This method enables distinguishing subtle oxidation state changes within a noisy, experimental SI.
- The validity and usefulness of the three strategies proposed has been tested with both simulated and experimental data, with positive results.

In chapter 3.1 the organic synthesis of $\text{FeO}_x@\text{SiO}_2$ NPs was assessed. Several findings were obtained through the HRTEM, STEM-HAADF and EELS characterization of the $\text{FeO}_x@\text{SiO}_2$ NPs at different stages of its synthesis:

- HRTEM analysis of the iron oxide seeds is compatible with magnetite phase. The oleic acid coating of the NPs can be directly observed through EELS mapping.
- After the addition of an acetate complex, the carbon coating is observed, by EELS mapping, to become radically different whilst the iron oxide lattice remains as magnetite.
- Cryo-TEM images of the sample show the formation of iron oxide NP clusters when dispersed into an aqueous solution. As samples are observed at different points of the synthesis, silica grows onto the NPs forming a cluster, finally ejected leaving an apple bite-like feature in the shell.
- In the latter stages of the synthesis, smaller (around 1nm) NPs of iron oxide are found in the sample, indicating possible breakage of the original iron oxide NPs.
- A carbon coating is found on the outside of the silica shell and between the iron oxide core and the silica shell, through EELS mapping. The EELS analysis also confirms that no oxidation/reduction occurs in the iron oxide cores throughout the process.
- These findings lead to the development of a microscopic model of the synthesis that involves a previously unreported exchange of oleic/acetate ligands on the surface of the iron oxide NPs through breakage of small particles on its surface.

In chapter 3.2, concerning Au-Ag-Se cation exchange reactions the following findings were made:

- The following products of the exchange reactions of Ag_2Se NPs with gold ion solutions were found when varying the reaction conditions:
 - Pure fischerite nanocrystals, by using TOAB ligand.
 - Au- Ag_2Se hybrid NPs, by using DDA ligand and short reaction times.
 - Au- Ag_2AuSe_2 hybrid NPs, by using DDA ligand and long reaction times.
- This was found through HRTEM imaging, EELS mapping and HAADF imaging of the NPs
- A selenium rich layer is observed on the outside of the Au- Ag_2Se and Au- Ag_2AuSe_2 NPs.
- No epitaxial relationship was found between the gold and silver/gold selenide domains in the hybrid NPs. The interface was found to be amorphous.
- From these observations, the role of the external layer of the Ag_2Se seeds as a sacrificial reduction layer for gold ions previous to their diffusion into the crystalline lattice was proposed.

Regarding to the Au-Ag-S system, similar mechanisms were observed:

- In the Au-Ag-S system, The HRTEM and STEM-HAADF characterization revealed the following products when the reaction conditions were varied:
 - Au- Ag_3AuS_2 NPs when a 3:1 silver to gold ratio was used.
 - Au-AgAuS NPs when a 1:1 silver to gold ratio was used.
 - Hollow Au_2S NPs when a 1:10 silver to gold ratio was used.
- Different crystalline phases were identified in the Ag_2S seed NPs.
- Multiple gold domains and defects were observed in the Au-AgAuS NPs.
- The decrease in Ag/Au ratio between the Ag_3AuS_2 and AgAuS nanocrystals was measured by EDX.
- Samples with the same reaction conditions but with rod-shaped Ag_2S seeds were characterized, obtaining rod-shaped Au- Ag_3AuS_2 NPs, Au-AgAuS NPs and hollow Au_2S NPs.
- The full exchange cycle from silver sulphide NPs to gold sulphide NPs was observed, proving that all the intermediate phases were formed in the process.

Chapter 4 was devoted to the characterization of different NPs with an emphasis on the direct observation the oxidation state of its constituents through EELS. In chapter 4.1 , the synthesis of $\text{MnO}_x/\text{Fe}_3\text{O}_4$ core/shell NPs was assessed:

- The standard synthesis process yielded fully-dense core/shell NPs, while a synthesis with addition of water produces hollow core/shell NPs.
- In the fully dense NPs, a diffusion of iron ions into the manganese oxide core was observed.
- The manganese oxide core was found to be Mn_3O_4 for the hollow NPs and MnO for the dense NPs, indicating that water oxidizes the seeds.
- Pinholes at the surface and the empty core were observed for the hollow NPs through STEM-HAADF tomography.
- From these descriptions, a galvanic process promoted by the oxidation of the manganese oxide seeds was deduced to be the origin of the hollowing process. Subsequent syntheses with degassed and bubbled water confirmed this point. The presence of oxidizing agents dissolved in the water at the high synthesis temperatures was shown to oxidize the manganese oxide seeds.

In chapter 4.2, the measurement of oxidation state at atomic resolution in spinel crystals was proposed as a method to assess cation inversion in the crystal. The necessary methods were developed and applied to iron oxide/manganese oxide core/shell NPs, obtaining the following results:

- The characterized samples consisted in $\text{Fe}_3\text{O}_4/\text{Mn}_3\text{O}_4$ core/shell NPs. The shell grew epitaxially on the core, which lead to stress in the lattice, inducing the formation of crystalline defects.
- By assuming a linear relationship between the oxidation state of a given element and an ELNES parameter of its EELS edge, it was possible to calculate the inversion parameter from two EELS spectra corresponding to different atomic columns. With this method, an inversion parameter of $x = 0.84 \pm 0.02$ for the iron oxide cores was obtained.
- With the same method and by calculating the average Mn L_3 chemical shift between atomic columns with either tetrahedral or octahedral coordination, an inversion parameter of $x = 0.39 \pm 0.1$ was found.
- Macroscopic XAS measurements were performed, obtaining inversion parameters of $x = 0.44$ for the manganese oxide and $x = 0.86$ for the iron oxide, in good agreement with the ELNES based methods.
- If a PCA decomposition is obtained and its factors can be assigned to the contributions of ions with different oxidation state, it was proposed to

calculate the inversion parameter for each pixel of the SI as the ratio of the corresponding PCA loadings in the atomic columns with a tetrahedral oxygen coordination. This method resulted in $x=0.35$ for the manganese oxide, compatible with the ELNES based method and the XAS measurement.

- The PCA enabled method evidenced an “inversion gradient” towards the core-shell interface of the NP.

Chapter 5 was devoted to the combination of EELS and tomography. In chapter 5.1 the synthesis of cobalt oxide/cobalt ferrite (CoO@CFO) core/shell NPs and cobalt oxide/manganese ferrite (CoO@MFO) NPs was investigated.

- Both types of NPs presented a polycrystalline structure with cracks on the surface.
- EELS tomography of both samples was performed by integrating the intensity of different EELS edges to obtain element sensitive tilt-series. The reconstructions showed, for both samples, the presence of holes and voids inside the particles. Diffusion of the shell elements inside into the core of the NPs was also observed.
- With the observed morphology of cracks and voids in the sample it was deduced, as for the case studied in chapter 4.1, that a galvanic process took place during the synthesis. The presence of Co_3O_4 supports this process.

Chapter 5.2 was focused on the achievement of an oxidation state-sensitive tomographic reconstruction:

- The studied sample consisted of $\text{FeO}_x/\text{FeO}_y$ core/shell NPs that grew with an adapted crystalline lattice and that showed a very similar HAADF contrast. Therefore, they could only be distinguished by EELS.
- A PCA decomposition was obtained. Its factors matched reference spectra for oxides containing exclusively either Fe^{2+} or Fe^{3+} .
- After performing an intensity correction with information from the HAADF coacquired tilt-series, it was possible to use a compressed sensing tomography algorithm to reconstruct the loading maps of the Fe^{2+} and Fe^{3+} components in 3D.
- The intensity ratios of these components in the core and shell demonstrated that the core of the NP was FeO ($\text{Fe}^{3+}:\text{Fe}^{2+} = 1$) and the shell was most likely Fe_3O_4 ($\text{Fe}^{3+}:\text{Fe}^{2+} = 2$).

- The widths and thicknesses of core and shell components were measured, and the interface was found to be sharp. The tomographical measurements matched the magnetic characterization of the sample.
- These results constitute the first MVA-Based EELS tomography with ELNES information.

CHAPTER 7: References

- (1) Feynman, R. P. *Eng. Sci.* **1960**, *23*, 22–35.
- (2) Crowther, R. A.; Amos, L. A.; Finch, J. T.; De Rosier, D. J.; Klug, A. *Nature* **1970**, *226* (5244), 421–425.
- (3) De Rosier, D. J.; Klug, A. *Nature* **1968**, *217* (5124), 130–134.
- (4) Klug, A.; Finch, J. T. *J. Mol. Biol.* **1968**, *31* (1), 1–12.
- (5) Klug, A.; Finch, J. T. *J. Mol. Biol.* **1965**, *11* (2), 403–423.
- (6) Knoll, M.; Ruska, E. *Zeitschrift Fur Phys.* **1932**, *78* (5–6), 318–339.
- (7) Shechtman, D.; Lang, C. I. *MRS Bull.* **1997**, *22* (11), 40–42.
- (8) Portier, R.; Shechtman, D.; Gratias, D.; Cahn, J. J. *Microsc. Spectrosc. Electron.* **1985**, *10* (2), 107–116.
- (9) Shechtman, D.; Blech, I. A. *Metall. Trans. A* **1985**, *16* (6), 1005–1012.
- (10) Shechtman, D.; Blech, I.; Gratias, D.; Cahn, J. W. *Phys. Rev. Lett.* **1984**, *53* (20), 1951–1953.
- (11) Schultz, P.; Dubochet, J.; Adrian, M.; Chang, J.-J.; Homo, J.-C.; Lepault, J.; McDowell, A. W.; Schultz, P. *Q. Rev. Biophys.* **1988**, *21* (2), 129–228.
- (12) Frank, J.; Radermacher, M.; Penczek, P.; Zhu, J.; Li, Y.; Ladjadj, M.; Leith, A. *Journal of Structural Biology*. Academic Press January 1, 1996, pp 190–199.
- (13) van Heel, M.; Frank, J. *Ultramicroscopy* **1981**, *6* (2), 187–194.
- (14) Warne, T.; Serrano-Vega, M. J.; Baker, J. G.; Moukhametzianov, R.; Edwards, P. C.; Henderson, R.; Leslie, A. G. W.; Tate, C. G.; Schertler, G. F. X. *Nature* **2008**, *454* (7203), 486–491.
- (15) Henderson, R.; Unwin, P. N. T. *Nature* **1975**, *257* (5521), 28–32.
- (16) Button, G.; Hawkes, P.; Spence, J. C. In *Science of microscopy*; Springer, 2008; pp 273–405.
- (17) Muller, D. a; Kourkoutis, L. F.; Murfitt, M.; Song, J. H.; Hwang, H. Y.; Silcox, J.; Dellby, N.; Krivanek, O. L.; Fitting Kourkoutis, L.; Murfitt, M.; Song, J. H.; Hwang, H. Y.; Silcox, J.; Dellby, N.; Krivanek, O. L. *Science*

- (80-). **2008**, 319 (5866), 1073–1076.
- (18) D’Alfonso, A. J.; Freitag, B.; Klenov, D.; Allen, L. J. *Phys. Rev. B - Condens. Matter Mater. Phys.* **2010**, 81 (10), 100101.
- (19) Kohno, Y.; Okunishi, E.; Tomita, T.; Ishikawa, I.; Kaneyama, T.; Ohkura, Y.; Kondo, Y.; Isabell, T. *Microsc. Anal.* **2010**.
- (20) Krivanek, O. L.; Nellist, P. D.; Dellby, N.; Murfitt, M. F.; Szilagy, Z. In *Ultramicroscopy*; North-Holland, 2003; Vol. 96, pp 229–237.
- (21) Ricolleau, C.; Nelayah, J.; Oikawa, T.; Kohno, Y.; Braidy, N.; Wang, G.; Hue, F.; Florea, L.; Pierron Bohnes, V.; Alloyeau, D. *J. Electron Microsc. (Tokyo)*. **2013**, 62 (2), 283–293.
- (22) Schlossmacher, P.; Klenov, D. O.; Freitag, B.; Harrach, S. Von; Steinbach, A. *Microsc. Anal. Nanotechnol. Suppl.* **2010**, 24, S5–S8.
- (23) Bosman, M.; Keast, V. J.; García-Muñoz, J. L.; D’Alfonso, A. J.; Findlay, S. D.; Allen, L. J. *Phys. Rev. Lett.* **2007**, 99 (8), 086102.
- (24) Kimoto, K.; Asaka, T.; Nagai, T.; Saito, M.; Matsui, Y.; Ishizuka, K. *Nature* **2007**, 450 (7170), 702–704.
- (25) Chu, M. W.; Liou, S. C.; Chang, C. P.; Choa, F. S.; Chen, C. H. *Phys. Rev. Lett.* **2010**, 104 (19), 196101.
- (26) Wang, Z. L.; Yin, J. S.; Jiang, Y. D. *Micron* **2000**, 31 (5), 571–580.
- (27) Colliex, C.; Manoubi, T.; Ortiz, C. *Phys. Rev. B* **1991**, 44 (20), 11402–11411.
- (28) Papworth, A. J.; Kiely, C. J.; Burden, A. P.; Silva, S. R. P.; Amaratunga, G. A. J. *Phys. Rev. B - Condens. Matter Mater. Phys.* **2000**, 62 (19), 12628–12631.
- (29) Tomoko, S.; Koji, K.; Takashi, A.; Yasuhiro, M. *Jpn. J. Appl. Phys.* **1998**, 37 (6B), L694.
- (30) Krivanek, O. L.; Lovejoy, T. C.; Dellby, N.; Aoki, T.; Carpenter, R. W.; Rez, P.; Soignard, E.; Zhu, J.; Batson, P. E.; Lagos, M. J.; Egerton, R. F.; Crozier, P. a. *Nature* **2014**, 514 (7521), 209–212.
- (31) Eljarrat, A.; López-Conesa, L.; López-Vidrier, J.; Hernández, S.; Garrido, B.; Magén, C.; Peiró, F.; Estradé, S. *Nanoscale* **2014**, 6 (24), 14971–14983.
- (32) Jarausch, K.; Thomas, P.; Leonard, D. N.; Twesten, R.; Booth, C. R.

- Ultramicroscopy* **2009**, *109* (4), 326–337.
- (33) Yedra, L.; Eljarrat, A.; Rebled, J. M.; López-Conesa, L.; Dix, N.; Sánchez, F.; Estradé, S.; Peiró, F. *Nanoscale* **2014**, *6* (12), 6646–6650.
- (34) Yedra, L.; Eljarrat, A.; Arenal, R.; Pellicer, E.; Cabo, M.; López-Ortega, A.; Estrader, M.; Sort, J.; Baró, M. D.; Estradé, S.; Peiró, F. *Ultramicroscopy* **2012**, *122*, 12–18.
- (35) Yedra, L. Towards a new dimension in analytical TEM: EELS, Tomography and the Spectrum Volume, Universitat de Barcelona, 2013.
- (36) Nelayah, J.; Kociak, M.; Stéphan, O.; De Abajo, F. J. G.; Tencé, M.; Henrard, L.; Taverna, D.; Pastoriza-Santos, I.; Liz-Marzán, L. M.; Colliex, C. *Nat. Phys.* **2007**, *3* (5), 348–353.
- (37) Ouyang, F.; Batson, P. E.; Isaacson, M. *Phys. Rev. B* **1992**, *46* (23), 15421–15425.
- (38) Park, J.; Heo, S.; Chung, J. G.; Kim, H.; Lee, H.; Kim, K.; Park, G. S. *Ultramicroscopy* **2009**, *109* (9), 1183–1188.
- (39) Egerton, R. F. *Electron Energy-Loss Spectroscopy in the Electron Microscope (3rd Edition)*; Boston, MA, 2011.
- (40) Schmid, H. K.; Mader, W. *Micron* **2006**, *37* (5), 426–432.
- (41) Otten, M. T.; Coene, W. M. J. *Ultramicroscopy* **1993**, *48* (1–2), 77–91.
- (42) Coene, W.; Janssen, G.; Op De Beeck, M.; Van Dyck, D. *Phys. Rev. Lett.* **1992**, *69* (26), 3743–3746.
- (43) Kisielowski, C.; Freitag, B.; Bischoff, M.; Van Lin, H.; Lazar, S.; Knippels, G.; Tiemeijer, P.; Van Der Stam, M.; Von Harrach, S.; Stekelenburg, M.; Haider, M.; Uhlemann, S.; Müller, H.; Hartel, P.; Kabius, B.; Miller, D.; Petrov, I.; Olson, E. A.; Donchev, T.; Kenik, E. A.; Lupini, A. R.; Bentley, J.; Pennycook, S. J.; Anderson, I. M.; Minor, A. M.; Schmid, A. K.; Duden, T.; Radmilovic, V.; Ramasse, Q. M.; Watanabe, M.; Erni, R.; Stach, E. A.; Denes, P.; Dahmen, U.; Muller, H.; Hartel, P.; Kabius, B.; Miller, D.; Petrov, I.; Olson, E. A.; Donchev, T.; Kenik, E. A.; Lupini, A. R.; Bentley, J.; Pennycook, S. J.; Anderson, I. M.; Minor, A. M.; Schmid, A. K.; Duden, T.; Radmilovic, V.; Ramasse, Q. M.; Watanabe, M.; Erni, R.; Stach, E. A.; Denes, P.; Dahmen, U. *Microsc. Microanal. Off. J. Microsc. Soc. Am. Microbeam Anal. Soc. Microsc. Soc. Canada* **2008**, *14* (5), 469–477.
- (44) Carpenter, R. ; Xie, H.; Lehner, S.; Aoki, T.; Mardinly, J.; Vahidi, M.; Newman, N.; Ponce, F. A. *Microsc. Microanal.* **2014**, *20* (S3), 70–71.

- (45) W. Carpenter, R.; H. Xie; T. Aoki; A. Ponce, F. *Microsc. Microanal.* **2015**, *21* (S3), 657–658.
- (46) Kimoto, K. *Microscopy* **2014**, *63* (5), 337–344.
- (47) Tsuno, K. *Nucl. Instruments Methods Phys. Res. Sect. A Accel. Spectrometers, Detect. Assoc. Equip.* **2011**, *645* (1), 12–19.
- (48) Tiemeijer, P. C.; Bischoff, M.; Freitag, B.; Kisielowski, C. *Ultramicroscopy* **2012**, *118*, 35–43.
- (49) Mukai, M.; Warner, J.; Kim, J. S.; Omoto, K.; Sawada, H.; Kimura, a; Ikeda, a; Zhou, J.; Nellist, P. D.; Kirkland, a I.; Road, P. *Microsc. Microanal.* **2013**, *19* (Suppl 2), 310–311.
- (50) Mukai, M.; Kim, J. S.; Omoto, K.; Sawada, H.; Kimura, A.; Ikeda, A.; Zhou, J.; Kaneyama, T.; Young, N. P.; Warner, J. H.; Nellist, P. D.; Kirkland, A. I. *Ultramicroscopy* **2014**, *140*, 37–43.
- (51) Essers, E.; Benner, G.; Mandler, T.; Meyer, S.; Mittmann, D.; Schnell, M.; Höschel, R. *Ultramicroscopy* **2010**, *110* (8), 971–980.
- (52) Rose, H. *Ultramicroscopy* **1999**, *78* (1–4), 13–25.
- (53) Walther, T.; Quandt, E.; Stegmann, H.; Thesen, a.; Benner, G. *Ultramicroscopy* **2006**, *106* (11–12 SPEC. ISS.), 963–969.
- (54) Krivanek, O. L.; Ursin, J. P.; Bacon, N. J.; Corbin, G. J.; Dellby, N.; Hrcirik, P.; Murfitt, M. F.; Own, C. S.; Szilagy, Z. S. *Philos. Trans. R. Soc. A Math. Phys. Eng. Sci.* **2009**, *367* (1903), 3683–3697.
- (55) Krivanek, O. L.; Lovejoy, T. C.; Murfitt, M. F.; Skone, G.; Batson, P. E.; Dellby, N. *J. Phys. Conf. Ser.* **2014**, *522* (1), 012023.
- (56) Scherzer, O. *J. Appl. Phys.* **1949**, *20* (1), 20–29.
- (57) Yoshio Matsui; Shigeo Horiuchi; Yoshio Bando; Yoshizo Kitami; Masato Yokoyama; Shigeru Suehara; Isao Matsui; Teiji Katsuta. *Ultramicroscopy* **1991**, *39* (1–4), 8–20.
- (58) F. Phillipp; R. Höschel; M. Osaki; G. Möbus; M. Rühle. *Ultramicroscopy* **1994**, *56* (1–3), 1–10.
- (59) Max Haider; Harald Rose; Stephan Uhlemann; Eugen Schwan; Bernd Kabius; Knut Urban. *Ultramicroscopy* **1998**, *75* (1), 53–60.
- (60) Krivanek, O. L.; Dellby, N.; Lupini, A. R. *Ultramicroscopy* **1999**, *78*, 1–11.
- (61) Sawada, H.; Sasaki, T.; Hosokawa, F.; Yuasa, S.; Terao, M.; Kawazoe, M.;

- Nakamichi, T.; Kaneyama, T.; Kondo, Y.; Kimoto, K.; Suenaga, K. *J. Electron Microsc. (Tokyo)*. **2009**, *58* (6), 341–347.
- (62) Sawada, H.; Sasaki, T.; Hosokawa, F.; Suenaga, K. .
- (63) Suenaga, K.; Iizumi, Y.; Okazaki, T. *Eur. Phys. J. Appl. Phys* **2011**, *54* (33508).
- (64) Haider, M.; Müller, H.; Uhlemann, S.; Zach, J.; Loebau, U.; Hoeschen, R. *Ultramicroscopy* **2008**, *108*, 167–178.
- (65) Kabius, B.; Hartel, P.; Haider, M.; Ullmer, H.; Uhlemann, S.; Loebau, U.; Zach, J.; Rose, H. *J. Electron Microsc. (Tokyo)*. **2009**, *58* (3), 147–155.
- (66) Erni, R.; Rossell, M. D.; Kisielowski, C.; Dahmen, U. *doi.org* **2009**, *102* (9), 096101.
- (67) Rose, H. *Ultramicroscopy* **2005**, *103*, 1–6.
- (68) Linck, M.; Hartel, P.; Uhlemann, S.; Kahl, F.; Müller, H.; Zach, J.; Haider, M.; Niestadt, M.; Bischoff, M.; Biskupek, J.; Lee, Z.; Lehnert, T.; Börrnert, F.; Rose, H.; Kaiser, U. *Phys. Rev. Lett.* **2016**, *117* (7), 076101.
- (69) Samuel Reich, E. *Nature* **2013**, *499* (7457), 135–136.
- (70) Kahl, F.; Linck, M.; Hartel, P.; Müller, H.; Uhlemann, S.; Haider, M.; Zach, J. In *European Microscopy Congress 2016: Proceedings*; Wiley-VCH Verlag GmbH & Co. KGaA: Weinheim, Germany, 2016; pp 787–788.
- (71) Gubbens, A.; Barfels, M.; Trevor, C.; Twisten, R.; Mooney, P.; Thomas, P.; Menon, N.; Kraus, B.; Mao, C.; McGinn, B. *Ultramicroscopy* **2010**, *110* (8), 962–970.
- (72) Scott, J.; Thomas, P. J.; MacKenzie, M.; McFadzean, S.; Wilbrink, J.; Craven, A. J.; Nicholson, W. A. P. *Ultramicroscopy* **2008**, *108* (12), 1586–1594.
- (73) Angseryd, J.; Albu, M.; Andrén, H. O.; Kothleitner, G. *Micron* **2011**, *42* (6), 608–615.
- (74) Krivanek, O. L.; Ahn, C. C.; Keeney, R. B. *Ultramicroscopy* **1987**, *22* (1–4), 103–115.
- (75) Claus, G.; Colledani, C.; Deptuch, G.; Dulinski, W.; Gornushkin, Y.; Hu, Y.; Husson, D.; Orazi, G.; Turchetta, R.; Riester, J. L.; Winter, M. In *Nuclear Instruments and Methods in Physics Research, Section A: Accelerators, Spectrometers, Detectors and Associated Equipment*; North-Holland, 2001; Vol. 473, pp 83–85.

- (76) Turchetta, R.; Berst, J. D.; Casadei, B.; Claus, G.; Colledani, C.; Dulinski, W.; Hu, Y.; Husson, D.; Le Normand, J. P.; Riestler, J. L.; Deptuch, G.; Goerlach, U.; Higuieret, S.; Winter, M. *Nucl. Instruments Methods Phys. Res. Sect. A Accel. Spectrometers, Detect. Assoc. Equip.* **2001**, *458* (3), 677–689.
- (77) Rez, P.; Aoki, T.; March, K.; Gur, D.; Krivanek, O. L.; Dellby, N.; Lovejoy, T. C.; Wolf, S. G.; Cohen, H. *Nat. Commun.* **2016**, *7*, 10945.
- (78) Howie, A. *Ultramicroscopy* **2015**, *151*, 116–121.
- (79) Egerton, R. F.; Li, P.; Malac, M. *Micron* **2004**, *35* (6), 399–409.
- (80) Vasa, P.; Ropers, C.; Pomraenke, R.; Lienau, C. *Laser Photonics Rev.* **2009**, *3* (6), 483–507.
- (81) Chen, G.; Bonadeo, N. H.; Steel, D. G.; Gammon, D.; Katzer, D. S.; Park, D.; Sham, L. J. *Science (80-.)*. **2000**, *289* (5486), 1906–1909.
- (82) Ropers, C.; Park, D. J.; Stibenz, G.; Steinmeyer, G.; Kim, J.; Kim, D. S.; Lienau, C. *Phys. Rev. Lett.* **2005**, *94* (11), 113901.
- (83) Barwick, B.; Zewail, A. H. *ACS Photonics* **2015**, *2* (10), 1391–1402.
- (84) Carbone, F. *Chem. Phys. Lett.* **2010**, *496* (4–6), 291–295.
- (85) Carbone, F.; Kwon, O. H.; Zewail, A. H. *Science (80-.)*. **2009**, *325* (5937), 181–184.
- (86) Carbone, F.; Barwick, B.; Kwon, O. H.; Park, H. S.; Spencer Baskin, J.; Zewail, A. H. *Chem. Phys. Lett.* **2009**, *468* (4–6), 107–111.
- (87) García, J.; Abajo, M.; Kociak. *New J. Phys* **2008**, *10*.
- (88) Asenjo-Garcia, A.; García De Abajo, F. J. *New J. Phys.* **2013**, *15* (15).
- (89) Park, S. T.; Lin, M.; Zewail, A. H. *New J. Phys.* **2010**, *12* (12), 123028–123028.
- (90) Barwick, B.; Flannigan, D. J.; Zewail, A. H. *Nature* **2009**, *462*.
- (91) Garcia De Abajo, F. J.; Asenjo-Garcia, A.; Kociak, M. *Nano Lett.* **2010**, *10* (5), 1859–1863.
- (92) Park, S. T.; Zewail, A. H. *Phys. Rev. A - At. Mol. Opt. Phys.* **2014**, *89* (1), 013851.
- (93) García De Abajo, F. J. *Reviews of Modern Physics*. American Physical Society February 3, 2010, pp 209–275.

- (94) Radon, J. *Ber., Verch. Sach. Akad. Wiss.* **1917**, *69*, 262–277.
- (95) Midgley, P. A.; Weyland, M. *Ultramicroscopy* **2003**, *96* (3–4), 413–431.
- (96) Yedra, L.; Eljarrat, A.; Arenal, R.; López-Conesa, L.; Pellicer, E.; López-Ortega, A.; Estrader, M.; Sort, J.; Baró, M. D.; Estradé, S.; Peiró, F. *Analyst* **2016**, *141* (16), 4968–4972.
- (97) AlAfeef, A.; Bobynko, J.; Cockshott, W. P.; Craven, A. J.; Zuazo, I.; Barges, P.; MacLaren, I. *Ultramicroscopy* **2016**, *170*, 96–106.
- (98) Goris, B.; Turner, S.; Bals, S.; Tendeloo, G. Van; Van Tendeloo, G. *ACS Nano* **2014**, *8* (10), 10878–10884.
- (99) Arenal, R.; de la Peña, F.; Stéphan, O.; Walls, M.; Tencé, M.; Loiseau, A.; Colliex, C. *Ultramicroscopy* **2008**, *109* (1), 32–38.
- (100) Goris, B.; Meledina, M.; Turner, S.; Zhong, Z.; Batenburg, K. J.; Bals, S. *Ultramicroscopy* **2016**, *171*, 55–62.
- (101) Collins, S. M.; Fernandez-Garcia, S.; Calvino, J. J.; Midgley, P. A. *Sci. Rep.* **2017**, *7* (1), 5406.
- (102) de la Peña, F.; Berger, M.-H.; Hochepped, J.-F.; Dynys, F.; Stephan, O.; Walls, M. *Ultramicroscopy* **2011**, *111* (2), 169–176.
- (103) Suenaga, K.; Tencé, M.; Mory, C.; Colliex, C.; Kato, H.; Okazaki, T.; Shinohara, H.; Hirahara, K.; Bandow, S.; Iijima, S. *Science* (80-.). **2000**, *290* (5500), 2280–2282.
- (104) Suenaga, K.; Sato, Y.; Liu, Z.; Kataura, H.; Okazaki, T.; Kimoto, K.; Sawada, H.; Sasaki, T.; Omoto, K.; Tomita, T.; Kaneyama, T.; Kondo, Y. *Nat. Chem.* **2009**, *1* (5), 415–418.
- (105) Senga, R.; Suenaga, K. *Nat. Commun.* **2015**, *6*, 7943.
- (106) Arenal, R.; March, K.; Ewels, C. P.; Rocquefelte, X.; Kociak, M.; Loiseau, A.; Stéphan, O. *Nano Lett.* **2014**, *14* (10), 5509–5516.
- (107) Nicholls, R. J.; Murdock, A. T.; Tsang, J.; Britton, J.; Pennycook, T. J.; Koós, A.; Nellist, P. D.; Grobert, N.; Yates, J. R. *ACS Nano* **2013**, *7* (8), 7145–7150.
- (108) Susi, T.; Hardcastle, T. P.; Hofsäass, H.; Mittelberger, A.; Pennycook, T. J.; Mangler, C.; Drummond-Brydson, R.; Scott, A. J.; Meyer, J. C.; Kotakoski, J. *2D Mater.* **2017**, *4* (2), 021013.
- (109) Ramasse, Q. M.; Seabourne, C. R.; Kepaptsoglou, D.-M.; Zan, R.;

- Bangert, U.; Scott, A. J. *Nano Lett.* **2013**, *13* (10), 4989–4995.
- (110) Lin, Y. C.; Teng, P. Y.; Chiu, P. W.; Suenaga, K. *Phys. Rev. Lett.* **2015**, *115* (20).
- (111) García De Abajo, F. J.; Kociak, M. *Phys. Rev. Lett.* **2008**, *100* (10).
- (112) McPhedran, R. C.; Botten, L. C.; McOrist, J.; Asatryan, A. A.; de Sterke, C. M.; Nicorovici, N. A. *Phys. Rev. E - Stat. Physics, Plasmas, Fluids, Relat. Interdiscip. Top.* **2004**, *69* (1), 16.
- (113) Losquin, A.; Kociak, M. *ACS Photonics* **2015**, *2* (11), 1619–1627.
- (114) Losquin, A.; Zagonel, L. F.; Myroshnychenko, V.; Rodríguez-González, B.; Tencé, M.; Scarabelli, L.; Förstner, J.; Liz-Marzán, L. M.; García De Abajo, F. J.; Stéphane, O.; Kociak, M. *Nano Lett.* **2015**, *15* (2), 1229–1237.
- (115) Mirsaleh-Kohan, N.; Iberi, V.; Simmons, P. D.; Bigelow, N. W.; Vaschillo, A.; Rowland, M. M.; Best, M. D.; Pennycook, S. J.; Masiello, D. J.; Guiton, B. S.; Camden, J. P. *J. Phys. Chem. Lett.* **2012**, *3* (16), 2303–2309.
- (116) Cha, J. J.; Yu, Z.; Smith, E.; Couillard, M.; Fan, S.; Muller, D. A. *Phys. Rev. B - Condens. Matter Mater. Phys.* **2010**, *81* (11).
- (117) Haberfehlner, G.; Schmidt, F. P.; Schaffernak, G.; Hörl, A.; Trügler, A.; Hohenau, A.; Hofer, F.; Krenn, J. R.; Hohenester, U.; Kothleitner, G. *Nano Lett.* **2017**, *17* (11), 6773–6777.
- (118) Collins, S. M.; Ringe, E.; Duchamp, M.; Saghi, Z.; Dunin-Borkowski, R. E.; Midgley, P. A. *ACS Photonics* **2015**, *2* (11), 1628–1635.
- (119) Horl, A.; Haberfehlner, G.; Trugler, A.; Schmidt, F. P.; Hohenester, U.; Kothleitner, G. *Nat. Commun.* **2017**, *8* (1), 37.
- (120) Hörl, A.; Trügler, A.; Hohenester, U. *ACS Photonics* **2015**, *2* (10), 1429–1435.
- (121) Malinowski, E. R. *Factor analysis in chemistry*; Wiley, 2002.
- (122) Goetz, A. F. H.; Vane, G.; Solomon, J. E.; Rock, B. N. *Science (80-.)*. **1985**, *228* (4704), 1147–1153.
- (123) Beauchemin, S.; Hesterberg, D.; Beauchemin, M. *Soil Sci. Soc. Am. J.* **2002**, *66* (1), 83–91.
- (124) Horn, K. M.; Swartzentruber, B. S.; Osbourn, G. C.; Bouchard, A.; Bartholomew, J. W. *J. Appl. Phys.* **1998**, *84* (5), 2487–2496.
- (125) Bosman, M.; Watanabe, M.; Alexander, D. T. L.; Keast, V. J.

- Ultramicroscopy* **2006**, *106* (11–12 SPEC. ISS.), 1024–1032.
- (126) Bonnet, N.; Brun, N.; Colliex, C. *Ultramicroscopy* **1999**, *77* (3–4), 97–112.
- (127) Jolliffe, I. T. In *Principal component analysis*; Springer, New York, NY, 1986; pp 115–128.
- (128) Snyder Spencer, Martha L., Owings, Clyde L., Schneider, Lawrence W., R. G.; Snyder Spencer, Martha L., Owings, Clyde L., Schneider, Lawrence W., R. G. *SAE Tech. Pap.* **1975**.
- (129) de la Peña, F.; Burdet, P.; Ostasevicius, T.; Sarahan, M.; Nord, M.; Fauske, V. T.; Taillon, J.; Eljarrat, A.; Mazzucco, S.; Donval, G.; Zagonel, L. F.; Walls, M.; Iyengar, I. 2015.
- (130) Dobigeon, N.; Brun, N. *Ultramicroscopy* **2012**, *120*, 25–34.
- (131) Cueva, P.; Hovden, R.; Mundy, J. a; Xin, H. L.; Muller, D. a. *Microsc. Microanal.* **2012**, *18* (4), 667–675.
- (132) Torruella, P.; Arenal, R.; De La Peña, F.; Saghi, Z.; Yedra, L.; Eljarrat, A.; López-Conesa, L.; Estrader, M.; López-Ortega, A.; Salazar-Alvarez, G.; Nogués, J.; Ducati, C.; Midgley, P. A.; Peiró, F.; Estradé, S. *Nano Lett.* **2016**, *16* (8), 5068–5073.
- (133) Lichtert, S.; Verbeeck, J. *Ultramicroscopy* **2013**, *125*, 35–42.
- (134) Potapov, P. *Ultramicroscopy* **2016**, *160*, 197–212.
- (135) Spiegelberg, J.; Ruzs, J.; Thersleff, T.; Pelckmans, K. *Ultramicroscopy* **2017**, *174*, 14–26.
- (136) Bonnet, N. *Journal of Microscopy*. 1998, pp 2–18.
- (137) Bonnet, N.; Nuzillard, D. *Ultramicroscopy* **2005**, *102* (4), 327–337.
- (138) Li, G.; Rivarola, F. W. R.; Davis, N. J. L. K.; Bai, S.; Jellicoe, T. C.; De La Peña, F.; Hou, S.; Ducati, C.; Gao, F.; Friend, R. H.; Greenham, N. C.; Tan, Z. K. *Adv. Mater.* **2016**, *28* (18), 3528–3534.
- (139) Sanchez, A. M.; Beltran, A. M.; Beanland, R.; Ben, T.; Gass, M. H.; De La Peña, F.; Walls, M.; Taboada, A. G.; Ripalda, J. M.; Molina, S. I. *Nanotechnology* **2010**, *21* (14), 145606.
- (140) Genç, A.; Patarroyo, J.; Sancho-Parramon, J.; Arenal, R.; Duchamp, M.; Gonzalez, E. E.; Henrard, L.; Bastús, N. G.; Dunin-Borkowski, R. E.; Puentes, V. F.; Arbiol, J. *ACS Photonics* **2016**, *3* (5), 770–779.

- (141) Lee, D.; Seung, H. *Adv. Neural Inf. Process. Syst.* **2001**, No. 1, 556–562.
- (142) Nicoletti, O.; de la Peña, F.; Leary, R. K.; Holland, D. J.; Ducati, C.; Midgley, P. a. *Nature* **2013**, *502* (7469), 80–84.
- (143) Ringe, E.; Desantis, C. J.; Collins, S. M.; Duchamp, M.; Dunin-Borkowski, R. E.; Skrabalak, S. E.; Midgley, P. A. *Sci. Rep.* **2015**, *5*.
- (144) Oikonomakou, N.; Vazirgiannis, M. In *Data Mining and Knowledge Discovery Handbook*; Springer US: Boston, MA, 2009; pp 931–948.
- (145) Rokach, L. In *Data Mining and Knowledge Discovery Handbook*; Springer US: Boston, MA, 2009; pp 269–298.
- (146) Maimon, O.; Rokach, L. *Data mining and knowledge discovery handbook*; Springer, 2010.
- (147) Kaufman, L.; Rousseeuw, P. J. *Finding Groups in Data: An Introduction to Cluster Analysis*; Wiley Series in Probability and Statistics; John Wiley & Sons, Inc.: Hoboken, NJ, USA, 1990.
- (148) Salazar-Alvarez, G.; Lidbaum, H.; López-Ortega, A.; Estrader, M.; Leifer, K.; Sort, J.; Suriñach, S.; Baró, M. D.; Nogués, J. *J. Am. Chem. Soc.* **2011**, *133* (42), 16738–16741.
- (149) López-Ortega, A.; Estrader, M.; Salazar-Alvarez, G.; Estradé, S.; Golosovsky, I. V.; Dumas, R. K.; Keavney, D. J.; Vasilakaki, M.; Trohidou, K. N.; Sort, J.; Peiró, F.; Suriñach, S.; Baró, M. D.; Nogués, J. *Nanoscale* **2012**, *4* (16), 5138.
- (150) Estrader, M.; López-Ortega, A.; Estradé, S.; Golosovsky, I. V.; Salazar-Alvarez, G.; Vasilakaki, M.; Trohidou, K. N.; Varela, M.; Stanley, D. C.; Sinko, M.; Pechan, M. J.; Keavney, D. J.; Peiró, F.; Suriñach, S.; Baró, M. D.; Nogués, J. *Nat. Commun.* **2013**, *4*, 2960.
- (151) Yedra, L.; Xuriguera, E.; Estrader, M.; López-Ortega, A.; Baró, M. D.; Nogués, J.; Roldan, M.; Varela, M.; Estradé, S.; Peiró, F. *Microsc. Microanal.* **2014**, *20* (03), 698–705.
- (152) Varela, M.; Oxley, M. P.; Luo, W.; Tao, J.; Watanabe, M.; Lupini, a. R.; Pantelides, S. T.; Pennycook, S. J. *Phys. Rev. B - Condens. Matter Mater. Phys.* **2009**, *79* (8), 0851171-14.
- (153) Peña, F. de la; Ostasevicius, T.; Fauske, V. T.; Burdet, P.; Jokubauskas, P.; Nord, M.; Prestat, E.; Sarahan, M.; MacArthur, K. E.; Johnstone, D. N.; Taillon, J.; Caron, J.; Furnival, T.; Eljarrat, A.; Mazzucco, S.; Migunov, V.; Aarholt, T.; Walls, M.; Winkler, F.; Martineau, B.; Donval, G.; Hoglund, E.

- R.; Alxneit, I.; Hjorth, I.; Zagonel, L. F.; Garmannslund, A.; Gohlke, C.; Iyengar, I.; Chang, H.-W. **2017**.
- (154) Freestone, I.; Meeks, N.; Sax, M.; Higgitt, C. *Gold Bull.* **2007**, *40* (4), 270–277.
- (155) Espinosa, A.; Di Corato, R.; Kolosnjaj-Tabi, J.; Flaud, P.; Pellegrino, T.; Wilhelm, C. *ACS Nano* **2016**, *10* (2), 2436–2446.
- (156) He, W.; Ai, K.; Jiang, C.; Li, Y.; Song, X.; Lu, L. *Biomaterials* **2017**, *132*, 37–47.
- (157) Abadeer, N. S.; Murphy, C. J. *Journal of Physical Chemistry C*. American Chemical Society March 10, 2016, pp 4691–4716.
- (158) Akbayrak, S.; Tonbul, Y.; Özkar, S. *Appl. Catal. B Environ.* **2016**, *198*, 162–170.
- (159) Lu, J.; Zhou, W.; Wang, L.; Jia, J.; Ke, Y.; Yang, L.; Zhou, K.; Liu, X.; Tang, Z.; Li, L.; Chen, S. *ACS Catal.* **2016**, *6* (2), 1045–1053.
- (160) Sun, X.; Li, D.; Guo, S.; Zhu, W.; Sun, S. *Nanoscale* **2016**, *8* (5), 2626–2631.
- (161) Mazzola, L. *Nature Biotechnology*. Nature Publishing Group October 1, 2003, pp 1137–1143.
- (162) Sozer, N.; Kokini, J. L. *Trends in Biotechnology*. Elsevier Current Trends February 1, 2009, pp 82–89.
- (163) Popov, A. P.; Zvyagin, A. V.; Lademann, J.; Roberts, M. S.; Sanchez, W.; Priezzhev, A. V.; Myllylä, R. *Journal of Biomedical Nanotechnology*. October 1, 2010, pp 432–451.
- (164) Salazar-alvarez, G.; Sort, J.; Suriñach, S.; Baro, M. D.; Nogués, J. *J. Am. Chem. Soc.* **2007**, *129* (4), 9102–9108.
- (165) Seo, W. S.; Jo, H. H.; Lee, K.; Kim, B.; Oh, S. J.; Park, J. T. *Angew. Chem. Int. Ed. Engl.* **2004**, *43* (9), 1115–1117.
- (166) Lu, X.; Tuan, H.-Y.; Chen, J.; Li, Z.-Y.; Korgel, B. A.; Xia, Y. *J. Am. Chem. Soc.* **2007**, *129* (6), 1733–1742.
- (167) Huh, Y.; Jun, Y.; Song, H.; Kim, S.; Choi, J.; Lee, J.; Yoon, S.; Kim, K.; Shin, J.; Suh, J.; Cheon, J. *Jacs* **2005**, *127* (11), 12387–12391.
- (168) López-Ortega, A.; Estrader, M.; Salazar-Alvarez, G.; Roca, A. G.; Nogués, J. *Phys. Rep.* **2015**, *553*, 1–32.

- (169) Zhao, Z.; Zhou, Z.; Bao, J.; Wang, Z.; Hu, J.; Chi, X.; Ni, K.; Wang, R.; Chen, X.; Chen, Z.; Gao, J. *Nat. Commun.* **2013**, *4*, 2266.
- (170) Amstad, E.; Kohlbrecher, J.; Müller, E.; Schweizer, T.; Textor, M.; Reimhult, E. *Nano Lett.* **2011**, *11* (4), 1664–1670.
- (171) Hergt, R.; Dutz, S.; Müller, R.; Zeisberger, M. *J. Phys. Condens. Matter* **2006**.
- (172) Bixner, O.; Reimhult, E. *J. Colloid Interface Sci.* **2016**, *466*, 62–71.
- (173) Smolensky, E. D.; Park, H. E.; Berqu?, T. S.; Pierre, V. C. *Contrast Media Mol. Imaging* **2010**, No. July 2010, n/a-n/a.
- (174) Ling, D.; Hyeon, T. *Small* **2013**, *9* (9–10), 1450–1466.
- (175) Kim, T.; Hyeon, T. *Nanotechnology* **2014**, *25* (1), 012001.
- (176) Lee, N.; Yoo, D.; Ling, D.; Cho, M. H.; Hyeon, T.; Cheon, J. *Chem. Rev.* **2015**, *115* (19), 10637–10689.
- (177) Li, F.; Lu, J.; Kong, X.; Hyeon, T.; Ling, D. *Adv. Mater.* **2017**, *29* (14), 1605897.
- (178) Santra, S.; Tapeç, R.; Theodoropoulou, N.; Dobson, J.; Hebard, A.; Tan, W. *Langmuir* **2001**, *17* (10), 2900–2906.
- (179) Kertmen, A.; Torruella, P.; Coy, E.; Yate, L.; Nowaczyk, G.; Gapiński, J.; Vogt, C.; Toprak, M.; Estradé, S.; Peiró, F.; Milewski, S.; Jurga, S.; Andruszkiewicz, R. *Langmuir* **2017**, *33* (39), 10351–10365.
- (180) Park, J.; An, K.; Hwang, Y.; Park, J.-G.; Noh, H.-J.; Kim, J.-Y.; Park, J.-H.; Hwang, N.-M.; Hyeon, T. *Nat. Mater.* **2004**, *3* (12), 891–895.
- (181) Qiu, P.; Jensen, C.; Charity, N.; Towner, R.; Mao, C. *J. Am. Chem. Soc.* **2010**, *132* (50), 17724–17732.
- (182) Otero, V.; Sanches, D.; Montagner, C.; Vilarigues, M.; Carlyle, L.; Lopes, J. A.; Melo, M. J. *J. Raman Spectrosc.* **2014**, *45* (11–12), 1197–1206.
- (183) Tan, H.; Verbeeck, J.; Abakumov, A.; Van Tendeloo, G. *Ultramicroscopy* **2012**, *116*, 24–33.
- (184) Ewels, P.; Sikora, T.; Serin, V.; Ewels, C. P.; Lajaunie, L. *Microsc. Microanal.* **2016**, *22*, 717–724.
- (185) Chamritski, I.; Burns, G. *J. Phys. Chem. B* **2005**, *109* (11), 4965–4968.
- (186) Yan, S.; Zhang, L.; Tang, Y.; Lv, Y. *Analyst* **2014**, *139* (17), 4210.

- (187) Dong, B.; Li, C.; Chen, G.; Zhang, Y.; Zhang, Y.; Deng, M.; Wang, Q. *Chem. Mater.* **2013**, *25* (12), 2503–2509.
- (188) Zhu, C. N.; Jiang, P.; Zhang, Z. L.; Zhu, D. L.; Tian, Z. Q.; Pang, D. W. *ACS Appl. Mater. Interfaces* **2013**, *5* (4), 1186–1189.
- (189) Yarema, M.; Pichler, S.; Sytnyk, M.; Seyrkammer, R.; Lechner, R. T.; Fritz-Popovski, G.; Jarzab, D.; Szendrei, K.; Resel, R.; Korovyanko, O.; Loi, M. A.; Paris, O.; Hesser, G.; Heiss, W. *ACS Nano* **2011**, *5* (5), 3758–3765.
- (190) Jang, J.; Pan, F.; Braam, K.; Subramanian, V. *Adv. Mater.* **2012**, *24* (26), 3573–3576.
- (191) Husmann, A.; Betts, J. B.; Boebinger, G. S.; Migliori, A.; Rosenbaum, T. F.; Saboungi, M. L. *Nature* **2002**, *417* (6887), 421–424.
- (192) Sun, Y.; Fang, H.; Pan, L.; Han, M.; Xu, S.; Wang, X.; Xu, B.; Wu, Y. *Nano Lett.* **2015**, *15* (6), 3748–3756.
- (193) Cadavid, D.; Ibáñez, M.; Shavel, A.; Durá, O. J.; López de la Torre, M. A.; Cabot, A. *J. Mater. Chem. A* **2013**, *1* (15), 4864.
- (194) Day, T.; Drymiotis, F.; Zhang, T.; Rhodes, D.; Shi, X.; Chen, L.; Snyder, G. *J. J. Mater. Chem. C* **2013**, *1* (45).
- (195) Ferhat, M.; Nagao, J. *J. Appl. Phys.* **2000**, *88* (2), 813–816.
- (196) Conn, J. B.; Taylor, R. C. *J. Electrochem. Soc.* **1960**, *107* (12), 977–982.
- (197) Shi, W.; Zeng, H.; Sahoo, Y.; Ohulchanskyy, T. Y.; Ding, Y.; Wang, Z. L.; Swihart, M.; Prasad, P. N. *Nano Lett.* **2006**, *6* (4), 875–881.
- (198) Prusty, G.; Guria, A. K.; Mondal, I.; Dutta, A.; Pal, U.; Pradhan, N. *Angew. Chemie* **2016**, *713209* (8), 2755–2758.
- (199) Costi, R.; Saunders, A. E.; Banin, U. *Angewandte Chemie - International Edition*. Wiley-Blackwell June 11, 2010, pp 4878–4897.
- (200) Mokari, T.; Rothenberg, E.; Popov, I.; Costi, R.; Banin, U. *Science (80-.)*. **2004**, *304* (5678), 1787–1790.
- (201) Xiao, C.; Xu, J.; Li, K.; Feng, J.; Yang, J.; Xie, Y. *J. Am. Chem. Soc.* **2012**, *134* (9), 4287–4293.
- (202) Han, C.; Sun, Q.; Cheng, Z. X.; Wang, J. L.; Li, Z.; Lu, G. Q.; Dou, S. X. *J. Am. Chem. Soc.* **2014**, *136* (50), 17626–17633.
- (203) Ishiwata, S.; Shiomi, Y.; Lee, J. S.; Bahramy, M. S.; Suzuki, T.; Uchida, M.; Arita, R.; Taguchi, Y.; Tokura, Y. *Nat. Mater.* **2013**, *12* (6), 512–517.

- (204) Xiao, C.; Xu, J.; Cao, B.; Li, K.; Kong, M.; Xie, Y. *J. Am. Chem. Soc.* **2012**, *134* (18), 7971–7977.
- (205) Guin, S. N.; Chatterjee, A.; Negi, D. S.; Datta, R.; Biswas, K. **2013**, *6* (9).
- (206) Seryotkin, Y. V.; Bakakin, V. V.; Pal'yanova, G. A.; Kokh, K. A. *CrystEngComm* **2014**, *16* (9), 1675.
- (207) Seryotkin, Y. V.; Bakakin, V. V.; Palyanova, G. A.; Kokh, K. A. *Cryst. Growth Des.* **2011**, *11* (4), 1062–1066.
- (208) Gou, X.; Cheng, F.; Shi, Y.; Zhang, L.; Peng, S.; Chen, J.; Shen, P. *J. Am. Chem. Soc.* **2006**, *128* (22), 7222–7229.
- (209) Son, D. H. D. H. D. H.; Hughes, S. M. S. M.; Yin, Y.; Alivisatos, P. A.; Paul Alivisatos, a. *Science* **2004**, *306* (5698), 1009–1012.
- (210) Feng, S.; Xu, R. *Acc. Chem. Res.* **2001**, *34* (3), 239–247.
- (211) Schaak, R. E.; Mallouk, T. E. *Chemistry of Materials*. American Chemical Society 2002, pp 1455–1471.
- (212) Yang, J.; Sargent, E. H.; Kelley, S. O.; Ying, J. Y. *Nat. Mater.* **2009**, *8* (8), 683–689.
- (213) Gupta, S.; Kershaw, S. V.; Rogach, A. L. *Advanced Materials*. 2013, pp 6923–6944.
- (214) Aldakov, D.; Lefrançois, A.; Reiss, P. *J. Mater. Chem. C* **2013**, *1* (24), 3756–3776.
- (215) Akkerman, Q. A.; Genovese, A.; George, C.; Prato, M.; Moreels, I.; Casu, A.; Marras, S.; Curcio, A.; Scarpellini, A.; Pellegrino, T.; Manna, L.; Lesnyak, V. *ACS Nano* **2015**, *9* (1), 521–531.
- (216) Tan, J. M. R.; Scott, M. C.; Hao, W.; Baikie, T.; Nelson, C. T.; Pedireddy, S.; Tao, R.; Ling, X.; Magdassi, S.; White, T.; Li, S.; Minor, A. M.; Zheng, H.; Wong, L. H. *Chem. Mater.* **2017**, *29* (21), 9192–9199.
- (217) Van der Stam, W.; Geuchies, J. J.; Altantzis, T.; Van Den Bos, K. H. W.; Meeldijk, J. D.; Van Aert, S.; Bals, S.; Vanmaekelbergh, D.; De Mello Donega, C. *J. Am. Chem. Soc.* **2017**, *139* (11), 4087–4097.
- (218) Robinson, R. D.; Sadtler, B.; Demchenko, D. O.; Erdonmez, C. K.; Wang, L. W.; Alivisatos, A. P. *Science (80-)*. **2007**, *317* (5836), 355–358.
- (219) Luther, J. M.; Zheng, H.; Sadtler, B.; Alivisatos, A. P. *J. Am. Chem. Soc.* **2009**, *131* (46), 16851–16857.

- (220) Li, H.; Zanella, M.; Genovese, A.; Povia, M.; Falqui, A.; Giannini, C.; Manna, L. *Nano Lett.* **2011**, *11* (11), 4964–4970.
- (221) Bothe, C.; Kornowski, A.; Tornatzky, H.; Schmidtke, C.; Lange, H.; Maultzsch, J.; Weller, H. *Angew. Chemie - Int. Ed.* **2015**, *54* (47), 14183–14186.
- (222) White, S. L.; Smith, J. G.; Behl, M.; Jain, P. K. *Nat. Commun.* **2013**, *4* (1), 2933.
- (223) Casavola, M.; Van Huis, M. A.; Bals, S.; Lambert, K.; Hens, Z.; Vanmaekelbergh, D. *Chem. Mater.* **2012**, *24* (2), 294–302.
- (224) Miszta, K.; Gariano, G.; Brescia, R.; Marras, S.; De Donato, F.; Ghosh, S.; De Trizio, L.; Manna, L. *J. Am. Chem. Soc.* **2015**, *137* (38), 12195–12198.
- (225) Tu, R.; Xie, Y.; Bertoni, G.; Lak, A.; Gaspari, R.; Rapallo, A.; Cavalli, A.; Trizio, L. De; Manna, L. *J. Am. Chem. Soc.* **2016**, *138* (22), 7082–7090.
- (226) De Trizio, L.; Li, H.; Casu, A.; Genovese, A.; Sathya, A.; Messina, G. C.; Manna, L. *J. Am. Chem. Soc.* **2014**, *136* (46), 16277–16284.
- (227) De Trizio, L.; Manna, L. *Chem. Rev.* **2016**, *116* (18), 10852–10887.
- (228) Kundu, S.; Kundu, P.; Van Tendeloo, G.; Ravishankar, N. *Small* **2014**, *10* (19), 3895–3900.
- (229) Sahu, A.; Khare, A.; Deng, D. D.; Norris, D. J. *Chem. Commun.* **2012**, *48* (44), 5458.
- (230) Kirkland, E. *Advanced Computing in Electron Microscopy*; Springer, 2010; Vol. 40.
- (231) Dalmases, M.; Ibáñez, M.; Torruella, P.; Fernández-Altable, V.; López-Conesa, L.; Cadavid, D.; Piveteau, L.; Nachttegaal, M.; Llorca, J.; Ruiz-González, M. L.; Estradé, S.; Peiró, F.; Kovalenko, M. V.; Cabot, A.; Figuerola, A. *Chem. Mater.* **2016**, *28*, 7017–7028.
- (232) Klug, H. P.; Alexander, L. E. *X-ray Diffraction Procedures for Polycrystalline and Amorphous Materials*, 2nd ed.; John Wiley & Sons, Inc.: New York, 1974.
- (233) Cullity, B. D.; Stock, S. R. *Elements of X-Ray Diffraction*, 3rd ed.; Prentice-Hall Inc.: New York, 2001.
- (234) Newman, J. D. S.; Blanchard, G. J. *Langmuir* **2006**, *22* (13), 5882–5887.
- (235) Frueh, A. *J. Am. Mineral.* **1961**, *46*, 654–660.

- (236) Sadanaga, R.; Sueno, S. *Mineral. J.* **1967**, *5* (2), 124–148.
- (237) Grozdanov, I. *Appl. Surf. Sci.* **1995**, *84* (3), 325–329.
- (238) Jang, K.; Kim, S. Y.; Park, K. H.; Jang, E.; Jun, S.; Son, S. U. *Chem. Commun.* **2007**, *0* (43).
- (239) Yang, J.; Ying, J. Y. *Chem. Commun.* **2009**, *1* (22), 3187.
- (240) Yang, J.; Ying, J. Y. *Angew. Chemie - Int. Ed.* **2011**, *50* (20), 4637–4643.
- (241) Yang, J.; Ying, J. Y. *J. Am. Chem. Soc.* **2010**, *132* (7), 2114–2115.
- (242) Liu, M.; Zeng, H. C. *Langmuir* **2014**, *30* (32), 9838–9849.
- (243) Li, X.; Schaak, R. E. *Chem. Mater.* **2017**, *29* (9), 4153–4160.
- (244) Morris, T.; Copeland, H.; Szulczewski, G. *Langmuir* **2002**, *18* (2), 535–539.
- (245) Son, D. H.; Hughes, S. M.; Yin, Y.; Alivisatos, P. A. *Science (80-.)*. **2004**, *306* (5698), 1009–1012.
- (246) Bastús, N. G.; Gonzalez, E.; Esteve, J.; Piella, J.; Patarroyo, J.; Merkoçi, F.; Puentes, V. *Zeitschrift für Phys. Chemie* **2015**, *229* (1–2), 65–83.
- (247) Koo, B.; Xiong, H.; Slater, M. D.; Prakapenka, V. B.; Balasubramanian, M.; Podsiadlo, P.; Johnson, C. S.; Rajh, T.; Shevchenko, E. V. *Nano Lett.* **2012**, *12* (5), 2429–2435.
- (248) Ying, J. Y. *Chem. Eng. Sci.* **2006**, *61* (5), 1540–1548.
- (249) Shin, J.; Anisur, R. M.; Ko, M. K.; Im, G. H.; Lee, J. H.; Lee, I. S. *Angew. Chem. Int. Ed. Engl.* **2009**, *48* (2), 321–324.
- (250) An, K.; Hyeon, T. *Nano Today* **2009**, *4* (4), 359–373.
- (251) Anderson, B. D.; Tracy, J. B. *Nanoscale* **2014**, *6* (21), 12195–12216.
- (252) González, E.; Arbiol, J.; Puentes, V. F. *Science (80-.)*. **2011**, *334*, 1377–1380.
- (253) An, K.; Kwon, S. G.; Park, M.; Na, H. Bin; Baik, S.-I.; Yu, J. H.; Kim, D.; Son, J. S.; Kim, Y. W.; Song, I. C.; Moon, W. K.; Park, H. M.; Hyeon, T. *Nano Lett.* **2008**, *8* (12), 4252–4258.
- (254) Wang, C.; Baer, D. R.; Amonette, J. E.; Engelhard, M. H.; Antony, J.; Qiang, Y. *J. Am. Chem. Soc.* **2009**, *131* (25), 8824–8832.
- (255) Oh, M. H.; Yu, T.; Yu, S.-H.; Lim, B.; Ko, K.-T.; Willinger, M.-G.; Seo, D.-H.;

- Kim, B. H.; Cho, M. G.; Park, J.-H.; Kang, K.; Sung, Y.-E.; Pinna, N.; Hyeon, T. *Science* **2013**, *340* (6135), 964–968.
- (256) Estrader, M.; López-Ortega, A.; Golosovsky, I. V.; Estradé, S.; Roca, A. G.; Salazar-Alvarez, G.; López-Conesa, L.; Tobia, D.; Winkler, E.; Ardisson, J. D.; Macedo, W. a. a.; Morphis, A.; Vasilakaki, M.; Trohidou, K. N.; Gukasov, A.; Mirebeau, I.; Makarova, O. L.; Zysler, R. D.; Peiró, F.; Baró, M. D.; Bergström, L.; Nogués, J. *Nanoscale* **2015**, *7* (7), 3002–3015.
- (257) Bronstein, L. M.; Huang, X.; Retrum, J.; Schmucker, A.; Pink, M.; Stein, B. D.; Dregnea, B. *Chem. Mater.* **2007**, *19* (15), 3624–3632.
- (258) Lottini, E.; López-Ortega, A.; Bertoni, G.; Turner, S.; Meledina, M.; Van Tendeloo, G.; de Julián Fernández, C.; Sangregorio, C.; One-pot synthesis of strongly exchange coupled CoreShell nanoparticles with high magnetic anisotropy. *Submitted*.
- (259) Zhang, K.; Han, X.; Hu, Z.; Zhang, X.; Tao, Z.; Chen, J. *Chem. Soc. Rev.* **2015**, *44* (3), 699–728.
- (260) Gawande, M. B.; Goswami, A.; Felpin, F. X.; Asefa, T.; Huang, X.; Silva, R.; Zou, X.; Zboril, R.; Varma, R. S. *Chem. Rev.* **2016**, *116* (6), 3722–3811.
- (261) Reddy, D. H. K.; Yun, Y. S. *Coord. Chem. Rev.* **2016**, *315*, 90–111.
- (262) Lima-Tenório, M. K.; Tenório-Neto, E. T.; Hechenleitner, A. A. W.; Fessi, H.; Pineda, E. A. G. *J. Colloid Sci. Biotechnol.* **2016**, *5* (1), 45–54.
- (263) Naoi, K.; Naoi, W.; Aoyagi, S.; Miyamoto, J. I.; Kamino, T. *Acc. Chem. Res.* **2013**, *46* (5), 1075–1083.
- (264) Sanna Angotzi, M.; Musinu, A.; Mamei, V.; Ardu, A.; Cara, C.; Niznansky, D.; Xin, H. L.; Cannas, C. *ACS Nano* **2017**, *11* (8), 7889–7900.
- (265) Song, Q.; Zhang, Z. *J. Am. Chem. Soc.* **2012**, *134* (24), 10182–10190.
- (266) Lee, J. H.; Jang, J. T.; Choi, J. S.; Moon, S. H.; Noh, S. H.; Kim, J. W.; Kim, J. G.; Kim, I. S.; Park, K. I.; Cheon, J. *Nat. Nanotechnol.* **2011**, *6* (7), 418–422.
- (267) Anil Kumar, P.; Ray, S.; Chakraverty, S.; Sarma, D. D. *Appl. Phys. Lett.* **2013**, *103* (10), 102406.
- (268) Perumbilavil, S.; López-Ortega, A.; Tiwari, G. K.; Nogués, J.; Endo, T.; Philip, R. *Small* **2018**, *14* (6), 1701001.
- (269) Hu, H.; Guan, B.; Xia, B.; Lou, X. W. *J. Am. Chem. Soc.* **2015**, *137* (16), 5590–5595.

- (270) Sickafus, K. E.; Wills, J. M.; Grimes, N. W. *J. Am. Ceram. Soc.* **2004**, *82* (12), 3279–3292.
- (271) O’Quinn, E. C.; Shamblin, J.; Perlov, B.; Ewing, R. C.; Neufeind, J.; Feygenson, M.; Gussev, I.; Lang, M. *J. Am. Chem. Soc.* **2017**, *139* (30), 10395–10402.
- (272) Tielens, F.; Calatayud, M.; Franco, R.; Recio, J. M.; Pérez-Ramírez; Minot, C. *J. Phys. Chem. B* **2006**, *110* (2), 988–995.
- (273) Ndione, P. F.; Shi, Y.; Stevanovic, V.; Lany, S.; Zakutayev, A.; Parilla, P. A.; Perkins, J. D.; Berry, J. J.; Ginley, D. S.; Toney, M. F. *Adv. Funct. Mater.* **2014**, *24* (5), 610–618.
- (274) Chiang, Y. M.; Wang, H.; Jang, Y. I. *Chem. Mater.* **2001**, *13* (1), 53–63.
- (275) Muche, D. N. F.; Marple, M. A. T.; Hung, I.; Gan, Z.; Castro, R. H. R.; Sen, S. *J. Phys. Chem. C* **2017**, *121* (25), 13898–13905.
- (276) Yang, A.; Chinnasamy, C. N.; Greneche, J. M.; Chen, Y.; Yoon, S. D.; Chen, Z.; Hsu, K.; Cai, Z.; Ziemer, K.; Vittoria, C.; Harris, V. G. *Nanotechnology* **2009**, *20* (18), 185704.
- (277) Lüders, U.; Barthélémy, A.; Bibes, M.; Bouzouane, K.; Fusil, S.; Jacquet, E.; Contour, J. P.; Bobo, J. F.; Fontcuberta, J.; Fert, A. *Adv. Mater.* **2006**, *18* (13), 1733–1736.
- (278) Lin, C. C.; Tsai, Y. T.; Johnston, H. E.; Fang, M. H.; Yu, F.; Zhou, W.; Whitfield, P.; Li, Y.; Wang, J.; Liu, R. S.; Attfield, J. P. *J. Am. Chem. Soc.* **2017**, *139* (34), 11766–11770.
- (279) Veal, T. D.; Feldberg, N.; Quackenbush, N. F.; Linhart, W. M.; Scanlon, D. O.; Piper, L. F. J.; Durbin, S. M. *Adv. Energy Mater.* **2015**, *5* (24), 1501462.
- (280) Greenwald, S.; Pickart, S. J.; Grannis, F. H. *J. Chem. Phys.* **1954**, *22* (9), 1597.
- (281) Gobbi, G. C.; Christoffersen, R.; Otten, M. T.; Miner, B.; Buseck, P. R.; Kennedy, G. J.; Fyfe, C. A. *Chem. Lett.* **1985**, *14* (6), 771–774.
- (282) Armstrong, A. R.; Dupre, N.; Paterson, A. J.; Grey, C. P.; Bruce, P. G. *Chem. Mater.* **2004**, *16* (16), 3106–3118.
- (283) Martins, F. H.; Silva, F. G.; Paula, F. L. O.; de A. Gomes, J.; Aquino, R.; Mestnik-Filho, J.; Bonville, P.; Porcher, F.; Perzynski, R.; Depeyrot, J. *J. Phys. Chem. C* **2017**, *121* (16), 8982–8991.

- (284) López-Ortega, A.; Roca, A. G.; Torruella, P.; Petrecca, M.; Estradé, S.; Peiró, F.; Puntès, V.; Nogués, J. *Chem. Mater.* **2016**, *28* (21), 8025–8031.
- (285) Tan, H.; Turner, S.; Yücelen, E.; Verbeeck, J.; Van Tendeloo, G. *Phys. Rev. Lett.* **2011**, *107* (10), 107602.
- (286) Chardon, B.; Vigneron, F. *J. Magn. Magn. Mater.* **1986**, *58* (1–2), 128–134.
- (287) El Mendili, Y.; Abdelouas, A.; Bardeau, J.-F. *Phys. Chem. Chem. Phys.* **2013**, *15* (23), 9197–9204.
- (288) Estradé, S.; Yedra, L.; López-Ortega, A.; Estrader, M.; Salazar-Alvarez, G.; Baró, M. D.; Nogués, J.; Peiró, F. *Micron* **2012**, *43* (1), 30–36.
- (289) Laffont, L.; Gibot, P. *Mater. Charact.* **2010**, *61* (11), 1268–1273.
- (290) Van Aken, P. a; Liebscher, B.; Styrsa, V. *J. Phys. Chem. Miner.* **1998**, *25* (5), 323–327.
- (291) Yang, A.; Chen, Z.; Zuo, X.; Arena, D.; Kirkland, J.; Vittoria, C.; Harris, V. *G. Appl. Phys. Lett.* **2005**, *86* (25), 1–3.
- (292) Lelis, M. F. F.; Porto, A. O.; Gonçalves, C. M.; Fabris, J. D. *J. Magn. Magn. Mater.* **2004**, *278* (1–2), 263–269.
- (293) Carta, D.; Casula, M. F.; Falqui, A.; Loche, D.; Mountjoy, G.; Sangregorio, C.; Corrias, A. *J. Phys. Chem. C* **2009**, *113* (20), 8606–8615.
- (294) Shiga, M.; Tatsumi, K.; Muto, S.; Tsuda, K.; Yamamoto, Y.; Mori, T.; Tanji, T. *Ultramicroscopy* **2016**, *170*, 43–59.
- (295) Gholizadeh, A. *J. Am. Ceram. Soc.* **2017**, *100* (8), 3577–3588.
- (296) Daou, T. J.; Pourroy, G.; Bégin-Colin, S.; Grenèche, J. M.; Ulhaq-Bouillet, C.; Legaré, P.; Bernhardt, P.; Leuvre, C.; Rogez, G. *Chem. Mater.* **2006**, *18* (18), 4399–4404.
- (297) Yuan, J.; Menon, N. K. *J. Appl. Phys.* **1998**, *81* (8), 5087.
- (298) Hoppe, W.; Langer, R.; Knesch, G.; Poppe, C. *Naturwissenschaften* **1968**, *55* (7), 333–336.
- (299) Gilbert, P. *J. Theor. Biol.* **1972**, *36* (1), 105–117.
- (300) Batenburg, K. J.; Bals, S.; Sijbers, J.; Kübel, C.; Midgley, P. A.; Hernandez, J. C.; Kaiser, U.; Encina, E. R.; Coronado, E. A.; Van Tendeloo, G. *Ultramicroscopy* **2009**, *109* (6), 730–740.

- (301) Leary, R.; Saghi, Z.; Midgley, P. A.; Holland, D. J. *Ultramicroscopy* **2013**, *131*, 70–91.
- (302) Saghi, Z.; Holland, D. J.; Leary, R.; Falqui, A.; Bertoni, G.; Sederman, A. J.; Gladden, L. F.; Midgley, P. a. *Nano Lett.* **2011**, *11* (11), 4666–4673.
- (303) Leary, R.; Leary; Rowan. In *European Microscopy Congress 2016: Proceedings*; Wiley-VCH Verlag GmbH & Co. KGaA: Weinheim, Germany, 2016; pp 3–4.
- (304) Haberfehlner, G.; Orthacker, A.; Albu, M.; Li, J.; Kothleitner, G. *Nanoscale* **2014**, *6* (23), 14563–14569.
- (305) Jolliffe, I. *Principal Component Analysis*; Balakrishnan, N., Colton, T., Everitt, B., Piegorsch, W., Ruggeri, F., Teugels, J. L., Eds.; John Wiley & Sons, Ltd: Chichester, UK, 2014.
- (306) Hyvärinen, A.; Karhunen, J.; Oja, E. *Independent Component Analysis*; John Wiley & Sons, 2004.
- (307) Smigelskas, A.; Kirkendall, E. *Clasa E Met. Technol.* **1946**, *XIII*, 2071.
- (308) Yin, Y.; Rioux, R. M.; Erdonmez, C. K.; Hughes, S.; Somorjal, G. A.; Alivisatos, A. P. *Science (80-.)*. **2004**, *304* (5671), 711–714.
- (309) Fontaíña-Troitiño, N.; Liébana-Viñas, S.; Rodríguez-González, B.; Li, Z. A.; Spasova, M.; Farle, M.; Salgueiriño, V. *Nano Lett.* **2014**, *14* (2), 640–647.
- (310) Li, Z. A.; Fontaíña-Troitiño, N.; Kovács, A.; Liébana-Viñas, S.; Spasova, M.; Dunin-Borkowski, R. E.; Müller, M.; Doennig, D.; Pentcheva, R.; Farle, M.; Salgueiriño, V. *Sci. Rep.* **2015**, *5*.
- (311) Troitiño, N. F.; Rivas-Murias, B.; Rodríguez-González, B.; Salgueiriño, V. *Chem. Mater.* **2014**, *26* (19), 5566–5575.
- (312) Vasilakaki, M.; Trohidou, K. N.; Nogués, J. *Sci. Rep.* **2015**, *5*, 9609.
- (313) Deepak, F. L.; Mayoral, A.; Arenal, R. *Advanced Transmission Electron Microscopy: Applications to Nanomaterials*; Deepak, F. L., Mayoral, A., Arenal, R., Eds.; Springer International Publishing, 2015.
- (314) Keenan, M. R.; Kotula, P. G. *Surf. Interface Anal.* **2004**, *36* (3), 203–212.
- (315) Hyvärinen, A. *IEEE Trans. neural networks* **1999**, *10* (3), 626–634.
- (316) Pedregosa, F.; Varoquaux, G.; Gramfort, A.; Michel, V.; Thirion, B.; Grisel, O.; Blondel, M.; Prettenhofer, P.; Weiss, R.; Dubourg, V.;

- Vanderplas, J.; Passos, A.; Cournapeau, D.; Brucher, M.; Perrot, M.; Duchesnay, É. *J. Mach. Learn. Res.* **2011**, *12* (Oct), 2825–2830.
- (317) Garvie, L. a J.; Buseck, P. R. *Nature* **1998**, *396* (December), 667–670.
- (318) Thomas, J. M.; Leary, R.; Midgley, P. A.; Holland, D. J. *J. Colloid Interface Sci.* **2013**, *392*, 7–14.
- (319) Richter, D.; Basse-Lüsebrink, T. C.; Kampf, T.; Fischer, A.; Israel, I.; Schneider, M.; Jakob, P. M.; Samnick, S. *Z. Med. Phys.* **2014**, *24* (1), 16–26.
- (320) Lustig, M.; Donoho, D.; Pauly, J. M. *Magn. Reson. Med.* **2007**, *58* (6), 1182–1195.
- (321) Davenport, M. a; Duarte, M. F.; Eldar, Y. C. Y.; Kutyniok, G. In *Compressed Sensing: Theory and Applications*; 2011; pp 1–68.
- (322) Nogués, J.; Sort, J.; Langlais, V.; Skumryev, V.; Suriñach, S.; Muñoz, J. S.; Baró, M. D. *Phys. Rep.* **2005**, *422* (3), 65–117.

Appendix A: Instrumentation list

The following is a list of all the equipment that has been used at one point to produce data for the present thesis.

@ CCIT – Universitat de Barcelona:

- Jeol JEM 2100, operating at 200 kV, equipped with a Oxford Instruments EDX system and bright field/dark field STEM detectors.
- Jeol JEM 2010F, operating at 200 kV, equipped with a Gatan GIF EELS detector and bright field/dark field STEM detectors. A Fischione tomography holder was used in this TEM.

@ ICN2:

- FEI Tecnai G² F20, operating at 80 kV-200 kV, equipped with a Gatan Quantum GIF EELS detector and bright field/dark field STEM detectors.

@ Ecole CentraleSupélec:

- Probe corrected FEI Titan3 operating at 200 kV, equipped with an X-FEG source, a Bruker EDX analyser and bright field/dark field STEM detectors.

@ CNME – Universidad complutense de Madrid:

- Probe corrected Jeol JEM ARM200cF operating at 80-200 kV, equipped with a Gatan Quantum GIF EELS detector and bright field/dark field STEM detectors. A Gatan double tilt cryo-holder (model 636) was used in this TEM.

@ CNBM – Adam Mickiewicz university:

- Probe corrected Jeol JEM ARM200F operating at 80-200 kV, equipped with a Gatan Quantum GIF EELS detector, Jeol EDX detector and bright field/dark field STEM detectors. A Fischione tomography holder was used in this TEM.

@ LMA – Instituto de Nanociencias de Aragón:

- Probe Corrected, monochromated FEI TITAN Low-base, operating at 80kV and equipped with a Gatan Tridiem 866 EELS spectrometer, an

EDAX EDX detector and bright field/dark field STEM detectors. A Fischione tomography holder was used in this TEM.

Appendix B: Collaborations

Much of the work presented in this thesis has been carried out with the help of and in collaboration with other researchers. The aim of this section is to acknowledge their contribution to the presented results.

The study presented in chapter 3.1 was developed in collaboration with Ahmet Kertmen, Slawomir Milewsky and Dr. Ryszard Andruszkiewicz from the Gdansk University of Technology; Dr. Emerson Coy, Dr. Grzegorz Nowaczyk, Jacek Gapiński and Prof. Stefan Jurga from the NanoBioMedical Centre at Adam Mickiewicz University; Dr. Carmen Vogt and Prof. Muhammet Toprak from the KTH-Royal Institute of Technology in Stockholm, and Dr. Luis Yate from CIC biomaGUNE center at San Sebastián. The synthesis, Raman spectroscopy and cryo-TEM measurements were performed by these collaborators.

The study presented in chapter 3.2 was performed in collaboration with colleagues from Universitat de Barcelona. The synthesis of the ternary systems and the initial assessment of the obtained NPs crystalline phases through x-ray diffraction was carried out by Mariona Dalmases and Dr. Albert Figuerola from the Functional Molecules and Magnetism Group (GMMF) in the Inorganic Chemistry Department of University of Barcelona.

In chapter 4, the synthesis of all NPs was carried out by collaborators Dr. Alberto López-Ortega, Università degli Studi di Firenze, and Dr. Alejandro G. Roca and Prof. Josep Nogués from the Catalan Institute of Nanoscience and Nanotechnology (ICN2). They also contributed by performing X-ray diffraction measurements (presented in the first half of the chapter) and X-ray Absorption Spectroscopy measurements (presented in the second half). The same group must be credited with the synthesis of the nanocubes in chapter 5.2.

Some of the HAADF images and EEL-SI at high resolution of chapter 4.2 were acquired at Université Paris-Sud in collaboration with Alicia Ruiz and Dr. Michael G. Walls.

The synthesis of the octahedral nanoparticles shown in chapter 5.1 must be credited to Dr. Beatriz Rivas-Murias, Dr. Alicia Prieto-Troitiño, Dr. Martín Testa-Anta, Dr. Miguel A. Ramos-Docampo, Dr. Benito Rodríguez-González and Dr. Verónica Salgueiriño, from the Applied Physics Department at Universidade de Vigo.

In chapter 5.2, Dr. Francisco de la Peña, Dr. Zineb Saghi and Prof. Paul Midgley, contributed with the development of the compressed sensing tomography algorithm used in the reconstruction.

Appendix C: Resum en català

L'adveniment de la nanotecnologia està portant amb ell l'aparició d'una gran quantitat de nous materials, compostos i aplicacions. En el seu desenvolupament, sovint té lloc fenomenologia sorprenent, o encara no ben entesa. Per omplir aquests forats en el nostre coneixement i poder desenvolupar noves aplicacions és de vital importància esbrinar la configuració estructural i química a nivell subnanomètric d'aquests components.

Per la seva gran resolució espacial, la microscòpia electrònica de transmissió ha esdevingut una eina indispensable en aquest context. A més, en un microscopi electrònic es poden combinar una gran varietat de tècniques que poden donar una quantitat d'informació enorme. Una d'aquestes tècniques és l'espectroscòpia de pèrdua d'energia dels electrons (EELS). Aquesta tècnica ha permès en els últims anys el mapejat d'elements químics i ions columna atòmica per columna atòmica, arribant a uns dels nivells més íntims als que es pot conèixer la matèria en estat sòlid.

L'objectiu d'aquesta tesi ha estat fer ús de l'EELS i d'altres tècniques emprades en microscòpia electrònica per entendre els processos químics que tenen lloc en diferents síntesis de nanopartícules. En aquest procés s'han desenvolupat també una sèrie d'eines enfocades al processat de les dades d'EELS ja sigui per a facilitar la seva interpretació, limitar problemes derivats de la seva adquisició (i. e. soroll) o calcular propietats concretes del material estudiat. A més aquesta tècnica s'ha combinat amb mètodes de reconstrucció 3D per obtenir una informació completa dels sistemes estudiats.

Pel que fa a les síntesis de nanopartícules estudiades, es presenten 5 casos concrets:

El primer d'ells és la síntesi de nanopartícules d'òxid de ferro cobertes d'òxid de silici basada en emulsions de reactius orgànics. En aquesta reacció s'identifiquen diferents estadis. Primerament la preparació de nanopartícules d'òxid de ferro cobertes en àcid oleic. Seguidament es produeixen esferes a partir de l'acumulació de nanopartícules d'òxid de ferro a la interfície d'una emulsió de elements hidrofòbics en aigua. Després té lloc un intercanvi de l'àcid oleic per acetats a la superfície de les partícules. Finalment es produeix un creixement de silici a partir de la difusió de precursors a l'interior de les esferes formades a partir de nanopartícules. Els diferents estadis han estat

caracteritzats per diverses tècniques de microscòpia electrònica i s'ha aconseguit realitzar les següents observacions:

- Imatges de TEM d'alta resolució mostren que les nanopartícules d'òxid de ferro són fase magnetita. El recobriment d'àcid oleic s'ha pogut observar directament a partir de mapes d'EELS.
- Després de l'addició d'un complex acètic s'observa a partir de mapes d'EELS un canvi morfològic important en el cobriment orgànic de les nanopartícules, mentre que la seva estructura cristal·lina de magnetita no es veu afectada.
- A partir d'imatges de Cryo-TEM s'ha demostrat la formació de clústers de nanopartícules de magnetita en ser dispersades en solució aquosa. Obtenint imatges d'aquesta nanopartícules a diferents intervals de temps, s'observa que l'òxid de silici creix sobre les nanopartícules mentre aquestes formen el clúster, un procés que s'atura un cop son ejectades. En sortir del clúster queda una marca en forma de mossegada a la superfície de les partícules.
- En els últims estadis de la síntesi, s'ha observat l'aparició de partícules d'òxid de ferro extremadament petites (al voltant de 1 nm). Això indica el possible trencament de parts de la superfície de la partícula d'òxid de ferro original.
- A partir del mapejat EELS, s'observa un recobriment orgànic a la superfície de l'òxid de silici crescut a sobre de les partícules d'òxid de ferro. Aquestes anàlisis també confirmen que no té lloc cap procés d'oxidació/reducció durant la síntesi.
- Aquestes observacions han permès el desenvolupament d'un model microscòpic per explicar els processos que tenen lloc durant la síntesi d'aquestes nanopartícules. Aquest model, demostra un intercanvi de lligands inesperat a la superfície de l'òxid de ferro a partir del seu trencament.

La segona síntesi estudiada està basada en intercanvis catiónics en el sistema Au-Ag-Se. Aquest tipus de reaccions comencen amb la síntesi de nanopartícules amb un sol tipus de catió, en aquest cas Ag_2Se , seguides de l'exposició a una solució amb un segon tipus de catió, en aquest cas Au(III) i algun tipus d'agent que faciliti la difusió dels cations cap dins i fora de l'estructura cristal·lina. En el cas presentat s'estudia una varietat de reaccions d'intercanvi en les que es canvien les condicions de temperatura, temps de reacció i agent d'intercanvi, amb l'objectiu d'entendre millor aquest tipus de reacció.

- Els productes obtinguts en les reaccions d'intercanvi iònic entre nanopartícules de seleniür de plata i ions d'or han estat identificats com a nanocristalls de fischerita pura, nanocristalls híbrids d'Au/Ag₂S i nanocristalls híbrids d'Au/Ag₂AuSe₂, en variar les diferents condicions de lligands (DDA o bé TOAB) i el temps de reacció (d'uns pocs segons fins a 30 minuts).
- Les estructures anteriors han estat identificades mitjançant TEM d'alta resolució, mapejat EELS i imatges HAADF.
- S'ha observat una capa rica en seleni a l'exterior de les partícules híbrides.
- No hi ha cap relació cristal·lina entre els dominis d'or metàl·lic i els de seleniür. La interfície entre dominis és amorfa.
- De les observacions es dedueix que la capa externa de les partícules originals de seleniür de plata actua com a una capa de sacrifici per a reduir els ions de la solució abans que aquests es difonguin a l'estructura cristal·lina.

Seguidament, en un treball paral·lel es presenta l'estudi de reaccions d'intercanvi iònic en el sistema Au-Ag-S, d'on s'han obtingut les següents observacions importants:

- Entre les diverses reaccions estudiades, mitjançant TEM d'alta resolució i imatges HAADF, s'observen dímers Au-Ag₃AuS₂, Au-AgAuS, i partícules buides de Au₂S.
- Diferents fases cristal·lines d'Ag₂S han estat observades en les partícules inicials, mitjançant HRTEM.
- Múltiples dominis d'or per partícula i defectes cristal·lins han estat observats en les partícules híbrides Au-AgAuS
- Les proporcions de concentració d'Ag/Au mesurades mitjançant EDX decreixen a la mostra Au-AgAuS respecte de la Au-Ag₃AuS.
- S'han sintetitzat mostres amb les mateixes condicions d'intercanvi iònic però partint de nanopartícules el·lipsoidals de sulfur de plata, obtenint el mateix tipus de nanocristalls finals però amb forma el·lipsoidal.
- L'intercanvi complet de cations de plata per cations d'or ha estat observat, demostrant que s'obtenen totes les fases intermèdies estables del sistema Au-Ag-S durant el procés.

La següent síntesi estudiada es troba al capítol 4. En ell, es presenten casos en els que s'ha fet ús de la informació que conté l'estructura dels pics d'EELS associats a un element per a calcular-ne propietats, com ara el seu estat

d'oxidació. La síntesi en qüestió és la de partícules core/shell d'òxid de manganès/òxid de ferro, en què es van fer les següents observacions:

- El procés estàndard de la síntesi dona lloc a partícules core/shell completes mentre que l'adició de baixos percentatges d'aigua dona lloc a partícules amb l'interior buit.
- En les partícules plenes s'observa la difusió d'ions de ferro cap a l'interior del nucli d'òxid de manganès a partir de les mesures d'EELS.
- L'òxid de manganès es correspon amb Mn_3O_4 per les partícules buides i amb MnO per les plenes, indicant que la presència d'aigua ha oxidat les partícules.
- A partir de tomografia STEM-HAADF s'han observat petits canals a la superfície i l'interior de les partícules buides.
- Les mesures realitzades demostren que el buidat de les partícules en presència d'aigua és degut a un procés galvànic iniciat per l'oxidació parcial de l'òxid de manganès. En síntesis subseqüents fent ús d'aigua desgasada i aigua amb aire dissolt es va confirmar que eren els agents oxidants dissolts en aigua combinats amb les altes temperatures de la síntesi els que modifiquen l'òxid de manganès.

L'última síntesi recollida en aquesta tesi és la de partícules core/shell octaèdriques d'òxid de cobalt, ferro i manganès. S'han estudiat paral·lelament, nanopartícules d'òxid de cobalt/ cobalt ferrita ($CoO@CFO$) i d'òxid de cobalt/ manganès ferrita ($CoO@MFO$) mitjançant mapejat d'EELS i tomografia EELS, obtenint el següents resultats:

- Els dos tipus de nanopartícules presenten una estructura policristal·lina, amb esquerdes a la superfície.
- A la mostra $CoO@CFO$ s'observa una escorça amb una proporció entre cobalt i ferro de 2:1.
- Imatges de resolució atòmica de partícules $CoO@MFO$ mostren que l'estructura cristal·lina correspon a Co_3O_4 .
- S'ha realitzat una reconstrucció tomogràfica de la distribució de cobalt oxigen, ferro i manganès a les mostres. Aquesta reconstrucció ha estat realitzada a partir de la integració dels pics d'EELS corresponents a cada element.
- Les reconstruccions mostren forats que travessen les partícules, així com la difusió dels elements de la capa superficial cap a l'interior de la partícula.

- L'observació de forats i difusió així com la valoració dels diferents potencials redox relatius mostren, com en el cas de la síntesis anterior, que té lloc un procés galvànic que dissol l'interior de les partícules. L'observació de Co_3O_4 en comptes de l'esperat CoO també recolza aquesta conclusió.

Durant el transcurs d'aquests treballs també s'han desenvolupat una sèrie d'eines i nous mètodes de caracterització per a l'estudi de nanopartícules. A continuació es detallen les contribucions més destacades de la present tesi en aquest aspecte.

Al capítol dos s'introdueix el concepte d'anàlisi de clústers ("clustering"), una eina utilitzada en el camp de l'anomenat "Big Data", aplicat a dades d'EELS. En aquesta secció s'expliquen diferents mètodes per aplicar clustering obtenint les següents conclusions:

- Els espectres EELS poden ser entesos com un objecte amb una sèrie d'atributs, els seus canals. A partir d'aquí es pot definir una mètrica, que representa la "distància" entre dos espectres. Amb aquestes definicions es pot començar a agrupar els espectres més pròxims en clústers, aconseguint una segmentació d'un espectre imatge d'EELS en funció de la composició dels diferents materials que hi apareguin.
- Aquesta segmentació pot ser utilitzada com a màscara per a aplicar anàlisi de components principals a posteriori, obtenint informació sobre gradients de composició en cada clúster de manera acurada.
- Alternativament es pot primer realitzar una descomposició MVA i aplicar clustering als mapes assignats a cada component obtenint de nou una segmentació amb informació química, aquest cop reduint el soroll associat a l'adquisició de cada espectre.
- Aquest tres mètodes han estat aplicats a imatges espectre d'EELS de partícules d'òxid de ferro/òxid de manganès, recuperant correctament la seva composició en un procés virtualment sense intervenció de l'usuari.
- S'ha demostrat que l'aplicació de clustering a dades d'EELS no només és possible si no que a més pot facilitar la interpretació de les dades i la detecció de tots els diferents compostos presents en un mapa d'EELS.

A la segona meitat del capítol 4 s'introdueixen diferents mètodes per calcular el paràmetre d'inversió en estructures espinela. Aquest paràmetre avalua l'ordenament catiònic en aquest tipus de compostos ternaris i és de gran rellevància en les propietats dels cristalls resultants. Fins a la realització d'aquest

treball els únics mètodes coneguts per a mesurar aquest valor tenien una resolució molt pobre, promitjant milions de cel·les unitat. El desenvolupament del nou mètode a partir de mapes amb resolució atòmica d'EELS acaba amb aquesta barrera de resolució espacial. Els mètodes han estat desenvolupats per a l'estudi de partícules core/shell d'òxid de ferro/òxid de manganès. S'han obtingut les següents conclusions:

- Les mostres estudiades consisteixen en partícules core/shell de $\text{Fe}_3\text{O}_4/\text{Mn}_3\text{O}_4$. L'escorça creix epitaxialment respecte al nucli, induint tensions a l'estructura cristal·lina.
- Si s'assumeix una relació lineal entre l'estat d'oxidació d'un dels cations i un paràmetre d'ELNES del seu pic EELS associat, és possible obtenir una fórmula que relaciona el paràmetre d'inversió del cristall amb el paràmetre d'ELNES de dos espectres corresponents a columnes atòmiques no equivalents.
- Aplicant aquesta fórmula s'obté un valor de $x = 0.84 \pm 0.02$ per als nuclis d'òxid de ferro.
- Amb el mateix mètode i a partir del canvi en la posició del pic Mn L_3 en columnes atòmiques amb coordinació tetraèdrica i octaèdrica, s'obté un valor per al paràmetre d'inversió de l'òxid de manganès de $x = 0.39 \pm 0.1$.
- Mesurant el paràmetre d'inversió amb un mètode ben establert, l'absorció de rajos X (XAS), s'obtenen els valors de $x = 0.44$ per al manganès i $x = 0.86$ per al ferro. Aquesta bona correspondència valida el càlcul a partir d'espectres EELS.
- S'ha desenvolupat un segon mètode de càlcul del paràmetre d'inversió a partir de la descomposició PCA dels mapes d'EELS obtinguts de les partícules. Si s'obtenen dos factors cada un amb contribucions d'un tipus de ió amb un estat d'oxidació concret respectivament, es pot calcular el paràmetre d'inversió a partir de la proporció dels seus mapes associats. Amb aquest càlcul s'obté un paràmetre d'inversió de $x = 0.35$ per al manganès.
- El mètode basat en PCA permet avaluar gradients en el paràmetre d'inversió. En les partícules observades s'aprecia un gradient d'inversió cap a la interfície core/shell de les partícules.

Finalment a la segona meitat del capítol 5 es demostra com obtenir una reconstrucció 3D que contingui tota la informació d'un espectre EELS a cada vòxel. Aquesta reconstrucció ha està obtinguda per un nanocub d'òxid de ferro. La informació obtinguda permet visualitzar l'estat d'oxidació del ferro a cada

punt de la partícula. Una combinació innovadora d'adquisició tomogràfica combinada amb algoritmes de anàlisi multivariable i de "compressed sensing" han permès obtenir aquesta anàlisi. Els resultats poden resumir-se de la següent manera:

- La mostra estudiada consisteix en una partícula core/shell de $\text{FeO}_x/\text{FeO}_y$. L'estructura és epitaxial i dona un contrast molt similar entre els seus dos components per HAADF. Per tant, l'única possibilitat de ser observada és mitjançant mesures de l'ELNES en mapes d'EELS.
- S'ha obtingut una descomposició PCA en la que una de les components correspon a la contribució als espectre d'EELS de ions Fe^{2+} i una segona a la de ions Fe^{3+} .
- Després de realitzar una correcció a la intensitat dels mapes obtinguts mitjançant la sèrie tomogràfica HAADF coadquirida, és possible utilitzar algoritmes de tomografia "compressed sensing" per a reconstruir-los en 3D.
- Les relacions d'intensitat entre aquestes reconstruccions a les zones corresponents a l'escorça de la partícula i al nucli indiquen que està composta de Fe_3O_4 ($\text{Fe}^{3+}:\text{Fe}^{2+} = 2$) i FeO ($\text{Fe}^{3+}:\text{Fe}^{2+} = 1$) respectivament.
- Les mides i gruix del nucli i l'escorça han esta mesurades en 3D, i la interfície s'ha avaluat com a menor de 1 nm. La caracterització per tomografia EELS explica correctament les propietats magnètiques de la mostra
- Aquest resultats constitueixen la primera reconstrucció 3D d'EELS basada en mètodes MVA demostrant informació corresponent a l'ELNES.

Amb els resultats exposats, s'aconsegueix l'objectiu inicial de la present tesi: aconseguir explicacions detallades dels processos que tenen lloc en la síntesi de nanopartícules mitjançant espectroscòpia EELS així com desenvolupar noves eines que permetin obtenir més informació a partir d'aquest tipus de mesures.

Appendix D: Scientific Curriculum

Relevant work experience

March 2018 – Present Electron Microscopy Facility Technician.
Universitat Autònoma de Barcelona.
Responsible for the Material Science area of the microscopy core facility of UAB including SEM, TEM and sample preparation services.

Education

2014 – 2019 PhD in Nanoscience.
Universitat de Barcelona.

2013 Master in Nanoscience.
Master Thesis: “Transmission Electron Microscopy Beam Precession: Imaging and chemical analysis applications.”
Universitat de Barcelona.

2008 – 2012 Bachelor degree in Physics.
Universitat de Barcelona.

Scientific publications

1. P. Torruella et al., Atomic-Scale Determination of Cation Inversion in Spinel-Based Oxide Nanoparticles. *Nano Lett.* (2018), doi:10.1021/acs.nanolett.8b02524.

2. A. Kertmen et al., Photoelectrochemically Active N-Adsorbing Ultrathin TiO₂ Layers for Water-Splitting Applications Prepared by Pyrolysis of Oleic Acid on Iron Oxide Nanoparticle Surfaces under Nitrogen Environment. *Adv. Mater. Interfaces*, 1801286 (2018).
3. P. Torruella et al., Clustering analysis strategies for electron energy loss spectroscopy (EELS). *Ultramicroscopy*. 185, 42–48 (2018).
4. A. Quintana et al., Voltage-Controlled ON-OFF Ferromagnetism at Room Temperature in a Single Metal Oxide Film. *ACS Nano*. 12 (2018), pp. 10291–10300.
5. M. Dalmases et al., Gradual Transformation of Ag₂S to Au₂S Nanoparticles by Sequential Cation Exchange Reactions: Binary, Ternary, and Hybrid Compositions. *Chem. Mater.* 30, 6893–6902 (2018).
6. J. Blanco-Portals et al., Atomistic modelling and high resolution electron microscopy simulations of CeO₂ nanoparticles. *Appl. Phys. Lett.* 111, 223107 (2017).
7. E. Fantechi et al., Seeded Growth Synthesis of Au–Fe₃O₄ Heterostructured Nanocrystals: Rational Design and Mechanistic Insights. *Chem. Mater.* 29, 4022–4035 (2017).
8. E. Coy et al., High Electrocatalytic Response of a Mechanically Enhanced NbC Nanocomposite Electrode Toward Hydrogen Evolution Reaction. *ACS Appl. Mater. Interfaces*. 9, 30872–30879 (2017).
9. A. Kertmen et al., Acetate-Induced Disassembly of Spherical Iron Oxide Nanoparticle Clusters into Monodispersed Core-Shell Structures upon Nanoemulsion Fusion. *Langmuir*. 33, 10351–10365 (2017).
10. T. Berestok et al., Tuning Branching in Ceria Nanocrystals. *Chem. Mater.* 29, 4418–4424 (2017).
11. P. Torruella et al., Assessing Oxygen Vacancies in Bismuth Oxide through EELS Measurements and DFT Simulations. *J. Phys. Chem. C*. 121, 24809–24815 (2017).

12. A. López-Ortega et al., Galvanic Replacement onto Complex Metal-Oxide Nanoparticles: Impact of Water or Other Oxidizers in the Formation of either Fully Dense Onion-Like or Multicomponent Hollow MnOx/FeOx Structures. *Chem. Mater.* 28, 8025–8031 (2016).
13. P. Torruella et al., 3D Visualization of the Iron Oxidation State in FeO/Fe₃O₄ Core-Shell Nanocubes from Electron Energy Loss Tomography. *Nano Lett.* 16, 5068–5073 (2016).
14. M. Dalmases et al., Synthesis and Thermoelectric Properties of Noble Metal Ternary Chalcogenide Systems of Ag – Au – Se in the Forms of Alloyed Nanoparticles and Colloidal Nanoheterostructures. *Chem. Mater.* 28, 7017–7028 (2016).
15. V. Fernández-Altable et al., Au-assisted growth of anisotropic and epitaxial CdSe colloidal nanocrystals via in situ dismantling of quantum dots. *Chem. Mater.* 27, 1656–1664 (2015).
16. L. Yedra et al., Precessed electron beam electron energy loss spectroscopy of graphene: Beyond channelling effects. *Applied Phys. Lett.* 105, 053117 (2014).

Congress contributions

1. “Fe oxidation state 3D mapping of core-shell nanoparticles.”, Torruella, P.; Arenal, R.; Saghi, Z.; Yedra, L.; Eljarrat, A.; de la Peña, F.; Midgley, P.; Estradé, S.; Peiró, F.; **9e edition des Journées EELS** (2014). Oral.
2. “3D Mapping of Oxidation States in Heterostructured Nanomaterials”, Torruella, P.; Arenal, R.; Saghi, Z.; Yedra, L.; Eljarrat, A.; López-Conesa, L.; de la Peña, F.; Estrader, M.; Salazar-Álvarez, G.; López-Ortega, A.; Nogués, J.; Midgley, P.A.; Peiró, F.; Estradé, S.; **International Microscopy Congress 18** (2014). Poster.
3. “3D mapping of oxidation states in heterostructured nanomaterials”, Torruella, P.; Arenal, R.; Saghi, Z.; Yedra, L.; Eljarrat, A.; López-Conesa, L.; de la Peña, F.; Estrader, M.; Salazar-Álvarez, G.; López-Ortega, A.; Nogués, J.; Midgley, P.A.; Peiró, F.; Estradé, S.; **MRS Fall Meeting** (2014). Oral.

4. "Transmission Electron Microscopy Beam Precession: Imaging and chemical analysis applications" Torruella, P.; Estradé, S.; Mendoza, J.; Portillo, J.; Peiró, F.; **Electron Crystallography School** (2014). Poster.
5. "Silver chalcogenide-based hybrid nanocrystals with enhanced thermoelectric properties", Figuerola, A.; Dalmases, M.; Martínez, A.; Ibañez, M.; Cabot, A.; Llorca, J.; Torruella, P.; Estradé, S.; Fernández-Altabel, V.; **Fourth International Conference on Multifunctional, Hybrid and Nanomaterials** (2015). Poster.
6. "Silver chalcogenide-based hybrid nanocrystals with enhanced thermoelectric properties.", Figuerola, A.; Dalmases, M.; Martínez, A.; Ibañez, M.; Cabot, A.; Llorca, J.; Torruella, P.; Estradé, S.; Fernández-Altabel, V.; **Advances in Functional Materials** (2015). Oral.
7. "Multidimensional EELS: from spectrum image to spectrum volume and beyond.", Torruella, P.; Arenal, R.; Saghi, Z.; Yedra, L.; de la Peña, F.; Eljarrat, A.; Estrader, M.; López-Conesa, L.; Martín, G.; López-Ortega, A.; Salazar-Alvarez, G.; Nogués, J.; Midgley, P.A.; Peiró, F.; Estradé S.; **Energy Materials Nanotechnology Spain** (2015). **INVITED**.
8. "Energy Loss Spectroscopy of Bi₂O₃", Torruella, P.; Eljarrat, A.; Coll, C.; López-Conesa, L.; Martín, G.; Vila, M.; Díaz-Guerra, C; Piqueras, J.; Estradé, S.; Peiró, F.; **Microscopy at the Frontiers of Science** (2015). Oral.
9. "Accessing the Chemical and Optoelectronic Properties of Nanostructures in 3D: The EELS Spectrum Volume.", Torruella, P.; Arenal, R.; Saghi, Z.; Yedra, L.; de la Peña, F.; Eljarrat, A.; Estrader, M.; López-Conesa, L.; Martín, G.; López-Ortega, A.; Salazar-Alvarez, G.; Nogués, J.; Midgley, P.A.; Peiró, F.; Estradé S.; **Energy Materials Nanotechnology Open Access Week** (2015). **INVITED**.
10. "Oxide Wizard as a new tool to probe magnetic properties at the nanoscale.", Torruella, P.; Yedra, L.; Xuriguera, E.; Estrader, M.; López-Ortega, A.; Baró, M.; Nogués, J.; Roldan, M.; Varela, M.; Estradé, S.; Peiró, F.; **20th International Conference on Magnetism** (2015). Poster.

11. "Dimer-like Au-Ag₃AuSe₂ hybrid nanocrystals for thermoelectric Applications", Dalmases, M.; Figuerola, A.; Torruella, P.; Estradé, S.; Peiró, F.; Ibáñez, M.; Cabot, A.; Llorca, J.; Fernández-Altable, V.; **E-MRS Fall Meeting** (2015). Poster.
12. "Silver chalcogenide-based hybrid and ternary nanocrystals with enhanced thermoelectric properties." Dalmases, M.; Figuerola, A.; Torruella, P.; Estradé, S.; Peiró, F.; Ibáñez, M.; Cabot, A.; Llorca, J.; Fernández-Altable, V.; **E-MRS Fall Meeting** (2015). Oral.
13. "Determination of the local oxidation state of transition metals in 3D: application to magnetic nanoparticles.", S. Estradé; P. Torruella; R. Arenal; L. Yedra; A. Eljarrat; L. López-Conesa; F. Peiró; M. Estrader; A. López-Ortega; G. Salazar- Alvarez; J. Nogués; **20th International Conference on Magnetism** (2015). Oral.
14. "EELS-tomography. Pushing the spatial and spectral resolution". P. Torruella; R. Arenal; Z. Saghi; Ll. Yedra; A. Eljarrat; F. de la Peña; M. Estrader; G. Salazar-Alvarez; A. López-Ortega; J. Nogués; P. A. Midgley; F. Peiró; S. Estradé; **EUROMAT** (2015). Oral.
15. "EELS-Tomography: enabling 4D chemical and oxidation state characterization of complex metal-oxide nanostructured materials.", P. Torruella; R. Arenal; Z. Saghi; L. Yedra; A. Eljarrat; J. Rebled; F. de la Peña; M. Estrader; G. Salazar-Alvarez; A. López-Ortega; J. Nogués; Paul A. Midgley; S. Estradé; F. Peiró; **NanoToday** (2015). Poster.
16. "EELS tomography: recovering the spectrum volume from MVA methods .", Torruella, P.; Eljarrat, A.; Martín, G.; Rebled, J.M.; López-Conesa, L.; Coll, C.; Ruiz, A.; Plana, S.; Estradé, S.; Peiró, F.; **10ème édition des Journées de l'EELS** (2016). Oral.
17. "DFT simulations of α -Bi₂O₃ and β -Bi₂O₃ EEL spectra.", Coll, C.; Torruella, P.; Vila, M.; Díaz-Guerra, C.; Piqueras, J.; Estradé, S.; Peiró, F.; **10ème édition des Journées de l'EELS** (2016). Oral.
18. "3D oxidation state characterisation in magnetic nanoparticles". Estradé, S.; Torruella, P.; Yedra, Ll.; Eljarrat, A.; López-Conesa, L.; Arenal, R.; de la Peña, F.; Saghi, Z.; Estrader, López-Ortega, A.; Salazar-

- Alvarez, G.; Nogués, J.; Midgley, P.A.; Peiró, F.; **Energy Materials and Nanotechnology Croatia Meeting** (2016). Oral.
19. “EELS-Tomography: Enabling 4D chemical and oxidation state characterization of nanostructured materials.”, Torruella, P.; Arenal, R.; Saghi, Z.; Yedra, Ll.; Eljarrat, A.; Rebled, J.M.; de la Peña, F.; Estrader, M.; Salazar-Alvarez, G.; López-Ortega, A.; Nogués, J.; Midgley, P.A.; Estradé, S.; Peiró, F.; **NanoTech Poland International Conference** (2016). **INVITED**.
20. “Characterization of silica coated, mono-dispersed iron oxide nanoparticles and their cellular uptake by *Saccharomyces Cerevisiae* as eukaryotic cell models.”, Kertmen, A.; Torruella, P.; Przysiecka, L.; Coy, E.; Estradé, S.; Peiró, F.; Scheibe, B.; Jurga, S.; Andruszkiewicz, R.; Milewski, S.; **NanoTech Poland International Conference** (2016). Oral.
21. “Synthesis and Characterization of Ag₂Se-Based Hybrid and Ternary Semiconductor Nanocrystals with potential thermoelectric Applications.”, Torruella, P.; Dalmases, M.; Fernández-Altable, V.; Cabot, A.; Ibáñez, M.; Llorca, J.; López-Conesa, L.; Martín, G.; Estradé, S.; Peiró, F.; **16th European Microscopy Conference** (2016). Oral.
22. “Impact of water and oxidation states in the galvanic replacement formation of hollow oxide nanoparticles.”, Torruella, P.; López-Ortega, A.; Roca, A.; Petrecca, M.; Estradé, S.; Peiró, F.; Puentes, V.; Nogués, J.; **16th European Microscopy Conference** (2016). Poster.
23. “A Route to the Superparamagnetic Mono-Dispersed Iron Oxide / Silica Core-Shell Nanoparticles.”, Kertmen, A.; Torruella, P.; Tadyszak, K.; Chybczynska, K.; Coy, E.; Estradé, S.; Vogt, C.; Scheibe, B.; Peiró, F.; Jurga, S.; Milewski, S.; Toprak, M.; Andruszkiewicz, R.; **E-MRS Fall Meeting** (2016). Oral.
24. “Colloidal Au-Ag-Chalcogen-Based Ternary Nanocrystals for Energy Conversion Applications.”, Figuerola, A.; Dalmases, M.; Ibáñez, M.; Torruella, P.; Fernández-Altable, V.; López-Conesa, L.; Cadavid, D.; Piveteau, L.; Nachtegaal, M.; Llorca, J.; Luisa Ruiz-González, M.L.; Estradé, S.; Peiró, F.; Kovalenko, M.V.; Cabot, A.; **Applied**

Nanotechnology and Nanoscience International Conference (2016).
Oral.

25. "A journey through the secret life of nanoparticles: from 2D high resolution images to 3D oxidation state mapping.", Torruella, P.; Arenal, R.; Saghi, Z.; Yedra, L.; Eljarrat, A.; Rebled, J.; de la Peña, F.; Estrader, M.; Salazar-Alvarez, G.; López-Ortega, A.; Nogués, J.; Midgley, P.A.; Estradé, S.; Peiró, F.; **3rd edition of the NanoBio&Med International Conference (2016).** Oral.
26. "Colloidal Au-Ag-Chalcogen-Based Heterostructured and Alloyed Nanocrystals for Energy Conversion Applications .", Figuerola, A.; Dalmases, M.; Ibáñez, M.; Torruella, P.; Fernàndez-Altable, V.; López-Conesa, L.; Cadavid, D.; Piveteau, L.; Nachtegaal, M.; Llorca, J.; Ruiz-González, M. L.; Estradé, S.; Peiró, F.; Kovalenko, M. V.; Cabot, A.; **13th International Conference on Nanosciences & Nanotechnologies (2016).** Oral.
27. "Controlled synthesis of Ag-Au-S ternary nanostructured semiconductors.", Dalmases, M.; Vidal, A.; Rosolen, I.; Figuerola, A.; Torruella, P.; Estradé, S.; Peiró, F.; **Applied Nanotechnology and Nanoscience International Conference (2016).** Poster.
28. "High resolution mapping of oxidation states in core-shell nanoparticles.", Torruella, P.; Ruiz-Caridad, A.; Walls, M.G.; Gómez-Roca, A.; Nogués, J.; López-Conesa, L.; Estradé, S.; Peiró, F.; **Microscopy at the Frontiers of Science (2017).** Oral.
29. "Elucidation of the structure of octopod branched ceria nanocrystals by transmission electron microscopy: contrast simulations and electron tomography.", Blanco-Portals, J.; Berestok, T.; Torruella, P.; Coll, C.; López-Conesa, L.; Guardia, P.; Cabot, A.; Estradé, S.; Peiró, F.; **NanoTech Poland International Conference (2017).** INVITED.
30. "Revealing magnetic core-shell nanoparticles structure at the nanoscale.", A. Ruiz-Caridad; M.G. Walls; A. Gómez-Roca; J. Nogués; P. Torruella; L. López-Conesa; S. Estradé; F. Peiró; **International Union of Materials Research Societies and 15th International Conference on Advanced Materials (2017).** INVITED.

31. "Formation of Mn_3O_4/Fe_3O_4 hollow oxide nanoparticles by galvanic replacement.", López-Ortega, A.; Roca, A.G.; Torruella, P.; Petrecca, M.; Estradé, S.; Peiró, F.; Puentes, V.; Nogués, J.; **International Union of Materials Research Societies and 15th International Conference on Advanced Materials** (2017). **INVITED.**
32. "EELS assessment of Oxidation state in Bi_2O_3 .", Torruella, P.; Coll, C.; Martín, G.; López-Conesa, L.; Vila, M.; Díaz-Guerra, C.; Varela, M.; Ruiz-González, M.L. Piqueras, J.; Peiró, F. and Estradé S.; **FFSCI Nanoscience and EMN Croatia Meeting** (2017). **INVITED.**
33. "Understanding the synthesis of $Au-Fe_3O_4$ nanocrystals for biomedical applications .", A.G. Roca, E.; Fantechi, A.; López-Ortega, N.; G. Bastus; P. Torruella; S. Estradé; F. Peiró; B. Sepúlveda; V. Puentes; J. Nogués; **78th Japan Society of Applied Physics (JSAP) Autumn Meeting** (2017). **INVITED.**
34. "My hovercraft is full of EELS: Making the most of Core-Loss Electron Energy Loss Spectroscopy for Materials Science.", Estradé, S.; Yedra, L.; Eljarrat, A.; López-Conesa, L.; Rebled, J. M.; Torruella, P.; Martín-Malpartida, G.; Coll-Benejam, C.; Plana, S.; Ruiz-Caridad, A.; Blanco, J.; Peiró, F.; **Microscopy at the Frontiers of Science** (2017). **INVITED.**
35. "Atomistic Modelling and High Resolution Electron Microscopy Simulations of CeO_2 Octapods .", Blanco-Portals, J.; Berestok, T.; Torruella, P.; Coll, C.; López-Conesa, L.; Guardia, P.; Coy, E.; Cabot, A.; Estradé S.; and Peiró, F.; **Microscopy at the Frontiers of Science** (2017). **Oral.**
36. "Unveiling the secrets of Mn_xO_y/Fe_xO_y core-shell nanoparticles through electron microscopy techniques.", Torruella, P.; López-Conesa, L.; Ruiz-Caridad, A.; Walls, M.; Roca, A.G.; López-Ortega, A.; Nogués, J.; Estradé, S.; Peiró, F. ; **5th International Conference on Analytical Science and Technology** (2017). **INVITED.**
37. "Assessment of octopod morphology of branched ceria nanocrystals.", Blanco-Portals, J.; Berestok, T.; Torruella, P.; Coll, C.; López-Conesa, L.;

Guardia, P.; Coy, E.; Cabot, A.; Estradé S.; and Peiró, F.; **5th Nano Today Conference** (2017). Poster.

38. "Seeded growth synthesis of Au-Fe₃O₄ heterostructured nanocrystals for possible biomedical Applications.", Fantechi, E.; Roca, A.G.; Sepúlveda, B.; Torruella, P.; Estradé, S.; Peiró, F.; Coy, E.; Jurga, S.; Pineider, F.; Bastús, N. G.; Puentes, V.; Nogués, J.; **24th Annual International Conference on Composites and Nano Engineering** (2017). **INVITED.**
39. "Controlled formation of Mn₃O₄/Fe₃O₄ hollow oxide nanoparticles, with possible biomedical applications, by galvanic replacement.", López-Ortega, A.; Roca, A.G.; Torruella, P.; Petrecca, M.; Estradé, S.; Peiró, F.; Puentes, V.; Nogués, J.; **24th Annual International Conference on Composites and Nano Engineering** (2017). **INVITED.**
40. "Atomic resolution spatially-resolved inversion parameter in spinel oxides.", Torruella, P.; Ruiz-Caridad, A.; Walls, M.; Roca, A.G.; Lopez-Ortega, A.; Blanco-Portals, J.; Lopez-Conesa, L.; Nogués, J.; Peiro, F.; Estrade, S.; **19th International Microscopy Congress** (2018). Oral.
41. "Some clues and misconceptions from high resolution scanning-transmission electron microscopy of advanced functional materials.", Peiró F; López-Conesa, J.; Coll, C.; Rebled J.M; Blanco J.; Barrigón E; Barrutia L; Rey-Stolle, I.; Algora, C.; Magén C.; Sánchez F.; Fontcuberta J.; Berestok T; Torruella P.; Guardia P.; Coy E.; Cabot A.; Estradé S.; **Caribbean Conference on Functional Materials** (2018). **INVITED.**
42. "Synthesis & Applications of Colloidal Au-Ag-Chalcogen-Based Ternary Nanocrystals with Tunable Composition.", Figuerola, A.; Dalmases, M.; Torruella, P.; Estradé, S.; Peiró, F.; **III International Symposium on Nanoparticles/Nanomaterials and Applications** (2018). Oral.
43. "Simulations to avoid misconceptions from high resolution scanning-transmission electron microscopy of advanced functional materials.", Peiró, F.; López-Conesa, L.; Coll C.; Rebled, J.; Barrigón, E.; Barrutia, L.; Rey-Stolled, I.; Algora, C.; Magén, C.; Sánchez, F.; Fontcuberta, J.; Torruella, P.; Estradé, S.; **NanoTech Poland International Conference and Exhibition** (2018). **INVITED.**

44. "Use of clustering analysis for the treatment of large EELS datasets.", López-Conesa, L.; Torruella, P.; Blanco-Portals, J.; Estradé, S.; Peiró, F.; **2nd ELECMI International Workshop** (2018). Oral.
45. "EELS + DFT on the study of oxygen deficient α -Bi₂O₃.", Coll-Benejam, C.; Torruella, P.; Martín-Malpartida, G.; López-Conesa, L.; Vila, M.; Díaz-Guerra, C.; Varela, M.; Ruiz-Gonzalez, M. L.; Piqueras, J.; Estradé, S.; Peiró, F.; **19th International Microscopy Congress** (2018). Poster.